Imaging of Orientation and Geometry in Microstructures:

Development and Applications of High Energy X-ray Diffraction Microscopy

by

Li, Shiu Fai Frankie

Submitted in partial fulfillment of the
requirements for the degree of
Doctor of Philosophy
at
Carnegie Mellon University
Department of Physics
Pittsburgh, Pennsylvania

Advised by Professor Robert M. Suter

May 3, 2011

Contents

1 Introduction **1**
- 1.1 Motivation . . . 1
- 1.2 Overview . . . 2
- 1.3 Outline . . . 2

2 High Energy X-ray Diffraction Microscopy **5**
- 2.1 Overview . . . 5
- 2.2 Review of Scattering Physics . . . 6
  - 2.2.1 Kinematic Scattering . . . 6
  - 2.2.2 Rotation Method . . . 10
- 2.3 HEDM Measurements . . . 11
  - 2.3.1 Overview . . . 11
  - 2.3.2 Experimental Setup . . . 12
  - 2.3.3 Experimental Procedure . . . 12
- 2.4 Data Reduction . . . 17
- 2.5 Conclusion . . . 18

3 Orientation Imaging Through Digital Reconstruction **19**
- 3.1 Overview . . . 19
- 3.2 Methods of Orientation Reconstruction . . . 21
  - 3.2.1 Problem Statement . . . 21
- 3.3 Review of Existing Reconstruction Techniques . . . 22
  - 3.3.1 Shortcomings of Peak Center of Intensity Methods . . . 25
- 3.4 Forward Modeling . . . 26
  - 3.4.1 Overview . . . 27
  - 3.4.2 Definitions . . . 27
  - 3.4.3 Cost Function . . . 29
  - 3.4.4 Cost Function Landscape . . . 32
  - 3.4.5 Existence and Uniqueness of A Global Optimum . . . 33
- 3.5 Orientation Search Algorithm . . . 35
  - 3.5.1 Orientation Discretization . . . 35
  - 3.5.2 Exhaustive Search . . . 39

3.5.3 Stratified Monte Carlo Pruning . . . 40
3.5.4 Simple Spatial Resolution Model . . . 43
3.5.5 Validations . . . 44
3.5.6 Experimental Parameter Bootstrap Optimization . . . 51
3.6 Summary . . . 54
3.6.1 Major Advances in Orientation Reconstruction . . . 54
3.6.2 Future and Ongoing Work . . . 55

4 Robust Geometric Extraction **57**
4.1 Overview . . . 57
4.2 Extraction of Geometries and Topologies . . . 58
4.2.1 Data Representations . . . 58
4.2.2 Interpolations and Approximation . . . 61
4.2.3 Approximation vs. Interpolation in Surface Mesh Generation . . . 64
4.3 Mesh Generation . . . 65
4.3.1 Overview . . . 65
4.3.2 Related Work . . . 66
4.3.3 Implementation . . . 72
4.4 Geometric Extraction . . . 78
4.4.1 Mean Width . . . 78
4.4.2 Noise and Reconstructed Surfaces . . . 79
4.4.3 Resolution Studies of Extracted Geometry . . . 80
4.4.4 Multiple Microstructure Registration . . . 84
4.4.5 Grain Tracking . . . 91
4.4.6 Boundary Tracking . . . 93
4.5 Conclusion . . . 93
4.6 On-going and Future Directions . . . 93

5 Non-destructive Observation of Grain Coarsening in 3D, Initial Report **95**
5.1 Overview . . . 95
5.2 Experimental Procedure . . . 98
5.2.1 Sample Preparation . . . 98
5.2.2 Orientation Imaging Procedures . . . 99
5.3 Analysis . . . 100
5.3.1 Orientation Reconstruction . . . 101
5.3.2 Grain Extraction . . . 103
5.3.3 Microstructure Geometry . . . 103
5.4 Results . . . 104
5.4.1 Grain Statistics . . . 104
5.4.2 Direct Observations of Grain Geometry Evolution . . . 107
5.4.3 Direct Observations of Grain Topology Evolution . . . 114

5.5 Discussion . . . 115
5.6 Future Work . . . 115

6 In Situ Observation of Spatially Resolved Orientation Evolution in the Deformation of High Purity Copper Wire 117
6.1 Preliminaries . . . 117
6.2 Introduction . . . 117
6.3 Methods . . . 119
6.3.1 Adaptation of Near-field HEDM for *in situ* Study of Deformed States . . . 119
6.3.2 Apparatus and Sample . . . 122
6.3.3 Volume Measurement Procedures . . . 122
6.3.4 Diffraction Signals . . . 123
6.4 Analysis . . . 125
6.4.1 Forward Modeling Validation . . . 125
6.4.2 Stability of Forward Modeling Reconstruction . . . 128
6.5 Results . . . 136
6.5.1 Lattice Rotations . . . 136
6.6 Conclusions . . . 143
6.7 On-going and future work . . . 143

Appendices

A Examples of Reconstructed Orientation Maps 147

B Reconstructed Surface Meshes 151

C Volumetric Map Examples 153

List of Tables

5.1 Grain size (interior only) and annealing time for each of the measured states. 101

List of Figures

2.1 Scattering of an X-ray by a charge distribution at the origin. 7

2.2 Geometry of a rotating crystal method for X-ray diffraction in the analysis coordinate system. (a) Coordinates used to solve for ω where $\vec{G}_{hkl}$ satisfies the Bragg condition. (b) Rotating crystal method setup, with $\vec{g}$ as the reciprocal lattice vector, and ω is rotated about the $\hat{z}$ axis. 10

2.3 Schematic of the HEDM setup at Sector 1-ID:B of the Advanced Photon Source. Only the most relevant parts are shown. SampX, SampY, and SampZ are the sample translation motors. PreciH is the air-bearing rotation stage with $\leq 0.1\mu m$ eccentricity. The entire sample column is placed on top of StageZ and StageX, two linear motors with $1\mu m$ precision. The detector column is mounted on the motors DetX, DetY, and DetZ, which are used to adjust image plane location with respect to the sample (top of the sample column). The scattered X-rays from the sample are imaged with a detector system: a scintillator converts X-ray radiation to visible light, which is reflected by a 45° mirror (blue) and magnified by the focusing optics (red) onto a CCD detector. The direct beam is stopped after the sample at the beam block (green). IDB6 and IDB5 are ion chambers used to monitor the flux of the incoming beam. The horizontal and vertical X-ray absorbing slits (JJs) can be used to reduce the beam size for cases like the raster scan described below. 13

2.4 An example of a raster scan for a tilted detector. The blue dots indicate the locations of the direct beam as the detector is translated to four different locations. The objective of detector calibration is to align so that the grid lines are parallel to the plane of the X-ray beam (into the page). When the optical focus is set on the center of the detector, the aberration will be most noticeable near the edges of the detector. This is problematic as the high $|\vec{Q}|$ peaks contribute most to the spatial and orientation resolution of the reconstructed orientation map. An ad hoc solution to this problem is to optimize focus on the annulus around the center (shown in green) so that the center is still within the depth of focus ($\approx 2\mu m$). In this configuration, almost no aberration is observed. 16

3.1 Coordinate system for a rotating crystal experiment. This is the convention used at the APS beamline. The line-focused incident beam propagates with $\vec{k_i} \parallel \vec{z}$ and, if not blocked, would intersect the detector along the blue line. The red rectangle at the coordinate origin represents the sample region being measured. The blue element, $v(\vec{x})$, is a particular volume element in the sample space which, at rotation position ω, produces a diffracted wavevector $\vec{k_o}$ intersecting pixel (j, k) of the CCD detector (with $nX \times nY$ pixels). The polycrystalline nature of the sample suggests that intensity, $I(j, k)$, can be a result of not only $v(\vec{x})$, but also its neighboring volume elements. This is known as "accidental overlap." The diffraction peak due to $\vec{k_o}$ is considered a qualified peak as it satisfies the geometrical constraints of the system (it strikes the detector at both L_1 and L_2). Notice that the diffracted intensity originating from $v(\vec{x})$ due to this $\vec{G}_{hkl}$ could lie on any point along the dotted arc (2θ-ring) if the crystal lattice were rotated about the incident beam; this is true even for volume elements that are off the rotation axis. On the other hand, rotations about this $\vec{G}_{hkl}$ leave this peak position unaltered. All other rotations about axes with a component along y or z, will cause the Bragg condition to be satisfied at a different ω; those not parallel to y will change both ω and η. For off-axis volume elements, changes in ω change the location of the origin of the scattering, and hence move the peak to a shifted 2θ-ring. The coupled, complex motion of the many diffraction spots observed from each volume element (as a function of lattice orientation) is the key to resolving both crystal orientations and corresponding positions. . . . 23

3.2 Discretization of a microstructure. A microstructure can be represented by an orientation field, $\mathcal{O}(\vec{x})$, where $\vec{x}$ is a point in the sample space. A discretized sample space (right) is used in the Forward Modeling method. 26

3.3 Representative landscape of the cost function for a single voxel. (a), (b), and (c) are successively expanded scale representations of the same cost function $\mathcal{C}$ for the reconstruction of a single simulated voxel in absence of any other diffraction spots, i.e., a single crystal experiment. The misorientation angle (x-axis) indicates the distance away from the known orientation solution, which goes up to $\approx 62^\circ$ because of the fundamental zone restriction. The sampling rate of the cost function is lowered in (a) to show the local minima structure typical to $\mathcal{C}$. The plot in (d) shows the features of a single-voxel cost function in a polycrystalline sample ($Q_{max} = 10$). Features seen here are indicative of well ordered crystals (500 randomly oriented grains). Multiple local minima occur across the fundamental zone plotted, with a significant number showing up around 60°, which is attributed to rotations about high symmetry axes. General broadening of the cost function can also be observed when Q_{max} is reduced. This restriction amounts to lowering the total number of peaks used for orientation reconstruction. This feature is exploited in the adaptive search method (Algo. 3). 36

3.4 Pictorial representation of the refinement process. The intersections of the black lines represent the uniform grid used to sample globally. The blue circles indicate regions of shallow, broad minima of the cost function. Green circles indicate sharp false minima, while the solid red circle is the true global minimum for the specific Q_{max} used for this reconstruction. At each iteration going from (a) to (c), the angular resolution of the cost function is increased by increasing Q_{max}. 42

3.5 Reconstruction test using a synthetic microstructure (a) designed to be difficult for the reconstruction code due to the successively neighboring twin structures that lead to significant peak overlaps. The reconstructed map (b) with its confidence plot (d) indicates that while most "grains" are reconstructed, about ten distinct points appear to have below expected confidence. The blue ring around the reconstructed confidence map indicates that the analysis code is unable to find suitable orientations for these points, which is in agreement with the synthetic structure. (c) is a plot of the distribution of the confidence. 46

3.6 Orientation reconstruction test for plastically deformed Ti. (a) Plastic deformation, manifested as orientation gradients across each grain (shown as variations of the false color) on titanium was simulated using finite element methods [18]. (b) Diffraction signals of the deformed Ti generated using the forward modeling method. It is shown that the diffraction patterns are smeared across many images and pixels (both η and ω directions). (c) Reconstructed orientation map from the deformed Ti diffraction patterns. This test shows the viability of reconstructing materials with orientation gradients. (d) Point-to-point misorientation comparison between the original and reconstructed orientation map. We see that the errors in the orientation reconstruction are relatively low and that the grain boundary geometries across the two maps are very similar. It should be emphasized that the reconstruction grid and forward simulation grids are deliberately incommensurate so that reconstruction noise is not artificially suppressed. . . . 48

3.7 Orientation noise variation with Q_{max} and reconstructed resolution. Noise is measured by a locally, or kernel, averaged misorientation calculation (the strained copper wire data and kernel averaging are discussed in detail in Chapter 6). (a-d) A comparison of the effects of different spatial and reciprocal space resolutions on reconstructed orientation maps. A progression of degradation of features can be seen as spatial resolution is decreased. Reduced number of peaks used for orientation reconstruction leads to significant increase of orientation noise, as seen in (a). Finally, while overall features of kernal averaged misorientation remain relatively stable as spatial resolutions were varied, changes in Q_{max} significantly alter the global result. 49

3.8 A histogram comparing the variation of the distribution of local average misorientation (Fig. 3.7 as a function of Q_{max}, sample spatial resolution, and L-distance. All fits were performed at $Q_{max} = 12$ except for the case indicated otherwise. Broadening of the local misorientation distribution can be seen in the $Q_{max} = 10$ case. Along with the spatially resolved KAM map, this indicates that the use of lower Q_{max} results in a generally noisier reconstructed orientation map. 50

3.9 Orientation maps reconstructed using different intensity thresholds of the diffracted peaks. Each map is thresholded at 0.6 confidence. Different intensity ranges of the diffraction peaks correspond to different regions of the reconstructed grains. 52

3.10 Confidence plots for reconstructed maps with different intensity thresholds. Only regions around grain boundaries are reconstructed in cases where the high intensity portion of the diffraction peaks, i.e., central regions, are removed. 53

4.1 A graph G provides an abstract representation of the two-dimensional microstructure shown. Each grain is represented by a vertex v (numbered.) Each connection between a pair of grains are represented by an edge $e(v, v')$. Two grains are limited to neighbor at most once with each other (i.e., the graph G is undirected, and there exists at most one edge for each pair of vertices.). Edges of G therefore provide an abstract representation of boundaries between each pair of grains. . . 60

4.2 A schematic showing a common way to use linear interpolation functions to help define boundaries in a multi-domained material. In this two-dimensional example, the three different colors indicated correspond to three different domains with grain indices 1, 2, and 3. The interpolation scheme shifts the entire image by $(\frac{\Delta x}{2}, \frac{\Delta y}{2})$, which does not affect the outcome of the defined boundaries. Bilinear interpolation is applied to the indicator functions χ_i to define $\chi_i(\vec{p})$ everywhere in the domain. The interpolation parameters, α and β are defined by the location of $\vec{p}$ with respect to the reference point ($\vec{x}_0$ in this diagram) in the interpolating domain D_n. 62

4.3 Interface between two regions with red being regions of $f(p_{i,j,k}) < 0$ and white being $f(p_{i,j,k}) > 0$. The voxels (shown only as a two-dimensional projection) approximate the plane indicated by the blue line. As we decrease the voxel size in the sample grid, the distance between the approximate isocontour (grid steps) and the actual isocontour will converge to zero. However, since each facet of the grid point is fixed, the local normal estimate will never converge. 67

4.4 The two-dimensional version of Marching Cubes for illustrative purposes. In the pixelized region, red and blue indicate regions of two different gray levels. New vertices (white) are placed on the edges of the cube based on the configuration of signs in each cube (green square). Because the vertex placement is determined locally, some configurations (center and right) do not produce unique isocontouring. 68

4.5 An octree is used to decompose the domain of $f(p_{i,j,k})$. A two-dimensional schematic is shown here. Meshes produced from a spatially adaptive octree will exhibit the same hierarchical features. This means large triangles will be used to represent regions with large features, and small triangles will be used in sharp regions to ensure that the meshed surface conforms to the true isosurface. 69

4.6 A two-dimensional schematic of Dual Contouring. Red and blue pixels represent two regions separated by an isocontour. The green box represents the octree (quadtree in $2D$). The cell with the dotted line is expanded to demonstrate the calculation of the minimizer point (green dot). The normals $\hat{n}_1$ and $\hat{n}_2$ are estimated using the trilinear interpolation of $f(p_{i,j,k})$. The minimizer point, the intersection of the two tangent lines of the estimated isocontour at the points p_1 and p_2, is obtained by minimizing the quadratic error function (Eq. (4.12)). The levels of the quadtree are chosen for illustrative purposes only. 70

4.7 A $2D$ schematic of surface reconstruction using Delaunay refinement. The diagram on the left shows the point set $\mathbf{P}$ (black dots) sampling the domain. The Delaunay triangulation is shown by the black and green edges. The green edge (triangle in $2D$) corresponds to the facet that represents the isocontour B, indicated by the red curve. The purple lines are the Voronoi edges. Note that the dual Voronoi edge of the boundary facet intersects the isocontour (green dot). A *Delaunay ball* (black circle), a ball circumscribing the vertices of the initial facet (two points in $2D$, three points in $3D$), is centered on the intersection point between the surface Voronoi edge and the isocontour. To refine the triangulation, a vertex is inserted at the center of the surface Delaunay ball. The original triangle (tetrahedron in $3D$) is removed, and the Delaunay triangulation is updated (right). As a consequence, the new facets (green and brown edges) better approximate the isocontour, i.e., the distance δ will decrease for some number of the new facets [8]. The algorithm will continue to refine any triangles containing facets with δ larger than some predetermined threshold value (green dot contrasted with red dot in (b)). 73

4.8 An illustration of the sampling of a sharp feature. The black lines indicate the isocontour, and the red line segments represent the reconstructed surface. Blue dots are used to show the locations of the vertices of these 1-facets. The dashed circle indicates the problematic region. The refinement scheme shown in Fig. 4.7 will not be able to reproduce the isocontour unless a vertex is placed at the sharp corner. The result is a reconstructed surface with a large number of facets, many of which intersect the isocontour. This is undesirable for microstructures, as it produces significant error in the mean width calculation (discussed below). 74

4.9 A pixelized boundary (left) is interpolated on the right, as indicated by pixels with cut corners. The black line indicates the true boundary. Since the true boundary is not faithfully represented by the pixelized, interpolated data, resolution of the reconstructed boundary is limited by pixel size. Surface reconstruction methods can at best capture this interpolated boundary from the discrete data (edges shared by both red and blue regions). While reducing the parameter δ below the pixel side length to something arbitrarily small will lead to the convergence of the reconstructed surface to the interpolated surface, it may not necessarily converge to the true boundary. The resulting surface may also contain artifacts, such as noisy surface normals (white), where a relaxed δ could lead to a smoother surface (green). 76

4.10 Resolution parameters' effect on unconstrained reconstructed meshes is shown here for a rotated cube in a rectilinear grid. The facet-to-boundary parameter decreases from $\delta = 2$ to $\delta = 0.5$ going from left to right. Moving down the columns, we can see the effect of maximum edge length going from $e_c = 0.1$ to $e_c = 1$ in normalized units. Corners and sharp edges tend to become noisy with lower δ, while larger δ results in meshes that poorly approximate the original shape. 80

4.11 A schematic describing the approximation parameter δ, which specifies the maximum distance between the facet (red) and the grain boundary (black curve). Facets in two-dimensions (edge) and three-dimensions (triangle) are shown on the left side and right side respectively. 82

4.12 Relative mean width error of a free sphere. (a) Relative error is plotted against $\frac{s}{L(D)^2}$, where s is the voxel side length. Near linear scaling is attributed to a good convergence of the mean width as a function of resolution. A line indicating $y = x$ is supplied as a reference. Note that error bars shown are smaller than symbol size, indicating minimal orientation variation in the relative reconstruction error, which is expected for a sphere. (b) A plot of the relative error as a function of $L(D)$ better shows the convergent behavior. 85

4.13 Relative mean width error of a free cube. (a) Significant variation is found in the errors estimated, indicating directional dependence of the discretization, which is expected. (b) A plot of the relative error as a function of $L(D)$ to show an exception in the convergent behavior ($\delta = 0.5$). In both plots, $\delta = 0.5$ produces an error that does not follow any scaling. This is an indication that the mean width error is dominated by the noise in the reconstructed surface mesh. The scale of the error seen here is not dramatically worse than the sphere case. 86

4.14 Relative mean width error of a constrained cube. (a) Marked difference in the error scaling behavior can be seen here. Notice here that the error from the case of $\delta = 0.5$ is significantly higher. This is mostly attributed to noise in the triple line reconstruction. Variation as a function of orientation is also dramatically larger than observed for the free sphere or the free cube. (b) All cases except for $\delta = 0.5$ converged rapidly with increasing resolution. 87
4.15 Relative volume error of a free sphere. (a) Relative volume error scaling with $\frac{s}{V(D)^{\frac{1}{3}}}$, where s is the voxel side length for a sphere. Note again that the error bars are below symbol size. (b) Relative error plotted against volume to demonstrate convergence criteria. 88
4.16 Relative volume error of a free cube. (a) Variation of volume approximation error is significantly lower than that of the mean width calculation. (b) It can be seen that the volume converges much more sharply than the mean width approximation. However, noting the scale indicates here that the relative errors can become significantly higher (up to 0.25 in the volume approximation in contrast to 0.15 in the mean width test). 89
4.17 Relative volume error of a constrained cube. (a) It is seen that all four values of δ result in very similar volume approximations. The non-convergent behavior seen in the $\delta = 0.5$ case of mean width is not present here. Error variation across different orientations is also significantly lower. (b) Compared to the free sphere and the free cube, we see that the volume approximation here converges much more slowly. Note again that δ seems to have no effect on the reconstruction. . . . 90
4.18 A schematic of how a maximum intersection grain tracking scheme may lead to misleading results. Grains of the same color in the diagram are considered to have the same orientation. As grain boundaries move, even with perfect registrations between two states, it is possible that the same grain across two states cannot simply be identified by having maximum intersection and minimum misorientation. 92

5.1 (a) A representative orientation map from the nickel sample. The color is a mapping of the orientation space to red, green, and blue (RGB). The confidence map (b) shows the fit quality of the orientation map. 100
5.2 Mean and median grain volume for each of the anneal states. 102
5.3 (a) An example of a grain with non-trivial geometry found in the initial and the first anneal state. The region that is "wrapped around" by the grain is identified as an in-growing twin. (b) Evolution of a grain across four states going from initial to final (left to right). Dramatic changes can be seen at the narrowest part of this grain throughout the annealing process. 103

5.4 Grain size distribution, plotted as normalized radius, $\frac{R_{eq}}{\langle R \rangle}$, where $R_{eq} = \left(\frac{3V}{4\pi}\right)^{\frac{1}{3}}$ is the spherical equivalent radius. Annealing progresses from (a) to (d). 105

5.5 Single parameter misorientation distribution for four (initial to third anneal state in the order of (a) - (d)) out of six anneal states measured. The discrepancy in the second anneal state is at this time believed to be an artifact due to errors in the experimental parameters, pending results from the final error analysis. 106

5.6 Sub-spaces of the five parameter grain boundary character distribution selected by the misorientation. Annealing proceeds from left to right. Each figure is a plot of the boundary normal distribution, represented in the stereographic projection form and plotted as multiples of random. (a)-(c) $\Sigma 3$, $(60°, [111])$ Note the strengthening of the [111] peak by a factor of 100 across the annealing process, which indicates the alignment of boundary normals with the rotation axis. (d)-(f) $\Sigma 5$, $(36.87°, [100])$ and (g)-(i) $\Sigma 11$, $(50.49°, [110])$ Signals from both $\Sigma 5$ and $\Sigma 11$ are much weaker that those seen in $\Sigma 3$. One reason is the significantly lower statistics (count of 28007 boundary patches for $\Sigma 3$ in contrast to 1185 and 804 for $\Sigma 5$ and $\Sigma 11$). Secondly, the energy of the $\Sigma 3$ coherent twin corresponds to a much deeper minimum than $\Sigma 5$ and $\Sigma 11$. 108

5.7 Distribution of apparent grain boundary motion between initial and first anneal state. The horizontal axis is the number of microns shifted, and the vertical axis is the faction of boundary patches. The total number of boundary patches is also displayed to exhibit the difference in the population sizes. A Gaussian (red) is fitted to the distributions in an attempt to isolate random components of the shifts from potential signal. The raw data is shown in blue, and the Gaussian subtracted signal is shown in black. 109

5.8 An example of the global plot of the grain boundary motion distribution seen in Fig. 5.7 for $\Sigma 3$ (a) and $\Sigma 25a$ (b). A small number (less than 10) of boundary patches is found to have noticeably large motion (upwards of 20 μm). However, these patches are more prone to misidentification across the two anneal states. 110

5.9 Apparent grain boundary movement, classified by misorientation type, plotted as projections of the boundary normal weighted by multiples of the mean boundary shifted. For each plot, the mean boundary shift is classified by the boundary normals and binned according to the two angles, (ϕ, ψ), which represent the normal in the upper hemisphere. The average shift in each bin is compared with the shift of all boundaries. 111

5.10 A test of the MacPherson-Srolovitz relationship $dV = -2\pi M\gamma(L(D) - \frac{1}{6}\sum e)$ for the 16 grains tracked across four volumes. Aside from globally not following MacPherson-Srolovitz's relationship, deviation for each of the grain is markedly different from what is expected for isotropic grain growth. 113

5.11 Evolution of topological class and volume for 16 grains tracked across four of the six anneal states. It is shown that the change of grain volume is correlated with the change in topological classes. 114

6.1 (a) Side view schematic of the experiment, with the blue arrow indicating the diffracted X-ray beam. The diffracted peaks are measured at distances L_1 and L_2. The dotted green line indicates the location of the copper wire in tension, and the red region indicates the gauge section being imaged. (b) An expanded side view of the sample holder in (a). The $1mm$ wire can be seen here to be fixed by set screws (red section at the top and bottom). The sample housing around the wire is made out of Macor, an X-ray transparent ceramic. (c) A photograph of the actual sample after electropolishing (the image was cleaned up to remove some of the residual lacquer). The narrowest section of the necked wire is roughly $250\mu m$ in diameter. (d) The load cell reading plotted as a function of displacement. Green dots indicate states where HEDM imaging was performed. 119

6.2 Images corresponding to the same 1° integration interval in states S0, S1, S2, and S3. These are background subtracted images for a layer at a sample location equivalent to $z16$, the 16th layer of state S1. Since the sample is moved and deformed noticeably during strain steps, layers measured do not have a direct correspondence between different states. Best match layers are shown here instead. Significant deformation of the sample can be observed as peak broadening in the η direction. Note that we do not expect any observation of elastic strain since it is on the order of 10^{-4} for copper, which is below our resolution limit. . . 121

6.3 Tomographic reconstruction of the four deformed states. 124

6.4 (a) - (i) Observed evolution of a diffraction peak as the sample rotates about the $\hat{z}$-axis. Experimental diffracted intensity is shown in grayscale, while simulated pixels are plotted as green dots. The simulation overlap is typically concentrated in the higher intensity area of the experimental peak, in spite of the fact that no explicit intensity fitting is used in this reconstruction. (See Chapter 3). 126

6.5 Diffraction spots generated from forward modeling reconstruction, with intensity approximated by Eq. (6.1). Each image (a) - (i) shows a diffraction peak in one out of nine consecutive integration intervals. It can be seen that the peak splitting in the simulated result is similar to that in the measured images. 127

6.6 Vertical and horizontal intensity profiles from Fig. 6.4 and Fig 6.5. The stacking of profiles vertically indicates successive integration intervals. In all four figures, red indicates simulated intensity profile, and black indicates experimental results. (a), (b) Binarized integrated intensity profiles. (c), (d) Integrated intensity using Eq. (6.1) to estimate intensity contributions from each diffracted peak. It is shown in all four cases that diffraction spots and peak splitting are tracked across multiple integration intervals by the Forward Modeling reconstruction method. 129

6.7 (a), (b) Orientation reconstruction for the same layer at two different optimized positions ($L_1 = 6.3732$ and $L_1 = 6.3948$). Orientations are represented by a mapping of the Rodriguez vector to RGB (red, green blue) colors. We notice that while small features (i.e., grain in green at the intersection of four other grains) and boundary locations differ across the two maps, the two reconstructions are largely similar. (c), (d): Comparison of local misorientation properties for the corresponding orientation maps. Notice again that qualitative features are similar. 131

6.8 Kernel averaged misorientation computed for reconstructions with the beam origin at different detector pixel k locations ($\approx 3\mu m$ difference in the z direction). This is equivalent to vertical sample position. Note that both reconstructions are done at $Q_{max} = 12\mathring{A}^{-1}$ 133

6.9 Kernel averaged misorientation computed for reconstructions at different Q_{max} and diffraction origin. (a) $Q_{max} = 10\mathring{A}^{-1}$. (b) $Q_{max} = 12\mathring{A}^{-1}$. 134

6.10 Aliasing effects are reduced as sampling rate is increased. As spatial resolution is increased from (a) to (c), sharpening of boundaries is observed. More importantly, the KAM features seem to be converging with the increase of spatial resolution, with no large ($\geq 2.4\mu m$) feature in (b) that is missing in (a). These reconstructions all use $Q_{max} = 12\mathring{A}^{-1}$. 135

6.11 (a) - (c) Reconstructed orientation maps for the reference layer of states S0, S1, and S2. Changes in the grain boundaries can be attributed to deformation induced microstructure evolution, but quantitative comparison of geometrical features is difficult due to alignment issues. Texture evolution is observed by comparing the point-to-point misorientation of these three reconstructed maps. (d) - (f) Confidence maps showing the goodness-of-fit for the reconstructed orientations. Degradation of fit quality along the grain boundaries is expected, but marked changes are seen between (e) and (f), resulting in a "hole" in the orientation map. This hole indicates that the diffractions originating from this region have unusually low signal-to-noise ratios. 137

6.12 Distribution of [001] crystal axis in the sample frame for the layers corresponding to z16 S1 across all three states. Color represents multiples of random, plotted in log_{10} scale. 138

6.13 (a), (b) Spatially resolved grain rotation across successive states (S0 to S1, and S1 to S2). The false color represents the magnitude of rotation from one state to the other on a 5° scale. Both images are created first by registering two layers across the two states through minimization of total misorientation. Because the sample both stretched and moved across different states, exact registration is impossible. Only lattice rotation below 5° is shown here to remove misorientation due to boundary shifts between different states. (c), (d) A distribution symmetrizing the projection of the rotation axis from (a) and (b) to the $x-y$ plane of the sample frame, measured in multiples of random. The number of rotation axes along the [001] sample direction (the tensile axis, out of the page) is markedly less than along any other directions. 140

6.14 Distribution of the magnitude of lattice rotation between the different strain states at different bin sizes. Marked difference can be observed in the angle distribution between states. (a) and (b) show the same data sets on different horizontal scales. To demonstrate the effects of registration by minimization of misorientation, the unoptimized lattice rotation distribution is also plotted. 142

6.15 (a) Lattice rotation of random points selected from the point-to-point misorientation. Here, the lattice rotation is represented by the movement of the tensile axis in the crystal frame, plotted in the usual stereological triangle. (b) Spatially resolved lattice rotation showing the tensile axis movement at each point in the sample space. 144

A.1 Reconstructed orientation maps for the same layer of NiMnGa before (a) and after (b) thermal cycling. Distance is measured in unit of millimeters. False color indicates orientations in the tetragonal fundamental zone. Very minute changes are detected between the two maps. This is attributed to the disconnectedness of each grain as shown in Fig. A.4. 147
A.2 Confidence map for the two layers shown in Fig. A.1. The region of low confidence is confirmed to be void by the tomographic reconstruction seen in Fig. A.4. Hints of crack formation after thermal-cycling is seen by comparing the bottom right of (a) and (b), but confirmation requires a full three-dimensional map (not currently available). . . . 148
A.3 Kernel averaged misorientation (KAM) for each of the maps in Fig. A.1. Deformation is expected to scale with local misorientation, thus resulting in higher KAM. The relatively higher KAM and more concentrated KAM values seen here suggest that local deformations is manifested as mosaicity in the orientation of each grain. 148
A.4 Reconstruction from X-ray transmission tomography. Scale is shown here as pixels ($1.48\mu m$ side length). Lighter color is used to indicate regions of high density. The black curves indicate that the sample contains grains that are not in contact at the layers we have imaged. 149

B.1 Grain boundary surface mesh for the initial state of the nickel sample described in Chapter 5. Boundary colors correspond to misorientation in degrees. A corner of the surface mesh is cut away to better show the smoothness of the boundaries. 151
B.2 Grain boundary surface mesh for the first anneal state. Little or no changes is noticeable between the meshes shown here and Fig. B.1, as evidenced by the analysis in Chapter 5. 152

C.1 Initial state of the high purity nickel volume. Each grain ID is associated with a false color (RGB) value. 154
C.2 First anneal state. No noticeable changes can be seen. (Recall that the volumes presented are not yet aligned.) 154
C.3 Second anneal. Grains can be seen to be markedly smoother. 155
C.4 Third anneal state. Some number of annealing twins can be seen as thin, plate-like grains in the volume (red on the left, blue near the middle inside a grain). 155
C.5 Three-dimensional grain map of a piece of copper, used as an initial state for an upcoming deformation experiment in collaboration with Los Alamos National Lab. The imaged section of the specimen is). $1.1mm$ in diameter and $0.760mm$ in height. A total of 11999 grains were identified. 156

C.6 Progression of a piece of copper wire under uni-axial tension (data from Chapter 6). Starting from left to right, the true strain reads 0%, 0% (to within sensitivity), 6.2%, and 26.9%. False color again indicates identified grains (IDs are not related between different states). We caution that this is result from the preliminary analysis, and it is presented here to show some of the cutting-edge applications of HEDM. 156

Acknowledgments

I would like to first express my gratitude to my advisor Bob Suter. Simply put, this thesis would not exist without his patience and support; his original insight into the problem of orientation reconstruction was key to the success of this project. I would also like to thank Tony Rollet for the various insightful discussions, especially the times where I "cornered" him after meetings (and take valuable time out of his busy schedule). Ulrich Lienert of Sector 1 at the Advanced Photon Source is probably the single most important person in making the physical realization of HEDM a reality. Without him, we would probably still have trouble searching for the X-ray beam. I must also acknowledge the support from the rest of the Sector 1-ID staff at Advanced Photon Source. This includes Ali Mashayekhi, Roger Ranay, Sarvjit Shastri, Dean Haeffner, and Jon Almer. Software and systems integration support by Brian Tiemann, Kurt Goetze, and Xuesong Jiao from the software and electronics (BCDA) groups of APS proved to be invaluable; many eleventh hour data acquisition and electronic crises were averted because of their help.

I would also like to acknowledge my colleagues Jonathan Lind, Chris Hefferan, and Reeju Pokharel, as the experiments performed in this thesis were largely the result of a group effort. Jon and Reeju were instrumental in preparing the necked copper wire sample used in the experiment described in Chapter 6, and Jon spent a significant amount of time helping me with building and machining the load frame. The annealing study measurements presented in Chapter 5 are also part of the thesis of Chris Hefferan and its associated publications; the sample preparation required was largely performed by Chris and Jon. Jon and Chris are also responsible for part of the data acquisition performed in Chapters 5 and 6.

Abstract

Near-field High Energy X-ray Diffraction Microscopy (HEDM) is a synchrotron based imaging technique capable of resolving crystallographic orientation in a bulk, polycrystalline material non-destructively. Recent advances in data acquisition and analysis methods have led to micron-scale spatial resolution and $\leq 0.1^\circ$ angular resolution of the measured volumetric orientation maps across millimeter sized samples. This is a significant improvement over the previous generation of three-dimensional X-ray techniques, which provides us with the access of statistically significant microstructure volumes. Combined with the use of state-of-the-art surface mesh generation algorithms, this markedly improved resolution results in the capability to directly measure geometrical evolution, such as grain boundary motion, and material deformation in the form of lattice rotations.

In this thesis, the algorithms and analysis methods recently developed for HEDM are discussed. This includes the descriptions of the robust geometrical extraction methods used for microstructure feature characterization. A set of validation tests for the Forward Modeling Method and the newly developed orientation reconstruction algorithm, the Stratified Monte Carlo Pruning method, is also detailed. By using HEDM to measure the annealing of high purity nickel, grain boundary motion for different boundary types are measured and presented. Moreover, the use of HEDM enabled us to observe the first ever spatially resolved lattice rotation in a high purity copper wire under uni-axial tension, thus demonstrating HEDM's applicability to defected materials.

Chapter 1

Introduction

1.1 Motivation

The interest to observe microstructure of materials with multiple internal interfaces is widespread in solid states physics, and the demand from both the scientific and engineering communities are increasing. Because material properties are generally anisotropic with respect to crystallographic orientations, orientation preferences, or texture in a polycrystalline material typically dictates its bulk properties. Moreover, interfaces created inside a material significantly affect the material both microscopically and macroscopically. As an example, the critical current density in a high T_c superconductor sample (YBaCuO) depends on both the location and the types of its grain boundaries [124]. A superconductor's technological application hence depends on the control of its microstructure [10, 12, 11].

As a more common example, three-dimensional measurements of deformation and annealing processes in metals have been largely limited to statistical studies and two-dimensional inferences up until recent years. Advances in synchrotron based X-ray techniques such as $3D$ X-ray Diffraction Microscopy [88], High Energy X-ray Diffraction Microscopy (HEDM) [116, 62, 83], and Differential Aperture X-ray Microscopy (DAXM) [55] have demonstrated the possibility of using X-rays for non-destructive orientation imaging in three-dimensions. The first set of results showed *in situ* observation of the growth of a single grain [104], measurement of growth mode of superconducting thin-film [10], and observation of subgrain structure formation [47], just to name a few.

More generally, the capability to characterize three-dimensional polycrystalline systems is of both scientific and technological importance. However, this often requires not only the ability to non-destructively measure volumetric orientation maps for arbitrary materials, but also the numerical and computational tools necessary to take advantage of these data sets. For example, in the case of grain growth, robust and reliable grain boundary extraction from the measured orientation map is a precondition to a successful analysis. The ability to track thousands of features across

a sample is required if microstructure evolution is of any interest. While historically, geometrical features are extracted manually, the same can not be done for three-dimensional data sets with anywhere between 100 to 10000 grains. Without the use of automation, the ability to analyze measurements from these synchrotron based experiments is greatly diminished. In fact, significant development and progress was made in automated geometric extraction [59, 26, 27].

On the other hand, the increasing use of computation and automation leads to the logistical problem of error magnification, commonly known as "garbage-in-garbage-out." The fact that roughly 2 TB (Terabytes) worth of data (typical of a HEDM experiment) gets turned into around 1 GB (Gigabyte) of orientation maps semi-automatically means that any small errors in the initial input gets propagated rapidly and thoroughly into the final result. The origin of such error is difficult to find and is often random. Consequently, any effort to produce reliable, usable data sets would require a significant amount of validation, stability testing, and sensitivity a study of the analysis pipeline and algorithm. The ability to characterize analysis failure is sometimes as important as the analysis itself.

The simple goal of non-destructively characterizing polycrystalline material then only requires synchrotron X-ray experimental techniques, algorithmic development, and error analysis. Numerous types of progress in these areas have been made in the context of HEDM and these form the basis for this thesis.

1.2 Overview

The scope of this dissertation is focused mainly in three areas: 1) Implementation and analysis methods of HEDM, 2) statistical, geometrical, and topological analysis of volumetric orientation maps, and 3) applications of HEDM. Understanding of the HEDM implementation is crucial to its analysis, as the reconstruction methods requires numerous experimental inputs. While an effective analysis method was already in existence for HEDM [116], dramatic improvement in data acquisition speed (factor of 10-20) leads to demands for faster and more robust reconstruction software. Taking advantage of a recently maturing computational geometry library (CGAL) [1], various aspects of geometrical and topological extraction of volumetric orientation maps were developed. These results are crucial for the analysis of grain growth in a high purity nickel sample – an application of HEDM to well-ordered polycrystalline material. The culmination of all of the reconstruction and data analysis is applied to the study of plastically deformed copper.

1.3 Outline

The physical implementation and data acquisition methods in HEDM are presented in Chapter 2. A brief survey of simple X-ray diffraction is provided, which forms the

basis of our experiment, and the rotation method is described in some detail. The experimental procedure, including sample alignment, data acquisition, and detector calibration is included. Some discussion of methods used to improve system reliability of HEDM is also presented.

Chapter 3 provides the basis for orientation reconstruction from HEDM diffraction data. In this chapter, a review of existing algorithms used for analysis of $2D$ and $3D$ diffraction data is presented. The Forward Modeling Method [116] is discussed at length to provide a foundation for the analysis of orientation reconstruction in a polycrystalline sample. Because the Forward Modeling Method reconstructs orientations based on an auxiliary cost function, a great deal of time is devoted to discuss its properties. While theoretical understanding of the orientation reconstruction problem at large is inadequate, Chapter 3 argues that the Forward Modeling Method is in fact stable based on a number of numerical results. With this result in hand an augmentation of the Forward Modeling Method is presented. Finally, real world validation results are presented.

Chapter 4 focuses on the geometrical analysis of reconstructed orientation maps. Since many materials problems such as grain growth and grain boundary percolation requires the measurement of grain boundaries and their evolution, surface and volumetric meshes are sometimes required as part of the analysis. Consequently, a significant amount of Chapter 4 is devoted to understanding boundary reconstruction, also know as isocontouring. Theoretical development of surface reconstruction using Delaunay triangulation is be presented as a summary to motivate and support the application and implementation of a feature preserving boundary surface reconstruction method [3, 9]. Error analysis is performed and presented at the end of Chapter 4.

Application of HEDM to an annealing study of a high purity nickel sample is discussed in Chapter 5, and the result of the initial analysis is presented. By applying the tools developed in Chapters 3 and 4, we are able to measure the evolution of microstructure statistics as the sample anneals. Grain boundary motion is measured from the surface mesh generated from the orientation maps, and the relationship between boundary type and its motion is examined. Finally, taking advantage of the grain tracking capabilities developed in Chapter 4, we are able to demonstrate the anisotropic nature of nickel annealing through the measurement of the parameters in the Macpherson-Srolovitz relations.

Pushing the limits of HEDM, a deformed polycrystalline copper sample was imaged before and after multiple *in situ* uni-axial tension tests; the results are discussed in Chapter 6. Plastic deformation, manifested as lattice rotations and local misorientations are observed in the measured orientation maps. Unlike results from previous experiments [89, 47], measurements of lattice rotations are spatially resolved; thus for the first time, grain neighbor information is measured and tracked in an *in situ* deformation experiment. Because the use of the Forward Modeling method to analyze diffraction patterns from a deformed material is largely a new endeavor, detailed val-

idation tests are performed and shown. The ability of the Forward Modeling method to track peak splitting and broadening is also demonstrated.

Chapter 2

High Energy X-ray Diffraction Microscopy

2.1 Overview

High Energy X-ray Diffraction Microscopy (HEDM) is primarily enabled by the availability of third generation synchrotron sources, such as the Advanced Photon Source. A typical HEDM experiment requires the use of a micro-focused beam, high energy (upwards of 50-100 keV), and high brilliance to ensure reasonable measurement time and signal-to-noise ratio. This makes HEDM particularly difficult to implement in a bench-top setting. As a reference, brilliance at the Argonne National Lab's Advanced Photon Source is around 12 orders of magnitude larger than the brightest X-ray tube. This is due in part to the naturally small opening angle of synchrotron X-ray beams and the small source size due to the small electron beam cross-section. The high brilliance reduces the loss of efficiency due to focusing optics; this is something unavailable in any of the bench top setups.

In this chapter, the implementation of HEDM at the Advanced Photon Source will be described in detail. We will start with a brief review of synchrotron and scattering physics and move to diffraction peak imaging using the rotating single crystal method. Because of the diverse references already available for synchrotron physics, only parts relevant to our experiment will be reviewed. Some time will be spent on X-ray diffraction, with specific focus to kinematic scattering. This is important for understanding of features such as peak broadening due to deformation in some of our experiments. Because of the imperfect nature of the detection system, attention must be paid to background subtraction. A discussion will be provided on the simplistic noise model used in our analysis. Similarly, because of measurement uncertainty and the requirements of a high precision description of the experimental geometry, methods were developed to improve reliability of the overall measurement process. These methods, including rotation axis alignment and focus optimization provide a basis for calibrations, and will be discussed in this document.

By applying HEDM to bulk samples, we are able to produce volumetric orientation maps ($\approx 1mm$ diameter, and $\approx 0.3mm$ height) at microns spatial resolution and 0.1° angular resolution. The origins of the resolution limits will be discussed in the context of a discretized 2D detector and focusing optics. By examining the optical component of HEDM, we will also see where and how spatial distortion in the detector affects the resulting orientation images. Finally, we will conclude by examining the data reduction process.

2.2 Review of Scattering Physics

Knowledge of scattering physics required for the application of HEDM is embarrassingly rudimentary. In this section, we will develop the machinery required for Bragg scattering. For the purpose of understanding intensity variation and peak shapes due to crystals with defects, discussion of atomic and structure form factors will be included. Similarly, a limited overview of perfect crystal scattering theory will be included for the purpose of understanding the monochromator used in the HEDM setup. It should be noted that as the development of analysis techniques of HEDM matures (Chapter 3), the analysis of higher order effects become possible. For example, the most up-to-date HEDM analysis code uses binarized intensity data. Even so, effects of deformation are observable through the broadening of peaks in the detector space. Further analysis, for example with intensity fitting, would require an explicit intensity model.

2.2.1 Kinematic Scattering

While X-ray scattering contains contributions from both elastic (Thomson) and inelastic (Compton) components, only results from classical kinematic X-ray scattering are discussed for the purpose of our application. This is because inelastic scattering is incoherent, and hence no diffraction "peaks" in the usual sense are produced. It should be noted however that inelastic scattering can sometimes be a major contributor to background noise in some of the HEDM experiments.

Given an electron at the origin and an incident plane wave, represented by the electric field, $\vec{E} = E_0 e^{i\omega t}\hat{z}$, where $\hat{z}$ is the polarization direction, the magnitude of the scattered electric field at location $\vec{R}$ due to scattering from the origin is given by

$$E_s = \left(\frac{q_e^2 \sin\phi E_0}{m_e c^2 |\vec{R}|}\right) e^{i\omega t}, \tag{2.1}$$

where $\phi = \cos^{-1}(\hat{R}\cdot\hat{z})$, m_e and q_e are mass and charge of the electron, respectively. In the approximation of $|\vec{R}| \gg \ell$, where ℓ is the diffraction sample size, the distribution

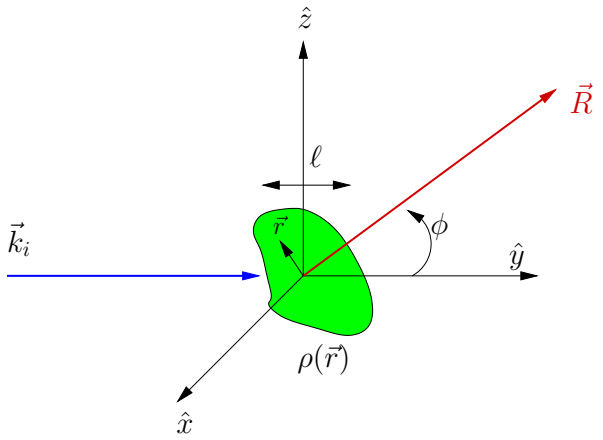

Figure 2.1: Scattering of an X-ray by a charge distribution at the origin.

of electrons $\rho(\vec{r})$ will produce an electric field with magnitude of

$$E_s = \frac{q_e^2 E_o \sin\phi}{mc^2|\vec{R}|} e^{i(\omega t - 2\pi\frac{|\vec{R}|}{\lambda})} \int e^{i2\pi\left(\frac{\hat{k}-\hat{k}_o}{\lambda}\right)\cdot\vec{r}} \rho(\vec{r})\, dV \tag{2.2}$$

where $\hat{k}, \hat{k}_o$ are the directions of the incoming and outgoing wave vectors (REF Warren.) We identify the summation here as a sum of phase factors associated with scattering from position $\vec{r}$. For an atomic electron density distribution of $\rho(\vec{r})$, the atomic form factor is given by

$$f = \int e^{i\vec{Q}\cdot\vec{r}} \rho(\vec{r}) d^3r. \tag{2.3}$$

Here, we have switched to the usual convention of $\vec{Q} = \frac{2\pi}{\lambda}(\hat{k} - \hat{k}_o)$. Applying the same ideas to a set of atoms at positions $\{\vec{r}_j\}$, a structure factor for a crystal can be calculated, namely

$$F = \sum_j f_j(\vec{Q}) e^{i\vec{Q}\cdot\vec{r}_j}, \tag{2.4}$$

where $\vec{r}_j$ identifies the location of the j-th atom. f is the Fourier transform of the atomic electron density.

Two properties become apparent from this short summary. First, the electronic form factor depends on $\vec{Q}$ and this dependence modulations the scattering associated with the crystal structure. Moreover, f falls off rapidly (with a width of order the inverse atomic radius) as a function of $\vec{Q}$, which contributes to the decrease of observed intensity in higher $|\vec{Q}|$ peaks. Because of the sharp drop off of intensities at high $|\vec{Q}|$ and the limited dynamic range of detectors, effective integration times for an X-ray measurement are bounded in both directions. With too low an integration time, most of the intensity from high $|\vec{Q}|$ peaks will not be detectable. Saturation and "bleeding" (smearing of high intensity peak across a wide detector region) of the low $|\vec{Q}|$ peaks occurs when the integration time is set too high.

By summing the structure factor over the crystal lattice, we get

$$F_{tot} = \sum_j f_j(\vec{Q}) e^{i\vec{Q}\cdot\vec{r}_j} \overbrace{\sum_n e^{i\vec{Q}\cdot\vec{R}_n}}^{\text{Lattice sum}}, \tag{2.5}$$

where the first sum is over the basis atoms associated with a single unit cell and $\vec{R}_n = m_1\hat{a}_1 + m_2\hat{a}_2 + m_3\hat{a}_3$ runs over the entire crystal lattice, specifying unit cell locations. This is the usual way to arrive at the Bragg condition from the Laue Equation of $\vec{Q} = \vec{G}_{hkl}$, where $\vec{G}_{hkl}$ is the reciprocal lattice vector representing the scattering plane. An extension of equation 2.5 that allows deviations in either the

atomic positions, $\vec{r}_i$ or the unit cell positions $\vec{R}_n$, leads to results such as the Debye-Waller factor and peak broadening from stacking faults in a crystal. For example, $\vec{R}_n$ might be replaced by

$$\vec{R}_n = m_1\hat{a}_1 + m_2\hat{a}_2 + m_3\hat{a}_3 + \vec{\delta}_n, \tag{2.6}$$

where $\vec{\delta}_n$ represents deviation of the n-th unit cell from its lattice location. The exact form of $\vec{\delta}_n$ depends on the underlying physics. For example, in the case of lattice vibrations, $\vec{\delta}_n$ has the property that $\langle\vec{\delta}_n\rangle = 0$. The resulting modified structure factor is given by

$$F = \sum_n f(Q)e^{i\vec{Q}\cdot\left(\vec{r}_n+\vec{\delta}_n\right)}. \tag{2.7}$$

The integrated intensity from this form factor reads,

$$I = \langle FF^*\rangle = \left\langle \left(\sum_n f(Q)e^{i\vec{Q}\cdot\left(\vec{r}_n+\vec{\delta}_n\right)}\right)\left(\sum_m f^*(Q)e^{-i\vec{Q}\cdot\left(\vec{r}_m+\vec{\delta}_m\right)}\right)\right\rangle \tag{2.8}$$

$$= \sum_m\sum_n f(Q)f^*(Q)e^{i\vec{Q}\cdot(\vec{r}_m-\vec{r}_n)}\left\langle e^{i\vec{Q}\cdot(\vec{\delta}_m-\vec{\delta}_n)}\right\rangle. \tag{2.9}$$

In this way, the "perturbation" to the ideal Bragg scattering is captured by the time averaged term, $\left\langle e^{i\vec{Q}\cdot(\vec{\delta}_m-\vec{\delta}_n)}\right\rangle$, which becomes $e^{Q^2|\vec{\delta}_m-\vec{\delta}_n|^2} = e^M$ in the case of lattice vibrations.[1]. More detailed exposition can be found in references. [4, 126]

The relevance in mentioning the Debye-Waller term can be seen in the design of *in situ* phase transition measurements using HEDM. In the standard notation, $M = B_T|\vec{Q}|^2$, where, for the isotropic case ($\langle u^2\rangle = \langle u_x^2 + u_y^2 + u_z^2\rangle = 3\langle u_Q^2\rangle$),

$$B_T = = \frac{11492T}{A\Theta^2}\phi\left(\frac{\Theta}{T}\right) + \frac{2874}{A\Theta},$$

$$\phi(x) = \frac{1}{x}\int_0^x \frac{x'}{e^{x'}-1}dx' \tag{2.10}$$

where B_T is given by $\mathring{A}^2$, A is the atomic mass number, and Θ is the Debye temperature. [4] All temperatures are given in Kelvins. Measured intensity falls off as $e^{-B_T|Q|^2}$, which implies that the signal to noise drops off rapidly for high Q peaks, and this problem is exacerbated in high temperature experiments. This is particularly problematic, as higher order peaks contribute significantly to the spatial and orientation resolution of our measurements. Simply increasing integration time is possible since the diffracted intensities for different Q span multiple decades, which exhausts the dynamic range of the detector system. The use of attenuators may also produce undesirable results, as we will describe in the later sections.

[1] This result is reached by assuming that the displacement is Gaussian, and by the application of Baker-Housdorff theorem, we have $\langle e^{ix}\rangle = e^{\frac{1}{2}x^2}$

2.2.2 Rotation Method

HEDM is, in principle, a simple extension of the rotation X-ray diffraction method to a polycrystalline sample. The geometry of the standard rotation method is shown in the figure 2.2. A single crystal sample is located at the origin of the coordinate system, represented by a box in figure 2.2b. The plane wave incoming X-ray beam, represented by the wave vector $\vec{k}_i$, is monochromatic and has an energy bandwidth that is negligible. The diffracted beam is represented by $\vec{k}_o$. The sample rotated by $\omega\hat{z}$. By using the Bragg condition of $\vec{k}_o - \vec{k}_i = \vec{G}$, we can solve for the rotations about

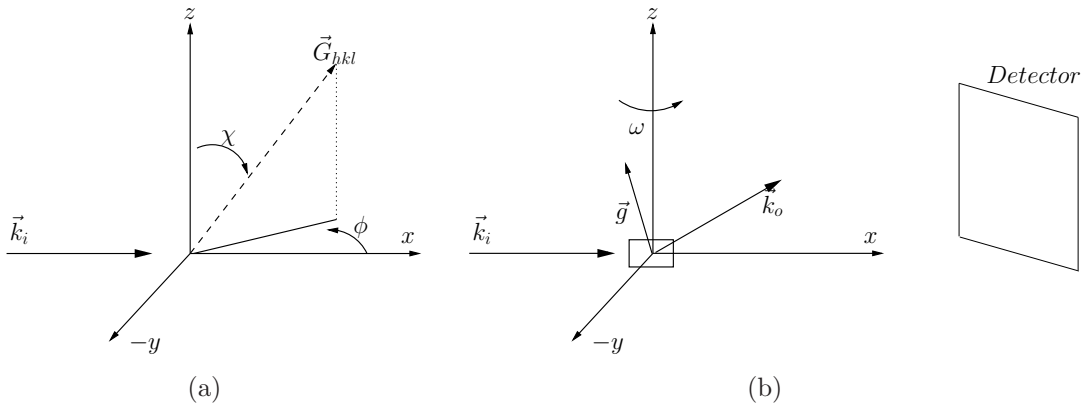

Figure 2.2: Geometry of a rotating crystal method for X-ray diffraction in the analysis coordinate system. (a) Coordinates used to solve for ω where $\vec{G}_{hkl}$ satisfies the Bragg condition. (b) Rotating crystal method setup, with $\vec{g}$ as the reciprocal lattice vector, and ω is rotated about the $\hat{z}$ axis.

$\hat{z}$, $\omega\hat{z}$, that bring $\vec{G}$ into compliance with Bragg condition [115, 116]. By considering $\vec{G}$ to point along the direction of $\vec{k}_i$ initially, and parameterizing the rotation from this position by the angle ϕ, we can arrive at

$$\vec{G} = G\left(\sin\chi\cos\phi\hat{i} + \sin\chi\sin\phi\hat{j} + \cos\chi\hat{k}\right), \tag{2.11}$$

where χ is the inclination angle of $\vec{G}$ from the z-axis [116], as shown in Fig. 2.2a. By rewriting the Bragg condition as $\vec{k}_i \cdot \vec{G} = -\frac{1}{2}|\vec{G}|^2$, we get the equation,

$$\cos\phi = \frac{|\vec{G}|}{2|\vec{k}_i|\sin\chi}. \tag{2.12}$$

In the case of any arbitrary $\vec{G}$ not in the $z-x$ plane, we will define

$$\begin{aligned} \phi_0 &= \tan^{-1}\frac{G_x}{G_y} \text{ and} \\ \sin\chi &= \sqrt{1-\left(\frac{G_z}{|\vec{G}|}\right)^2} \end{aligned} \tag{2.13}$$

Then, Bragg condition is satisfied for $\vec{G}$ at two points,

$$\begin{aligned} \omega &= \phi_0 + \phi \\ \omega &= \pi - \phi + \phi_0. \end{aligned} \tag{2.14}$$

This can be directly translated into the integration interval where $\vec{G}$ satisfies the Bragg condition, and the detector coordinate where the diffraction spot is measured can be computed by simple projection along $\vec{k}_o$. The integrated intensity measured at this detector location is presented in the next Section.

2.3 HEDM Measurements

2.3.1 Overview

High Energy X-ray Diffraction Microscopy (HEDM) is implemented at the 1-ID beam line of the Advanced Photon Source, Argonne National Lab. At its most basic level, HEDM is an orientation and strain imaging technique using high energy X-rays. Roughly speaking, there are two variants of HEDM, namely the near- versus far- field. Based on the rotating crystal method mentioned in section 2.2.2, near-field HEDM is usually limited to crystallographic orientation imaging for polycrystalline materials, although recent advances intend on including limited strain mapping capabilities. Taking advantage of the large detector-to-sample distance, the far-field method is used mostly for strain mapping without high spatial resolution. Both HEDM techniques leverage heavily on the high brilliance and high energy nature of the synchrotron radiation, unique to 1-ID and a handful of other beam lines in the world. With the combination of precision monochromator and X-ray focusing optics, 1-ID can produce planar, a microfocused wide beam ($FWHM \approx 6\mu m$ vertically, $1mm$ width) with better than 1% energy resolution. In this section, a summary of the near-field HEDM experimental setup will be provided. Limited discussion concerning monochromator, X-ray focusing, scintillators, and optics will be provided to form a working understanding needed for HEDM. Experimental calibration procedures developed to improve overall reliability and precision will also be discussed in this section, while software, "bootstrap" methods are described in Chapter 3.

2.3.2 Experimental Setup

The near-field HEDM setup is described in figure 2.3, with various parts labeled. The planar X-ray beam is produced by a combination of monochromator and X-ray focusing optics. The resulting microfocused beam illuminates a planar cross section of the sample, which is mounted on a precision rotation stage ($\leq 1\mu$ shift in the rotation axis.) As with the rotating crystal method mentioned in section 2.2.2, the sample is rotated about the axis perpendicular to the X-ray beam (in APS coordinates, $\hat{y}$). Integrated intensities are recorded while the sample is rotating at constant angular velocity with a CCD camera system, which digitizes images from the scintillator. While a small fraction of the incoming X-ray beam is scattered, most of it ends up penetrating the entire sample. With the direct beam being around 10^3 more intense than most diffracted peaks, the presence of the direct beam in the recorded image leads significant saturation of the detector system. The result is an unreasonably high background in the recorded images. Consequently, a single crystal beam attenuator is placed along the beam after the sample.

2.3.3 Experimental Procedure

The goal of HEDM is to measure the crystallographic orientation field for some subvolume of a polycrystalline sample. In most cases, such as aluminum and nickel, this crystallographic field represents a set of grains, where grains are defined to be collections of spatial points with orientations that are very close to each other. The set of grain boundaries associated to these grains are also recovered in this process, and the local variations of orientations within each grain (local misorientation) are also measured.

Orientation maps measured in HEDM are two-dimensional slices, as they are produced by the planar, micro-focused X-ray beam. The diffraction images for the predetermined integration (ω-rotation) intervals at different detector-to-rotation axis distances (L-distances) are used to reconstruct the spatially resolved orientation maps. This is done with the reconstruction software, which associates each of the diffraction peaks in the recorded image with a point in the sample space. In general, the crystallographic orientation of a point in the sample space can be determined by indexing at least three diffraction spots corresponding three non-collinear reciprocal lattice vectors. Because peak shapes on the detector are projections of a grain, the microstructure geometry is recovered by performing HEDM over large numbers of integration intervals so as to yield many different projection geometries.

The ability to reconstruct orientation maps from a set of $2D$ detector images depends on the precise knowledge of the experimental geometry. Namely, the location and perpendicularity of the rotation axis relative to the x-ray beam plane completely specifies the coordinate system origin, which determines the spatial location of the reconstructed orientations. The detector tilt (to within 0.5° from the nominal orientation) and focus determine the exact projection geometry, and therefore contribute

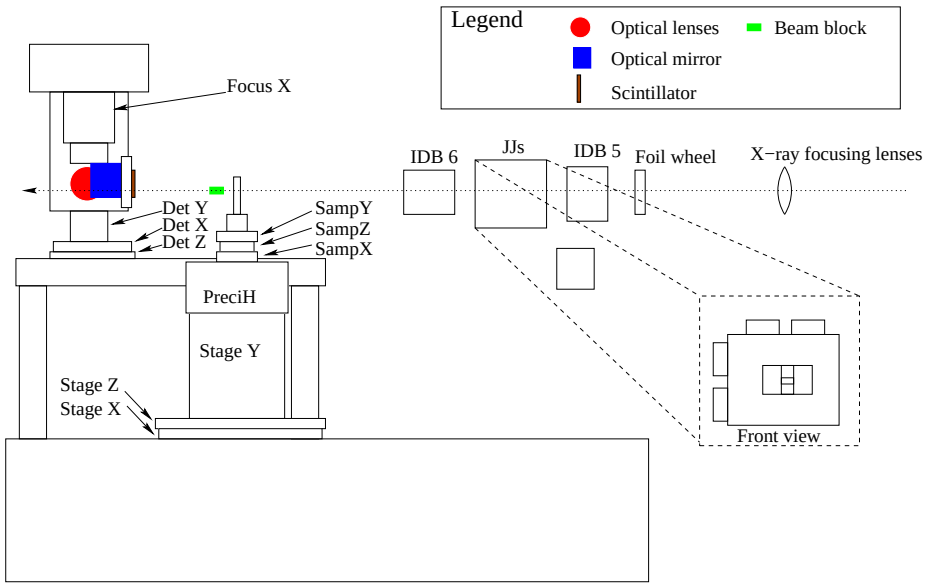

Figure 2.3: Schematic of the HEDM setup at Sector 1-ID:B of the Advanced Photon Source. Only the most relevant parts are shown. SampX, SampY, and SampZ are the sample translation motors. PreciH is the air-bearing rotation stage with $\leq 0.1\mu m$ eccentricity. The entire sample column is placed on top of StageZ and StageX, two linear motors with $1\mu m$ precision. The detector column is mounted on the motors DetX, DetY, and DetZ, which are used to adjust image plane location with respect to the sample (top of the sample column). The scattered X-rays from the sample are imaged with a detector system: a scintillator converts X-ray radiation to visible light, which is reflected by a 45° mirror (blue) and magnified by the focusing optics (red) onto a CCD detector. The direct beam is stopped after the sample at the beam block (green). IDB6 and IDB5 are ion chambers used to monitor the flux of the incoming beam. The horizontal and vertical X-ray absorbing slits (JJs) can be used to reduce the beam size for cases like the raster scan described below.

to the resolution of grain boundary locations.

Rotation Axis

The distance between the rotation axis and the detector (L-distance) has a large effect on the HEDM measurement. Unfortunately, the location of the rotation axis cannot be directly measured with the current set-up because the sample holder column is independent from the detector housing (Fig. 2.3); i.e., the two sets of apparatus are not coupled in a precise, known way. Instead of direct measurements, L-distances are recovered by ray-tracing a set of indexed peaks to their diffraction origin. Unfortunately, this is particularly difficult for polycrystalline samples because the diffraction peaks can come from any of the numerous grains in the sample. Finite grain size (of around $20\mu m$ to $100\mu m$ also adds to the uncertainty in the extrapolated scattering origin. To obtain initial estimates of the L-distances, a small diameter ($30\mu m$) gold wire is used as a calibration sample. By placing this wire on the rotation axis, we can assume that the diffraction center is effectively at the origin for each of the diffraction spots recorded, which makes the initial guess of the L-distances much simpler (accurate to around $50\mu m$). The wire is centered on the rotation axis before the L-distance calibration so that the position of the sample does not depend on the integration interval; moreover, centering on the rotation axis keeps the sample within the limits of the incoming X-ray beam.

Because it is generally difficult to determine the perpendicularity of the rotation axis with respect to the X-ray beam by diffraction images, a calibration procedure was developed and used for each HEDM measurement. We start by inserting the top of a gold wire into the direct beam such that no more than $1\mu m$ of the tip is above the X-ray beam. The wire is put into an "off-axis" position so that when the sample stage rotates, and the tip of the sample traces a circle of radius $R \approx 300\mu m$ around the rotation axis. The location and attenuation of the tip is observed by the intensity profile on the detector. Because the sample is no more than $1\mu m$ above the beam, any deviation from perpendicular of more than $1\mu m$ over $600\mu m$ can be observed. This corresponds to 0.1° accuracy in the perpendicularity of the rotation axis.

Direct Beam Block

Because the fraction of scattered X-rays is minuscule ($\approx 10^{-3}$) compared to those transmitted through the sample, a direct beam block must be used to prevent detector saturation. The beam block is necessarily made out of a high Z material to obtain the necessary attenuation of the high energy X-rays. In present case, a single crystal (moasicity $\leq (10^{-2})^\circ$) of Tungsten is used. The use of a single crystal allows us to position the beam block such that none of its diffraction peaks are incident on the detector. This is particularly important as the diffracted intensity from the single crystal beam block tends to be several factors larger than sample signals. In the HEDM geometry, suboptimal positioning can also result in sample diffraction signals

striking the beam block and being attenuated or removed. To minimize these effects, the location of the beam block is typically only a few tens to a hundred microns above the direct beam. An unintended side effect is the contribution of grazing angle reflection on the rough surface of the beam block. This effect could be minimized by applying the appropriate polishing procedures to the beam block.

Monochromator

A monochromator is needed to produce a monochromatic X-ray beam from the polychromatic synchrotron source. Although a detailed discussion of Darwin widths and dynamical diffraction theory is not included in this chapter, some relevant key results are relevant. Roughly speaking, a monochromator selects out a single energy from a white beam by the means of Bragg diffraction,

$$n\lambda = 2d\sin\theta, \tag{2.15}$$

where d is the lattice spacing and λ is the X-ray wavelength. With well defined d and θ, the output energy is fixed by λ: $E = \frac{hc}{\lambda} = \frac{12.4\text{keV}\cdot\mathring{\text{A}}}{\lambda[\mathring{\text{A}}]}$. In fact, Bragg scattering is never a true δ-function, so a finite range of wavelengths are included. This implies that variations in energy, $\frac{\Delta E}{E} = \frac{\Delta\lambda}{\lambda}$ are obtained. The monocrhomator system [63] uses diffraction off of two separate Si crystals (for one thing to obtain a horizontal output beam). With the bent crystal Si (111) reflections used at 1-ID, we obtain $\frac{\Delta E}{E} \sim 10^{-3}$. Because a significant amount of energy is deposited onto the first monochromator crystal, temperature variation is inevitable. To maintain small ΔE and maintain a precise output energy, the monochromator crystal must having minimal thermal expansion with temperature variations. As it turns out, single crystal silicon is perfect for this task, because of the near zero coefficient of expansion around the boiling point of liquid nitrogen.

From Eq. (2.15), it can be seen that for a given d and θ, not only will photons with wavelength λ be selected, but so will any $n\lambda$ where n is an integer. This problem is generally mitigated by using a multiple bounce (diffractions) monochromators tuned so that $\frac{I_1}{I_n} \gg 1$ for any $n \geq 2$, where I_n is the intensity of the n-th harmonic. Also, at high energies, the spectrum of radiation from the undulator source falls with energy reducing the intensity of the higher harmonics. However, as mentioned before, it is sometimes convenient to perform measurements using a lower flux (e.g., when using two different detectors of different sensitivity), and therefore an attenuator is placed upstream of the sample. Because attenuation is energy dependent, it is possible to result to have an attenuated beam where higher harmonics are not negligible. The resulting diffraction patterns are not analyzable with the current methods.

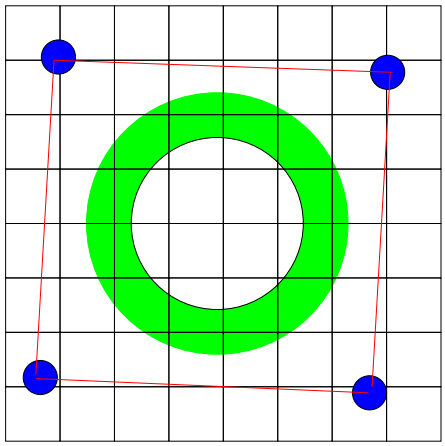

Figure 2.4: An example of a raster scan for a tilted detector. The blue dots indicate the locations of the direct beam as the detector is translated to four different locations. The objective of detector calibration is to align so that the grid lines are parallel to the plane of the X-ray beam (into the page). When the optical focus is set on the center of the detector, the aberration will be most noticeable near the edges of the detector. This is problematic as the high $|\vec{Q}|$ peaks contribute most to the spatial and orientation resolution of the reconstructed orientation map. An ad hoc solution to this problem is to optimize focus on the annulus around the center (shown in green) so that the center is still within the depth of focus ($\approx 2\mu m$). In this configuration, almost no aberration is observed.

Detector Calibration

As in the case of the rotation axis, the detector parameters are not known a priori in the HEDM setup. The scintillator screen has to be translated to put it at the focal point of the optical system and the orientation (relative to the x-ray beam plane) and the effective pixel pitch, γ (pixel dimension), have to be measured. Data collection macros have been written and associated analysis developed for these purposes using Matlab.

Pixel pitch calibration is measured using the so-called "raster" scan. In this scan, the detector is translated in front of a fix x-ray beam to a set vertical and horizontal locations using the associated set of linear translations (Fig. 2.4). A small X-ray beam, produced from the usual line focused beam by restricting the horizontal size with the JJ slits to roughly $5\mu m$, is imaged at each of these grid points. Because the linear motions are precise (or are measured) to within $\pm 1\mu m$, the distance between the grid points is well defined. The locations of the measured spots in the images is contrasted with the expected grid locations to yield γ in microns per pixel. With an optimized focus setting, the detector pixel size should be determined by the magnification of the optical focusing component and physical CCD pixel size. Given that the physical pixel size is $\ell = 7.4\mu m$, and a $5\times$ focusing optic is used, the effective pixel size should be $1.48mum$. Our measurements typically yield $\gamma = 1.47 \pm 0.01\mu$m. For an L-distanceof $5mm$, the angular resolution of a pixel is given by $\tan^{-1}\left(\frac{1.48}{5000}\right) \approx 0.02^{\circ}$.

To optimize the optical focus, the beam height is measured as a function of the focus (scintillator) position, again at a set of beam positions on the detector (the "focus raster" scan). The aberration in the optical system is manifested as a spatial variation of the optimal focus position approximated by

$$z_f(j,k) = A(j-j_c)^2 + B(k-k_c)^2 + z_0, \tag{2.16}$$

where z_f is the focus position, (j_c, k_c) is the center of the focal axis, and z_0 is the optimal focus position for (j_c, k_c) on the detector coordinates. Therefore, $z_f(j,k)$ is measured by running the raster scan at different focus positions around the z_0. The resulting parabola is used to optimize both the detector tilt and global focus position. See Fig. 2.4. When optimized, the coefficients, A and B are around $10^{-5}[\mu m^{-1}]$, contributing to a $10\mu m$ difference in focus location across the detector, which is negligible by noticeable given the $\approx 3\mu m$ depth of focus.

2.4 Data Reduction

While in principle explicit peak segmentation and peak identification are not necessary for the Forward Modeling reconstruction method (Chapter 3), the relatively large sizes of the raw diffraction images makes them difficult to handle. Therefore, data reduction is performed by a simple background (median) subtraction and rough peak

identification. This process reduces the input data size by a factor of roughly 100. Note that each of the peaks identified could be composed of intensity contributions from multiple regions of the sample, which is sometimes referred to as accidental peak overlap. In most other analysis methods, peak overlaps are detrimental to reconstruction, as it results in non-unique orientation solutions [56, 90, 105]. However, it is shown in Chapter 3 that accidental peak overlaps have minimal effects on the Forward Modeling reconstruction algorithm.

In the data reduction, the intensity of each pixel as a function of the ω is analyzed, and the background intensity is assumed to be additive; this is,

$$I_{\text{exp}}(j,k,\omega) \quad = \quad I_{\text{background}}(j,k,\omega) + I_{\text{signal}}(j,k,\omega), \tag{2.17}$$

where (j,k) are the usual detector coordinates. Here the background is simply taken as the median of $I_{\text{exp}}(j,k,\omega)$ To remove random, single pixel noise (hot pixels), a 3×3 median filter is applied to the background subtracted images. Peaks in the background subtracted images are identified using a connected component algorithm, and "tails" of the peaks are removed by applying intensity thresholding. In other words, given a set of pixels, $\{p_i\}$, forming a connected component, only the subset $\{p_i : I(p_i) \geq f I_{max}(\{p_i\})\}$ is accepted as diffraction signal, where $f \in [0,1]$, and I_{max} returns the maximum intensity from a set of pixels. This thresholding method can be considered as an ad hoc way to remove broadening effects of diffraction peaks due to the finite resolution of the detection system including hallowing effects due to the scintillator being thicker that the depth of focus of the optical system. As a reference, typical value of f is between 0.05 - 0.1 based on visual inspection and trial orientation reconstructions.

2.5 Conclusion

In this chapter, we have described some of the experimental set-up and calibration procedures of HEDM; in so doing, we have presented the foundation needed to discuss the analysis methods and orientation reconstructions of Chapter 3. The components of the HEDM set-up are sketched out, and the coordinate systems used in APS and the analysis are also defined. A brief overview of kinematic scattering was presented, and we have pointed out some of the results relevant to the experimental design.

The ability to spatially resolve orientation turns out to depend critically on the precision with which the experimental parameters are determined, and several calibration methods are developed and presented in this chapter to help minimize parameter errors. Further details of these effects and further minimization procedures can be found in Chapters 3 and 6. The data reduction method is also presented as a brief description of "peak" or "signal" extraction. While the Forward Modeling method (Chapter 3) has no explicit dependence on the way diffraction peaks are identified, the data reduction method serves as a means to control peak-dependent broadening in the detection system (finite resolution effects).

Chapter 3

Orientation Imaging Through Digital Reconstruction

3.1 Overview

Similar to orientation imaging using electron backscatter diffraction microscopy (EBSD), both high energy X-ray diffraction microscopy (HEDM) and three dimensional X-ray diffraction (3DXRD) microscopy leverage heavily on recent advances in computational techniques for orientation reconstruction based on digitally recorded diffraction patterns.[1] In the case of EBSD, diffraction (Kikuchi line) patterns produced by a point focused electron beam are captured from one spatial location on the sample at a time. In this way, spatial location is well defined. HEDM refers to a class of high energy X-ray diffraction methods that measure orientation and strain states of individual crystalline grains inside of bulk materials. Under standard terminology, "far-field" HEDM refers to measurements having detector-to-rotation axis distance (L-distance) of at least $1m$ (with a large area, large pixel size detector), whereas "near-field" refers to L-distances of a few millimeters using a small but high resolution detector. Far-field measurements concentrate on measuring crystallographic elastic strain states whereas near-field measurements are used for orientation mapping. For orientation mapping, the so-called "rotation method" is used with a line focused X-ray beam. The detector records diffraction images from many grains simultaneously, as discussed in Chapter 2. Consequently, reconstruction of orientation maps requires simultaneous determination of crystallographic orientation and diffraction origin from a set of superimposed diffraction patterns.

While X-ray orientation imaging is vastly more difficult than EBSD, a significant

[1] HEDM and 3DXRD are essentially equivalent measurement techniques and the acronyms are used almost interchangeably. 3DXRD was coined by Poulsen et al [88] to refer to work primarily at the European Synchrotron Radiation Facility (ESRF). HEDM was coined at and specifically refers to work at the APS. While experimental parameters may be different, the real divergence in the context of this thesis lies in the analysis methods (as discussed below).

set of advantages makes the X-ray approach attractive. First, with the use of high energy X-rays, the penetration depth provides access to bulk information (sample radius up to $1mm$). Three dimensional structure can be accessed and re-measured after a variety of treatments to the sample. In contrast, the penetration depth of elastically backscattered ~ 20 keV electrons in EBSD is on the order of nanometers. Thus, EBSD is inherently a surface technique. Three dimensional information can only be gathered by sectioning off the previously measured surface layer. Moreover, the quality of orientation maps from EBSD is heavily dependent on surface properties. For example, oxidation or poor polishing lead to diffraction patterns that are not indexable, which significantly reduces the reliability of the resulting orientation maps. Since high energy X-rays probe inside bulk material, surface preparation and smoothness are not issues.

Not all 3D X-ray orientation imaging techniques use the rotation method. Differential aperture X-ray microscopy (DAXM) [55] is quite similar to EBSD. Grid points along the sample surface are scanned, and orientations are measured using the Laue diffraction patterns generated by a polychromatic incident beam. Sub-micron focusing yields excellent spatial resolution and careful analysis yields sensitivity to deviatoric strains. On the other hand, DAXM suffers from some of the same drawbacks as EBSD. While micron scale depth resolution is possible, penetration is limited by the lower energy of the probing X-rays (≤ 20 keV). This leads to the inability to collect data from sample volumes in excess of $500\mu m^3$. The fact that the technique requires at least a detector image per measured volume element implies extremely large data volumes (and data collection times) for measurements that resolve shapes of large numbers of crystals. Large volume characterizations are crucial to statistically significant studies of phenomena such as grain growth or so-called "extreme-events" (e.g., crack formation).

Intrinsically three-dimensional problems are difficult to address using standard two-dimensional imaging techniques. For example, measurement of residual strains on a fracture surface is a problem of three-dimensional nature. Studies by Fields and company [108] (cite Fields, EBSD book) suggest that residual strains tend to relax at a free surface. Therefore, observation of strain states in the depths sampled by EBSD may not reflect the pre-crack state. X-ray techniques provide the possibility of measuring strains in bulk material prior to crack formation. Another example is the problem of grain growth in $3D$. While statistical analyses using stereology [54, 99] have helped advance the understanding of $3D$ grain growth, numerous *a priori* assumptions are required [44, 99]. With the advent of automated serial sectioning by combining ion-beam milling with EBSD, three-dimensional data structures have become more readily available. However, the destructive nature of serial sectioning measurements makes direct observation of microstructure dynamics difficult or impossible.

Due to the relatively complex nature of the orientation search problem in HEDM and 3DXDR, significant focus has been placed on reconstruction algorithms, and

numerous advances have been made in recent years. Various techniques have been developed by Risoe/Danish Technical University [87, 105, 56, 91], for example GrainDex, GrainSweeper, and algebraic reconstruction methods. A brief review of these techniques, including some of their shortcomings will be presented in this Chapter. The application of the forward modeling method (FMM) [116] has led to advances in orientation reconstruction of deformed microstructures. The forward modelling method also paved the way for the development of Stratified Monte Carlo Pruning (SMCP) and several ongoing importance-sampling based algorithms in orientation searches. Because the forward modelling method and orientation searches form the foundation of the HEDM method, we will devote the first half of this Chapter to their development and details. The orientation reconstruction problem is inherently an inverse problem, so we will address some of the questions regarding existence and uniqueness of an optimal solution. This includes examination of some of the objective functions used in the forward modelling orientation search. To provide a concrete characterization of errors, a set of parameter studies is conducted. Results are reported in the second half of this Chapter. Finally, some ongoing work which extends the most recent advances is summarized.

3.2 Methods of Orientation Reconstruction

3.2.1 Problem Statement

Single Grain Diffraction

Consider a perfect single crystal at the origin, and a collimated, monochromatic incident X-ray beam along $\hat{z}$. In the kinematic (single scattering) approximation, diffracted X-ray beams will be visible in discrete spots dictated by Bragg's Law:

$$\vec{k_i} - \vec{k_o} = \vec{G}_{hkl} \tag{3.1}$$

$$|\vec{k_i}| = |\vec{k_o}|, \tag{3.2}$$

where $\vec{k_i}$ is the incoming X-ray wavevector, and $\vec{k_o}$ is the diffracted X-ray wavevector. The reciprocal lattice vector for the sets of planes specified by (hkl) is denoted by $\vec{G}_{hkl}$. Due to the monochromatic nature of the X-rays in our experiments, diffraction spots are only expected at discrete locations, which can be parametrized by $(\omega, \eta, 2\theta)$, as shown in (Fig. 3.1). The crystallographic orientation of a diffracting single crystal is defined to be the rotation required to transform from the sample coordinate system to the crystal coordinate system. To specify the crystal system relative to the sample system at least three linearly independent vectors, or a set of basis vectors must be specified. This information, which is obtainable by indexing of diffraction peaks measured from the rotating crystal method, is in principle sufficient for the orientation determination of a single crystal.

Ideal Peak Indexing

In general, peak indexing refers to identifying the *hkl* values of measured reciprocal lattice vectors. Since the incoming wavevector in a measurement is well defined by the synchrotron source and the monochromator, peak indexing solely relies on determining the geometry of a given diffraction pattern. Given a single crystal of negligible size and assuming that the detector is perfectly efficient with zero noise and that the physical setup exhibits no drift, the direction of the diffracted wavevector, $\hat{K}_o$, is defined by the scattering origin and the location the diffraction spot. For convenience, let us define the detector origin as the projection of the diffraction origin onto the $2D$ detector, which is assumed to be perpendicular to the incident beam. Diffraction peaks must lie on discrete 2θ rings (fixed radii) because of the Bragg condition. In principle, ambiguity due to closeness of 2θ rings are resolved by indexing large numbers of diffraction peaks. In reality, the use of the rotating crystal method with finite sample size results in ambiguous diffraction origin, as any sample point not on the origin would necessarily circle about the rotation axis. To resolve this problem, both peak index and diffraction origin must be identified simultaneously.

3.3 Review of Existing Reconstruction Techniques

Extensive literature can be found on the existing reconstruction techniques [88, 87], and therefore only a brief survey will be provided here to justify the need for the work described in this section.

Reconstruction and indexing of diffraction spots are thoroughly studied by Poulsen et al and an indexing algorithm has been written; the program is called GRAINDEX [56]. Roughly speaking, it works by identifying diffraction spots from a set of $2D$ images by a combination of background subtraction and image segmentation [81, 84]. Diffraction spot centers-of-intensity, also sometimes known as centers-of-mass, for multiple detector locations and ω values are used to track the direction of the diffracted momentum vectors, $\hat{k}_o$. Given the definition of η and θ in Fig. 3.1, the lab frame reciprocal lattice vectors can be described by

$$\frac{\vec{G}}{|\vec{G}|} = \cos\theta \begin{pmatrix} -\sin\eta \\ \cos\eta \\ -\tan\theta \end{pmatrix}. \tag{3.3}$$

Given the center-of-intensity position for each of the peaks, the values of η and θ can be estimated (the algorithm works best in the far-field limit where sensitivity to the position of origin is minimal). Consequently, a reciprocal lattice vector can be assigned for each of the diffraction spots. By associating diffraction spots and reciprocal lattice vectors to a grain, a coordinate system representing the crystal frame is defined. The crystallographic orientation of a grain is found by determining the transformation required to go from the sample frame to the crystal frame. In practice,

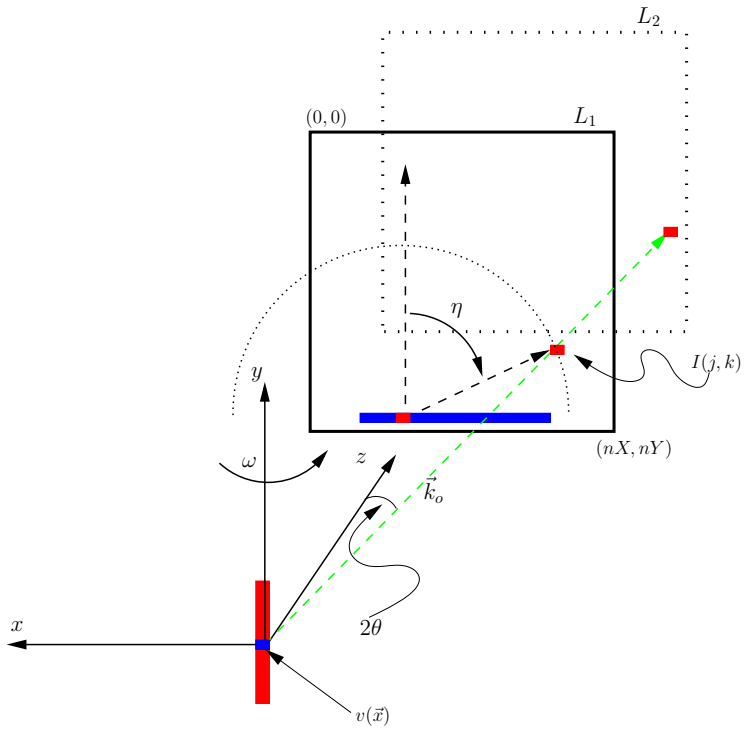

Figure 3.1: Coordinate system for a rotating crystal experiment. This is the convention used at the APS beamline. The line-focused incident beam propagates with $\vec{k_i} \parallel \vec{z}$ and, if not blocked, would intersect the detector along the blue line. The red rectangle at the coordinate origin represents the sample region being measured. The blue element, $v(\vec{x})$, is a particular volume element in the sample space which, at rotation position ω, produces a diffracted wavevector $\vec{k}_o$ intersecting pixel (j,k) of the CCD detector (with $nX \times nY$ pixels). The polycrystalline nature of the sample suggests that intensity, $I(j,k)$, can be a result of not only $v(\vec{x})$, but also its neighboring volume elements. This is known as "accidental overlap." The diffraction peak due to $\vec{k}_o$ is considered a qualified peak as it satisfies the geometrical constraints of the system (it strikes the detector at both L_1 and L_2). Notice that the diffracted intensity originating from $v(\vec{x})$ due to this $\vec{G}_{hkl}$ could lie on any point along the dotted arc (2θ-ring) if the crystal lattice were rotated about the incident beam; this is true even for volume elements that are off the rotation axis. On the other hand, rotations about this $\vec{G}_{hkl}$ leave this peak position unaltered. All other rotations about axes with a component along y or z, will cause the Bragg condition to be satisfied at a different ω; those not parallel to y will change both ω and η. For off-axis volume elements, changes in ω change the location of the origin of the scattering, and hence move the peak to a shifted 2θ-ring. The coupled, complex motion of the many diffraction spots observed from each volume element (as a function of lattice orientation) is the key to resolving both crystal orientations and corresponding positions.

center-of-intensity is determined by identifying and raytracing the same diffraction spots measured at multiple detector-to-rotation axis distances (L-distance) when the diffraction origin is resolvable by the detector (near-field HEDM).

Unfortunately, GRAINDEX is very sensitive to peak shape, as center-of-intensity positions can be significantly altered in imperfect grains. For example, when a peak splits under deformation, the resulting center-of-intensity may not correspond to that of the original peak. Accidental peak overlap from separate grains also presents a challenge in this analysis. To alleviate these problems, multiple indexed reciprocal lattice vectors can be used simultaneously to construct an orientation matrix. This forms the basis of the program GrainSweeper.

Another way to understand the problem of orientation reconstruction is to generalize it to solving the full inverse problem of diffraction in $6D$ [87]. This is known as the Algebraic Reconstruction Technique (ART). Specifically, the spatial geometry and crystallographic orientation of the sample can be represented in the $6D$ space of $\mathbf{H} = \mathbb{R} \otimes SO(3)$. Intensities recorded by the X-ray detector are then produced by a function, $f : \mathbf{H} \to \mathbb{R}^3$, where $\mathbb{R}^3$ is a scalar field describing intensity on a set of $2D$ detector images. The objective of ART is to find $f^{-1} : \mathbb{R}^3 \to \mathbf{H}$ such that the $6D$ configuration from measured diffraction intensities is recovered. Unlike the case of a Radon transform in transmission tomography, the explicit inverse of the transform f specified in this case is unknown. There is a significant amount of freedom in both constructing and parametrizing $\mathbf{H}$. For example, one could use a product of direct space ($\mathbb{R}^3$) with quaternions, Rodriguez-Frank vectors ($\mathbb{RF}$), or even Euler matrices. It is even possible to forgo the use of direct space altogether and use dual quaternions. When the direct product space $\mathbb{R} \otimes \mathbb{RF}$ is used, the optimization problem becomes

$$A_{ijklmnp}\, x_{jklmnp} = b_i, \tag{3.4}$$

where the indices are summed over the direct product space of spatial and angular degrees of freedom. The matrix elements are defined to be

$$A_{ijklmnp} = T_{ijlkmnp}\, \mu_{jklmnp}\, I(|F|, \mathbb{G}), \tag{3.5}$$

where T is the transfer function describing the fraction of the intensity from element, x_{jklmnp}, that is transfered to b_i, μ is the measure in $\mathbb{H}$ associated with the $6D$ voxel x_{jklmnp}. The intensity normalization factor is given by $I(|F|^2, \mathbb{G})$ for a given scattering form factor F and experimental geometry $\mathbb{G}$. No summation is performed on repeated indices in Eq. (3.5). The reconstruction is then performed by minimizing $|\mathbf{A}x - b|$. The detector geometry is hidden inside the function $I(|F|^2, \mathbb{G})$, which also has implicit dependencies on x_{jklmnp}. Moreover, very little is known about $\mathbf{A}$ other than the fact that it is sparse. In most realistic situations, output from GRAINDEX and GrainSweeper are used as input for ART.

The Filtered Back Projection method [21] from computed transmission tomography (CT), can also be used under the assumption of perfect grains. The use of

this technique is associated with the so-called "box-beam" setup [68], a favorable configuration when speed is needed. This is because, while typical near-field HEDM and 3DXRD setups use a micro-focused planar beam of a few microns in height, a box-beam is hundreds of microns tall and may fully illuminate up to several grain volumes at a time. Here, $3D$ grain shapes are projected non-perpendicularly onto the $2D$ detector. This amounts to a modified version of the Radon transform [67, 88, 91].

3.3.1 Shortcomings of Peak Center of Intensity Methods

The particular reliance on diffraction peak segmentation, peak identification, and center-of-intensity estimate in orientation reconstruction leads to significant shortcomings in the GRAINDEX-like reconstruction methods. The use of digital image processing techniques such as image segmentation often depend heavily on a set of *a priori* assumptions on the physical properties of the diffraction peaks. These assumptions sometimes lead to highly undesirable results, some of which are discussed in this section.

The most obvious problem is that peak identification, more generally known as image segmentation, is fairly difficult in the most general case [81, 84]. While advances in both charge-coupled device CCD and scintillator technology have drastically improved signal-to-noise ratios, there are still significant challenges in identifying diffraction peaks from non trivial samples. For example, a single X-ray diffraction image (one integration interval) for a piece of well annealed, high purity Nickel contains many peak overlaps, especially in the low 2θ region. Peak overlap is due mostly to the large number of crystals in the cross section, typically more than 1000 for an interesting sample $1mm$ in diameter. Since measurement of polycrystalline samples with large numbers of grains is important for statistical reasons, we are not likely to see any reduction in this number.

In the case of sharp diffraction peaks, center-of-intensity positions easily translate to grain center positions through the use of ray-tracing (following the diffracted beam from the sample to the recorded peak). Also, albeit sometimes challenging, the detection system's point-spread function maybe measured ahead of time. In this way, grain shape may be recovered either from backward projection or algebraic reconstruction of the deconvolved peak. However, peak overlaps make it difficult to attribute peaks to their corresponding grain. *A priori*, it is difficult to know what the contributing peaks look like given the composite peak. The problem gets further complicated in cases where many overlapping peaks are present. This happens much more commonly than one would hope in real materials, as orientation preference in samples (texture) is prevalent in both naturally occurring and engineered materials. The result is that the combination of multiple peaks in the same region pushes the response of the detection system into the non-linear regime, or worse, saturation, making both deconvolution and peak separation extremely difficult.

In considering more complicated experiments such as *in situ* observations of strain,

annealing, and phase transitions, both elastic and plastic deformation lead to peak broadening. In these cases, plastically deformed regions contain networks of very low angle boundaries. Here, even center-of-intensity may be misleading. This is analogous to peak shifting and broadening due to a concentration of stacking faults in powder diffraction experiments [126]. Because peak shifts due to deformation are usually asymmetric, the original reciprocal lattice vector is not recoverable without fully fitting the intensity of the entire peak.

Because center-of-intensity values of segmented peaks are used to estimate a set of reciprocal lattice vectors for each of the expected grain centers, the choice of image process implicitly dictates the possible orientations of the final microstructure. This is advantageous in the case of perfect image processing, where peaks are isolated correctly without error. Unfortunately, real-world subtraction significantly influences the final outcome of the orientation reconstruction. This can be seen easily in cases where diffraction peaks are removed through either background subtraction or segmentation. In the most extreme case, with enough diffraction peaks removed, mis-indexing may occur. Symmetrically related orientations may produce a significant number of overlaps in a diffraction pattern. This problem is exacerbated in the case of deformed materials. In addition, long tails in diffraction peaks can be mistakenly subtracted, resulting in missing orientation variations inside a grain.

3.4 Forward Modeling

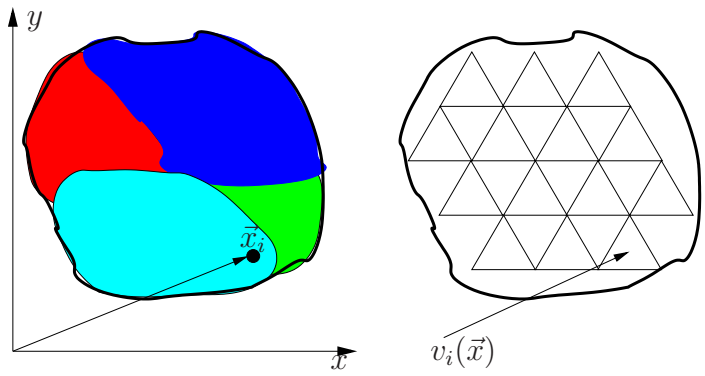

Figure 3.2: Discretization of a microstructure. A microstructure can be represented by an orientation field, $\mathcal{O}(\vec{x})$, where $\vec{x}$ is a point in the sample space. A discretized sample space (right) is used in the Forward Modeling method.

3.4.1 Overview

All of the methods mentioned so far are only able to address the orientation reconstruction problem in the case of little to no peak overlap in each recorded diffraction image. An additional requirement of well ordered grains is also necessary if we desire reliable reconstruction. This poses a problem, as most interesting polycrystalline systems are far from being simply a collection of well ordered crystals. Defects are introduced during many kinds of processing. Deformation can be present from a variety of sources, ranging from mechanical loads to phase transitions. And, while in some cases complete and perfect orientation reconstructions may be impossible (for example, deformation of copper under high shock rate) reliable partial reconstructions will still prove invaluable. The Forward Modeling Method, coupled with orientation search, has the required robustness to address these difficult cases. While the forward model method is extremely simple conceptually, it is extremely powerful in its demonstrated ability to recover crystallographic orientation states in deformed and highly polycrystalline microstructures. The motivation for this alternate approach to orientation reconstruction will be discussed in this section. Also some basic definitions will be provided to understand orientation reconstruction in the context of the Forward Modeling Method.

3.4.2 Definitions

Forward Modeling Simulation

A microstructure can be represented by an orientation field $\mathcal{O}(\vec{x})$, where regions with similar orientations represent grains. In this light, grain boundaries are discontinuities in the orientation field. The Forward Modeling method is simply the simulation of diffraction patterns given a discretized input orientation field. The sample space is discretized into volumetric pixels (voxels), which represent a small volume element, $v(\vec{x})$ in the sample space. The orientation field, $\mathcal{O}(\vec{x})$, is then defined on this discretized sample space as $\mathcal{O}(v(\vec{x}))$. Forward Modeling then corresponds to a simulation of the rotating crystal experiment. Note that the term "voxel" and volume elements are sometimes used interchangeably to represent the discretization of the sample space.

Orientation Search

Similar to the Algebraic Reconstruction Technique (ART), reconstructing the orientation field $\mathcal{O}(v(\vec{x}))$ amounts to solving an inverse problem of the form $\mathbf{A}\vec{x} = \vec{b}$. To do this, a search is performed on each element v_i to find the best crystallographic orientation that leads to simulated diffraction patterns that best match the measured ones. This is known as the orientation search. In principle, the orientation search is done by exhaustively checking every possible crystallographic orientation for sample

point, v_i. Because the rotation group, $SO(3)$, is continuous, a complete exhaustive search by enumerating all of its elements is impossible. The orientation search must in practice be considered as an optimization problem with respect to some objective function, $\mathcal{C}$. Generally speaking, this objective function measures the similarity between the simulated intensity, $I(\mathcal{O}^t)$ and the experimentally measured diffraction patterns, $I(\mathcal{O})$, where $\mathcal{O}^t$ and $\mathcal{O}$ are the trial solution and the real orientation field, respectively. The reconstructed orientation field is also referred to as the reconstructed orientation map.

Provided that the discretization of the sample space is sufficiently fine, and that an optimum for the objective function, $\mathcal{C}$ over the orientation space exists and is unique, the Forward Modeling method provides a way to reconstruct the crystallographic orientation of an unknown microstructure. This method is powerful in that it allows for approximations of the scattering physics and microstructure properties to be inserted systematically. *A priori*, no assumptions of the features in the microstructure is made, and the definition of a "grain" is not predetermined. This removes the somewhat arbitrary nature in these geometrical feature definitions that could easily bias the reconstruction results. In this section, we will detail an implementation of the Forward Modeling method which uses only Bragg scattering and an ideal detector model. Furthermore, we will see that a binary intensity model is sufficient for robust microstructure reconstructions that proved challenging to the center-of-intensity methods.

Scattering Physics

The scattering physics calculation is based on elastic scattering. The location of a diffraction peak on the detector is determined by the Bragg condition, as it specifies the 2θ, η, and ω Fig. 3.1 where the diffraction spot occurs. The intensity of each Bragg peak is determined by the structure factor. For a given reciprocal lattice vector, $\vec{G}_{hkl}$, the diffracted intensity is given by

$$\begin{aligned} A &= \sum_n f_n(\vec{G}) e^{-i\vec{G}\cdot\vec{r}_n} \\ I &\propto A^* A, \end{aligned} \tag{3.6}$$

where $\vec{r}_n$ is location of the nth atom, and f_n is its atomic form factor. To account for the finite resolution effect in a rotation method (Chapter 1), an extra term of $\frac{1}{\sin 2\theta \sin \eta}$ (the Lorentz factor) is incorporated as the pre-factor in the intensity equation. Since no explicit intensity fitting is done in the current implementation of the orientation search, each diffraction peak is binarized based on some predetermined threshold value to exclude weak peaks from the simulation. The comparison of simulated versus measured diffraction peaks is done by looking at their pixel-to-pixel overlap.

Simulated Detector Model

Typically, a point spread function, $\sigma_n(x)$ is associated with each point on a detector. This point spread represents the imperfect spatial response of the detection system. For example, in one dimension, suppose that an ideal intensity distribution is given by $I(x)$ (with units of energy or photons per unit length). A pixelated detector in which pixel p_n is centered at x_n and extends over $x_n \pm \gamma/2$ will see an intensity

$$I_n = \int_{x_n-\gamma/2}^{x_n+\gamma/2} dx \int I(x')\sigma_n(x-x')dx' \tag{3.7}$$

The inner integral accounts for the point spread while the outer accounts for the finite pixel size. If $\sigma_n(x)$ is uniform over the detector and sharply peaked so that its width is less than γ, the point spread can be approximated by a δ-function and ignored.

In our case, the detection system includes the scintillator, the CCD camera, and the focusing optics. The pixel pitch is $\gamma = 1.47\mu$m. For present purposes, we make the δ function approximation. This is justified by a number of optical tests in which we see sharp feature edges with widths on the order of the pixel size. As a consequence of using thresholded intensity values, the point spread function will only act to dilate diffraction patterns in a detector image. This amounts to adding a border of pixels around each measured peak.

Additional effects are neglected as well. For example, the scintillator is finite in thickness and this causes a characteristic smearing of intensity between pixels at non-normal incidence. The scintillator that we currently use is 20μm thick, so at 30° off normal incidence, this parallax effect can cause 10μm streaking and this can in fact be seen around strong peaks. However, the depth of focus of the optical system is only $2\mu m$ (FWHM) and this results in the streaks being weak compared to the central peak. In principle, such effects could be included in the forward model of the experiment, but our observation is that thresholded peaks contain very little contamination.

3.4.3 Cost Function

Under ideal Bragg conditions, diffraction peaks collected from HEDM are perfectly sharp spatially and in ω, and the peak shape on the detector is the projection of the shape of the diffracting region in the sample. In the present geometry (Fig. 3.1), the observed angles ω and η uniquely determine the orientation of a specific reciprocal lattice vector, $\vec{G}_{hkl}$, while 2θ gives $|\vec{G}_{hkl}|$. The list of measured $\{\omega, \eta, 2\theta\}$, or equivalently $\{\vec{G}^{(e)}_{hkl}\}$ completely determines, up to crystallographic symmetry, the orientation $\mathcal{O}$ for a volume element v_i, provided that the list $\{\vec{G}^{(e)}_{hkl}\}$ contains at least three linearly independent reciprocal lattice vectors.

The purpose of the cost function is to measure the difference or distance between the measured orientation $\mathcal{O}_e \leftrightarrow \{\vec{G}^{(e)}_{hkl}\}$ and trial orientations $\mathcal{O}_t \leftrightarrow \{\vec{G}^{(t)}_{hkl}\}$. The

cost function should increase with increasing distance between the two orientations, $d(O_t, O_e)$, where this distance is known as the misorientation, which is simply the angle of fixed-axis rotation required to get from O_t to O_e. In this spirit, a cost function can be defined as

$$\mathcal{C}(\mathbf{O_t}) = \frac{1}{N} \sum_{h,k,l} |\cos^{-1}\left(\hat{G}_{hkl}^{(t)} \cdot \hat{G}_{hkl}^{(e)}\right)|, \tag{3.8}$$

where N is the total number of simulated peaks, and $\hat{G}_{hkl}$ is a unit vector in the $\vec{G}_{hkl}$ direction. It should be emphasized here that the angular deviations $\cos^{-1}\left(\hat{G}_{hkl}^{(t)} \cdot \hat{G}_{hkl}^{(e)}\right)$ are not generally equal to the misorientation between simulated and measured orientations.

We should note at this point that the reciprocal lattice vectors, $\vec{G}_{hkl}^{(e)}$, are in fact not explicitly measured. They are specified by the pixel locations of diffraction spots on the detector. This can be denoted as $(\omega, \eta, 2\theta)$ as defined in Fig. 3.1. For small angle deviations between $\vec{G}_{hkl}^{(e)}$ and $\vec{G}_{hkl}^{(t)}$ outside the singular range of $\eta \to 0$, the cost function of Eq. (3.8) can be approximated by

$$\mathcal{C}(\mathbf{O_t}) = \frac{1}{N} \sum_{i} \sqrt{\delta\omega_i^2 + \delta\eta_i^2}, \tag{3.9}$$

where $\delta\omega_i$ and $\delta\eta_i$ are the experimental deviations in ω and η from their simulated values. Here we make the following observations:

1. If we produce the list $\{G_{hkl}^{(e)}\}$ from the center-of-intensity positions of each diffraction peak, and we take the sample voxel v_i to be a grain, then we recover the same optimization problem as in the case of center-of-intensity based orientation reconstruction.

2. By not having explicit definition of peaks, we have effectively defined an optimization problem that requires the fitting of the list, $\{G_{hkl}^{(e)}\}$, for each lit pixel in the binarized diffraction data against the set of discretized sample elements, $v_i \ll V_{grain}$, where V_{grain} would be the volume element that encompasses the entire grain. In other words, the result from the optimization of the cost function in Eq. (3.9) is analogous to running the center-of-intensity optimization for every pixel against many different sample points inside each of the grains of the sample.

3. The deviation between experimental and simulated diffraction, $\delta\omega_i \to 0, \delta\eta_i \to 0$ is equivalent to having experimental and simulated diffraction overlap.

In practice, the cost function of Eq. (3.9) is fairly expensive computationally. The angular deviations defined must be calculated for each lit pixel. By drawing a

simple bounding box (axis-aligned bounding box, or AABB) around each isolated connected region of lit pixels, we can speed up the angular deviation calculation by replacing $\delta\omega_i$ and $\delta\eta_i$ by the upper bound of their values. Unfortunately, the fact that this computation scales as the number of peaks observed on the detector makes it extremely costly. To simplify matters, we can take advantage of observation (see Fig. 3, below) and create a cost function with similar features to Eq. (3.9). This requires the definition of the number of peak overlaps as

$$\begin{aligned} \mathcal{N} &= \sum_{n,j,k} \chi(I_s(\omega_n, j, k,), I_e(\omega_n, j, k)), \\ \chi(I_s, I_e) &= \begin{cases} 1 & \text{if } I_s > 0 \wedge I_e > 0 \\ 0 & \text{otherwise,} \end{cases} \end{aligned} \tag{3.10}$$

where I_e is the experimentally observed binarized intensity at pixel location (j, k), and I_s is the simulated intensity for all of the reciprocal lattice vectors, $\{G_{hkl}\}$ selected. Here the location of diffracted intensity is explicitly represented as detector coordinate instead of 2θ, ω and η. In this way, maximum peak overlap corresponds to minimum angular deviation. To incorporate the data observed by multiple detectors and to ensure that the measure is consistent with observation, we can enforce consistency requirements to the peak overlaps. This amounts to modifying χ such that peak overlap must occur on all detectors, satisfying a geometrical constraint: the coordinates of recorded intensities on all detectors must lie on a straight line including the diffraction origin on the sample. We call a peak that satisfies this geometrical constraint a **qualified peak** (Fig. 3.1). In practice, it is cumbersome to define a cost function over all detector pixels for each of the voxels as prescribed by Eq. (3.10). Since diffraction spots amount to only a small fraction of the pixels on a detector, it is convenient to define overlap for the reciprocal lattice vectors generated as

$$\begin{aligned} \mathcal{N}(G_{hkl}) &= \chi\left(I_s(\omega_g, i_g, k_g), I_e(\omega_g, i_g, k_g)\right), \\ \mathcal{N} &= \sum_{hkl} \mathcal{N}(G_{hkl}), \end{aligned} \tag{3.11}$$

where ω_g, i_g and k_g are the detector and pixel coordinates of intensity produced by $\vec{G}_{hkl}$. Because the number of qualified peaks depends on the orientation and location of the sample voxel, we must normalize the cost function to form a useful "goodness-of-fit" across all points in the sample space. This results in the **confidence** [116],

$$\mathcal{C} = \frac{1}{N_{qual}} \sum_{hkl} \mathcal{N}(\vec{G}_{hkl}). \tag{3.12}$$

Up to this point, we have been assuming the sample voxel, v_i to have a side length that is less than the typical pixel size, γ. This implies that all peaks are weighted equally regardless of the projected size of the grain. To generalize this cost function

to the case where the v_i is larger than the pixel size, a weighting factor in front of χ in the overlap function $\mathcal{N}$ can be added ($\frac{N_{\text{pixel overlap}}}{N_{\text{pixel lit}}}$). This weighted confidence is known as the **quality**. In cases of small numbers of detectors (≤ 2), a secondary weighting factor is added in front of χ to discriminate against accidental overlaps, which are prevalent in polycrystalline samples.

3.4.4 Cost Function Landscape

By using the peak overlap function of Eq. (3.10), we have replaced $\sqrt{\delta\omega_i^2 + \delta\eta_i^2}$ from Eq. (3.9) by an indicator function, χ, which is binarized. As a consequence, the optimum of the cost function $\mathcal{C}$ is sharply peaked in orientation space. Intuitively, this is because the orientation deviation allowed while keeping total peak overlap is roughly $\approx \frac{\gamma}{L}$, where γ is the pixel side length, and L is the detector-to-diffraction-origin distance. In practice, because each grain inside a sample is of appreciable size, the cost function is broadened by the spatial extent of the diffraction peaks (Fig. 3.3).

The polycrystalline and finite grain size nature of the sample lead to some unintended effects. While orientations are uniquely determined by the degree of simulated overlap, significant accidental overlap can occur for orientations that are crystallographically similar. For example, two orientations off by a 60° rotation about [111] in FCC crystals can share up to $\frac{1}{3}$ of the diffraction peaks due to crystal symmetry.

While the contribution to the confidence function by each reciprocal lattice vector is binarized, the cost and confidence functions themselves are smooth due to the spatial extent of each peak (an effect of finite grain size). Deviations of a trial orientation away from the true orientation will result in a shift of diffracted peak positions. However, this does not affect all peaks equally, leading to a smooth drop in the confidence. The width of this drop off is roughly equal to the angular extent of the peak size, or approximately $\tan^{-1}\left(\frac{r}{L}\right) \approx \frac{r}{L}$, where r is the longest dimension of the peak and L is the detector-to-sample-rotation-axis distance. This local peak width of the cost function is extremely important in speeding up orientation reconstruction.

Somewhat surprisingly, the binarized cost function contains much more abrupt discontinuities across the ω direction than the other directions. This is a result of both the explicit removal of the ω dependency from Eq. (3.9) (in the approximation) and the large integration interval in this direction. To illustrate this problem, consider a set of diffraction intensities $I(\mathbf{A})$ generated by an element v at orientation $\mathbf{A}$. If we rotate this element by a small angle around the $\hat{y}$ direction by ω to arrive at orientation $\mathbf{A}'$, we'd find the diffracted intensities shifted both in the η and ω directions. Because the equivalent angular resolution of our area detector is given by the $\frac{\gamma}{L}$, and $L \approx 1000\gamma$, we have an effective resolution of around 0.1°. Therefore, any small shift can be captured easily and continuously as the peaks move along $\hat{\eta}$. On the other hand, the integration interval for ω suggests that there exists some cutoff positions, $[\omega_n, \omega_{n+1})$ where the diffraction spot due to a $\delta\omega$ shift will move from image k to $k \pm 1$. While the diffraction spot sharpness is around $\approx 5°$ equivalent

angular width in the η direction due to sample size effects, the angular sharpness remains $\approx 0.1^\circ$ for perfect crystals. Therefore, given a peak generated from $\vec{G}_{hkl}$ at orientation $\mathbf{A}$ that lands on $\omega_{n+1} - \delta$ and ω_{n+1} at $\mathbf{A}'$, the peak overlap count due to $\vec{G}_{hkl}$ will vanish for any sufficiently small δ. In contrast, a shift δ in the η direction must be at least greater than $\frac{\gamma}{L}$, if not $\frac{r_{grain}}{L}$ before making the contribution to χ vanish. This results in some interesting consequences in both the orientation search algorithm and the resolution.

3.4.5 Existence and Uniqueness of A Global Optimum

The orientation reconstruction problem in HEDM and 3DXRD, viewed as an inverse problem, is not well-posed. In developing the algebraic reconstruction technique (ART), Poulsen et al. recast the orientation reconstruction problem as a linear system of the form

$$A_{ijklmnp}x_{jklmnp} = b_i, \tag{3.13}$$

where $A_{ijklmnp}$ is defined by the detector geometry and crystallographic properties (Chapter 2). One would hope that by formally defining the inverse problem, its study would become easier. Unfortunately, the formal form of the linear optimization is not entirely enlightening, as the detector geometry and scattering physics are buried deep inside the matrix A, the exact nature of which determines the existence and uniqueness of a solution. Regularization schemes involving removal of singular elements may be applied to specific reconstruction problems, but it is generally difficult to see if an inverse matrix exists.

There are practical reasons of mathematical interest to solve the orientation reconstruction problem. At the very least, it gives a sense of confidence to reconstructed orientation maps. We will only briefly describe our attempt to analyze the existence and uniqueness of a forward modeling solution, and the discussion will focus on the limiting cases of very small and very large grains.

Single Grain Samples

In the case of a single crystal, the maximum value of the overlap function, and therefore the confidence function, corresponds to complete overlap between simulated and experimental diffraction peaks. This also simultaneously minimizes the angular deviation between the simulated and measured reciprocal lattice vectors, $\{\vec{G}^{(t)}_{hkl}\}$ and $\{\vec{G}^{(e)}_{hkl}\}$, respectively. Since we have established that we only need three linearly independent vectors to define the coordinate systems or the crystallographic orientation, the existence of a global optimum is guaranteed given $\{\vec{G}^{(e)}_{hkl}\}$ spans the reciprocal lattice vector space. Similarly, uniqueness, taking symmetry multiplicity into account, is guaranteed by this condition.

Polycrystalline Samples

Determination of existence and uniqueness is much less transparent in the case of polycrystalline samples. Work by Schmidt et al. (REFER work done by Risoe regarding peak overlap probability) has calculated peak overlap probabilities for an untextured sample as a function of the number of grains. However, no explicit consideration for spatial separation between diffraction origins of grains is made in their treatment. Because our near-field HEDM technique has a field of view and detector-to-rotation-axis distance of $4mm$, the spatial separation of diffraction origins becomes a very important consideration in peak overlap analysis. In this case, grains of identical orientation will not necessarily yield overlapping peaks if they are sufficiently separated in space. Nonetheless, the work by Schmidt et al. still proves useful as an upper-bound for peak-overlap probability.

Large-Grain Limit

We define the large-grain limit to be $\frac{r}{\gamma} \gg 1$, where γ is the pixel side length, and r is the average grain radius. For a sample radius of $1mm$, this approximation leads to roughly $10 - 100$ grains per cross section, resulting in an overlap probability of $0.3 - 0.4\%$ at 0.1° grain mosaicity [106]. Given that each sample point is fitted with more than 100 qualified peaks, the chances of all coming from overlapping peaks is very low. This suggests that the cost function for large-grain polycrystalline samples will be similar to that of a single grain.

Small-Grain Limit

Analysis of the small-grain limit is much more difficult. We define the small-grain limit as $\frac{r}{\gamma} \approx O(1)$. In this case, the number of grains in the sample is above 1000. If significant peak overlap is present, the single crystal analysis presented above is no longer justified. Consequently, we rely on understanding the landscape of our cost function. In particular, most of our knowledge comes from numerical simulations of different polycrystalline structures, as shown in Fig. 3.3. From these, we can extract the following:

1. Our binarized cost function contains multiple maxima (corresponding to minimum angular error) in most polycrystalline samples. These maxima are a consequence of rotations in the cubic lattice that leaves a significant fraction of the reciprocal lattice vectors unchanged (i.e., 60° about [111]).

2. Given a sample element v, the cost function $\mathcal{C}(v)$ has a global maximum which corresponds to a point in orientation space located within a radius d from the true orientation. This d depends on the spatial extent and mosaicity of the diffracting crystal.

3. While our binarized cost function is not strictly monotonic due to noise, given an experimental orientation O, $\mathcal{C}(O')$ for any $O' \in \{O' | d(O', O) \leq r\}$ is smaller than in most other outside regions (Fig. 3.3(d)).

3.5 Orientation Search Algorithm

With the cost function defined in Eq. (3.12), and its features discussed in the previous section, we proceed to define the search algorithm. To begin, we will briefly review the original algorithm developed by Suter et al.[116] which recasted the orientation reconstruction problem as an exhaustive search over orientation space. Discretization and interpolation schemes in $SO(3)$ will be discussed, as they are an integral part of the search algorithm. Then, the new method of Stratified Monte Carlo Pruning, an improvement built on the original algorithm, will be presented. The correctness of these algorithms will be tested using simulated results and known pathological cases. Finally, their runtime complexity will be examined.

3.5.1 Orientation Discretization

Consider a sample specified by the set of points, $\vec{x_i}$. The forward modeling method finds the best orientation $\mathbf{O_i}$ such that the confidence function $\mathcal{C} = -\frac{1}{N_{qual}} \sum_{h,k,l} N_{h,k,l}$ is maximized. Because the cost function chosen is mostly flat with very small, localized maxima, a large sampling across the orientation space ($SO(3)$) is required. To ensure uniformity and reduce sampling noise (dispersion), an incremental, approximately uniform (instead of random) sampling is used [131]. This method provides us with controls of local resolution, which is crucial for the implementation of the Stratified Monte Carlo Pruning (SMCP) algorithm. While detailed proofs of this sampling algorithm are beyond the scope of this thesis, a brief summary of the results and some important properties are discussed in the following section.

Sampling Algorithm

Both the original exhaustive orientation search and SMCP algorithm use an orientation grid generated by the sampling method as the starting point. To construct an approximately uniform grid in $SO(3)$, we implement a modified version of the Deterministic Sampling Methods for Spheres (DSMS) [131]. This method is designed to sample any general S^d structure deterministically. To do so, DSMS takes advantage of the property that any regular polytope in $(d+1)$-dimensions can be centered on a circumscribing S^d sphere that intersects all its vertices. In so doing, the vertices v_i of the $(d+1)$-polytope partition S^d into f sections, where f is the number of faces of the polytope. For example, S^1, a circle, is sampled by a square. The vertices of the square partition the circle into four sections, one for each of the faces (edges). A

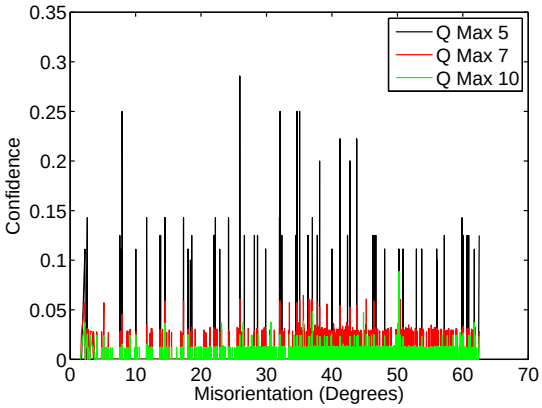

(a) Single pixel cost function (full fundamental zone)

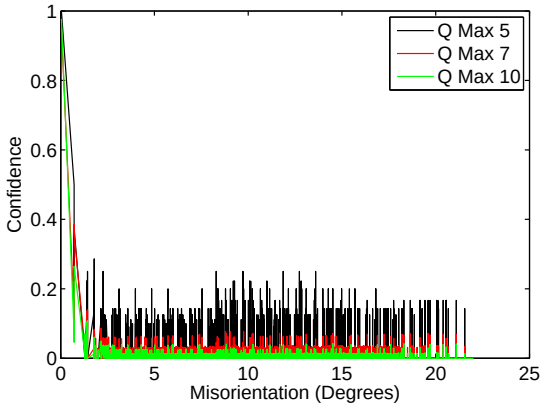

(b) Single pixel cost function (20 degrees angular radius)

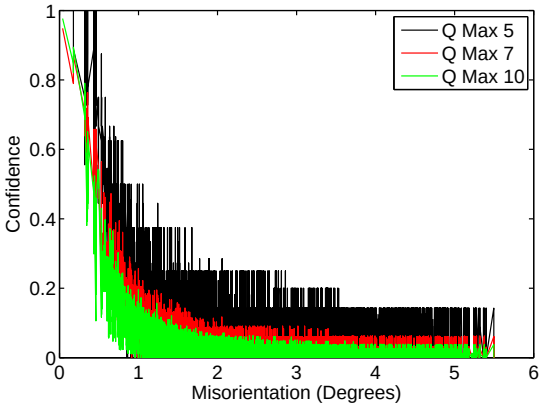

(c) Single pixel cost function (5 degrees angular radius)

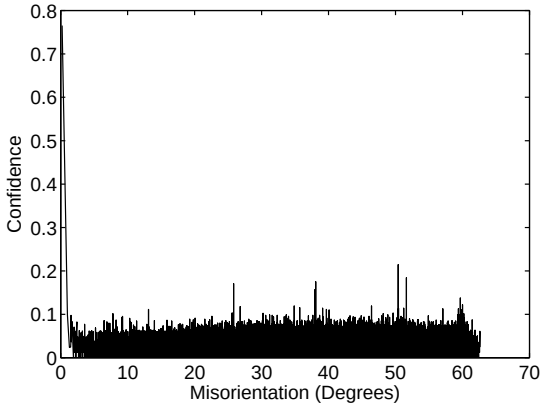

(d) Single pixel cost function, polycrystalline diffraction pattern (full fundamental zone)

Figure 3.3: Representative landscape of the cost function for a single voxel. (a), (b), and (c) are successively expanded scale representations of the same cost function $\mathcal{C}$ for the reconstruction of a single simulated voxel in absence of any other diffraction spots, i.e., a single crystal experiment. The misorientation angle (x-axis) indicates the distance away from the known orientation solution, which goes up to $\approx 62°$ because of the fundamental zone restriction. The sampling rate of the cost function is lowered in (a) to show the local minima structure typical to $\mathcal{C}$. The plot in (d) shows the features of a single-voxel cost function in a polycrystalline sample ($Q_{max} = 10$). Features seen here are indicative of well ordered crystals (500 randomly oriented grains). Multiple local minima occur across the fundamental zone plotted, with a significant number showing up around 60°, which is attributed to rotations about high symmetry axes. General broadening of the cost function can also be observed when Q_{max} is reduced. This restriction amounts to lowering the total number of peaks used for orientation reconstruction. This feature is exploited in the adaptive search method (Algo. 3).

hyper-cube is used in the case of $SO(3)$ sampling. To obtain approximately uniform sampling on S^d, regularly sampled points on each of the faces of the k-polytope are projected onto the d-sphere. In S^1, this is equivalent to uniformly sampling the sides of a circumscribed square and drawing a line between the center of the circle and sample points on each face.

The fact that the set of unit quaternions, $\mathbb{H}$, forms the surface of a 3-sphere, S^3, and that $\mathbb{H}$ is a double cover of $SO(3)$, with $\mathbb{H} \equiv -\mathbb{H}$ were exploited for the application of DSMS to $SO(3)$. Therefore, selecting sample points corresponding to one of the "hemi-3-spheres" would result in a uniform sampling of $SO(3)$. Furthermore, projecting regular sample points from the faces of the hyper-cube circumscribed by the unit 3-sphere amounts to applying trilinear spherical linear interpolation (SLERP) between the vertices (eight quaternions) that specify each of the hyper-faces, where SLERP is defined as

$$\begin{aligned} S(\mathbf{q}_1, \mathbf{q}_2, t) &= \mathbf{q}_1 \frac{\sin(t\Omega)}{\sin(\Omega)} + \mathbf{q}_2 \frac{\sin((1-t)\Omega)}{\sin(\Omega)}, \\ \Omega &= \cos^{-1}(\mathbf{q}_1 \cdot \mathbf{q}_2), \\ \text{for} \quad & 0 \leq t \leq 1. \end{aligned} \tag{3.14}$$

The sampling of $SO(3)$ thus corresponds to sample points $\{\mathbf{q} | q_3 \geq 0\}$, were q_3 is simply the third component of the quaternion $\mathbf{q}$. A trilinear-SLERP is simply applying SLERP three times. In this way, a mapping of $\mathbb{R}^3 \rightarrow SO(3)$ that approximately preserves the sampling structure of $\mathbb{R}^3$ is created. What is left is the sampling of $\mathbb{R}^3$. Any sampling, regular or otherwise, could be used; however, the layered Sukharev grid is chosen because it results in some very useful bounds on the sampled points.

Sampling Properties

Intuitively speaking, the problem with random sampling in a space S is that the dispersion could be too low in some local regions. This could happen even with perfectly random numbers without having a prohibitively large number of sample points. Specifically, we would like to guarantee low dispersion and discrepancy, two measures used to decide the uniformity of a sampling method. Roughly speaking, given a region R sampled by the point set P, dispersion ($\delta(P)$) is the maximum ball in R such that no point $p \in P$ lies inside. Suppose that a volume V of the region $r \subset R$ is estimated using the number of points in the point set P inside r, then, the discrepancy is the maximum difference between the estimated and the real volume in the sampled region. Formally speaking, let $X = [0,1]^d \subset \mathbb{R}^d$ be the region to be sampled, and R the set of possible of subsets of X. For example, R could be a set of rectangles that lies within X. Then, given that point set P samples R, and any $r \in R$, $P \bigcap r$, the point set P estimates the volume (area) of r. Suppose that for any

r, its volume can be measured by $\mu(r)$, then [130] defines discrepancy as

$$D(P, r) = \sup_{r \in R} \left| \frac{|P \bigcap r|}{N} - \mu(r) \right|, \tag{3.15}$$

where N is the number of sample points in the point set P, and $|P \bigcap r|$ is the "number of elements" in the intersection of the sets. Discrepancy can thus be identified as the volume of largest over- or under-sampling within the entire sample space. On the other hand, dispersion is formally defined as

$$\delta(P, \rho) = \sup_{q \in X} \min_{p \in P} \rho(p, q), \tag{3.16}$$

where ρ is any metric. In the case that we are interested in, the natural metric for points in $SO(3)$ parameterized by quaternions is given by

$$\rho(p, q) = \cos^{-1}(\mathbf{p} \cdot \mathbf{q}). \tag{3.17}$$

It can be shown [131] that the sampling method by Yershova et al. is bound by

$$\delta(P) \leq \frac{2\pi}{\sqrt[d]{n((2^d - 1) + 1)}}, \tag{3.18}$$

and for our case, $d = 3$ for the quaternion representation of $SO(3)$, and n is the number of sample points in the Sukharev grid. This gives us a direct way to control the sampling resolution in $SO(3)$ based on the number of points selected in $\mathbb{R}^3$.

Sampling in the Fundamental Zone

So far we have seen how an approximately uniform grid can be generated on $SO(3)$. Because of crystal symmetry, only a subsection of the entire $SO(3)$ produces unique orientations for a sample point. This is referred to as the fundamental zone. For the purpose of our orientation search, we would like to modify the orientation sampling method so that only the fundamental zone is sampled given a specific crystal symmetry. This amounts to finding the set of sample points in $SO(3)$. However, the operation of selecting sample points specifically for a fundamental zone sometimes destroys the dispersion guarantee around the zone edges. Therefore, an additional "hole-patching" operation via local SLERP is performed to restore the dispersion guarantee along the edges of the fundamental zone. Unfortunately, the remaining sample points still violate the discrepancy requirement in that the resulting point set oversamples the zone edges. This problem is ignored, as it does not affect the correctness of the search algorithm.

3.5.2 Exhaustive Search

As the name suggests, the exhaustive search algorithm follows the original forward modeling prescription, in that all discretized orientation sample points are searched. To improve performance, several well known searching techniques are implemented. First, the orientation space is searched sparsely in a global search. Taking advantage of the small but finite width of the cost function, the sampling grid is set such that the discrepancy $\delta \leq r$, where r is the radius of the cost function in orientation space. The set of grid points near a local minimum are saved. In the context of our cost function, this is indicated by $\sum_{h,k,l} \mathcal{N}_{h,k,l} > 0$. A local optimization, namely a zero temperature Monte Carlo, is used to find the optimal solution (Algo. 1). The algorithm is more concretely defined as follows.

Algorithm 1 ExhaustiveSearch for a given sample space element $v(\vec{x})$.

for all $\mathbf{o}_i \in SO(3)$ **do**
  $\chi \leftarrow$ Overlap$(\mathbf{o}_i, v)$
  if $\chi > 0$ **then**
    CandidateList $\leftarrow (\mathbf{o}_i, \chi)$
  end if
end for
Sort(*CandidateList*) { Sort candidate list by χ in decreasing order}
for $i = 1$ to min(*MaxCandidates*, size(CandidateList)) **do**
  $(\mathbf{o}_i, \chi) \leftarrow$ CandidateList[i]
  $c \leftarrow$ OrientationMonteCarlo$(\mathbf{o}_i)$
  if $c <$ *BestCost* **then**
    BestCost $\leftarrow c$
    BestSolution $\leftarrow \mathbf{o}_i$
  end if
end for

Algorithm 2 OrientationMonteCarlo for a given orientation, $\mathbf{o}$, maximum number of steps, N_{max}, and max accepted cost c_{max}

while $N < N_{max} \wedge c \geq c_{max}$ **do**
  $\zeta \leftarrow$ UniformRandomRotation(δ)
  $c' \leftarrow$ Cost($\zeta\mathbf{o}$, v)
  if $c' < c$ **then**
    $c \leftarrow c'$
    $\mathbf{o} \leftarrow \zeta\mathbf{o}$
  end if
  $N \leftarrow N + 1$
end while

The function "Cost" simply calculates the confidence function given in Eq. (3.12) when the voxel, v, is below pixel size. The "quality" generalization is used when v spans multiple pixels. The function "*UniformRandomRotation*," not detailed here, produces a uniform random rotation matrix centered at the identity with a radius of δ. In the case of small rotation deviations of a few degrees around $\mathbf{o}$, this is simply the infinitesimal rotation matrices, namely

$$\Theta(\delta_1, \delta_2, \delta_3) = \begin{pmatrix} 0 & \delta_3 & -\delta_2 \\ -\delta_3 & 0 & \delta_1 \\ \delta_2 & -\delta_1 & 0 \end{pmatrix}. \tag{3.19}$$

In the current implementation, a specialization of the method that maps $\mathbb{R}^3 \to SO(3)$ from Sec. 3.5.1 is used. The result is the ability to produce uniform random matrices around the origin out to a larger angular radius.

The need for local optimization arises naturally from the fact that $SO(3)$ is a continuous group. If the cost function is relatively smooth and continuous, a common optimization scheme such as conjugate gradient could have been used. Unfortunately, since the cost function is extremely sharp, usually ranging from 1° to 5° in width with many sharp local minima of 0.1° to 0.5° in width (Fig. 3.3), most optimization routines are unsuitable. As discussed in Sec. 3.4.4, this particular landscape of the cost function is due mostly to peak overlaps in a polycrystalline material.

On the other hand, the use of purely uniform grid points is extremely expensive. For a system with cubic symmetry, the volume of $SO(3)$ that produces a unique orientation is $\frac{8\pi^2}{24} radian^3$. To reach a resolution of 0.1° would require approximately 6×10^9 sample points. At conservatively 200 floating point operations (FLOP) per diffraction peak, and roughly 150 diffraction peak computations per orientation, roughly 2×10^{14} FLOP would be required for a single point in the sample space. As a comparison, at the time of this writing, a typical processor can perform roughly 10^{11} FLOP per second (FLOPS). Neglecting the fact that most of this computation is not instructive to the final optimized solution, it would take roughly three hours to optimize the solution of a sample point. Considering that the typical spatial resolution would require roughly 10^6 sample elements per layer, this method of orientation reconstruction becomes prohibitive. The use of local orientation Monte Carlo optimization is a way of adaptive refinement of the orientation space, which reduces the total number of sample points required.

3.5.3 Stratified Monte Carlo Pruning

Even with local orientation optimization, the exhaustive algorithm is still searching a significantly large number of grid points (10^5). Furthermore, low order peaks are much more likely to fit than higher order peaks due to the projection geometry and intensity drop-off of diffraction spots at high Q. That is, the cost function contribution

due to lower Q peaks tends to be more spread out in orientation space (Fig. 3.3). Consequently, the minima are wider due to the limited number of peaks.

A new, adaptive sampling method was developed for the purpose of orientation search to replace the uniform grid search. It was developed based on the following observations:

1. Most of the time spent in the uniform grid search does not produce any viable orientation candidates.

2. While, globally, the cost function contains many very deep false minima, the region around each minimum is relatively narrow and can be sampled explicitly. The "integral" of the cost function around some local minimum can be estimated, and thus the average value of the minimum can also estimated. This provides an estimated local bound for the cost function.

3. Regions with bounds below some threshold can be safely ignored since they are unlikely to produce any admissible solution. This is usually known as "bound and search."

4. The cost function, $\mathcal{C}(Q_{max})$ can be approximated by $\mathcal{C}(Q'_{max})$, for $Q'_{max} < Q_{max}$, which results in a lower angular resolution. This is because the number of peaks used evaluate the cost function decreases with decreasing Q_{max}. As a consequence, the approximated cost function can be computed quickly.

By taking advantage of these observations, the algorithm "prunes" the orientation space, and locally increases resolution in the regions of lower average cost. This process is performed iteratively until the algorithm reaches some local threshold resolution. The new algorithm is described below. We use a modified version of the exhaustive search at each step to find the list of candidate orientations to be optimized.

A pictorial representation of this algorithm can be found in Fig. 3.4.

The idea of applying an adaptive method to a problem with discrete cost functions is fairly well established. If the trajectory of the orientation search is mapped out as a graph, a search tree could be constructed. In this context, our search problem is closely related to many of the search problems in artificial intelligence (AI) and robotics [57], where a large, discrete solution space is to be searched. Similar to problems in AI, it is in general very difficult to decide if a candidate solution is near the optimal solution in the orientation search. The pruning method then allows us to estimate the final cost of a candidate solution by sampling around it rapidly. In so doing, large neighborhoods of orientations around a candidate solution can be eliminated quickly.

By the appropriate choice of δ and r in the adaptive reconstruction, we can see that the algorithm converges rapidly by re-sampling regions with low cost.

Algorithm 3 AdaptiveSearch. Find the best orientation given volume element v, minimum and maximum angular radius, δ and r, and initial maximum Q and Q-step, δQ.

Input: $v, \delta, Q_{max}, \delta Q, MaxLocalCandidates$ **Output:** $\mathbf{o}_{best}$

```
SearchGrid ← GetGlobalGrid(r)
CandidateList ← ExhaustiveSearch(SearchGrid, v, Q_max)
while r > δ ∧ |CandiateList| > 0 do
    r ← r/s {s is a tuning parameter for the search algorithm}
    for all o_i ∈ CandidateList do
        (c_j, o_j) ← EstimateLocalCost( v, o_i, Q_max, r) {Estimate local cost by locally
        sample around o_i}
        NewCandidates ← (c_j, o_j) { Insert the list into the set of possible candidates
        }
    end for
    Sort( NewCandidates ) {Sort by averaged cost, c_j in decreasing order.}
    N_max ← ⌊|LocalCandidates|, MaxLocalCandidates⌋
    Candidates ← NewCandidates[i, N_max]
    Q_max ← Q_max + δQ
end while
```

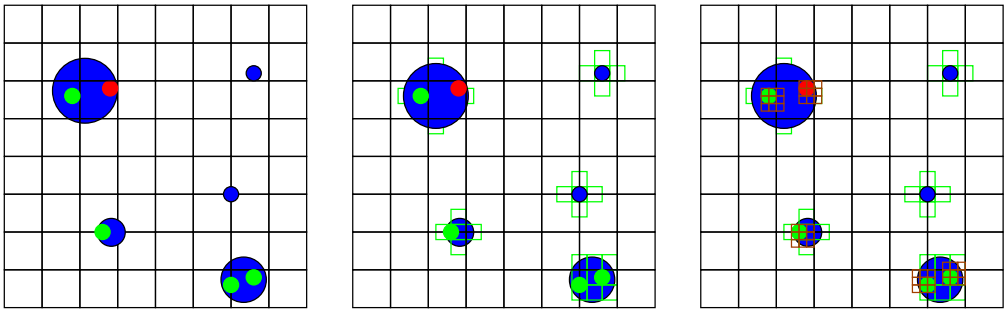

(a) Rough uniform grid over $SO(3)$ (b) Level 1 local refinement (c) Level 2 local refinement

Figure 3.4: Pictorial representation of the refinement process. The intersections of the black lines represent the uniform grid used to sample globally. The blue circles indicate regions of shallow, broad minima of the cost function. Green circles indicate sharp false minima, while the solid red circle is the true global minimum for the specific Q_{max} used for this reconstruction. At each iteration going from (a) to (c), the angular resolution of the cost function is increased by increasing Q_{max}.

3.5.4 Simple Spatial Resolution Model

Assuming perfect orientation reconstruction, the error in the determination of geometrical features can be prescribed using a simple ray-plane intersection. The sample space can be described by the plane equation as

$$\left(\vec{P} - \vec{O}\right) \cdot \hat{z} = 0, \tag{3.20}$$

where we have taken the sample plane to be perpendicular to the z axis for convenience. [inconsistent axes!] The point $\vec{O}$ is the origin of the sample plane, and $\vec{P}$ is any arbitrary sample point. Assuming that we are using only two detectors, then given two pixels measured at $\vec{a}, \vec{b}$ of detector 1 and 2 whose intensities are due to diffraction at $\vec{P}$, the points $\vec{P}, \vec{a}, \vec{b}$ form a line given by the equation,

$$\begin{aligned} \vec{P} &= t\hat{l} + \vec{b}, \\ \hat{l} &= \frac{\vec{a} - \vec{b}}{|\vec{a} - \vec{b}|}. \end{aligned} \tag{3.21}$$

To find $\vec{P}$, the intersection equation can be solved by

$$\begin{aligned} \left(t\hat{l} + \vec{b} - \vec{O}\right) \cdot \hat{z} &= 0 \\ t &= \frac{(\vec{O} - \vec{b}) \cdot \hat{z}}{\hat{l} \cdot \hat{z}} \\ \vec{P} &= \left(\frac{(\vec{O} - \vec{b}) \cdot \hat{z}}{\hat{l} \cdot \hat{z}}\right)\left(\frac{\vec{a} - \vec{b}}{|\vec{a} - \vec{b}|}\right) + \vec{b}. \end{aligned} \tag{3.22}$$

The location $\vec{P}$ is estimated by the average value, $\langle \vec{P} \rangle$ from many different diffraction peaks. Given that different diffraction peaks contribute $(\vec{a}_i, \vec{b}_i)$ with errors of $\delta\vec{a} = \delta\vec{b} = \delta\vec{x}$, we have the error of $\langle \vec{P} \rangle$ to be estimated by error propagation in the usual way, namely,

$$\begin{aligned} \sigma_i &= \sqrt{\left(\frac{\partial P}{\partial a_i}\delta a_i\right)^2 + \left(\frac{\partial P}{\partial b_i}\delta b_i\right)^2 + \left(\frac{\partial P}{\partial O_i}\delta O_i\right)^2}, \\ \sigma_{\langle P_i \rangle} &= \frac{\sigma_i}{\sqrt{N}}. \end{aligned} \tag{3.23}$$

Following the arithmetic, we find

$$\frac{\partial P_i}{\partial a_j} = (O_3 - b_3)\left[-\delta_{j3}\frac{|\vec{a}-\vec{b}|}{(a_3-b_3)^2} - \frac{1}{a_3-b_3}\frac{a_i-b_i}{|\vec{a}-\vec{b}|}\right]\frac{(a_i-b_i)}{|\vec{a}-\vec{b}|} \tag{3.24}$$

$$+ \left[\frac{\delta_{ij}}{|\vec{a}-\vec{b}|} + \frac{(a_j-b_j)(a_i-b_i)}{|\vec{a}-\vec{b}|^3}\right]\frac{(\vec{O}-\vec{b})\cdot\hat{z}}{\hat{l}\cdot\hat{z}} \tag{3.25}$$

$$\frac{\partial P_i}{\partial b_j} = \left[\frac{\delta_{j3}}{\hat{l}_3} + (O_3-b_3)\left(\frac{b_j-a_j}{|\vec{a}-\vec{b}|(a_3-b_3)} + \frac{\delta_{j3}|\vec{a}-\vec{b}|}{(a_3-b_3)^2}\right)\right]\frac{a_i-b_i}{|\vec{a}-\vec{b}|}$$

$$+ \frac{(\vec{O}-\vec{b})\cdot\hat{z}}{\hat{l}\cdot\hat{z}}\left(\frac{-\delta_{ij}}{|\vec{a}-\vec{b}|} - \frac{(a_j-b_j)(a_i-b_i)}{|\vec{a}-\vec{b}|^3}\right) + 1 \tag{3.26}$$

$$\frac{\partial P_i}{\partial O_j} = \left[\left(\frac{\delta_{i3}}{\hat{l}\cdot\hat{z}}\right)\frac{a_i-b_i}{|\vec{a}-\vec{b}|}\right] \tag{3.27}$$

Here, δ_{ij} is the usual Kronecker delta, and indicies $i \in \{1,2,3\}$ correspond to the spatial components.

General and somewhat unsurprising features are observed in this model. As expected, the error contributions are non-isotropic. This is expected as our measurement has a preferred direction. Secondly, all errors decrease with the increase of detector spacing. It should be noted that the detector spacing is limited by the field of view of the CCD camera. Ideally, micron-resolution area detector with field of view of 10's of centimeters would lead to much higher reciprocal (angular resolution around 1×10^{-6}) and real space resolution, but that is simply impractical at the time of this writing.

Of course, objections could be rightly raised here for the assumption of independence between different measured quantities. For example, the measurement of diffraction spots clearly depends on the origin, and the deviation between the two measurements at different L-distances certainly be correlated if the origin of the error comes from either the detector or the X-ray source. As such, the off diagonal elements of the error matrix should also be computed. Similarly, error estimates using Monte Carlo studies are also viable, but it is beyond the scope of this thesis. For these reasons, a number of "numerical experiments" were conducted on many different synthetic and experimental data sets in an effort to quantify the errors associated with experimental uncertainties, as described in the next section.

3.5.5 Validations

A series of validation tests were performed on the reconstruction method. Simulated scattering produced from a set of synthetic microstructures was used to test the reconstruction algorithm's sensitivity. Because of the significantly large parameter space

on the potential experimental configurations, synthetic microstructure characteristics, and detection noise, we have limited our studies to a selected few that directly affects some of the on-going experiments. Namely, synthetic microstructures with the following properties are used.

1. Random orientations.
2. Dense, symmetrically related orientations.
3. Plastic deformation reflected as orientation gradients.

The effects of random orientations is omitted in this thesis, as it has been thoroughly described in [40]. As a validation of the correspondence between peak and grain shapes, the reconstruction of segmented diffraction peaks in high purity Ni is also presented. Because of the large number of three-dimensional orientation maps produced thus far in this work, a representative selection of the reconstructed microstructures will be presented in the appendix. Some results from the analysis of these orientation maps are presented in Chapters 5 and 6.

Dense Symmetrically Related Orientations

To test the robustness of our orientation reconstruction algorithm against a potentially pathological case, a microstructure was created using only highly symmetric points in the orientation space. Moreover, curved surfaces meeting at sharp points are deliberately put into this microstructure to mimic boundary lines seen in nature. The synthetic microstructure was created by assigning orientations to regions on a $N \times M$ gird. Starting from the top left, orientations were assigned to regions centered at grid points (nx, my), where $n, m \in \{1, 2, 3, ...\}$ The traversal order is row major, in that n is incremented faster than m. At grid point $(0, 0)$, a random orientation, $\mathbf{O}(0, 0)$ was selected. At each successive point, $\mathbf{O}(l) = \Sigma_k \mathbf{O}(l-1), l = m \cdot N + n$. The rotation matrix Σ_k belongs to a set of specialized rotations such that for a large number of h, k, l, $\Sigma_n \mathbf{O} G_{hkl} = \mathbf{O} G_{hkl}$. These are typically rotations about some high symmetry axis of the crystal lattice, for example, rotation about [111] direction by 60°.

Diffraction patterns were generated using a grid that is incommensurate with the reconstruction grid. In so doing, accidental suppression of reconstruction noise, especially in the recovered grain boundaries is avoided. The reconstructed orientations are shown to agree with the test patterns from Fig. 3.5. A small number of regions were not reconstructed, and they are indicated by areas of low confidence. This is expected, as the convergence criteria were deliberately relaxed to demonstrate the failure mode of this reconstruction algorithm. The fact that regions of low confidence coincide exactly with regions of failed reconstruction suggests that confidence is in fact a good figure of merit. As expected, the confidence of the reconstructed map drops off rapidly outside of the synthetic microstructure. While this is true in general,

deviation in geometrical parameters, such as L-distance, or the introduction of noise into the measurement would certainly lead to less dramatic drop-off.

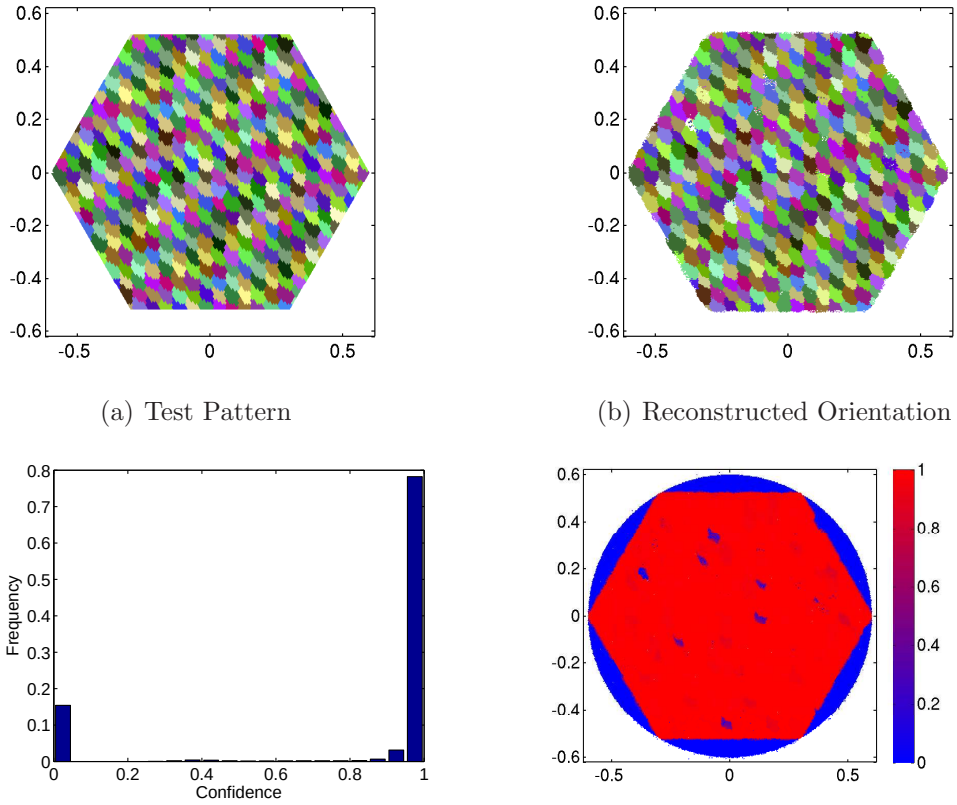

(a) Test Pattern

(b) Reconstructed Orientation

(c) Distribution of Confidence

(d) Reconstructed Confidence

Figure 3.5: Reconstruction test using a synthetic microstructure (a) designed to be difficult for the reconstruction code due to the successively neighboring twin structures that lead to significant peak overlaps. The reconstructed map (b) with its confidence plot (d) indicates that while most "grains" are reconstructed, about ten distinct points appear to have below expected confidence. The blue ring around the reconstructed confidence map indicates that the analysis code is unable to find suitable orientations for these points, which is in agreement with the synthetic structure. (c) is a plot of the distribution of the confidence.

Microstructure with Orientation Gradients

In most scientific and engineering applications, material defects and damage lead to orientation gradients across grains. In fact, arguably some of the most interesting applications of HEDM involve measurement of the degree of deformation in a sample. For example, the measurement of plastic deformation manifested as orientation gradients and local misorientation in an in-situ uni-axial strain experiment performed

on a high purity (99.9999%) copper wire is expected to be an unprecedented input for modeling calibrations (see Chapter 6). *In situ* observation of a structural phase transition of Ni-Mn-Ga will hopefully provide insights into the effects of strain on the phase transition temperature [103].

A microstructure produced from a simulation of a piece of deformed titanium was used as an input for the test of orientation gradient reconstruction [63]. This data set, obtained from the Dawson group at Cornell [18], indicates a likely mode of orientation evolution in a typical uni-axial load experiment, similar to those that we have performed on copper. As with other simulation tests, X-ray diffraction patterns were generated based on locally sharp Bragg scattering. While in general, the deformation model, and thus its effect on diffraction peaks should be input explicitly into the scattering model for a correct simulation of intensity, we have stayed with the assumption that each volume element (voxel) is a perfect crystal for the time being. This restricts the study to purely the limits of geometrically based orientation reconstruction, as the detailed effects of intensity variation is not considered. Moreover, intensity fitting requires optimization of, at the very minimum, multiple voxels across a grain simultaneously. This leads to extremely expensive reconstructions. Significant algorithmic development is required before intensity fitting could become accessible even for the present simulation study.

The typical effect of orientation gradients is the smearing of diffraction peaks across both ω and η direction. This can be seen in Fig. 3.6(b), where diffraction peaks are smeared into arcs. In fact, these arcs will be identified as single peaks using most typical image segmentation or peak identification algorithms. Consequently, estimated center-of-intensities are no longer useful for orientation reconstructions. Because the peak motion along the η and direction is a function of the sample rotation (different ω-integration intervals) and depends on the diffraction origin, the Forward Modeling method is still able to uniquely determine the orientation of each voxel (Fig. 3.6).

Convergence of Reconstructed Orientations

It is often difficult to determine the optimal value for the parameter, Q_{max} used for orientation reconstruction *a priori*. While a large upper limit can be determined based on the diffraction geometry, namely the field of view and the detector distance, other factors, such as peak intensity variation as a function of $|Q|$ are not so transparent. For example, the finite dynamic range of a detector places an upper and lower bound on $|Q|$ due to both saturation (low $|Q|$) and weak signal (high $|Q|$). Because the diffracted intensity drops off rapidly as a function of $|Q|$, higher order peaks have much lower signal to noise ratio. On the other hand, effects of strain and deformation are much more prominent for higher order peaks. For example, peak shift due to random stacking faults in general increase with Q [126]. As seen in Fig. 3.3, the representative cost function sharpens significantly upon increase of Q_{max}. The direct

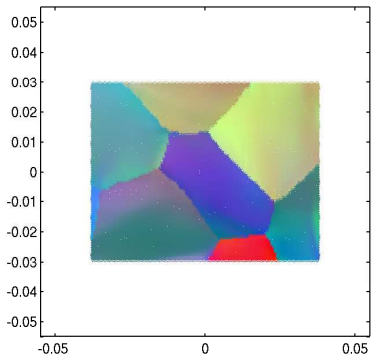

(a) Simulated microstructure of plastically deformed Ti

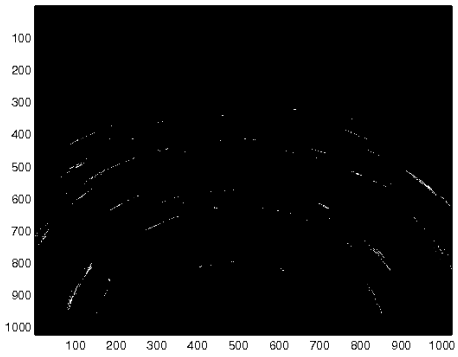

(b) Example diffraction image

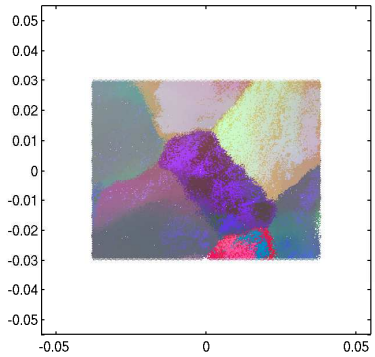

(c) Reconstructed microstructure.

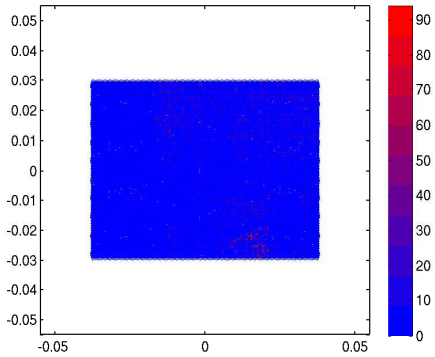

(d) Point to point misorientation

Figure 3.6: Orientation reconstruction test for plastically deformed Ti. (a) Plastic deformation, manifested as orientation gradients across each grain (shown as variations of the false color) on titanium was simulated using finite element methods [18]. (b) Diffraction signals of the deformed Ti generated using the forward modeling method. It is shown that the diffraction patterns are smeared across many images and pixels (both η and ω directions). (c) Reconstructed orientation map from the deformed Ti diffraction patterns. This test shows the viability of reconstructing materials with orientation gradients. (d) Point-to-point misorientation comparison between the original and reconstructed orientation map. We see that the errors in the orientation reconstruction are relatively low and that the grain boundary geometries across the two maps are very similar. It should be emphasized that the reconstruction grid and forward simulation grids are deliberately incommensurate so that reconstruction noise is not artificially suppressed.

effect of Q_{max} on the reconstructed microstructure is seen by comparing Fig. 3.7(a) with Fig. 3.7(b).

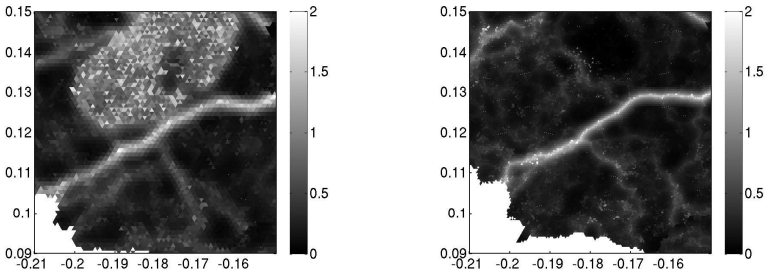

(a) $Q_{max} = 10, s = 0.6\mu m$

(b) $Q_{max} = 12, s = 0.6\mu m$

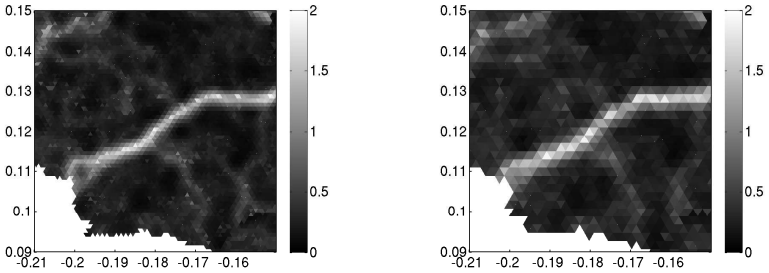

(c) $Q_{max} = 12, s = 1.2\mu m$

(d) $Q_{max} = 12, s = 2.4\mu m$

Figure 3.7: Orientation noise variation with Q_{max} and reconstructed resolution. Noise is measured by a locally, or kernel, averaged misorientation calculation (the strained copper wire data and kernel averaging are discussed in detail in Chapter 6). (a-d) A comparison of the effects of different spatial and reciprocal space resolutions on reconstructed orientation maps. A progression of degradation of features can be seen as spatial resolution is decreased. Reduced number of peaks used for orientation reconstruction leads to significant increase of orientation noise, as seen in (a). Finally, while overall features of kernal averaged misorientation remain relatively stable as spatial resolutions were varied, changes in Q_{max} significantly alter the global result.

Intensity Decomposition

The analysis method of HEDM indicates that geometrical information of each grain is encoded by the diffraction peak shape. Therefore, the outline of a grain at the observation geometry is considered to be represented by the outline of a diffraction pattern. Similar to absorption tomography, given sufficient number of diffraction spots, the shape of each grain could be recovered. In fact, there has been significant effort in applying backward filtered projection algorithms to reconstruct grain shapes [88, 91]. Unfortunately, as mentioned in Sec. 3.3.1, existing techniques such as those

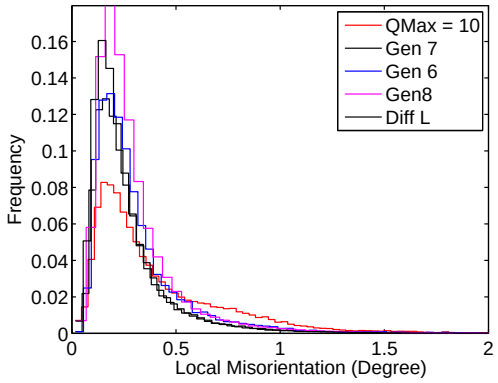

Figure 3.8: A histogram comparing the variation of the distribution of local average misorientation (Fig. 3.7 as a function of Q_{max}, sample spatial resolution, and L-distance. All fits were performed at $Q_{max} = 12$ except for the case indicated otherwise. Broadening of the local misorientation distribution can be seen in the $Q_{max} = 10$ case. Along with the spatially resolved KAM map, this indicates that the use of lower Q_{max} results in a generally noisier reconstructed orientation map.

in referenced in [87, 91] are limited to reconstruction of microstructures with low defect content.

To show that geometrical information is indeed reconstructed correctly using the forward modeling method, reconstruction of high purity nickel is compared at different intensity threshold levels. Using a method termed "intensity decomposition," diffraction peaks are split at different relative intensities before forward modeling reconstruction. In so doing, only part of the diffraction peak is fitted at a time. Specifically, given a set of diffraction intensities that are segmented into disjoint peaks after background subtraction, the maximum intensity of each peak is identified as $I_{max}(n)$, where n is the ID for this peak. For a given threshold range $[f_l I_{max}, f_u I_{max}]$, where $f_l,\ f_u \in [0, 1]$, the set of connected pixels $\{p_i\}$ that forms this peak within this intensity range is accepted.

For grains with low defect content, as expected for well annealed high purity nickel, diffracted peaks should have simple intensity contours corresponding the shape of each grain. As an example, taking $[I_0, I_1] = [0.1I_{max}, 0.2I_{max}]$, only the "bottom" contour corresponding to the grain edges is selected for each diffraction peak Fig. 3.9(b). While intensity decomposition of overlapped peaks may lead to undesirable result (e.g, cases where a strong peak and a weak peak overlap), it provides a good way to classify the source of experimentally observed diffraction signal and the corresponding reconstructed voxels.

The reconstruction results of the same measurement of high purity Ni at different decomposition levels are shown in Fig. 3.9 and Fig. 3.10. For comparison, reconstruction using data from standard background subtraction processing is also shown as a baseline. Confidence values in Fig. 3.10 show that the removal of peak centers leads to significantly lower confidence in the center of each grain. Moreover, a progression of regions with higher confidence can be seen as we move across the different threshold ranges in an expected manner. The reconstructed region moves toward the center as the both $[I_l, I_u]$ increases, thus approaching the diffraction peak centroids. Finally, comparison across all four of the orientation maps in Fig. 3.9 shows the marked consistency in orientations reconstructed amongst the different intensity ranges.

3.5.6 Experimental Parameter Bootstrap Optimization

As mentioned in Chapter 2, deviations in experimental parameters lead to significant differences in the quality of the reconstructed orientation maps. A numerical "bootstrap" method is used to estimate the geometrical parameters, as they are difficult to measure directly.

Taking advantage of the fact that the cost function in the Forward Modeling method varies with different geometrical parameters, an objective function is constructed as the sum of Eq. (3.12),

$$\mathcal{F}(\vec{g}) = \frac{1}{n}\sum_{i}^{n} \mathcal{C}[\vec{g}](\vec{x}_i), \tag{3.28}$$

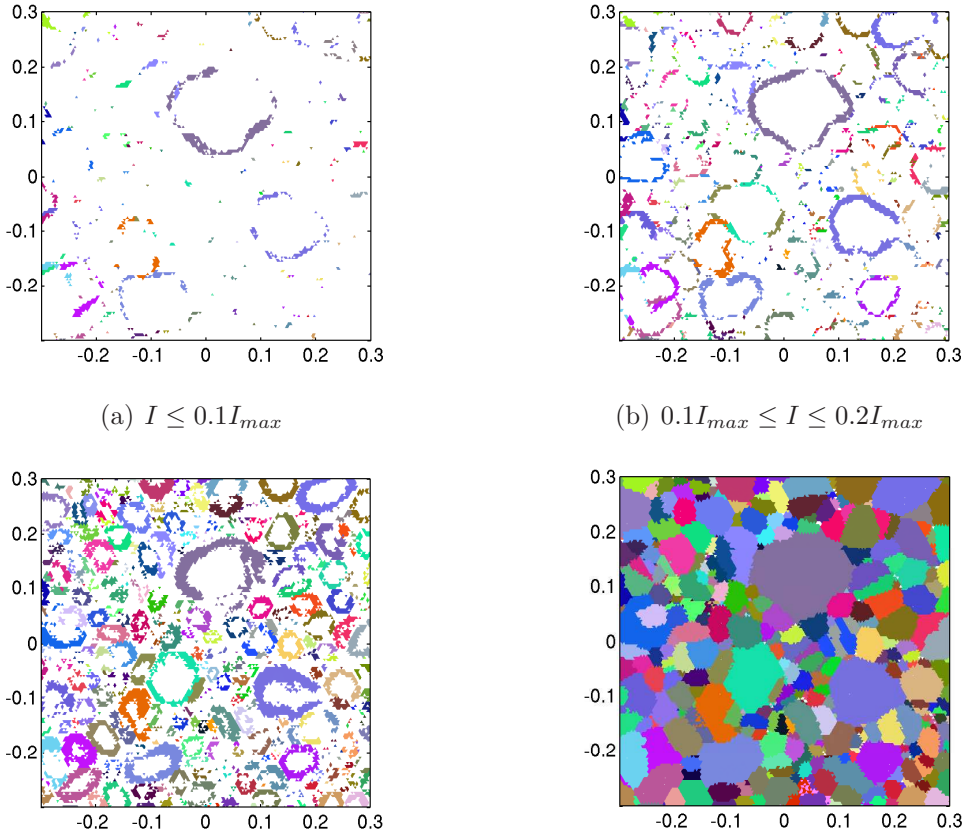

(a) $I \leq 0.1I_{max}$

(b) $0.1I_{max} \leq I \leq 0.2I_{max}$

(c) $0.2I_{max} \leq I \leq 0.3I_{max}$

(d) Complete Peak Intensity

Figure 3.9: Orientation maps reconstructed using different intensity thresholds of the diffracted peaks. Each map is thresholded at 0.6 confidence. Different intensity ranges of the diffraction peaks correspond to different regions of the reconstructed grains.

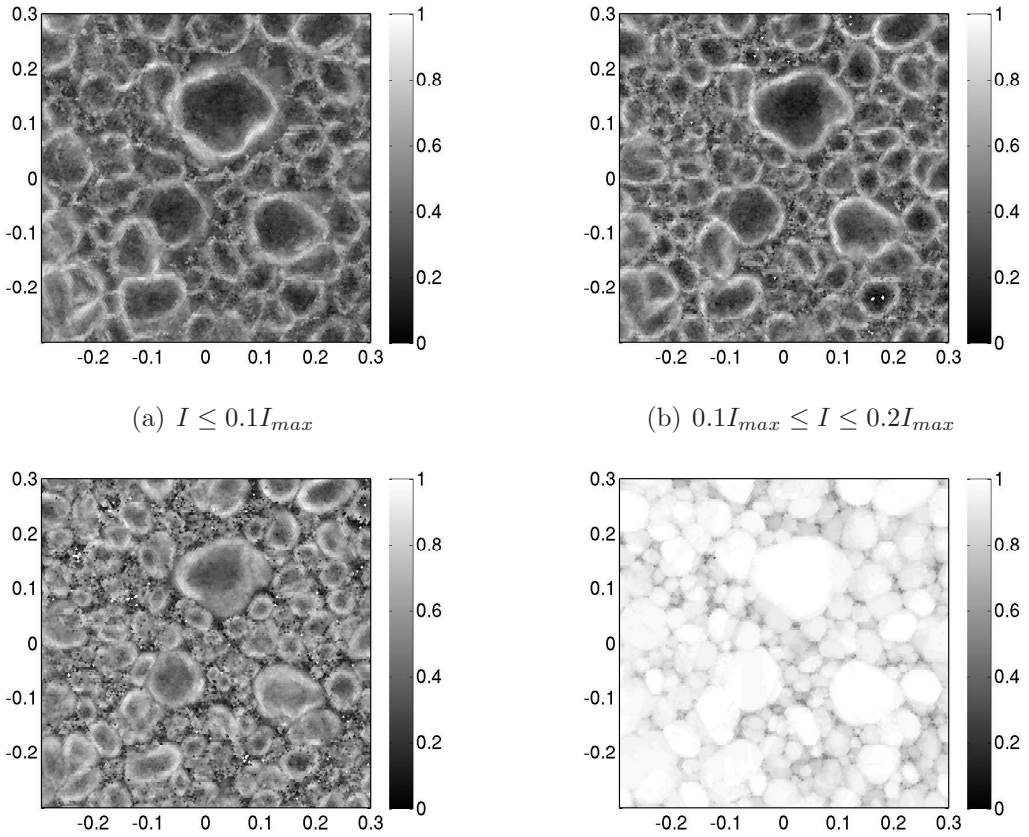

(a) $I \leq 0.1I_{max}$

(b) $0.1I_{max} \leq I \leq 0.2I_{max}$

(c) $0.2I_{max} \leq I \leq 0.3I_{max}$

(d) Complete Peak Intensity

Figure 3.10: Confidence plots for reconstructed maps with different intensity thresholds. Only regions around grain boundaries are reconstructed in cases where the high intensity portion of the diffraction peaks, i.e., central regions, are removed.

where $\vec{x}_i$ is a point in the sample space, represented by a voxel, $\vec{g}$ is the list of experimental parameters (i.e, L-distance, detector orientation, and pixel size), and n is the number of sample point used. The list of experimental parameters is recovered by maximizing $\mathcal{F}(\vec{g})$ by a parallel optimization method. This amounts to performing an orientation reconstruction on a set of voxels randomly sampled from the sample space at different $\vec{g}$ until $\mathcal{F}(\vec{g})$ is maximized. Because the experimental parameter space is large (six most relevant dimensions due to detector orientation and diffraction origin), the optimization can become very computationally consuming. Adaptive sampling in the parameter space and a judicious choices of voxels helps to reduce the total run time of the algorithm.

In the present case, the experimental parameter search space is sampled with low resolution initially (large step size) and successively refined as the cost improves. This is done using a finite temperature Monte Carlo method in the serial algorithm, but because the cost evaluation dominates the total CPU time (and takes up to minutes per evaluation), the serial optimization strategy is impractical. To reduce total run time, a parallel optimization heuristic is constructed by subdividing the experimental parameter space into M regions, where M corresponds to the number of processors used for optimization, and local optimization is performed in each subregion.

Since the basis of this optimization comes from maximizing the amount of the sample space with high reconstruction quality, a uniform random sampling is used for voxel selection in the initial optimization. However, as $\mathcal{F}(\vec{g})$ approaches its maximum, uniform random selection may not represent the optimal search as$\mathcal{F}(\vec{g})$ varies slowly for voxels selected from the interior of grains. In this case, selection of voxels along grain boundaries proves to be much more effective, as they remain sensitive to small parameter perturbations even when $\vec{g}$ is close to optimal.

Finally, from numerical experiments, it is found that the orientation reconstructions are not equally sensitive to all of the geometrical parameters. Specifically, deviations in L-distance and beam center typical dominate the reconstruction quality; detector orientations are only relevant after the displacement parameters are optimized; X-ray beam energy and detector pixel size (not counted above) are only relevant to the final optimization. Based on this observation, we restrict the initial experimental parameter space heuristically to a smaller subspace to save computational time.

3.6 Summary

3.6.1 Major Advances in Orientation Reconstruction

A plethora of three-dimensional orientation maps has been made available due to the recent increase in both robustness and efficiency of the digital orientation reconstruction method. Just as a scale, the total amount of data reconstructed with the first incarnation of the exhaustive search algorithm was less than 100 layers. It

amounted to approximately 1×10^8 total voxels. This is less than a single volumetric measurement consisting of ($\approx 2 \times 10^8$ - $\approx 4 \times 10^8$) at the time of writing. For the desired orientation resolution for highly deformed copper, we have determined that Monte Carlo pruning has reduced fitting time from ≈ 2000 to ≈ 150 seconds. The number of different materials measured and reconstructed is also increasing rapidly. For example, we have measured BaTiO, Ni-Mn-Ga, Zr, and shock loaded Cu, just to name a few.

Increased reconstruction efficiency, combined with rapidly improving acquisition speed, could lead to unprecedented access to real-time, high resolution, and statistically significant measurements. However, to keep up with increasing demand and data rate, continued improvement is necessary on both the computational optimization as well as the theoretical understanding of the reconstruction. While the idea of spatially resolved orientation reconstruction is straightforward, aside from very limited cases, very little is known regarding its convergence criteria. At the time of this writing, the conditions where an optimal solution exists and is uniqueness are not known. While numerical studies and experimental validation with existing techniques are helpful guidelines, they are anything but definitive. Practically speaking, the lack of theoretical understanding of the reconstruction problem is the reason for the slow reconstruction code; aside from empirical experience, it is simply difficult to decide if a reconstructed orientation map is optimal under the metrics considered.

3.6.2 Future and Ongoing Work

Ongoing development efforts are focused mainly on two aspects: the ability to use peak intensity profiles in the reconstructions, and optimization of the orientation search algorithm. The need for intensity fitting arises from the interest in spatially resolved elastic strain state measurements. Elastic strain in the crystal structure leads to changes in the lattice spacing, and consequently leads to peak shifts. Since the strain state for a single sample volume element is averaged across many unit cells, the resulting diffraction is a peak shape that is broadened non-trivially across ω, η, and 2θ. By fitting to peak shapes [90, 62, 83, 60], strain states can be recovered. However, thanks to the polycrystalline nature of the samples, intensity from each peak may be contributed by multiple sample points. While approaches such as ART [87] propose to use segmented and deconvolved peaks for orientation and strain state reconstruction, difficulties involving large sparse matrices stands in the way of practical applications.

While the development Stratified Monte Carlo Pruning method for orientation space searching has yielded significant improvement over existing search techniques, serious effort is still required for the algorithm to meet the ever increasing demand of spatial and angular resolution. As shown in Fig. 3.7, it can be seen that both spatial and orientation resolution are crucial for geometrical and differential feature extractions. Using $0.5\mu m$ resolution for most $1mm$ diameter samples typically requires between 10^8 - 10^9 voxels per layer. Even with the adaptive spatial resolution

methods implemented thus far, each of the 2D maps would still require approximately $20,000$ CPU hours for deformed materials. Some shortcuts can be made by using only local optimization on neighboring points. Based on this idea, orientations from random seed points in the sample are reconstructed using a global search, and the n-th neighbors of these seed points are selected in a breadth first traversal and fitted using local optimization. This breadth first traversal stops upon encountering sample points with confidences below some predetermined threshold. However, this shortcut only accelerates reconstructions for well ordered materials. The demand for high angular resolution also results in diminishing speedup, as the local orientation search dominates the run time.

It should be noted that the theoretical aspect of the orientation search function has been addressed inadequately thus far. In many ways, this has indirectly hindered the development of further algorithmic optimization. At the most basic level, it is not known if orientation reconstruction is a well-posed problem. Specifically, neither the uniqueness nor existence of a solution is sufficiently addressed in the polycrystalline case. While representative test cases have shown that when peaks are smeared across multiple images, reconstructed orientations become significantly unreliable, there is very little analytical understanding of the connection between peak broadening and reconstruction quality. While we observe from experimental results that the cost function we use seems disastrously sharp, it is not clear if a better behaving cost function exists. For example, could the set of optimal solutions occupy a volume of essentially zero measure in orientation space? The ability for intensity to resolve ambiguity is still mostly unknown, and so is the upper and lower bound on reconstruction complexity. For example, less effort should be spent on algorithmic optimization if any of our algorithms can be proven to be asymptotically optimal. Unfortunately, at the time of this writing, many of these questions are still left unanswered.

Chapter 4

Robust Geometric Extraction

4.1 Overview

In order to obtain useful physical insight from microstructure measurements, one must extract statistical, topological, and geometrical information. For example, grain boundary information is captured in 2D micrographs or orientation images, and grain size distribution and volume fraction may be obtained through stereology [99, 54, 100]. Since typical results of microstructure measurements are images, image processing becomes a crucial step in the data extraction and reduction. For example, noisy images due to instability in the data acquisition system could lead to uncertainty in orientation determinations. This could lead to artifacts in grain reconstructions and ultimately in the grain size and grain boundary character statistics. To mitigate these effects, a judicious amount of image clean-up has to be performed to remove artifacts while minimizing bias introduced to the measurement. With the widespread use of scanning orientation measurements such as EBSD, HEDM, and DAXM, three-dimensional, spatially resolved orientation and local differential properties such as orientation gradients are readily available. Robust estimation of both geometric and differential properties are important for materials characterization. For example, grain boundary character distribution depends on the extraction of boundary normals through the use of volumetric and surface mesh generation. Another example is to observe clusters of low dislocation content regions within a single grain. To measure dynamics in a polycrystalline system, the ability to identify and quantify morphologies of interesting regions becomes crucial. Grain boundary mobility in an annealing experiment is measured directly by the point-to-point difference beteween reconstructed surface mesh of two different states; deformation evolution is monitored by the development of low angle boundaries and grain mosaicity identified by isocontouring and kernel average misorientations. These capabilities must be automated, as tracking individual features by hand is simply impossible for a sample with upwards of a few thousand grains.

In this chapter, we will discuss the process of data extraction from reconstructed

HEDM orientation maps. We will first introduce the data representation used in HEDM reconstructions. We then discuss some issues regarding 2D data extraction and image processing. Some effort will be put into applications of simple graph theoretics to microstructure analysis. To extract geometry from a set of 2D orientation images, we will need to look at three dimensional mesh generation. Finally, we will discuss feature tracking in three dimensions as well as ways to generate non-manifold surface meshes to represent generalized low angle grain boundaries. The applications and developments of these techniques have been made in the context of 3D data sets obtained from focused ion beam-orientation imaging microscopy (FIB-OIM) in the last several years [59, 26, 27], and therefore a brief summary of prior work will also be provided as a reference.

4.2 Extraction of Geometries and Topologies

4.2.1 Data Representations

Reconstructed Data

In this chapter, reconstructed orientation points as opposed to diffraction spots or Kikuchi patterns will be considered as raw data. This distinction will help keep the discussion of data processing concise. We will implicitly assume that the uncertainty of the reconstruction will be characterized faithfully by the goodness of fit parameter associated with each of the data points. Of course, in a real measurement, we would often look at the diffraction images to help interpret the reconstruction results as well as the fit parameters. However, this is not easily quantifiable, especially in the context of feature extraction.

With HEDM, EBSD, and DAXM, data values are assigned to each of the sample points in the imaged volume. Some of the more typical data values are crystallographic orientation, goodness of fit, and strain tensor. The nature of the "point-by-point" assignment suggests that the raw data should be stored in similar manner to images, with values assigned to grid points that delineate the sample space. For the purpose of this chapter, we will only consider rectilinear grids for our reconstructed data representation. This results in $n \times m$ pixels for each layer of the orientation map. To represent multiple layers of orientation maps, we simply have k layers of $(n \times m)$ sized orientation maps, which results in $k \times m \times n$ pixels.

Historical Comment on the MIC File Format

Representations in most computer generated images are typically in some type of grid format. In the most common cases, an image is stored in a two-dimensional grid of $(n \times m)$ square pixels. Each pixel contains a value (binary, gray-scale, vector, or tensor) representing the imaged function at that sample point. To reduce image size, sometimes hierarchically sized pixels are used to better approximate local features of

different length scale. Historically, the development of the MIC (microstructure file) file format for HEDM had a similar intent. Started from the development of 3DXRD, grains were viewed as a single object with little or no resolvable internal structures. Therefore larger grains are seen to be representable by larger pixels. To this end, a single MIC file may contain pixels of different size, with boundaries containing significantly smaller "pixels," or triangles to accommodate for smaller local feature size. In many ways, a MIC file format is closer to a 2D mesh than a typical pixelated image. The MIC format is a set of equilateral triangles specified by the "left most" vertex (vertex with the minimum x-coordinate) and "up" or "down" designation. Since grain sizes are usually several orders of magnitude larger than boundary feature size, the potential saving using this representation is significant. Furthermore, the use of triangles allows for more directions representable in a typical boundary. However, with recent work in characterization of local orientation spread, there has been renewed interest in extracting intra-granular misorientation. Combined with the studies of angular resolution limits of HEDM to around $\leq 0.25°$, it has become apparent that many interesting intraganular features can be extracted from high spatial resolution orientation maps. This, combined with the use of linear interpolation, representations of boundaries can become more fluid than that given by grid discretization. Finally, some of the well established image processing operations are not well define on a triangular grid. For example, the application of a median filter on a triangular grid does not guarantee convergence. All these reasons significantly diminish the advantages from the MIC file format. As a part of the future work, orientation field information will be compressed and stored in a high resolution rectilinear grid format.

Grain Extraction

Given a grid representation, a nearest neighbor of a pixel (i, j) is defined to be pixels immediately adjacent to it, i.e., $(i \pm 1, j), (i, j \pm 1)$. When applying an $n \times n$ filter or a majority filter to the data structure, centered at pixel (i, j), a region of $n \times n$ pixels centered at (i, j) will be considered. In three-dimensions, a region of $n \times n \times n$ will be considered. For the purpose of this thesis, a grain is defined to be a set of nearest neighbor connected pixels satisfying the equivalence relation,

$$p_{i,j} \equiv p_{i',j'} \iff d(q_{i,j}, q_{i',j'}) \leq \theta_t \wedge \text{IsNearestNeighbor}(p_{i,j}, p_{i',j'}), \tag{4.1}$$

where misorientation $d(q, q')$ is defined in the usual way with respect to the fundamental zone of the measured sample. The use of this equivalence relation immediately allows us access to several connected component algorithms, most notably union-find, which is proven asymptotically optimal [117]. As a note, "burn algorithm" is the name used for connected component identification associated with grain extraction in the material science literature [97]. By defining the equivalence relationship with different properties, such as dislocation density and confidence, we can similarly define connected regions representing dislocation cells and high confidence grains. In

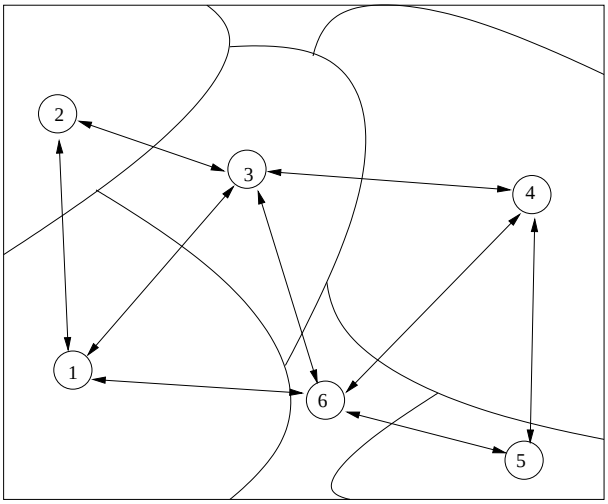

Figure 4.1: A graph G provides an abstract representation of the two-dimensional microstructure shown. Each grain is represented by a vertex v (numbered.) Each connection between a pair of grains are represented by an edge $e(v, v')$. Two grains are limited to neighbor at most once with each other (i.e., the graph G is undirected, and there exists at most one edge for each pair of vertices.). Edges of G therefore provide an abstract representation of boundaries between each pair of grains.

general, microstructure component extraction belongs to the larger class of problems know as image segmentation [84, 81].

Grain Graphs

Grain extraction naturally leads to discussion of grain neighbor statistics and networks, which allows us to easily compute grain-to-grain misorientation statistics. Naturally, connectivity amongst grains can be represented as mathematical graphs, $\mathbf{G}$, where edges represent grain boundaries, and nodes represents grains (Fig. 4.1). By interchanging edges for nodes in $\mathbf{G}$, the dual graph, $\mathbf{G}^*$ is obtained, which represents the grain boundary network. Not only does a graph provide easy access to information within a microstructure and therefore their statistics, graphs can also be readily analyzed using some of the standard methods. For example, finding the so-called "min-cuts" in $\mathbf{G}^*$ identifies the minimum number of boundaries required to be removed in a microstructure to separate the grain boundary network into two disjoint sets. Application of graph theoretics forms the basis of the present orientation map analysis code and could be potentially applicable to analysis of microstructure data in the context of grain boundary engineering and percolation theory [108, 31, 32].

4.2.2 Interpolations and Approximation

Even though the microstructure maps are measured on a fixed grid, it is sometimes necessary to provide well defined data values between grid points and layers. An example is the case of alignment of two different measured orientation maps. Since perfect alignment of different measurements is rarely possible, interpolation is often used to match values from the two grids being aligned. A potential drawback, though, is when kernel averaged misorientation is applied to a grain boundary. Orientations from two distinct grains would be averaged, and the result represents neither of the original values. To circumvent this problem, a discrete, indicator function based interpolation is used in the case of surface mesh generation. Details of each interpolation method will be reviewed in this section.

Linear Interpolation

Given a function $f(x)$ defined on the real line but only measured at discrete intervals $x_i = \{x_0 + \delta x\}$, the function values $f(x+\delta)$ for all $x + \delta \notin \{x_i\}$ can be defined via a linear interpolation,

$$\begin{aligned} x &\in [a, b), \\ f(x) &\approx lin(x, f(a), f(b)) \\ &= \frac{b-x}{b-a} f(a) + \frac{x-a}{b-a} f(b). \end{aligned} \tag{4.2}$$

This is also known as the lever-rule or convex combinations. A similar scheme can be generalized to two-dimensions. For a function $f(x, y)$, the linear interpolation for the point, $p(x, y) \in [a, b) \times [c, d)$ is defined as

$$\begin{aligned} f(x,y) &\approx lin(p, f(a,c), f(b,d), f(a,d), f(b,c)) \\ &= lin(y,\ lin(x, f(a,c), f(b,c)),\ lin(x, f(a,d), f(b,d))). \end{aligned} \tag{4.3}$$

This is known as bilinear interpolation. Further generalization into any nD rectilinear coordinate system is simply successive reapplication of the linear interpolation function. The space over which the interpolation is defined needs not be rectilinear. For example, interpolation within $SO(3)$ between two orientations can be defined as

$$\begin{aligned} q(t) &= q_0 \frac{\sin(\omega(1-t))}{\sin(\omega)} + q_1 \frac{\sin(\omega t)}{\sin(\omega)}, \\ \omega &= \cos^{-1}(q_0 \cdot q_1) \end{aligned} \tag{4.4}$$

where q is a quaternion representing an orientation. This is known as the spherical linear interpolation, or SLERP. It can be shown that the path traced out by $q(t)$ is in fact the geodesic in $SO(3)$ at constant angular velocity, which mimics the constant

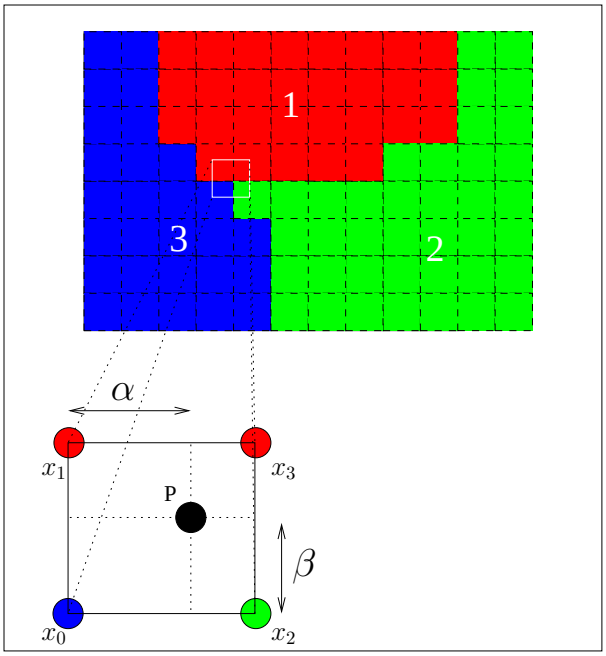

Figure 4.2: A schematic showing a common way to use linear interpolation functions to help define boundaries in a multi-domained material. In this two-dimensional example, the three different colors indicated correspond to three different domains with grain indices 1, 2, and 3. The interpolation scheme shifts the entire image by $(\frac{\Delta x}{2}, \frac{\Delta y}{2})$*, which does not affect the outcome of the defined boundaries. Bilinear interpolation is applied to the indicator functions* χ_i *to define* $\chi_i(\vec{p})$ *everywhere in the domain. The interpolation parameters,* α *and* β *are defined by the location of* $\vec{p}$ *with respect to the reference point (*$\vec{x}_0$ *in this diagram) in the interpolating domain* D_n*.*

derivative in the interpolated function as seen in rectilinear spaces [111]. In general, linear interpolation can be applied to any function $f(q) : SO(3) \rightarrow \mathbb{R}$ provided that it is smooth and differentiable. As it turns out, this is equivalent to having $f(q)$ satisfy the generalized Cauchy-Riemann equations for quaternions [66].

Linear interpolation is exploited thoroughly in the literature for the use of multi-domain surface mesh generation [135, 9, 82, 129]. While crystallographic orientation is useful for misorientation calculations, it is rather cumbersome to use in surface mesh generation (i.e., calculation of isocontours in an orientation field). Instead, grains are extracted, and their corresponding volumetric pixels (voxels) identified ahead of time with a grain index using a connected-component algorithm (Eq. (4.1)). Grain indexes are then assigned to a set of grid points. To help define grain boundaries, we will define the indicator function,

$$\chi_i(\vec{x}_n) = \begin{cases} 1 & \text{if } \vec{x}_n \in D_i \\ 0 & \text{otherwise} \end{cases} \tag{4.5}$$

We then define the linearly interpolated indicator function as θ_i. The two-dimensional version of θ_i (Eq. (4.2)) is defined as

$$\theta_i(\vec{p}) = lin(\alpha, \beta, \chi_i(\vec{x}_0), \chi_i(\vec{x}_1), \chi_i(\vec{x}_2), \chi_i(\vec{x}_3)) \tag{4.6}$$

(see Fig. 2). From this, the grain index of point p is defined everywhere by

$$I(p) = \arg\max_i \left(\theta_i(p)\right). \tag{4.7}$$

Grain boundaries are defined by the points where the index $I(p)$ changes.

Kernel Average Approximation

A kernel average approximation, also known as kernel average smoother in the non-parametric statistics literature, can be simply stated as

$$\begin{aligned} \phi(x) &= \int_D f(x')\rho(x'-x)dx' \\ \int_D \rho(x)dx &= 1. \end{aligned} \tag{4.8}$$

A discretized version can be found as

$$\phi(x) = \frac{\sum_i f(x_i)K(x_i - x)}{\sum_i K(x_i - x)}. \tag{4.9}$$

It should be noted that this kernel average approximation, or more generally kernel density estimate method is used widely ranging from astrophysics (Smooth Particle Hydrodynamics) to machine learning. It is not too surprising to find that one can generalize both the continuous and discrete kernel function from the form $K(x_i - x)$ to $K(x_i, x)$. One such example is the n-nearest-neighbor averaging, where $K(x_i, x)$ is defined as

$$K(x_i, x) = \begin{cases} \frac{1}{n} & \text{if } |x_i - x| < h \text{ and } x_i \text{ is the } m\text{−th nearest neighbor, } m < n \\ 0 & \text{otherwise.} \end{cases} \tag{4.10}$$

In fact, by using $f(\vec{x}) = \vec{x}$, we get the n-nearest neighbor smoothing function for triple lines and quadruple points used in the our implementation of feature preserving surface mesh reconstruction. In general, the kernel average smoothing method can be applied to relatively noisy data to produce a smooth, differentiable quantity. This step of noise removal is especially crucial when looking at quantities like the Nye tensor [78] estimate from an orientation map. Extra care must be taken when applying kernel smoothing to microstructure orientation data. The kernel averaged smoothing method has the side effect of averaging across discontinuities. Consequently, grain

boundaries, representing jump discontinuites in the microstructure, would be suppressed or removed. The resulting kernel averaged orientation would be far away from all its composite orientations. It is therefore convenient to introduce a cutoff kernel [72],

$$K(x_i, x) = \begin{cases} \frac{1}{n} & \text{if } |x - x'| < h,\ d(q(x), q(x')) \leq \theta_t \\ 0 & \text{otherwise} \end{cases} \tag{4.11}$$

where $d(q, q')$ is the misorientation between the two orientations with respect to the fundamental zone in the usual way. By setting the cutoff angle appropriately, only misorientations that would not have been classified as a boundary would be added to the kernel average contribution. One could certainly go on to cook up more complicated versions of this kernel that would ignore boundary points explicitly in a grain identified data structure.

4.2.3 Approximation vs. Interpolation in Surface Mesh Generation

The slight difference between approximation and interpolation should be clarified here before proceeding to the description of mesh generation, as both techniques are used to define the boundaries in a microstructure. Given a reconstructed surface represented by $S(\vec{x})$, it **interpolates** the measurement point set $\{p_0, p_1, p_2, \cdots p_i\}$ if and only if $S(\vec{x})$ passes through every point p_i. The surface function $S(\vec{x})$ **approximates** the points $\{p_i\}$ if $S(\vec{x})$ passes close to but not necessarily through the points $\{p_i\}$ [61]. The main choice of interpolation versus approximation rests solely on the reliability of the raw data. If the point set $\{p_i\}$ is faithfully representing the surface geometry, and the expected errors are negligible, then we would prefer our reconstructed surface to pass through these points. On the other hand, if the point set is known to be noisy, or if we know ahead of time that there is significant measurement uncertainty globally, then an approximation scheme may be better suited. In the context of surface mesh reconstruction used in this thesis, we assume that triple (3-junction) and quadruple (4-junction) points identified in two-dimensions have significantly better resolution than boundary points and triple lines estimated in three-dimensions. It will therefore be be sensible to interpolate through these points and approximate through the rest of the point set. This is justified by the typical in-plane measurement resolution of around $1\mu m$ versus the out of plane resolution of $\geq 4\mu m$. Furthermore, 3-junctions and 4-junctions identified within the two-dimensional map are resampled in the orientation space multiple times by the reconstruction algorithm. The chances of misidentifying triple and quadruple points directly from the $2D$ reconstructed orientation map is significantly lower than incorrect estimates of their location in $3D$.

4.3 Mesh Generation

4.3.1 Overview

Our primary interest in mesh generation, or more specifically, surface mesh generation is to identify grain boundaries, triple lines, and quadruple points. By identifying these geometrical features, we can fully characterize grain boundary properties, such as normals and curvatures, which allows us to measure the mobility and energy for each of the boundaries in a microstructure. The challenge is then to have a high fidelity representation of the measured grain boundaries. Unfortunately, simply estimating normals from the exterior surfaces of a set of 3D voxelized grains is not sufficient for grain boundary characterization. Cubic voxels will only provide six different orientations for each of the normals, and all triple lines are necessarily "stair-cased" due to the voxel representation.

Surface and volume reconstruction is not a problem unique to material science. Similar effort can be found in mesh generation for CT-scans (computed tomography), MRI (magnetic resonance imaging), and even LIDAR (Light Detection and Ranging). Different data collection schemes have different set of advantages and uncertainties, and the meshing procedures (algorithm and data preprocessing methods) designed for one method may not necessarily be optimal to the other. An example is the application of point-cloud reconstruction to LIDAR data. Point clouds designated by a set of points, $\{p_i\}$ are recorded by a LIDAR. Because points measured by LIDAR do not typically lie on a uniform grid, finding connectivity of points is not straightforward; therefore it is sometimes difficult to determine the geometry of the surface mesh in areas with sharp features [25, 43, 49, 73, 24]. Preprocessing is sometimes necessary to find connectedness between points [43]. In the example of CT-scan, difficulty may lie in segmentation of images with low resolution and contrast. CT image quality is sometimes lower than computationally desired because of the limitations on radiation exposure for a human patient. Similarities in electron density in different body parts (i.e., kidney and liver) contributes to the lack of contrast and therefore difficulties in segmentation. However, since most body parts are relatively smooth, CT-scan and MRI results usually do not have to worry about sharp, sliver like geometrical features often seen in three-dimensional microstructures. This indicates that curvature minimizing mesh smoothing techniques can be applied as a means for noise removal. Preservation of sharp features (i.e., triple line, quadruple point) is in fact crucial to microstructure analysis, as they often play a dominant role in determination of microstructure dynamics. For example, MacPherson-Srolovitz relations [70] indicate that isotropic grain growth is determined by the mean width and edge length of each grain. More generally, measurements of curvature for capillarity driven grain growth requires that noisy features be minimized on each boundary. This leads to a contradictory requirement of sharp features preservation and smoothing. Applications of anisotropic smoothing using geometric flow [134, 112, 23] were exploited

to address these concerns. This still leaves the uncomfortable question of exactly when smoothing would leads to bias in the resulting geometrical extraction, or worse, when does discretization alter the topology or geometry of the original surface. Our approach to geometrical extraction though mesh generation is in fact an application and extension of the feature preserving methods developed by ref [9]. Moreover we insist on applying explicit smoothing only as the last resort. We will view surface reconstruction in our microstructure as surface approximation[1] from predetermined, interpolated fixed triple lines and quadruple points using piece-wise linear functions [2]. To facilitate this approach, we have implemented [9] using CGAL [3], an open source geometrical algorithm library. By adaptively refining our three-dimensional Delaunay triangulation, we are able to control the distance between reconstructed mesh boundaries and the defined grain surface, leading to an alternative direction in data restricted smoothing.

4.3.2 Related Work

The problem of both two-dimensional and three-dimensional mesh generation has been extensively explored. We will only review a very abridged list of existing work that is relevant to this thesis. Roughly speaking, there are three classes of algorithms used for mesh surface reconstruction from voxelized data: primal type algorithms, such as Marching Cubes and its variants [64, 85], dual algorithms, such as Dual Contouring [48, 101], and Delaunay triangulation [8, 6, 16]. The first two are better known and extensively used in the imaging community [135], while Delaunay triangulation based surface reconstructions are more commonly studied in the computational geometry community [16, 6]. For the purpose of this review, the terms "isocontouring" and "surface reconstruction" will be used interchangeably. Furthermore, we will focus mostly on gray level isocontouring and discuss the multi-indexed version as an extension.

Isocontouring

Given a scalar function $f(\vec{x})$, the problem of isocontouring is simply to find the surface $f(\vec{x}) = C$, where C is constant. The isocontour of $f(\vec{x}) = C$, which is $\{\vec{x_i}|f(\vec{x_i}) = C\}$ is also known as the C-level set. Because experimental measurements are digitized, the maximum resolution of the reconstructed isocontour depends on the density of the sample grid, $p_{i,j,k}$, where $f(\vec{x})$ is defined. By using suitable interpolation schemes on a sufficiently dense sample grid, a number of guarantees can be made regarding the geometrical and topological properties of the approximated isocontour and the true contour [6, 8].

[1] To be clear, the surfaces must go through all constrained points but not all unconstrained boundary points.

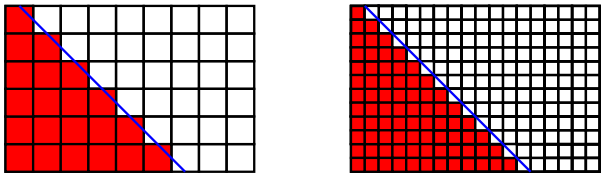

Figure 4.3: Interface between two regions with red being regions of $f(p_{i,j,k}) < 0$ and white being $f(p_{i,j,k}) > 0$. The voxels (shown only as a two-dimensional projection) approximate the plane indicated by the blue line. As we decrease the voxel size in the sample grid, the distance between the approximate isocontour (grid steps) and the actual isocontour will converge to zero. However, since each facet of the grid point is fixed, the local normal estimate will never converge.

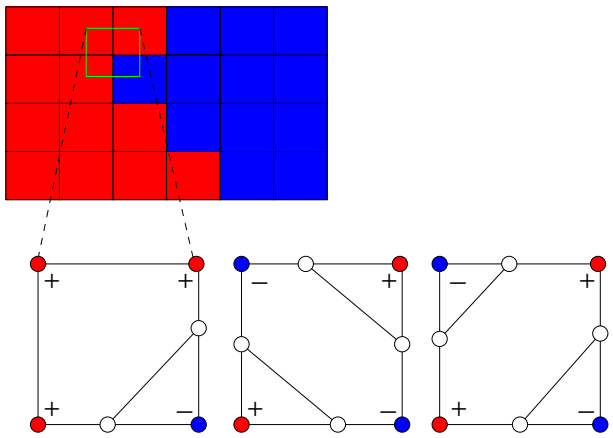

Figure 4.4: The two-dimensional version of Marching Cubes for illustrative purposes. In the pixelized region, red and blue indicate regions of two different gray levels. New vertices (white) are placed on the edges of the cube based on the configuration of signs in each cube (green square). Because the vertex placement is determined locally, some configurations (center and right) do not produce unique isocontouring.

To start, it is usually more convenient to work with $f(p_{i,j,k}) - C$. The isocontour in this case, also know as the 0-level set, is located between any grid points $p_{i,j,k}, p_{i',j',k'}$ with a sign change. However, a reconstructed isocontour obtained directly by applying this method to the discretized function, $f(p_{i,j,k})$, is necessarily "stair-cased." More importantly, we should note that while the approximated isocontour will converge point-wise to the true isocontour, the normals will not converge (see Fig. 4.3). This type of catastrophic failure is a classical problem seen in computational geometry. To alleviate the stair-casing problem, most applications of isocontour extraction involve interpolation or smoothing of the discretized data. It should not be too surprising that boundary reconstruction and isocontouring are the same problem. In this case, boundaries will be identified as locations where grain indices changes.

Marching Cubes

Originally designed for gray level isocontouring in medical imaging, Marching Cubes is well known for its easy look-up table based implementations. Since triangles and vertices are inserted independently for each cube associated with eight voxels (Fig. 4.4), run time of Marching Cubes scales linearly as the number of voxels. In addition to some minor preprocessing, there are essentially two steps to the Marching Cubes algorithm. A sign function based on $f(p_{i,j,k}) - C$ is computed across the image volume to determine the location of the isosurface. From this, sign crossing between two points x_i and $x_{i'}$ indicates crossing of the isosurface. The edges of each voxel can then be either sign-changing or sign-constant, and each cube will consequently have 2^8 possible configurations. The union of all triangles from each of the voxels

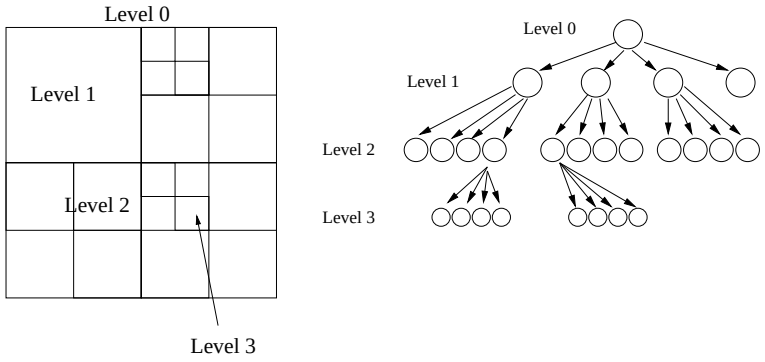

Figure 4.5: An octree is used to decompose the domain of $f(p_{i,j,k})$. A two-dimensional schematic is shown here. Meshes produced from a spatially adaptive octree will exhibit the same hierarchical features. This means large triangles will be used to represent regions with large features, and small triangles will be used in sharp regions to ensure that the meshed surface conforms to the true isosurface.

is identified as the reconstructed surface. Because the Marching Cubes method restricts the insertion of vertices to edges only, reconstructed features sometimes do not resemble the original geometry or topology, especially when sharp features are expected. Moreover, the output mesh from Marching Cubes tends to be dense, as the number of triangles is at least equal to the number of boundary voxels. Triangle quality also suffers from this vertex insertion restriction. These shortcomings have led to a plethora of work on topological and geometrical conforming Marching Cubes-like algorithms [76, 77, 52, 85, 20] In general, algorithms that place vertices on the edges are called "primal" methods, while algorithms that perform cell-interior vertex placement are called "dual" methods.

Dual Contouring

Using an octree to partition the domain of $f(p_{i,j,k})$, the Dual Contouring method triangulates by placing a vertex anywhere within each octree cell (Fig. 4.5). This significantly helps improve the triangle quality and geometrical conformity of the output mesh compared to constraining vertices to edges. The vertex placement is decided by minimizing the quadratic error function

$$E(\vec{x}) = \sum_i \left(\hat{n}_i \cdot (\vec{x} - \vec{p}_i)\right)^2 . \tag{4.12}$$

Conceptually, the quadratic error function minimizes the magnitude of the gradient of the reconstructed isocontour, as shown in Fig. 4.6.

Given that the octree level is chosen appropriately, the reconstructed mesh is guaranteed to have the same topology and geometry as the isocontour represented by the interpolated function, $f(p_{i,j,k})$ [102]. The point-wise distance between the reconstructed mesh and the true isocontour decreases with higher leveled, or more

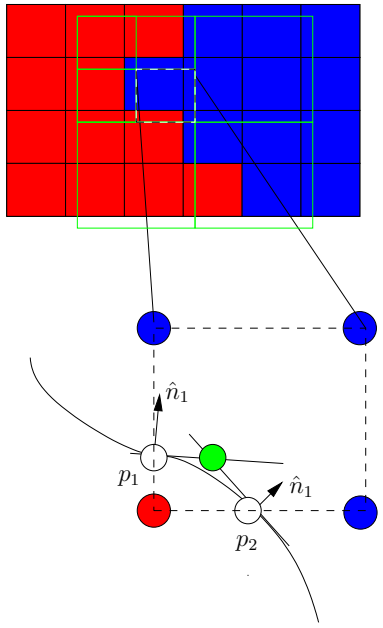

Figure 4.6: A two-dimensional schematic of Dual Contouring. Red and blue pixels represent two regions separated by an isocontour. The green box represents the octree (quadtree in 2D). The cell with the dotted line is expanded to demonstrate the calculation of the minimizer point (green dot). The normals $\hat{n}_1$ and $\hat{n}_2$ are estimated using the trilinear interpolation of $f(p_{i,j,k})$. The minimizer point, the intersection of the two tangent lines of the estimated isocontour at the points p_1 and p_2, is obtained by minimizing the quadratic error function (Eq. (4.12)). The levels of the quadtree are chosen for illustrative purposes only.

refined octree (Fig. 4.5). Taking advantage of this convergence property, a function can be defined to quantify the error for a mesh at octree level n,

$$\epsilon = \frac{|f^{i+1} - f^i|}{|\bigtriangledown f^i|}. \tag{4.13}$$

Here, f^{i+1} and f^i are the interpolated function values at octree levels $i+1$ and i, and $\bigtriangledown$ is the usual gradient operator [133, 118]. It can be seen from Eq. (4.13) that the octree level necessary for a fixed value of ϵ_t increases with local surface gradient, which translates to sharp features.

By refining only in local regions where the ϵ exceeds the predefined convergence error limit [132], it is possible to produce an adaptively sized mesh that preserves sharp features. Finally, to extend to the multi-index case, vertex placement is determined by calculating a minimizer point with the position and normal of all immediately neighboring domains. This method circumvents the possibility of having more than one minimizer point per dual contour cell, which results in not being able to have multiple grain edges intersect at a common point. It should be emphasized again here that some information loss during the discretization of $f(x)$ may not be recoverable in the surface reconstruction.

Delaunay Triangulation

Obtaining an isocontour with Delaunay triangulation is slightly more complicated than the previous two methods and the correctness and mesh quality of the resulting isocontour depends on several recent theoretical results on sampling and surface reconstruction. To be concise, we will only summarize briefly several key properties. A large body of literature ([16, 6, 109, 24, 25, 82, 15, 8], just to name a few) can be found on the details and proofs for the results stated here.

1. Given a set of sample points $\mathbf{P} = \{p_i\}$ on D, the domain where the scalar function $f(\vec{x})$ is defined, a Delaunay triangulation, $DT(\mathbf{P})$ is a triangulation where no point p_i lies inside the circumcircle (or circum-sphere in $3D$) of any triangles (tetrahedron in $3D$). Note that we will not discuss the result of Delaunay triangulation in terms of triangle qualities[2], as they are not important to our current analysis.

2. A Voronoi diagram is the geometric dual of the Delaunay triangulation. This means that every $(d-n)$-dimensional object in the Delaunay triangulation will become a n dimensional object in the Voronoi diagram. For example, in 3D a tetrahedron in a Delaunay triangulation becomes a point at its circumcenter in the Voroni diagram, and a point becomes a Voronoi cell.

[2]Triangle and tetrahedron qualities refer to the shape property. Roughly speaking, a triangle is "good" if it is close to an equilateral triangle [19, 110]. The origin of this measure comes from computational geometry and finite element analysis. Acute triangles with angles $\leq 15°$ can easily lead to singularities in a finite element calculation.

3. A restricted Delaunay triangulation, $DT(\mathbf{P})|_B$, is a triangulation of $\mathbf{P}$ restricted to a subset, $B \in D$. For the purpose of our discussion, B is simply the boundary or isocontour that we are interested in. Furthermore, given a Delaunay triangulation of the domain, $DT(D)$, the restricted Delaunay triangulation on B is a subset of simplices in $DT(D)$. Furthermore, this subset of simplices must also be the dual of Voronoi objects (i.e., Voronoi edge) that intersect B. Therefore, finding the "sign change Voronoi edges" is equivalent to finding triangles on $DT(D)$ that approximate the isocontour. Here, a "sign change Voronoi edge" is an edge with two Voronoi (sample) points of different signs (Fig. 4.7).

4. Given that point set $\mathbf{P}$ samples B sufficiently densely [6, 8], the restricted Delaunay triangulation $DT(P)|_B$ approximates both the topology and geometry of the boundary B. Furthermore, as the sample point density increases, the reconstructed surfaces, curvatures, and normals converges point-wise to B. Roughly speaking, because we have a Delaunay triangulation, the circumsphere of the tetrahedron neighboring the boundary triangle bounds the distance, δ, between the boundary triangle and the true isocontour (Fig. 4.7). Reducing the size of this tetrahedron simultaneously reduces its circumsphere and its distance bound. Thus, given some threshold value ϵ, one could locally refine the boundary tetrahedra until the desired bound on δ is achieved. The full details of the proofs are beyond the scope of this section and can be found in ref [15, 25, 8].

4.3.3 Implementation

Taking advantage of the theoretical machinery outlined above, surface mesh reconstruction using Delaunay triangulation is implemented and available as a package in CGAL [3]. We will use this as a starting point. This package gives us the following tools which are crucial in implementing feature preservation [9].

1. Three-dimensional Delaunay triangulation.

2. Adaptive Delaunay refinement based on generic criteria (specified as functions).

3. Ability to specify sampling points used for Delaunay triangulation.

4. Mesh quality improvement routines.

Surface Sampling with Delaunay Triangulation

We start with the surface reconstruction method implemented in CGAL, which uses a restricted Delaunay triangulation to sample the isocontour to be reconstructed, as outlined in Sec. 4.3.2. Roughly speaking, the accuracy of the reconstructed surface is controlled by the facet distance parameter (δ) (see Fig. 4.7 for an illustration). The

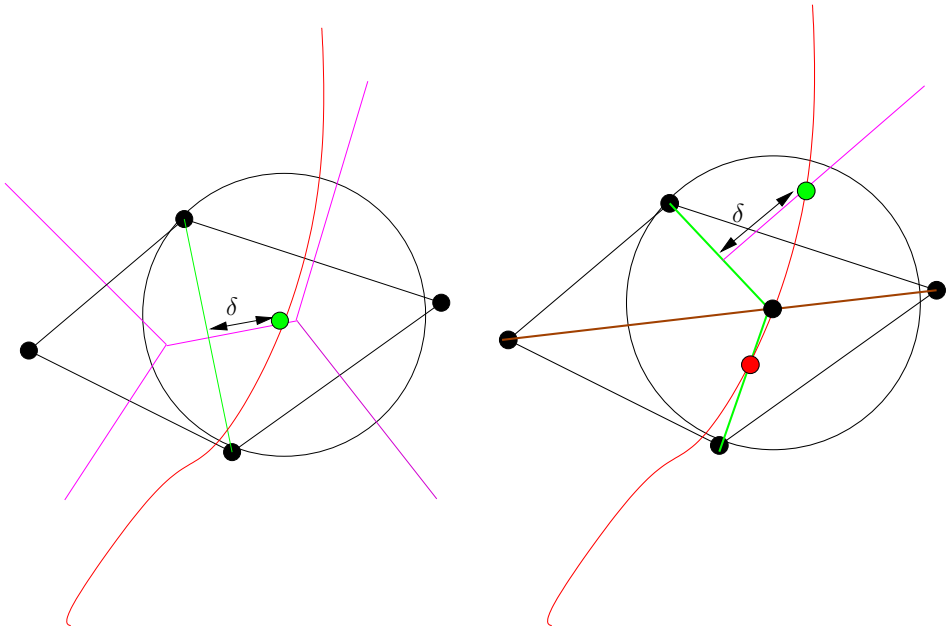

Figure 4.7: A 2D schematic of surface reconstruction using Delaunay refinement. The diagram on the left shows the point set $\mathbf{P}$ *(black dots) sampling the domain. The Delaunay triangulation is shown by the black and green edges. The green edge (triangle in 2D) corresponds to the facet that represents the isocontour* B*, indicated by the red curve. The purple lines are the Voronoi edges. Note that the dual Voronoi edge of the boundary facet intersects the isocontour (green dot). A Delaunay ball (black circle), a ball circumscribing the vertices of the initial facet (two points in 2D, three points in 3D), is centered on the intersection point between the surface Voronoi edge and the isocontour. To refine the triangulation, a vertex is inserted at the center of the surface Delaunay ball. The original triangle (tetrahedron in 3D) is removed, and the Delaunay triangulation is updated (right). As a consequence, the new facets (green and brown edges) better approximate the isocontour, i.e., the distance* δ *will decrease for some number of the new facets [8]. The algorithm will continue to refine any triangles containing facets with* δ *larger than some predetermined threshold value (green dot contrasted with red dot in (b)).*

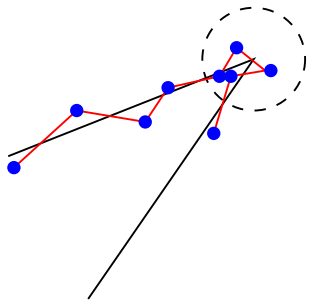

Figure 4.8: An illustration of the sampling of a sharp feature. The black lines indicate the isocontour, and the red line segments represent the reconstructed surface. Blue dots are used to show the locations of the vertices of these 1*-facets. The dashed circle indicates the problematic region. The refinement scheme shown in Fig. 4.7 will not be able to reproduce the isocontour unless a vertex is placed at the sharp corner. The result is a reconstructed surface with a large number of facets, many of which intersect the isocontour. This is undesirable for microstructures, as it produces significant error in the mean width calculation (discussed below).*

facet distance parameter acts as an L^1 measure between the reconstructed surface and the isocontour. The reconstruction adaptively refines the Delaunay triangulation around the boundary surfaces where δ is calculated to be larger than some predetermined threshold, δ_t (Fig. 4.7). As stated in Sec. 4.3.2, provided a sufficiently small δ is used, the reconstructed surface should be faithful to the isocontour. As the sampling rate becomes higher (via increasing number of Voronoi-objects used, or lowering of δ), the L^1 distance will be minimized. However, this is also assuming that the isocontour is C^2 continuous (a condition of the ϵ-sampling used for the surface reconstruction proved in [8, 5], which is not the case in many microstructures. Simply put, the sampling rate around a sharp object can increase substantially without resulting in L^1 convergence (Fig. 4.8); the resulting noise proves detrimental in some of the typical geometry estimates (mean width, triple line length). This is the motivation for the sharp feature preserving surface reconstruction method in [9].

As a side note, while ideally, $\delta = 0$ results in perfect reconstructions for a C^2 continuous surface, the number of sample points, and hence surface patches needed in the reconstruction mesh would grow dramatically. Since the computational complexity of point-insertion, or adding new points, in Delaunay triangulation is in the worst case $O(n^2)$, where n is the number of existing points, the computational time would become impractical. Moreover, when performing surface reconstruction from a voxelized data set, the reconstructed surface is not expected to have an L^1 norm error that is below the voxel size. Consequently, one voxel side length is the usual lower bound for δ.

Sharp Feature Specification

The correctness, or conformity of the reconstructed surface to the isocontour, of the Delaunay triangulation based surface reconstruction method outline above depends on the ability to produce a dense sample of the isocontour [8, 5]. However, with the present method, a dense sampling can only be produced if the isocontour C^2-continuous; in the presence of discontinuity and sharp features, the reconstructed surface may not conform to the isocontour[3]. Unfortunately, microstrctures often contain sharp features and nontrivial topologies (self-intersecting), and the preservation of both of these properties are crucial for analysis. To circumvent some of these problems, *a priori* knowledge of sharp features from the measured microstructure can be

[3]The meshing method used in this thesis is based on ϵ-sampling. The condition of point-wise and normal convergence is related to a quantity known as the medial axis. Concisely, the medial axis is the locus of centers of maximal balls B such that $B \bigcap \Sigma = \emptyset$, where Σ is the surface to be reconstructed. The isocontour to be constructed is further assumed to be C^2 continuous in the surface reconstruction methods [3]. Recent work aimed to address the theoretical aspects of the surface reconstruction problem in the presence of sharp features can be found in [14, 15]. The topics of surface reconstruction errors and ϵ-sampling is fairly broad, and much more extensive treatments than what we can present here already exist in a large body of literatures [5, 24, 25]. We refer the interested readers to these references for more details.

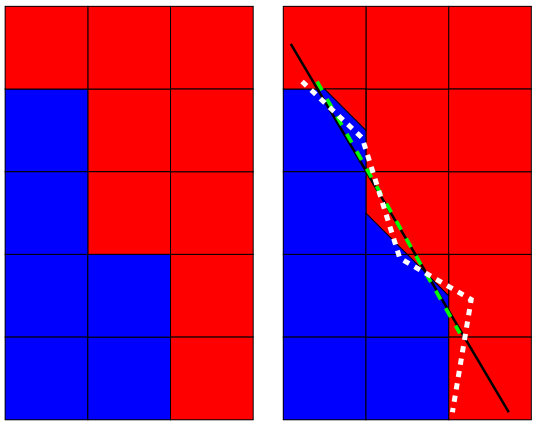

Figure 4.9: A pixelized boundary (left) is interpolated on the right, as indicated by pixels with cut corners. The black line indicates the true boundary. Since the true boundary is not faithfully represented by the pixelized, interpolated data, resolution of the reconstructed boundary is limited by pixel size. Surface reconstruction methods can at best capture this interpolated boundary from the discrete data (edges shared by both red and blue regions). While reducing the parameter δ below the pixel side length to something arbitrarily small will lead to the convergence of the reconstructed surface to the interpolated surface, it may not necessarily converge to the true boundary. The resulting surface may also contain artifacts, such as noisy surface normals (white), where a relaxed δ could lead to a smoother surface (green).

directly inputted into the surface reconstruction. Points and edges in the material are identified as constrained points, leaving the specification of boundary points to depend on the meshing algorithm [9].

In the present method, constrained points selected in our meshing algorithm are kernel averaged 3- and 4-junctions (triple and quadrupole points). 3- and 4-junctions are defined to be voxels whose neighboring voxels have two and three different unique IDs. Because of measurement noise, multiple apparent 3- and 4-junctions may appear within a small area of the order of measurement resolution. In many cases, insertion of these constrained points leads to artifacts in the reconstructed surface that are identified to be unphysical. A crude way to resolve this problem is to replace multiple constrained points within a small neighborhood (identified by the expected resolution of small features in the measurement) with a point at their center-of-mass location. The algorithm is explicitly defined in Algo. 4.

Algorithm 4 SpecifyConstrainedPoints. For a given voxelized data set and the smoothing length r, return a set of smoothed constrained points.

for all voxels $v_i(\vec{x})$ **do**
  $NgbList \leftarrow$ GetNeighbors(v_i)
  $IDList \leftarrow$ GetMaterialIDs(NgbList)
  if NumberUnique($IDList$) == 3 $\wedge$ NumberUnique($IDList$) == 4 **then**
    $ConstrainedPointList \leftarrow \vec{x}$
  end if
end for
for all $\vec{p}_i \in$ $ConstrainedPointList$ **do**
  $NgbPointList \leftarrow$ GetNeighborPoints($\vec{p}_i, r$)
  $SmoothedNgbPointList \leftarrow$ Average($NgbPointList$)
end for
return $SmoothedNgbPointList$

Note that the smoothing parameter also serves the second purpose of relaxing the constraints on the triple lines. Triple lines formed by connecting measured triple points necessarily are "stair-cased," which is an aliasing problem due to the voxelized data structure and is not reflective of the microstructure. By imposing a smoothing parameter, triple points are inserted sparsely, and the interpolation is again left for the meshing algorithm.

It should be mentioned that various groups have put significant effort into triple line smoothing [20, 112]. However, to simplify the implementation, we have chosen a simple kernel smoothing approach. Certainly, a more sophisticated moving finite element or anisotropic smoothing method is also possible. Our approach is unique in that we attempt to control the smoothing error by separately smoothing different components of the microstructure before the meshing procedure, but a comprehensive comparison amongst the different methods has not been done at present time.

Weighted Delaunay Triangulation

Because the mesh refinement algorithm [3] will remove any tetrahedron neighboring a "bad facet," indicated by either poor geometrical conformity or bad element quality (dihedral angle, for example), we have to explicitly protect constrained edges and tetrahedra from being removed. By placing a weight on constrained vertices, we have converted the Delaunay triangulation into a weighted one. Practically speaking, weight w placed on the vertices v specifies that no other vertex v' can be placed within distance w from v. By setting the appropriate weight for multiple vertices of boundary tetrahedra, T, we can ensure that vertex insertion will not be possible within T. This consequently ensures that T, along with its pre-specified boundary facets, will stay fixed, which preserves the sharp features in the domain. Through experience, we observe that setting the weight to be roughly $\frac{3}{4}$ of the desired final edge length is a good compromise between relatively smooth reconstructed triple lines and sharp features.

4.4 Geometric Extraction

Once a surface and volumetric mesh is produced, approximation of many typical geometrical qualities (surface area and volume) become fairly straightforward. However, error associated in the approximation is another matter. To get a better sense of reconstruction errors, resolution studies are performed on the meshing algorithm. Scaling of error as a function of resolution is examined. In the interest of experimental comparison with isotropic grain growth, a discussion of mean width and its approximation is provided. A discussion of microstructure evolution analysis with the use of reconstructed meshes, relevant to grain growth studies, is presented at the end of this chapter.

4.4.1 Mean Width

Mean width is a natural linear measure of an nD object. Most commonly, mean width is defined as $\frac{1}{\pi}$ times integral of mean curvature around an enclosed object[4] where mean curvature is defined as

$$K = \frac{\kappa_1 + \kappa_2}{2}, \tag{4.14}$$

[4] Actually, mean width simply refers to the natural linear measure for a domain D in n-dimensions that satisfies $L(D_1 \bigcup D_2) = L(D_1) + L(D_2) - L(D_1 \bigcap D_2)$. However, Hadwiger's Theorem (the original proof is in German, and a proof in English is found in [51]. A very good summary can be found in [107]) [70] states that for all linear measures $L(D)$ in any nD satisfying the condition above may only differ by an arbitrary multiplicative constant. In other words, the definition of mean width is $L(D) = C \int_{\partial D} K dS$ for any arbitrary C. The choice of constant C may differ between authors.

and κ_1 and κ_2 are the principal curvatures. Given a local patch of smooth, differentiable, specifically C^2 surface, S, in three-dimensions, the two principal curvatures can be defined by the two eigenvalues of the Hassian of the local height function. We represent S with the height function $z(x, y)$ from the local tangent plane, then the Hassian is defined as

$$H_{ij} = \partial_i \partial_j z, \tag{4.15}$$

and the curvatures are simply the diagonal terms. For example, the local curvature of a sphere is $\frac{1}{R}$ everywhere, and therefore so is the mean curvature. The mean width of a sphere is simply $4\pi R^2 \left(\frac{1}{R}\right)\left(\frac{1}{\pi}\right) = 4R$. Given a polygon mesh representation of an object, the most straightforward way to calculate the mean width is simply done by using the equation,

$$L(\mathbf{D}) = \frac{1}{2\pi} \sum_i |e_i| \alpha_i, \tag{4.16}$$

where α_i is the turning angle across the edge i and $|e_i|$ is the length of the edge. For a uniform polygonal mesh, the error converges as something like

$$\frac{|L(D) - L(P)|}{L(D)} \approx \alpha \left(\frac{\Delta x}{L(D)^2} \right), \tag{4.17}$$

where P is the polygon approximation of the domain D, and Δx is the side length of the polygon [70]. The multiplicative constant α in front of the scaling is associated with different reconstruction parameters and domain geometries. This error scaling gets a bit more complicated when the mesh is adaptive. Furthermore, the required assumption here is that the polygon mesh approximation converges both point-wise as well as via normal and curvature. A counter example would be a voxelized representation of the domain D. Since the normals and curvature estimation do not change as a function of voxel edge length Δx, the mean width will not converge.

4.4.2 Noise and Reconstructed Surfaces

Approximations and interpolations mentioned in the meshing section in terms of distance, δ, away from the isocontour or boundary surface are provided. However, the isocontours are often extrapolated from voxelized raw data. The sampling rate of boundaries are in fact limited by the density of the grid in the voxelized measurements. Therefore, no matter how densely we sample the voxelized data structure, any features missing between the measured object and the discretized measurement is not recoverable through surface reconstruction. In this context, we can specify a minimum feature size observable based on the size of each voxel. While there is no analytic expression to propagate the experimental error to the reconstructed surface,

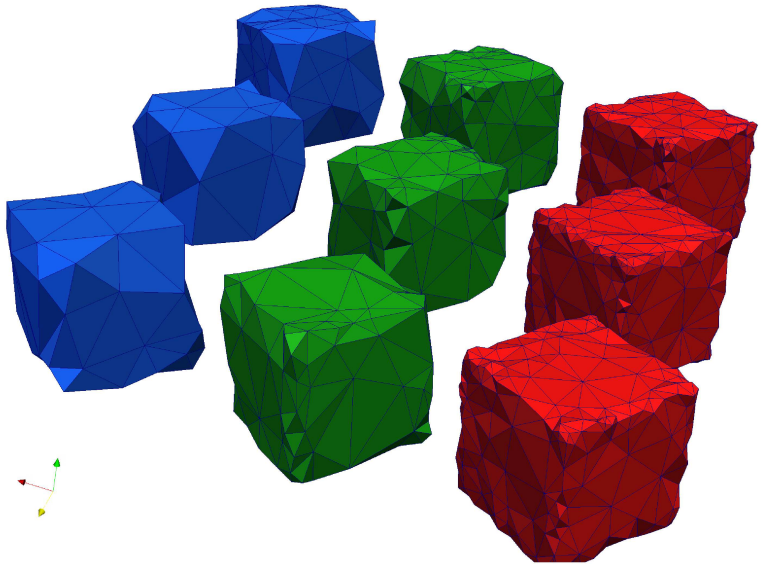

Figure 4.10: Resolution parameters' effect on unconstrained reconstructed meshes is shown here for a rotated cube in a rectilinear grid. The facet-to-boundary parameter decreases from $\delta = 2$ to $\delta = 0.5$ going from left to right. Moving down the columns, we can see the effect of maximum edge length going from $e_c = 0.1$ to $e_c = 1$ in normalized units. Corners and sharp edges tend to become noisy with lower δ, while larger δ results in meshes that poorly approximate the original shape.

we would like to know if 1) the result converges as we decrease voxel size and 2) if there is some minimum size below which extracted geometries are no longer reliable.

The above considerations are especially crucial for looking at microstructure geometry (volume, mean width, triple lines) and topology evolution. Topological infidelity can easily lead to miscounted numbers of neighbors, resulting in misidentification of critical events. Increasing variance with the decrease of voxels per grain affects the quality of extracted mean widths and volume, which are the main components in many of the grain growth theories [70, 125, 74]. Attempts to quantify the effects of surface reconstruction error will be performed with the help of numerical experiments. Specifically, the errors of extracted geometrical quantities for a number of representative shapes will be studied as a function of discretization resolution.

4.4.3 Resolution Studies of Extracted Geometry

Numerical Experiment Method

In this study, we have specifically looked at the error scaling behavior as a function of object size (in number of voxels) for constrained and unconstrained surface reconstruction using Delaunay triangulation. We have varied two parameters, the facet to boundary approximation, δ, and normalized maximum edge length, e_c. e_c is generally

used to reduce the total mesh size; however, the use of larger edge size and larger δ can also provide an ad hoc smoothing on the reconstructed mesh, as illustrated in Fig. 4.9. It can be seen, for example in Fig. 4.10, that the output mesh is adaptive. Triangles of the surface mesh tend to be smaller towards the edges as the number of sample points and refinements required to approximate the local feature increases. As the parameter, δ is decreased, the reconstructed surface is required to become closer to the boundary specified by the data. Thus, local surface refinement is initiated resulting in smaller triangles and shorter edge lengths ($e \leq e_c$). Element quality of the output mesh is ignored in this study, and therefore quality improvement methods such as sliver exudation [13] are not performed. This removes the complexity of having mesh quality improvement affect the errors of the reconstruction.

We chose to study the relative error as a function of voxel side length instead of mean or median triangle side length, s, to capture the error induced by the discretization and reconstruction altogether. Relative error, defined as $\frac{|f_p - f|}{f}$, where f is a geometrical quantity and f_p is its polygonal approximation, is computed for volume and mean width. The interest in these two quantities comes from the need to use reconstructed surface meshes for the analysis of curvature driven grain growth.

Convergence and variation behavior of the polygonal mean width and volume approximations were studied by reconstructed surfaces of the chosen shapes. We have chosen to use a free sphere, a free cube, and a constrained cube for our resolution analysis. The choice is by no means exhaustive, but they encompass the commonly encountered microstructure features, i.e. smooth surfaces, sharp edges, and sharp corners. Furthermore, analytic forms for both mean width and volume exist for spheres and cubes, which simplifies the error calculation. Neither the free sphere nor free cube have constrained points. In other words, their surfaces are not subjected to the restrictions of sharp feature preserving (i.e., insertion of sharp feature constrained points which align directionally with the voxelized grid); thus they provide a idealistic comparison between the errors from the two different classes of objects. On the other hand, the resolution study on the constrained cube will lead to error estimates that are more representative of the observed microstructures. Each object is produced from a voxelization of a region defined by an implicit function at varying resolution. Because discretization in a rectilinear grid results in orientation dependencies of the reconstructed surfaces, each object is randomly rotated before voxelization. Note that this is a study on L^1 norm type errors; a completely separate analysis would be required to estimate errors found in reconstructed curvatures and normals.

Results

Relative error scaling as a function of volume and mean width can be found in Fig. 4.12, Fig. 4.13, Fig. 4.14, Fig. 4.15, Fig. 4.16, and Fig. 4.17. Each study is fitted against the analytical form of the polygonal approximation error [70], i.e., $\Delta L \approx O\left(\frac{s}{L^2}\right)$ for mean width and $\Delta V \approx O\left(\frac{s}{V^{2/3}}\right)$. A straight line indicates agreement

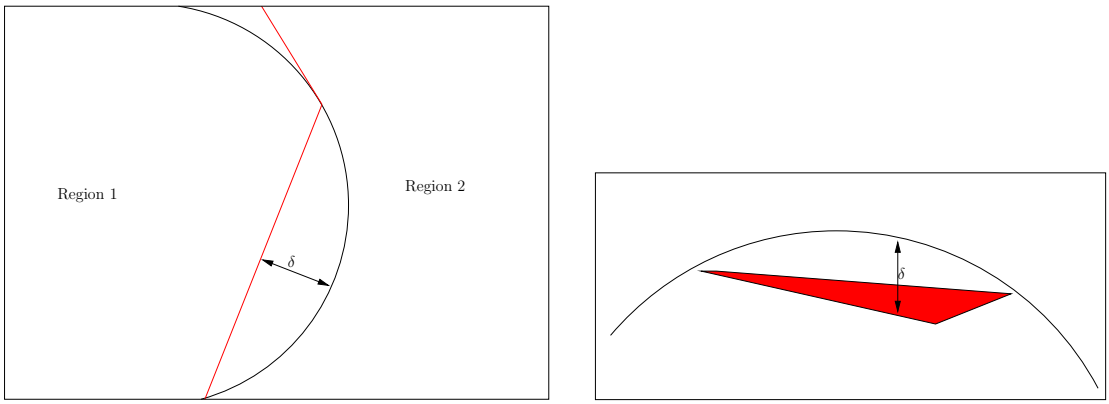

Figure 4.11: A schematic describing the approximation parameter δ, which specifies the maximum distance between the facet (red) and the grain boundary (black curve). Facets in two-dimensions (edge) and three-dimensions (triangle) are shown on the left side and right side respectively.

with the error scaling relationship. To better show the convergence behavior, a plot of ΔL vs. L and ΔV vs. V is also shown, and each data point is a result of averaging the object in 40 randomly chosen orientations. The variation of each error as a function of orientation is characterized by its standard deviation. The edge length indicated by e_c is measured in the normalized unit of object radius in voxel side length (i.e., for a sphere, it is the $\frac{\text{radius}}{\text{voxel side length}}$, and for a cube, it is $\frac{\text{half cube side length}}{\text{voxel side length}}$. Thus, e_c characterizes the number of voxels used to represent the object.

From the result of the mean width scaling, we can see that a range of reconstruction parameters leads to significant differences in the scaling factor, α, of the approximation error (Eq. (4.17)). For the case of a sphere, the error does not vary as a function of its orientation, which is consistent with the fact that the standard deviations are smaller than the symbol size. Furthermore, convergence behavior of the free sphere is markedly better than both the free cube and the constrained cube. This is attributed to the lack of sharp edges or corners, or more precisely, that the surface of a sphere is C^2 continuous. This also explains why the reconstructed surface using $\delta = 0.5$ (voxel side length) results in little or no increase in reconstructed noise, as evidenced by the mean width estimates. This suggests that given a C^2 surface, it is possible to approximate mean width with discretized data at high precision. Even with fewer than 10 voxel radius ($L_{sphere}(D) = 4r \implies r = \frac{30}{4}$), the approximation error remains less than 0.01 for $\delta = 0.5$. The deviation in the scaling seen in Fig. 4.12(a) in the $\delta = 0.5$ case can be attributed to the fidelity of the reconstructed surface to the isocontour surface. Recall that given a scalar function f defined on the voxelization grid, $\{\vec{x}_i\}$, all points $f(\vec{x})$ such that $\vec{x} \notin \{\vec{x}_i\}$ are defined by linear interpolation ($\tilde{f}$). Therefore, the isocontour representing the sphere is faceted at low resolution. In the limit of one voxel diameter, the sphere is represented by a single voxel, which is a cube.

On the other hand, the free and constrained cubes should be perfectly represented by the linear interpolation at all orientations. However, their corresponding reconstruction errors are not particularly better, as shown by Fig. 4.13 and Fig. 4.14. At around the same resolution ($L_{cube}(D) = 3\ell \implies \frac{\ell}{2} = \frac{60}{6}$), the relative error of the free and constrained cubes are between a factor of 2-20 larger than the free sphere case. Moreover, while the relative error of the free sphere converges below 0.01, the same cannot be said about either of the cube cases. This is attributed to the surface reconstruction error due to sharp corners, which is exacerbated significantly in the constrained case.

The marked error increase in the constrained cube case is due to the rudimentary sharp edge (triple-line) smoothing algorithm. As indicated before, sharp edge identification is done by simple averaging of neighbor positions, also known as nearest neighbor point simplification. While this works nicely for some cases (smooth triple-lines), it is particularly prone to errors in sharp corners, as those that are seen in a cube. This is particularly apparent when looking at Fig. 4.10, where corners of cubes have turned into the noisy surface illustrated in Fig. 4.8.

While the linearly interpolated scalar function $\tilde{f}$ retains the same shape under rotation, the triple-lines are seen to be distorted. Consequently, random rotation leads to different constrained points being placed at most $s\sqrt{3}$ (voxel diagonal) away from the isocontour; thus incorrectly constraining the location of the reconstructed surface. This is supported by the fact that the free cube has much lower error variations than the constrained cube. Advances in triple-line smoothing [20, 112] can be combined with the sharp feature preservation method outline here; however, this is still an on-going effort at the time of this writing.

Maximum allowable edge length (e_c), which characterizes the facet size is shown to have some small effect on the relative error of the mean width and volume approximations. This is attributed to the fact that the reconstructed mesh is adaptive. Consequently, in regions where higher resolution mesh is required, local adaptivity reduces the edge length significantly below e_c.

Since volume is a "bulk" measurement, the effect of surface reconstruction error tends to affect its approximation much more timidly. Generally speaking, the relative error in the volume estimate converges much more rapidly than those see in the mean width. This is attributed to the fact that the error in a volume estimate is only due to the surface tetrahedra. As the surface starts to dominate at low resolution, the relative error of the volume approximation diverges to up to ≈ 0.30.

4.4.4 Multiple Microstructure Registration

Unless successive microstructures are measured in situ, alignment of multiple meshes is particularly challenging. There are many ways to perform registration across multiple objects assuming that a fiducial mark exists. However, in the absence of a reliable fiducial mark, microstructure alignment depends on minimization of some distance between landmark objects. In the case of orientation imaging, alignment is done through global optimization of a point-to-point misorientation function across multiple maps. Specifically, given two orientation maps a and b, the mis-registration cost function is defined as

$$\mathcal{C} = \frac{1}{N} \sum_{i=1}^{N} d\left(q_a(\vec{x}_i), q_b(\mathbf{R}\vec{x}_i + \Delta\vec{x})\right), \tag{4.18}$$

where q is the orientation at point $\vec{x}$, $\mathbf{R}$ and $\Delta\vec{x}$ are the rotation and translation that are adjusted to best align the two orientation maps, and $d(q, q')$ is the misorientation function defined in the usual way. The number of points sampled, N helps determine the accuracy of the registration. The two orientation maps are aligned at the global minimum of $\mathcal{C}$. This registration is relatively straightforward if microstructures of the two states being registered are not too different, but it becomes problematic when dramatic changes occurred between the two different states. Multiple minima of $\mathcal{C}$ may occur in that case. Moreover, when the two orientation maps are grossly misaligned, the amount of time required to find $\mathbf{R}$, $\Delta\vec{x}$ such that $\mathcal{C}$ is minimized may

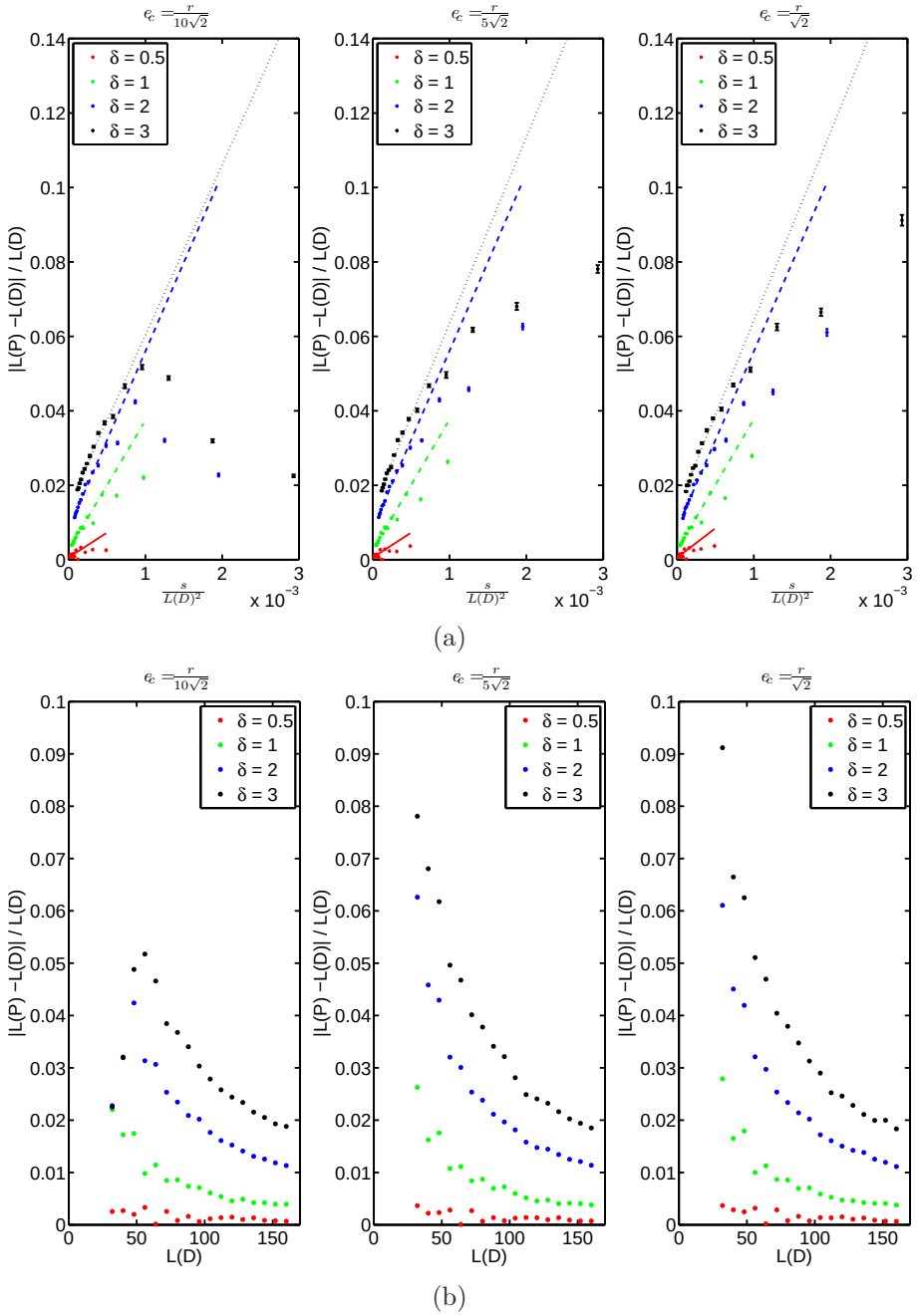

Figure 4.12: Relative mean width error of a free sphere. (a) Relative error is plotted against $\frac{s}{L(D)^2}$, where s is the voxel side length. Near linear scaling is attributed to a good convergence of the mean width as a function of resolution. A line indicating $y = x$ is supplied as a reference. Note that error bars shown are smaller than symbol size, indicating minimal orientation variation in the relative reconstruction error, which is expected for a sphere. (b) A plot of the relative error as a function of $L(D)$ better shows the convergent behavior.

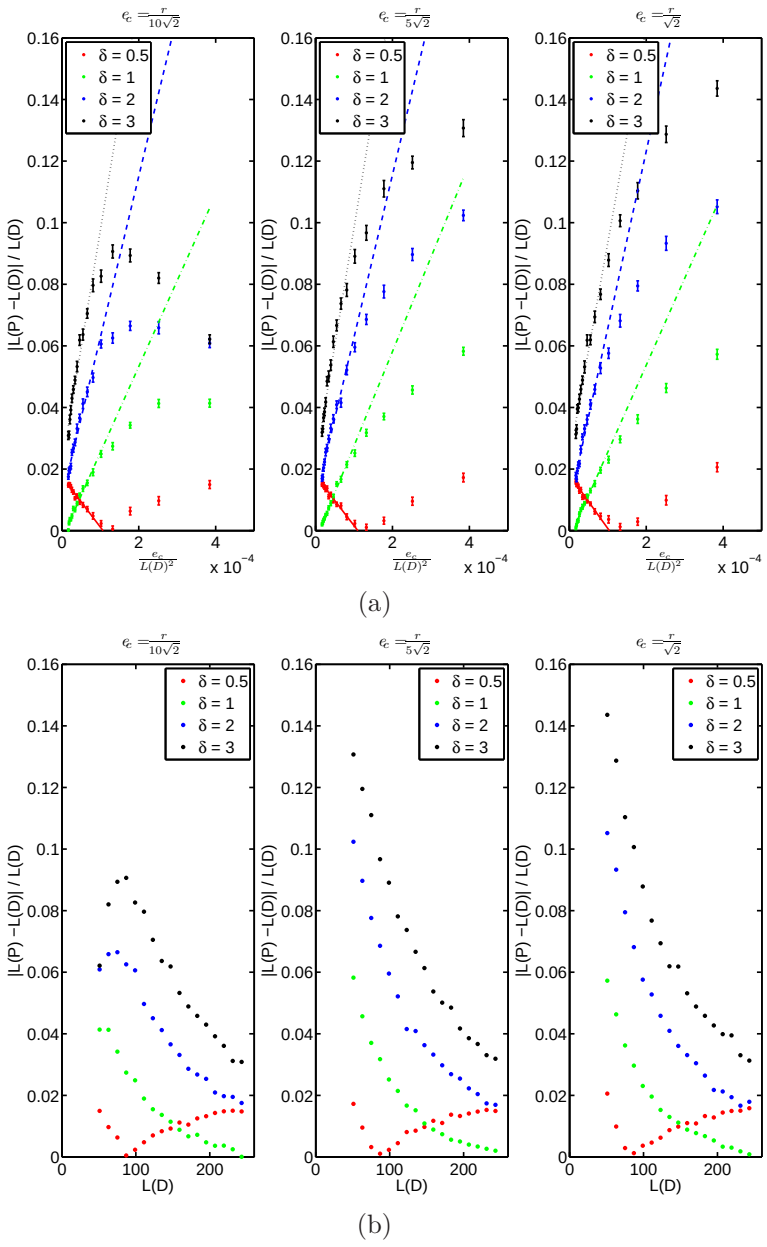

Figure 4.13: Relative mean width error of a free cube. (a) Significant variation is found in the errors estimated, indicating directional dependence of the discretization, which is expected. (b) A plot of the relative error as a function of $L(D)$ to show an exception in the convergent behavior ($\delta = 0.5$). In both plots, $\delta = 0.5$ produces an error that does not follow any scaling. This is an indication that the mean width error is dominated by the noise in the reconstructed surface mesh. The scale of the error seen here is not dramatically worse than the sphere case.

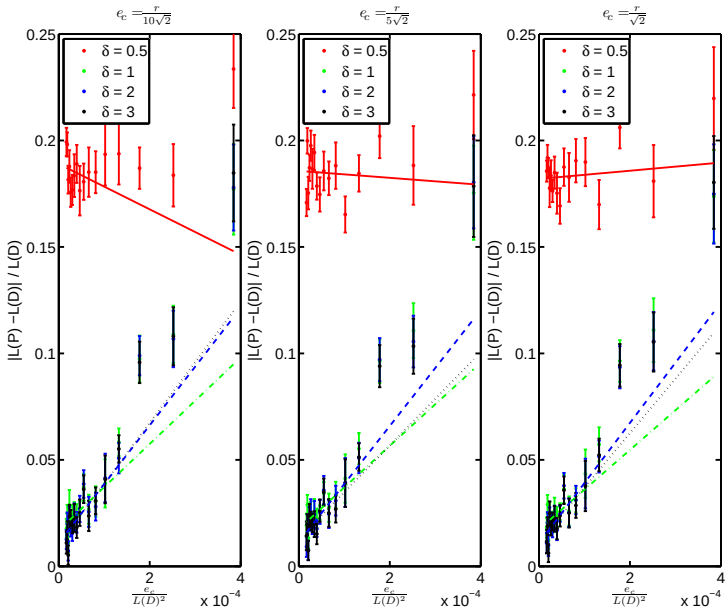

(a)

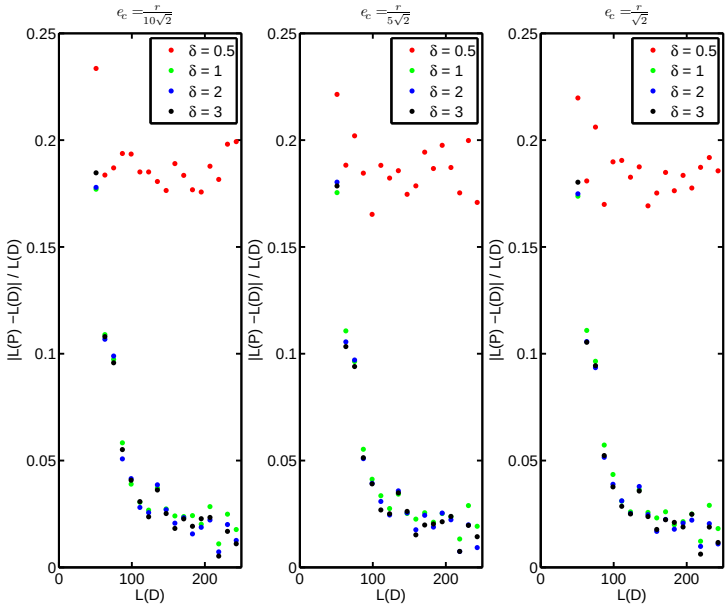

(b)

Figure 4.14: Relative mean width error of a constrained cube. (a) Marked difference in the error scaling behavior can be seen here. Notice here that the error from the case of $\delta = 0.5$ is significantly higher. This is mostly attributed to noise in the triple line reconstruction. Variation as a function of orientation is also dramatically larger than observed for the free sphere or the free cube. (b) All cases except for $\delta = 0.5$ converged rapidly with increasing resolution.

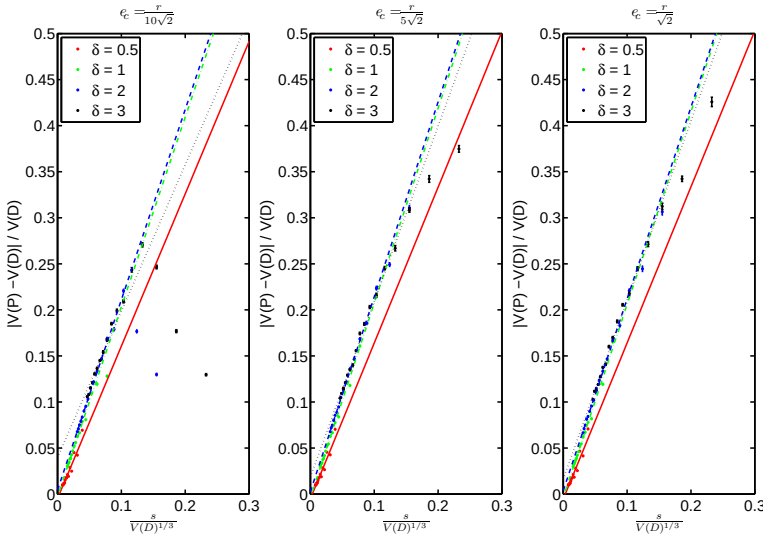

(a)

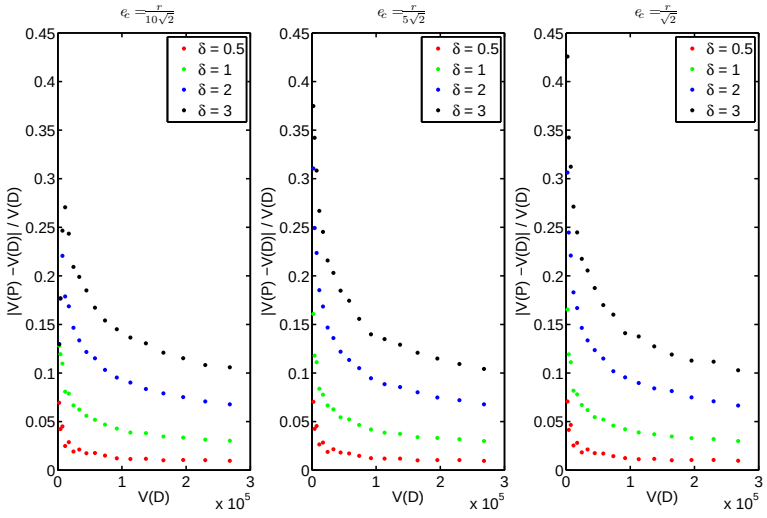

(b)

Figure 4.15: Relative volume error of a free sphere. (a) Relative volume error scaling with $\frac{s}{V(D)^{\frac{1}{3}}}$*, where* s *is the voxel side length for a sphere. Note again that the error bars are below symbol size. (b) Relative error plotted against volume to demonstrate convergence criteria.*

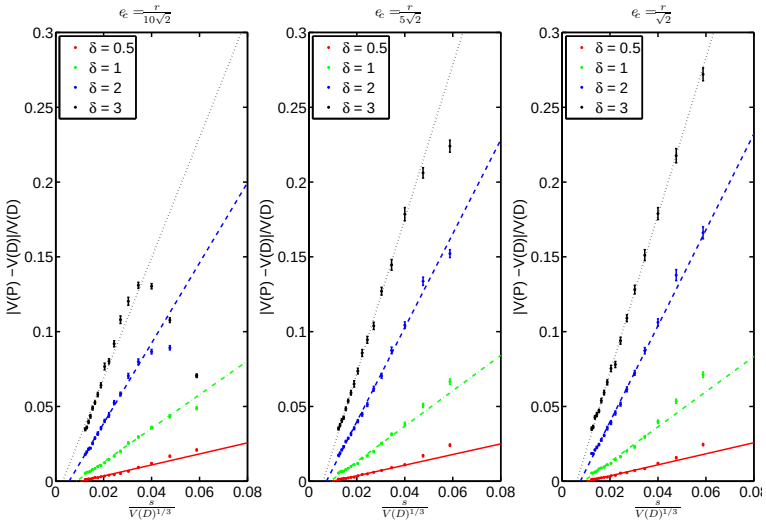

(a)

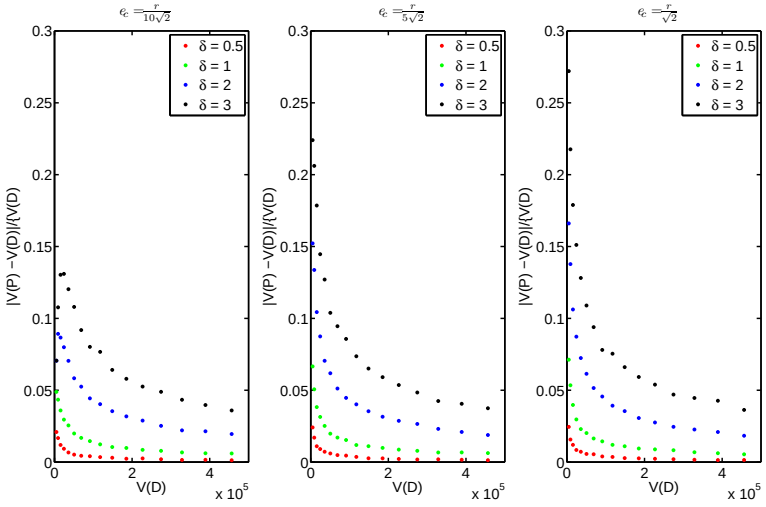

(b)

Figure 4.16: Relative volume error of a free cube. (a) Variation of volume approximation error is significantly lower than that of the mean width calculation. (b) It can be seen that the volume converges much more sharply than the mean width approximation. However, noting the scale indicates here that the relative errors can become significantly higher (up to 0.25 *in the volume approximation in contrast to* 0.15 *in the mean width test).*

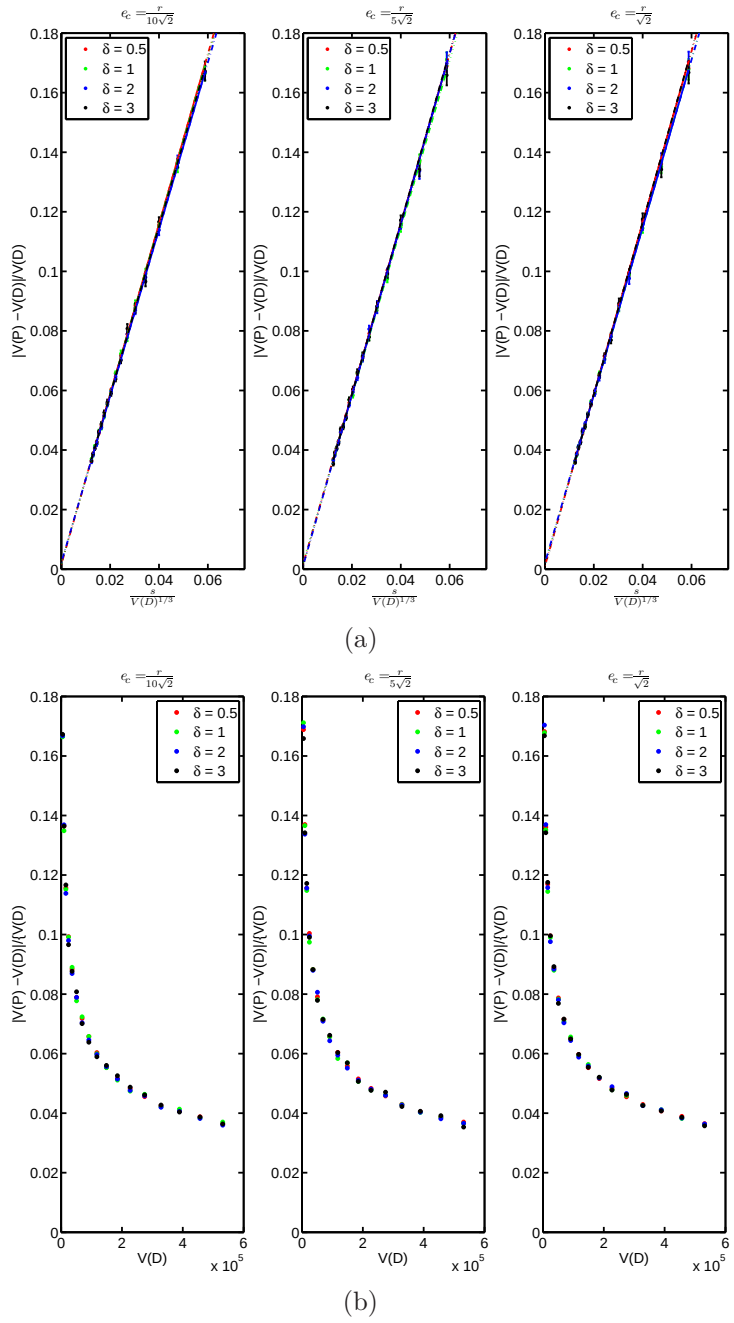

(a)

(b)

Figure 4.17: Relative volume error of a constrained cube. (a) It is seen that all four values of δ result in very similar volume approximations. The non-convergent behavior seen in the $\delta = 0.5$ case of mean width is not present here. Error variation across different orientations is also significantly lower. (b) Compared to the free sphere and the free cube, we see that the volume approximation here converges much more slowly. Note again that δ seems to have no effect on the reconstruction.

take a significantly long time. This alignment method is applied in the analysis of both Chapters 5 and 6.

4.4.5 Grain Tracking

Given grain G_a from state a, we would like to find grain G_b that corresponds to the same grain as G_a in state b. To simplify this problem, we will make the following assumptions.

1. If G_a and G_b correspond to the same grain in two different measurements (denoted by $G_a \equiv G_b$) and $D(G_a)$ and $D(G_b)$ correspond to the domain of the two grains, then $D(G_a) \bigcap D(G_b) \neq \emptyset$ (finite overlap).
2. The volume of the intersection $D(G_a) \bigcap D(G_b)$ is the maximum out of all of the two grains' respective neighbors, $Ngb(G_a), Ngb(G_b)$.
3. $G_a \equiv G_b$ implies that $d(q_a, q_b) \leq \theta_t$, where q_a, q_b are the crystallographic orientations of G_a, G_b.

The algorithm to perform the tracking is given in Algorithm. (5). Notice that this

Algorithm 5 TrackGrain. Given a grain G_a with orientation q_a from a microstructure represented by a volumetric mesh, M_a, find the same grain in a second measured state represented by the mesh M_b. The two meshes are assumed to be optimally aligned.

```
ClosestGrainInB ← Locate(M_b, G_a) {Locate G_a in M_b}
NgbGrainList ← GetNeighbors(M_b, ClosestGrainInB)
for all Grain g_i ∈ NgbGrainList do
  q_a ← GetAverageOrientation(g_i)
  V_⋂ ← IntersectionVolume(g_i, G_a)
  δθ_i ← d(q_i, q_a) {Calculation the misorientation between the grains}
  if δθ_i ≤ θ_t then
    GrainMatchList ← (g_i, δθ_i, V_⋂)
  end if
end for
return FindMaxIntersctionVolume( GrainMatchList ) { Return the grain with
maximum overlap.}
```

algorithm is currently unable to keep track of grains with significant orientation evolution, i.e., lattice rotation. Furthermore, this method is somewhat unreliable when grain sizes change drastically or asymmetrically (Fig. 4.18) as the intersection volume may not be all that telling. Also, no explicit attempt is made to identify disappearance and appearance of grains. This is particularly problematic in the case of grain growth studies. However, by imposing a strict threshold misorientation, θ_t, and insisting that $\Delta V = \frac{|V_a - V_b|}{V_a} \leq 1$, this method is sufficient to track a number of grains across four anneal states. The result of this method is shown in Chapter 5.

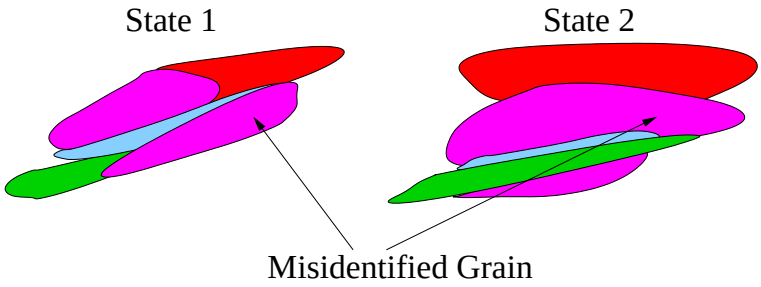

Figure 4.18: A schematic of how a maximum intersection grain tracking scheme may lead to misleading results. Grains of the same color in the diagram are considered to have the same orientation. As grain boundaries move, even with perfect registrations between two states, it is possible that the same grain across two states cannot simply be identified by having maximum intersection and minimum misorientation.

4.4.6 Boundary Tracking

Given that a microstructure in two anneal states is represented by the two surface meshes S_a and S_b, then boundary tracking determines the minimal distance traveled by each of the triangles between the two states. Specifically, for each triangle $T_a \in S_a$, a triangle $T_b \in S_b$ is found such that $d(T_a, T_b)$, the distance between the two triangles is minimal. This is accomplished by point location in S_b using vertices of the triangle in T_a. Roughly speaking, point location simply searches for the nearest region of triangle in a mesh given a point. The resulting set of triangles can be used to estimate a point-to-point shift between two meshes, which is applied to nickel grain growth analysis in Chapter 5. Because no explicit tracking of boundary types is performed, the current analysis is only valid for differential boundary movements.

4.5 Conclusion

A brief review of the surface reconstruction literature, although by no means exhaustive, is presented in this chapter. We have summarized the theoretical results used in the Delaunay triangulation based surface reconstruction method, and a rough description of the implementation details of a sharp feature preserving extension is included. Most of the analysis techniques developed in this chapter are used in analysis of the data discussed in Chapters 5 and 6.

A method was developed to quantify the error associated with discretization and surface reconstruction error for arbitrarily shaped objects defined by an implicit function. This method of error analysis is general, and it can be applied to estimate errors in experimentally measured materials. The result of our initial analysis shows reasonable convergence behavior in the reconstructed meshes, although significant caution must be used to avoid problems with constrained sharp features. Specifically, the directional dependence of sharp edges in the voxelization leads to markedly higher mean width and volume approximation errors. Attempting to address this problem is an on-going effort.

4.6 On-going and Future Directions

Clearly, much of the geometrical analysis is not in a completed state. For example, grain and grain boundary tracking are currently at a rudimentary state. Significant on-going effort is being put into a more robust grain tracking method based on minimum Hausdorff distance between grains. With the automated surface mesh generation and testing methods developed in this chapter, we would like to estimate the reconstruction error for general shapes that are representative of real objects inside a microstructure. The purpose is to provide a foundation to estimate errors in experimentally measured quantities, such as grain boundary mobility, energy, and

curvature. Some of the preliminary results from these techniques are shown in Chapter 5.

Chapter 5

Non-destructive Observation of Grain Coarsening in 3D, Initial Report

5.1 Overview

Grain coarsening is an interesting phenomenon both from a scientific and an engineering perspective. Since material properties are heavily influenced by grain size, the ability to predict and control grain growth in a manufacturing process is critical. In the most ideal and familiar case of curvature driven grain growth, movement of boundaries can be attributed to local curvature as exemplified by soap bubble coarsening, which could be described by

$$v = -M\gamma\kappa \tag{5.1}$$

where grain boundary curvature, κ, interfacial energy γ, and mobility M dictate the grain boundary velocity, v, the velocity perpendicular to the local tangent plane ($\kappa > 0$ for convex regions would lead to $v < 0$ or inward velocity). This way, velocity will be minimized and the grain boundary position stabilized as the curvature is minimized; intuitively, this is why grain boundaries become flatter as a microstructure is annealed.

In two dimensions, Eq. (5.1) leads to the famous $n - 6$ rule [125]. The rate of area swept out by the movement of a boundary segment dl at velocity $\vec{v}$ is given by

$$\frac{\delta A}{\delta t} = |\vec{v} \times d\vec{l}| = v\ dl, \tag{5.2}$$

where $\hat{l}$ is the tangent direction of the boundary curve, and we have assumed the direction of the velocity to be perpendicular to the local boundary tangent. Consequently, the total area change due to the motion of the boundary of the domain D,

∂D, is given by

$$\begin{aligned} \frac{dA}{dt} &= -\oint_{\partial D} v \, dl \\ &= -M\gamma \oint_{\partial D} \kappa \, dl. \end{aligned} \tag{5.3}$$

Taking advantage of the fact that curvature at any point on a $2D$ curve can be defined as $\kappa = \frac{d\phi}{dl}$, where ϕ is measured from an arbitrarily chosen origin leads to

$$\frac{dA}{dt} = -M\gamma \oint_{\partial D} d\phi. \tag{5.4}$$

If the grain boundary is smooth and continuous, the growth rate $\frac{dA}{dt}$ would be constant, as the closed contour integral is identically 2π for any shape. However, given that discontinuities occur where more than two boundary lines meet, the contour integral is given by

$$\begin{aligned} \oint d\phi &= \sum_i \int_{\beta_i}^{\beta_{i+1}} d\phi + \Theta_i \\ &= 2\pi + \sum_i \Theta_i, \end{aligned} \tag{5.5}$$

where Θ_i is the turning angle associated with the i-th discontinuity along the boundary [74]. By assuming triple lines mechanical equilibrium and isotropic boundary energy, all turning angles of the domain are given by $\Theta_i = \frac{\pi}{3}$, and we arrive at $n-6$ rule.

$$\frac{dA}{dt} = -M\gamma \left(2\pi - \sum_{i \in vertices} \Theta_i \right), \tag{5.6}$$

$$= 2\pi M\gamma \left(1 - \frac{1}{6} n \right). \tag{5.7}$$

Note that there are as many vertices as sides in a closed $2D$ loop. This states that grains with seven or more sides grow, grains with five or fewer sides shrink, and grains with six sides are stable. Equation 5.7 is left in this form to highlight the geometrical nature of the grain growth law. The three dimensional version of Von Neumann's $n-6$ rule proved elusive until work by MacPherson and Srolovitz [70] showed that

$$\frac{dV}{dt} = -2\pi M\gamma \left(L(D) - \frac{1}{6} \sum_{e \in E} e \right) \tag{5.8}$$

where D is now the three dimensional domain, $L(D)$ is the mean width of D, and E is the set of all edges of D, each of length e. In general, edges in $3D$ may be intersected

by any $n \geq 3$ domains; however, in the case of grain growth, triple lines are typically observed, since $n > 3$ leads to mechanical instability.

Experimental observation of $2D$ grain growth is possible in some limited cases [113, 29] while studies of three dimensional grain growth are dominated by computer simulations [37, 122, 136, 36, 46] and statistical analyses of $2D$ data via stereology [54, 99]. Until recently, microstructural measurements were limited to optical and scanning electron microscopy. The use of manual serial sectioning was done in an isolated heroic effort to observe the growth rate of aluminum in $3D$ [93]. In most of these cases, the study of grain boundaries was limited to geometry and topology. Recent advances in orientation imaging using electron backscattering diffraction microscopy (EBSD) have changed this significantly [128, 108]. The ability to measure crystallographic orientations for points on a 2D surface leads to significant advances in the understanding of microstructures. Although coupling results from EBSD orientation measurements with stereology enables statistical observations of 3D grain growth, restrictive assumptions, such as equiaxed grains is required [44, 99].

Full three dimensional measurement had not been practical until the advent of EBSD with dual-beam focused ion beam (FIB), which performs automated serial sectioning [121, 27, 98, 59, 96, 26]. Even then it is still not possible to track the same population of grains in 3D, as the measured part of the sample is destroyed during the measurement. Non-destructive measurement attempts were made using both Differential Aperture X-ray Microscopy (DAXM) [55] and 3DXRD [88] to observe recrystallization and grain growth of high purity aluminum [104]. However, the sample size limitation of DAXM precluded it from being able to conduct grain tracking through a statistically significant population of grains, as many of the grains measured from the initial states disappeared by the final anneal state. Attempts with 3DXRD have faltered due to limitations in the reconstruction technique; the inability to resolve grain boundaries to high precision inhibits any reliable resolution of grain boundary movement or curvature.

Finally, simply having the ability to produce grain maps or orientation maps proves insufficient to the study of grain growth or, more generally, any annealing process in real materials. For example, in Nickel, grain boundary mobility is highly anisotropic, varying by as much as four orders of magnitude [44, 79, 22]. Since a typical grain is bounded by a union of multiple boundaries, each of a different type, the variation of mobility can lead to some very non-intuitive results for volumetric changes, even if the growth mechanism is dominated by capillarity. Unfortunately, grain boundary mobility measurements are difficult. In the few exceptional instances of bi-crystal measurements [127], mobility measurements can only be carried out on a few select boundary types. A much more comprehensive survey of grain boundary mobility is necessary to empirically test grain growth theory.

High Energy X-ray Diffraction Microscopy (HEDM) helps circumvent several of the obstacles mentioned above by providing a means to image large volumetric orientation maps with statistically significant numbers of grains per cross section at

micron-scale boundary resolution. By measuring and following the crystallographic, geometrical, and topological evolution of thousands of grains simultaneously, HEDM affords us access to anywhere from $10^3 - 10^6$ unique points in the five dimensional macroscopic grain boundary character space. The geometrical resolution indicates that grain boundary curvature as well as motion can be tracked to within a micron.

In this chapter, we describe the non-destructive measurement of the evolution of a statistically significant population of grains in three dimensions using HEDM. This set of data provides an unprecedented view into grain growth and boundary motion. Due to the unprecedented data volume, development and validation of both data processing and analysis is still an ongoing effort. A subset of the initial results will be presented in this chapter to demonstrate the current capabilities of HEDM and its accompanying analysis tools. A set of common statistical distributions, such as normalized grain size distribution and grain-to-grain misorientation distribution are shown to validate of our measurements. Unlike most previous measurements, these statistical distributions follow and characterize the same ensemble of grains throughout their evolution. An initial characterization of grain boundary motion will be shown. Grain tracking and geometrical feature extraction (introduced in chapter 4) will be demonstrated. As an application, the evolution of 16 grains, tracked across four anneal states, is compared against predictions from the MacPherson-Srolovitz relations. Grain boundary character distributions (GBCD)[50] are compared between different anneal states to highlight changes in the grain boundary population. We conclude with some remarks on current developments and future directions.

5.2 Experimental Procedure

5.2.1 Sample Preparation

High purity, fully recrystallized nickel was prepared to have an initial grain size of approximately 25-50 microns using the procedure described in [39]. Further screening of the initial samples and calibration of the annealing procedures were done by optical microscopy and EBSD. Because fully recrystallized grains are expected to have very low dislocation content, boundary dynamics are expected to be largely dominated by curvature-driven motions. A cylindrical sample was cut to be approximately $1mm$ in diameter by $2cm$ in length using Electric Discharge Machine (EDM). To facilitate alignment between different measured states, a fiducial mark was produced by EDM at approximately $1mm$ above the measurement location. The sample was initially annealed at $750C^{\circ}$ for two hours in a forming gas ($3\%H, 97\%Ar$ hydrogen) ambient to achieve the desired initial grain size. Successive anneals between measurements were done *ex situ* using the same furnace setup for 23, 30, 25, 35, and 25 minutes, respectively, at $800C^{\circ}$.

5.2.2 Orientation Imaging Procedures

Volumetric orientation maps of this sample were measured using the HEDM setup at sector the 1-ID of Advanced Photon Source at Argonne National Lab. Using a monochromatic X-ray beam of 64.5 keV (monochromacy of 10^{-3}) micro-focused to $6\mu m$ FWHM vertically, and an effective width of $1200\mu m$ horizontally). A LuAG, (Lutetium aluminum garnate, $25\mu m$ thick) scintillator was used in conjunction with 5x focusing optics and a Photometric CoolSnap K4 CCD imaging system. The use of the 5x optical magnification on the $7.4\mu m$ pixels of the CCD results in an effective pixel size of $1.47\mu m$, which is confirmed experimentally using optical and X-ray characterization.

The effects of optical distortion after calibration are negligible. For optimal diffraction spot imaging, we chose detector-to-rotation-axis distances (L-distance) of approximately 4.8, 6.8, $8.8mm$. With this experimental geometry, typically 70 - 120 diffraction peaks are imaged for a random crystal across the 180 integration intervals ($\delta\omega = 1^\circ$). From our resolution studies [40] (presented in Chapter 2), this amounts to an angular resolution of 0.1°. As a validation, measurement of a "single crystal" ruby sample showed two regions separated by a low angle boundary of around 0.5°. This was found to be consistent with a measurement done using a rotating anode X-ray source[1], which shows a peak splitting of $\approx 1.2^\circ$. The latter measurement rotates about an arbitary axis relative to the misorientation axis, so the splitting should be $\leq 0.5^\circ$. The spatial resolution of the orientation image map is limited by the effective size of the detector system pixels.

To produce the volumetric orientation map, the sample was scanned one layer at a time. Optimally, resolution in-plane should be identical to that out-of-plane. However, limits of X-ray focusing as well as time constraints make this impractical. With a focused beam of approximately $6\mu m$ FWHM, we decided to use $4\mu m$ spacing between layers. This resulted in the ability to resolve grain boundaries for grains with radii of around $25\mu m$ (feature size prevalent in the initial state) with 5-6 sample points. As boundaries could be locally approximated as 2D quadratics on the tangent plane, the ability to acquire more than 3 sample points per direction was crucial to local curvature and normal estimation.

A total of six anneal states were observed for an imaging volume of $280\mu m \times 1mm$ for the first two states (anneal 0, anneal 1), $336\mu m \times 1mm$ for the next three states (anneal 2, 3, and 4), and $400\mu m \times 1mm$ for the final state. Successively larger volumes were used in an attempt to capture any grains protruding outside of the imaging volume.

Taking advantage of the non-destructive nature of HEDM, all six anneal states were imaged in approximately the same region of the sample. An unfocused X-ray beam ($1.3mm \times 0.3mm$ vertical) was used to produce transmission tomographic images of the sample, and the fiducial mark was used as a reference point to identify

[1] $\frac{\Delta E}{E} \approx 10^{-5}$

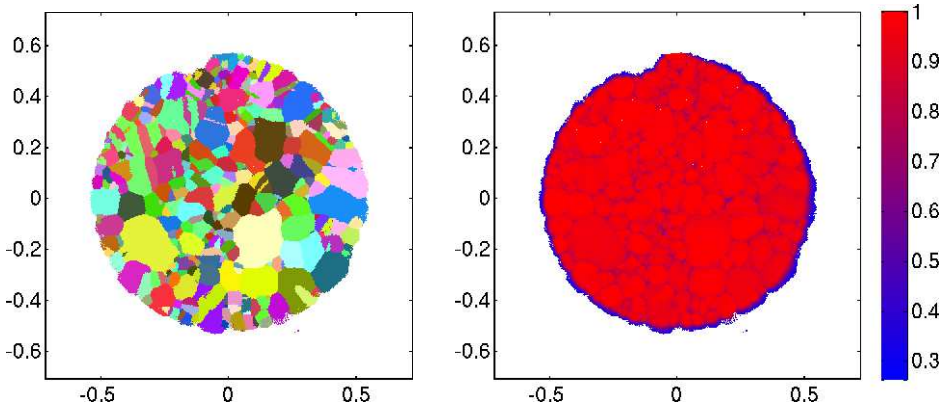

(a) Orientation Map (b) Confidence Map

Figure 5.1: (a) A representative orientation map from the nickel sample. The color is a mapping of the orientation space to red, green, and blue (RGB). The confidence map (b) shows the fit quality of the orientation map.

the imaging volume at each state. The resulting alignment is believed to be accurate within few detector pixels, or about $5\mu m$. Additionally, the orientation of the planar layer cutting across this fiducial mark was measured at the beginning of each volume. This allowed us to perform point-by-point matching of orientations between two different states to get optimally aligned structures.

Measuring the orientation map for each of the anneal states took approximately 24 hours, which implies potential problems with sensitivity to cumulative drifts in both the sample holding apparatus and the X-ray beam. These effects are observed and compensated using a novel optimization method in the orientation reconstruction (presented in Chapter 3).

5.3 Analysis

A total of six volumetric orientation maps were measured (one for each of the anneal states, see Table 5.1). A representative two-dimensional cross section of the initial state can be seen in (Fig. 5.1). Unlike in analysis methods used in 3DXRD and Diffraction Contrast Tomography [88, 68], orientation maps obtained from Forward Modeling analysis completely fill the measured volume. This is particularly important for grain boundary measurements. Mean grain volume was measured across the different states and found to be monotonically increasing (Fig. 5.2). It should be noted that it would be difficult to consider anneal states as time steps, as the annealing time varies for each step. The small number of time steps also makes it difficult to produce a reliable fit against the expected result of $\langle V \rangle \propto t^{\frac{1}{2}}$.

Since we would like to track small grain boundary movements to extract mobility

Table 5.1: Grain size (interior only) and annealing time for each of the measured states.

States	N_{Layers}	Volume measured (mm^3)	N_{3°	$\langle V \rangle$ (mm^3)	$\langle R_{eq} \rangle$ (mm)	Anneal Time (minutes)
0	71	0.269	2142	0.992×10^{-4}	0.0287	
1	71	0.269	1848	1.223×10^{-4}	0.0308	23
2	88	0.334	2295	1.310×10^{-4}	0.0315	30
3	87	0.330	2168	1.382×10^{-4}	0.0321	25
4	85	0.323	2036	1.429×10^{-4}	0.0324	35
5	104	0.395				25

and curvature changes, differential annealing was performed on the sample. To ensure that not too many grains had disappeared between successive states, we used partially fitted orientation maps from subregions of the measurement as a guide. Annealing time was adjusted at each step to help achieve the desired growth.

Consistent analysis of the final two anneal states is complicated by the development of a bend in the sample during annealing. A bend developed unexpectedly and became more pronounced in the specimen after the fourth and the fifth annealing steps. The exact cause of the deformation is unknown, but grain rotation is suspected. In the last two anneal states, several grains with radii between $\frac{1}{16}$ and $\frac{1}{8}$ of the sample's cross section radius were found. Rotations of these larger grains could easily affect the macroscopic shape of the specimen, causing a bend. We do not expect this to be a result of sample handling damage, as neither diffraction peak broadening nor increase in local orientation variations were observed. *Because sample alignment problems resulted from this, the analysis for the final anneal state is incomplete and will not form part of the discussion.*

5.3.1 Orientation Reconstruction

Volumetric orientation information for all six anneal states were reconstructed using **IceNine** (chapter 3), an implementation of the Forward Modeling Reconstruction Method (FRM) [116]. Each of the voxels were fitted independently with $Q_{max} = 10A^{-1}$. With our imaging geometry, this resulted in 70 - 120 fitted Bragg peaks per voxel. Fitted two-dimensional cross sections of the sample were stacked together to produce the volumetric orientation map. Drift between successive layers and throughout each volume measurement was found to be minimal, as verified from parameter optimizations and past comparisons with tomographic reconstructions. We found the orientation spread across each grain to be below 0.1°, which is our resolution limit. This figure remained consistent throughout the five anneal states.

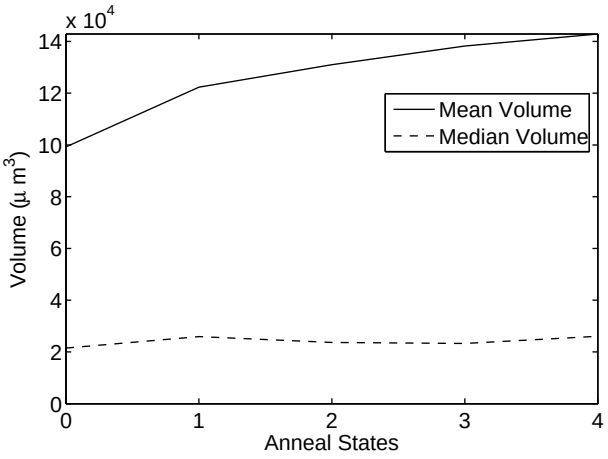

Figure 5.2: Mean and median grain volume for each of the anneal states.

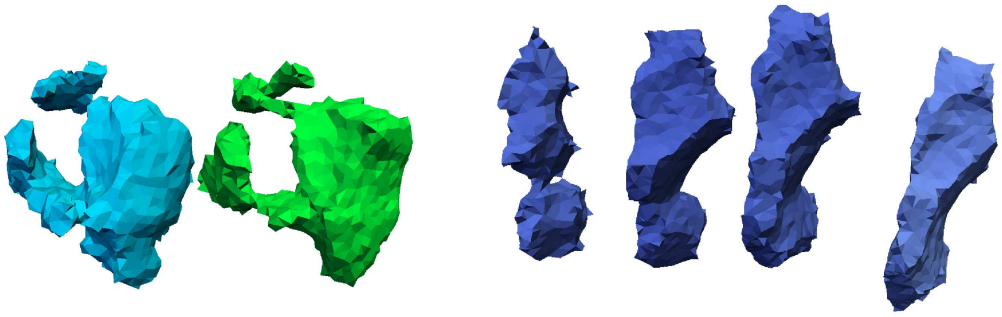

(a) (b)

Figure 5.3: (a) An example of a grain with non-trivial geometry found in the initial and the first anneal state. The region that is "wrapped around" by the grain is identified as an in-growing twin. (b) Evolution of a grain across four states going from initial to final (left to right). Dramatic changes can be seen at the narrowest part of this grain throughout the annealing process.

5.3.2 Grain Extraction

Grains are defined to be connected regions with similar crystallographic orientations. In the case of our orientation maps, this is a set of connected voxels. Two voxels in an orientation map are considered connected if and only if 1) they are first neighbors, and 2) the misorientation $\delta\theta$ between them is less than some threshold value θ_t, which was set to 3° in this analysis. The choice of orientation threshold is somewhat arbitrary, and depends on the expected orientation gradient in the sample. Since our specimen exhibited extremely well annealed grains, we expect the number of grains extracted to be quite stable with respect to orientation threshold variations.

Since reconstruction noise is expected at grain boundaries (i.e, orientations from neighboring grains mis-assigned across the boundary), image artifacts are sometimes present in the grain identified maps. A "majority filter," the discrete version of the median filter, is used to remove these artifacts. Given a $m \times m$ majority filter centered at (i, j), the voxel $v(i, j)$ would be assigned the majority grain ID of its $m \times m - 1$ neighbors. Note that no grain size restrictions are placed on the microstructure, and grains are not guaranteed to be simply connected[2], as indicated by Fig. 5.3.

5.3.3 Microstructure Geometry

Both volumetric and surface meshes are generated for all six of the anneal states. This enables us to define boundary normals, curvature, and mean widths of grains. Furthermore, the reconstructed geometry was used to track grains between anneal

[2]Simply connected is defined in the usual way, i.e. the region must not contain holes or self intersections.

states. Both meshes were generated using feature-preserving mesh generation [9], which was implemented with CGAL [1] (presented in Chapter 4). Because mesh quality (e.g., minimum dihedral angle, aspect ratio, edge-length-to-circumcircle radius) is unimportant in our calculations, most of our effort was directed at assuring that the surface mesh was a faithful representation of the microstructure. This was achieved by restricting the reconstructed surface mesh to be a maximum distance of two voxel side lengths from the surface indicated by the data.

5.4 Results

5.4.1 Grain Statistics

Single Parameter Statistical Characterizations

Normalized grain size distribution, misorientation distribution, and grain boundary character distributions are extracted for the four different anneal states. Three-dimensional grain size distributions are shown in Fig. 5.4. Unlike previous measurements, the evolution of grain size distributions shown here contains the same population of grains in $3D$, which is a first to the best of the author's knowledge.

Grain volumes are calculated from the reconstructed volumetric meshes. A sphere equivalent radius is calculated as $R_{eqv} = \left(\frac{3}{4\pi}V\right)^{\frac{1}{3}}$. It can be seen (Fig. 5.4) that the grain size distribution remains invariant throughout the anneal, which suggests statistical self similarity [75], a hallmark of curvature driven growth. It should be noted however that explicit comparison with proposed grain size distribution functions, such as Hillert [42], log-normal [30], and Rayleigh [65] may not be able to prove or disprove any particular grain growth model, as variations in each distribution may be achieved through adjustment and addition of parameters [33, 45].

A grain-to-grain misorientation distribution is computed using grain-averaged orientations, and the usual features are present (Fig. 5.5). The expected peaks for a fully recrystallized nickel sample, $\Sigma 3$, $\Sigma 9$, and $\Sigma 11$ are clearly visible, with $\Sigma 3$ $(60°, [111])$ being the most prominent. We see that the misorientation distribution remains relatively unchanged throughout the five states, with the exception of anneal state 2. This is due to the combination of reconstruction and alignment problems that is currently being addressed by on-going analysis. Aneal 2 was measured in two independent sessions due to beam time scheduling constraints. The difference in calibration characteristics and sample orientation resulted in some unexpected errors in the final, combined orientation maps. The result is a significant reduction in orientation resolution, which is indicated by the broadening of the 60° peak in Anneal 2.

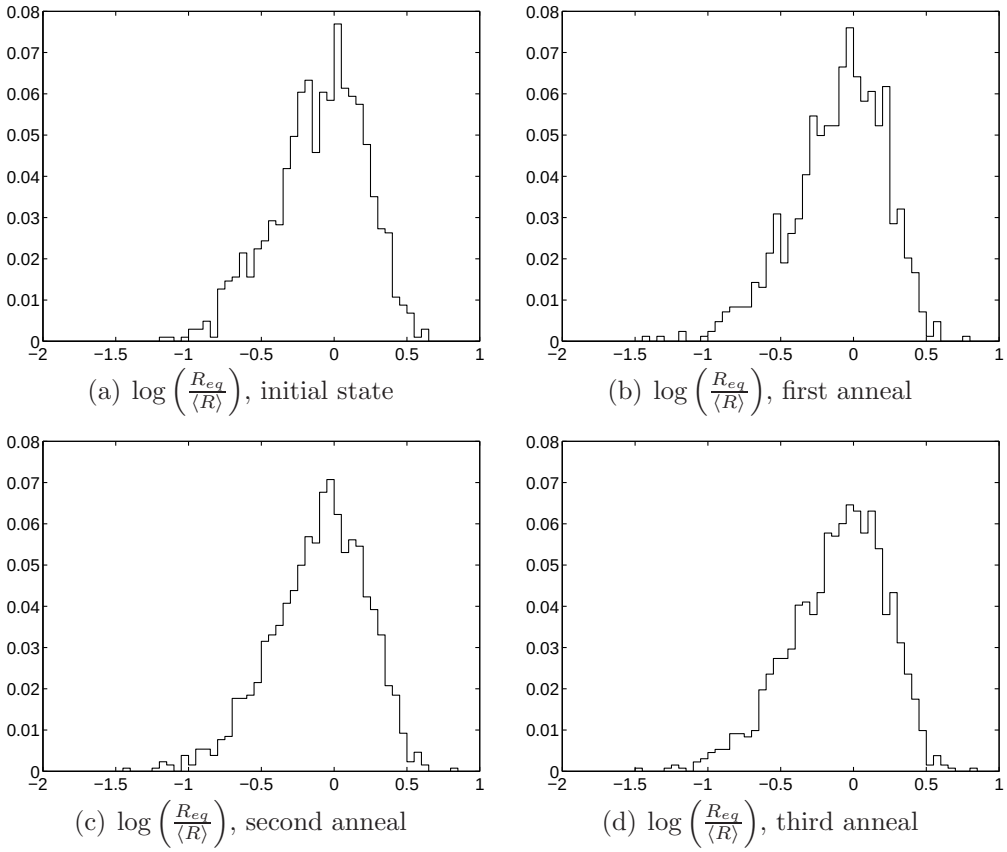

(a) $\log\left(\frac{R_{eq}}{\langle R\rangle}\right)$, initial state

(b) $\log\left(\frac{R_{eq}}{\langle R\rangle}\right)$, first anneal

(c) $\log\left(\frac{R_{eq}}{\langle R\rangle}\right)$, second anneal

(d) $\log\left(\frac{R_{eq}}{\langle R\rangle}\right)$, third anneal

Figure 5.4: Grain size distribution, plotted as normalized radius, $\frac{R_{eq}}{\langle R\rangle}$, where $R_{eq} = \left(\frac{3V}{4\pi}\right)^{\frac{1}{3}}$ is the spherical equivalent radius. Annealing progresses from (a) to (d).

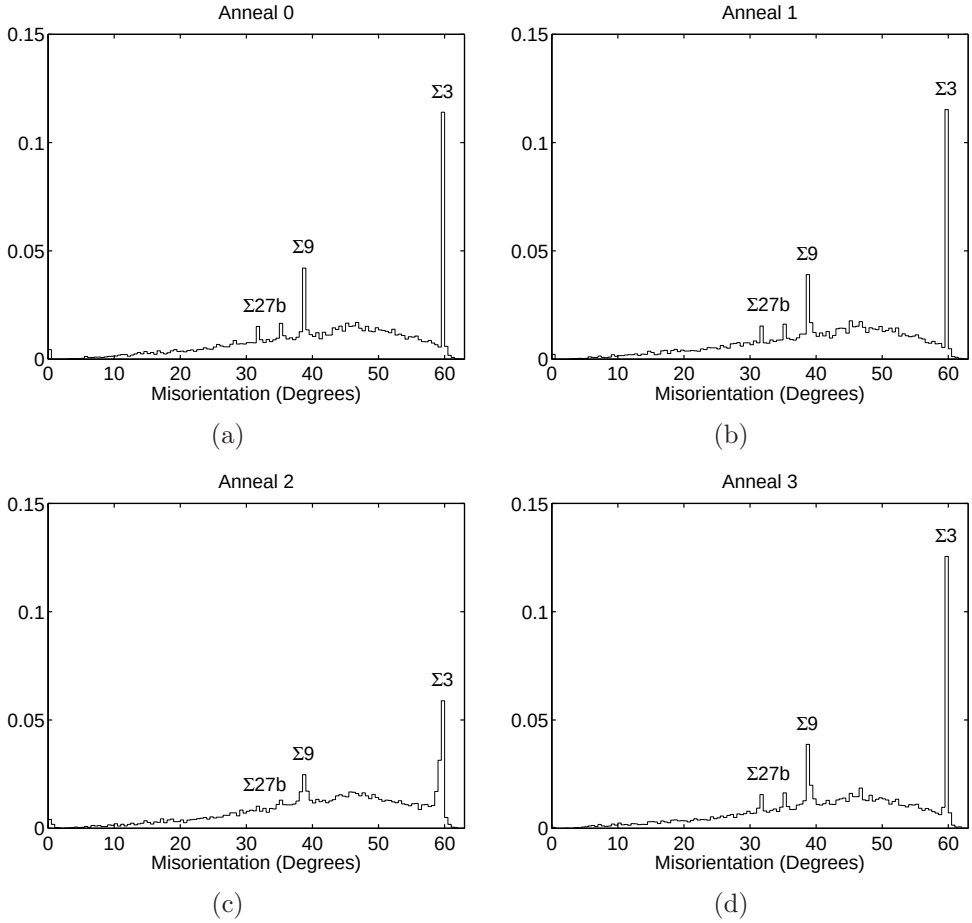

Figure 5.5: Single parameter misorientation distribution for four (initial to third anneal state in the order of (a) - (d)) out of six anneal states measured. The discrepancy in the second anneal state is at this time believed to be an artifact due to errors in the experimental parameters, pending results from the final error analysis.

Five parameter Grain Boundary Character Distribution

While the grain-to-grain misorientation distribution remains stable during the microstructure evolution, the same cannot be said regarding its five-parameter counterpart (grain boundary character distribution, or GBCD). The GBCD is measured from the combination of reconstructed surface mesh and the volumetric orientation maps. On the mesoscopic scale, grain boundaries can be described by the combination of misorientation and boundary normal. Given two grains **a** and **b** with orientations g_a and g_b, the misorientation is given by $\Delta g = g_a^{-1} g_b$. Because this misorientation is also a rotation operator, it can be quantified by a set of Euler angles, quaternions, or Rodriguez vectors. In any of these cases, three independent parameters are required. An additional two parameters are needed to define the local surface normal, which, along with the misorientation, results in a five parameter representation of grain boundaries. The GBCD is the area weighted distribution of different types of grain boundaries characterized by these five parameters.

By constructing a histogram in the five-parameter grain boundary character space the evolution of specific boundary type populations can be observed. It has been suggested that evolution of GBCD is intimately related to the boundary energy [27, 7]. For example, the so-called $\Sigma 3$ coherent twin boundaries, or grain boundaries with misorientations of $\mathbf{\Delta g} = R(60°, [111])$ with normals that point along the [111] direction, are found to have significantly lower energy than other high angle boundaries [86, 79, 80, 95]. Therefore, $\Sigma 3$ coherent twin boundaries are expected to increase in population during annealing process, as the total energy of the system is expected to be lowered. As expected, by plotting the evolution of the distributions for grain boundary normals of all boundaries with misorientation of $\mathbf{\Delta g} = R(60°, [111])$ (Fig. 5.6(a)-(c)), we observe an increase in population for the first two anneal states. From the geometrical perspective, Fig. 5.6 also shows the evolution of grain boundary normals. Alignment of the boundary normal with the rotation axis (shown as sharpening of the [111] peak) in the case of $\Sigma 3$ is also seen as an indicator of boundary smoothing, suggesting curvature minimization during the annealing. Similar behaviors are observed in the evolution of two other boundary populations ($\Sigma 5$ and $\Sigma 11$, Fig. 5.6(d)-(f), and (g)-(i)), and a more exhaustive search for features in the GBCD space is currently underway.

5.4.2 Direct Observations of Grain Geometry Evolution

Grain Boundary Movement

From Table 5.1, we expect subtle boundary motions to dominate the statistics: between the initial and first anneal states (which are analyzed here), the average grain radius changes from $29\mu m$ to $32\mu m$. This is consistent with our intention to achieve "differential" annealing that would allow comparison to boundary motion predictions based on curvature. It is shown here that our reconstructions and analysis procedures

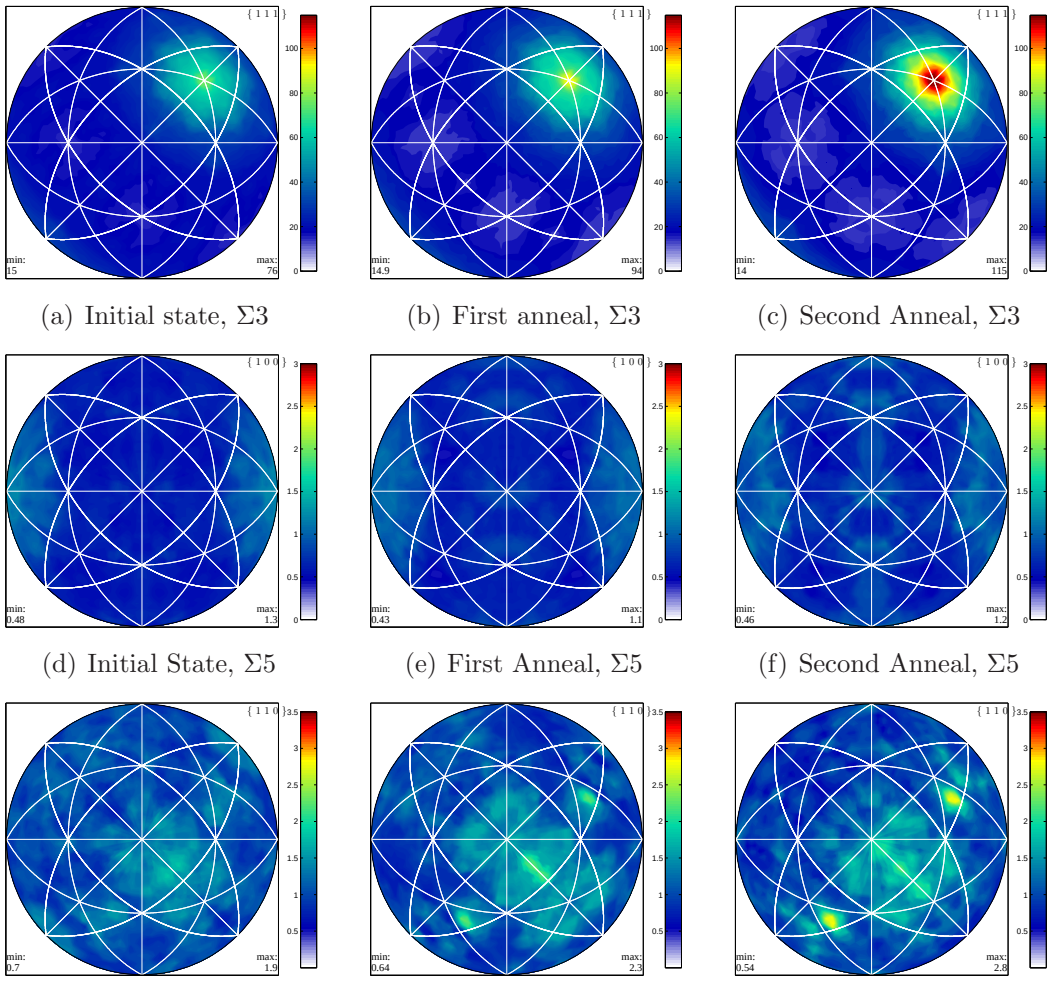

(a) Initial state, Σ3 (b) First anneal, Σ3 (c) Second Anneal, Σ3

(d) Initial State, Σ5 (e) First Anneal, Σ5 (f) Second Anneal, Σ5

(g) Initial State, Σ11 (h) First Anneal, Σ11 (i) Second Anneal, Σ11

Figure 5.6: Sub-spaces of the five parameter grain boundary character distribution selected by the misorientation. Annealing proceeds from left to right. Each figure is a plot of the boundary normal distribution, represented in the stereographic projection form and plotted as multiples of random. (a)-(c) Σ3, $(60°, [111])$ *Note the strengthening of the* [111] *peak by a factor of* 100 *across the annealing process, which indicates the alignment of boundary normals with the rotation axis. (d)-(f)* Σ5, $(36.87°, [100])$ *and (g)-(i)* Σ11, $(50.49°, [110])$ *Signals from both* Σ5 *and* Σ11 *are much weaker that those seen in* Σ3*. One reason is the significantly lower statistics (count of* 28007 *boundary patches for* Σ3 *in contrast to* 1185 *and* 804 *for* Σ5 *and* Σ11*). Secondly, the energy of the* Σ3 *coherent twin corresponds to a much deeper minimum than* Σ5 *and* Σ11*.*

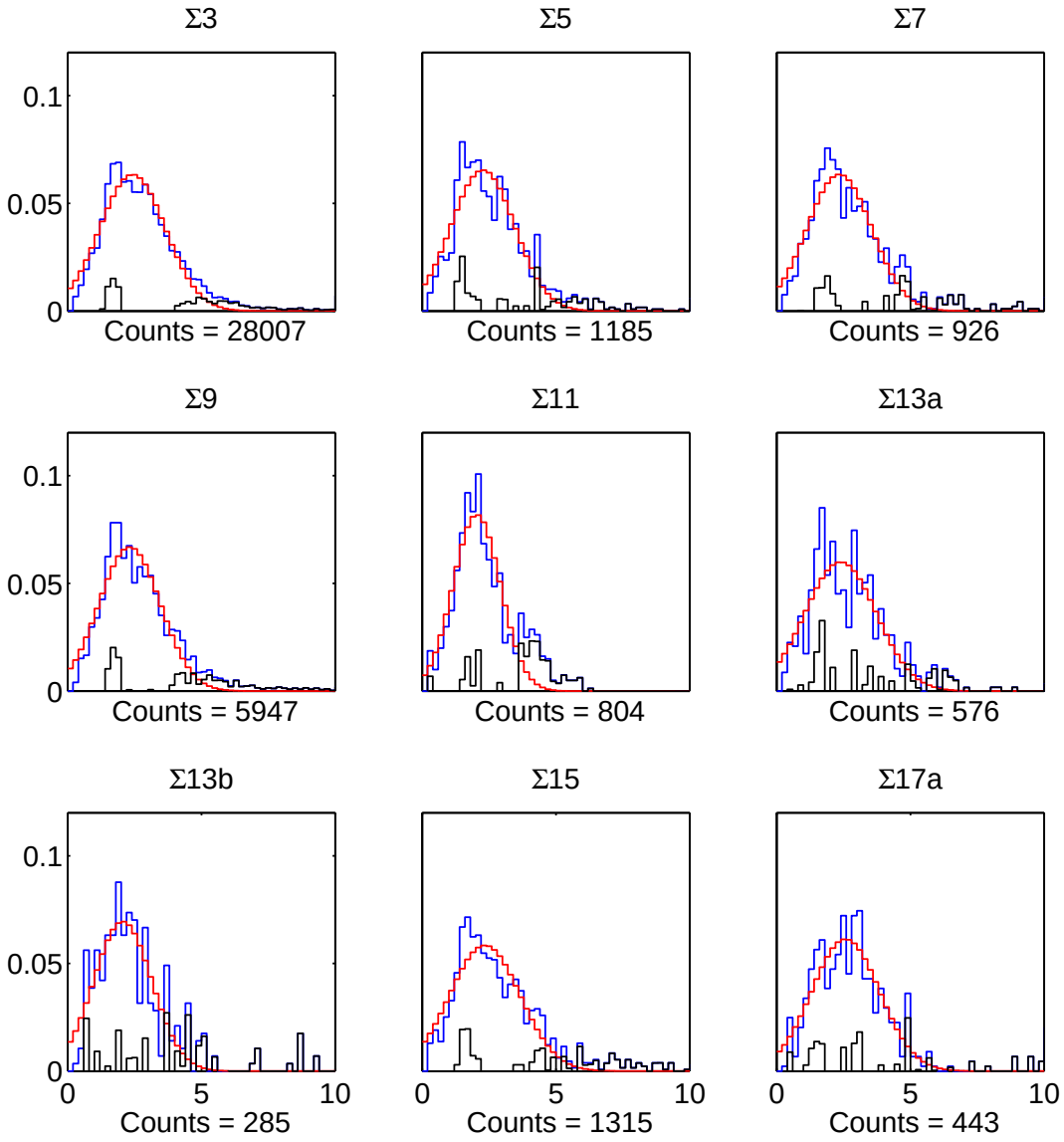

Figure 5.7: Distribution of apparent grain boundary motion between initial and first anneal state. The horizontal axis is the number of microns shifted, and the vertical axis is the faction of boundary patches. The total number of boundary patches is also displayed to exhibit the difference in the population sizes. A Gaussian (red) is fitted to the distributions in an attempt to isolate random components of the shifts from potential signal. The raw data is shown in blue, and the Gaussian subtracted signal is shown in black.

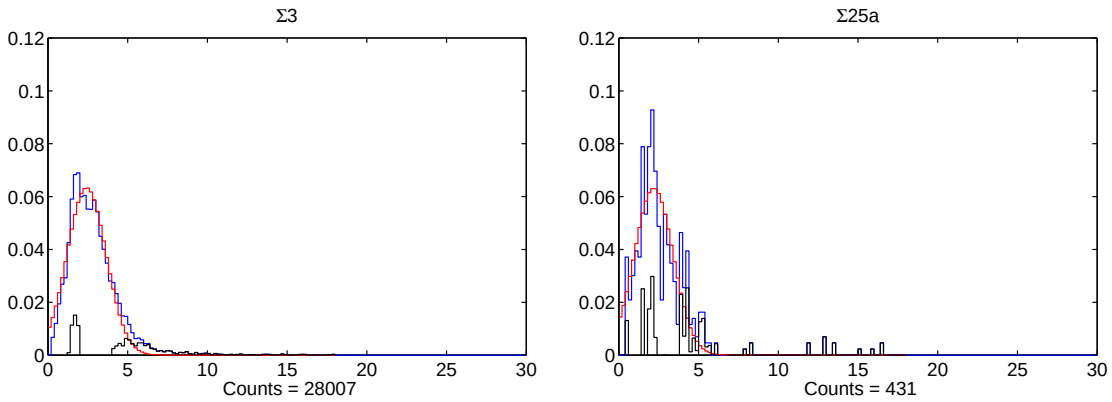

(a) (b)

Figure 5.8: An example of the global plot of the grain boundary motion distribution seen in Fig. 5.7 for Σ3 (a) and Σ25a (b). A small number (less than 10) of boundary patches is found to have noticeably large motion (upwards of 20 μm). However, these patches are more prone to misidentification across the two anneal states.

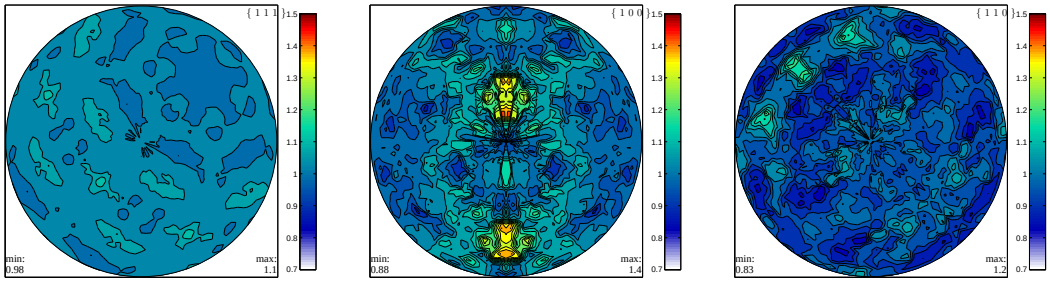

(a) Σ3 (b) Σ5 (c) Σ11

Figure 5.9: Apparent grain boundary movement, classified by misorientation type, plotted as projections of the boundary normal weighted by multiples of the mean boundary shifted. For each plot, the mean boundary shift is classified by the boundary normals and binned according to the two angles, (ϕ, ψ), which represent the normal in the upper hemisphere. The average shift in each bin is compared with the shift of all boundaries.

are sensitive to the relevant length scales but that we have not yet achieved clear resolution of such small motions. It appears that the current data sets may well be able to resolve these by using finer scale reconstruction meshes and, of course, applying the current methodology to later anneal states should certainly resolve larger boundary motions.

Boundary motions are extracted using reconstructed surface meshes. Surface and volumetric meshes for two of the five anneal states are aligned visually and boundary patches are associated across different anneal states. Specifically, grain boundary motion for the anneal states n and $n+1$ is estimated by the distance between patches of the two reconstructed surface meshes. Given a vertex $v(\vec{p})$ in state n, its motion is estimated by $\delta\vec{p} = \vec{p} - \vec{p}'$, where $\vec{p}'$ is the point where the closest vertex to v is located in state $n+1$. The distance shifted for a given surface patch $\mathcal{A}(v_1, v_2, v_3)$ is estimated as the average distance shifted amongst its vertices. A final alignment is done by computing the average boundary patch translation vector and subtracting this from all annealed state mesh node positions. While for any specific grain, the boundary shift measured may be directionally biased due to its physical motion and the voxel based surface reconstruction[3], motions in the sample-aggregate distribution are expected to be random. This is justified by the fact that large numbers of grains (2142) of different shapes are measured, thus allowing for reliable averaging.

In spite of the above resolution discussion, it is clear from, for example, Fig. 5.8 that there is boundary movement. This implies that small numbers of boundary patches dominate the motion statistics. This is further illustrated by the evolution of the grain seen in Fig. 5.3(b) where it is seen that only a small subset of the boundaries move significantly. A comparison of the later anneal states reveal clear

[3]Surface reconstruction errors are geometry dependent.

boundary motions. Note for example the change Fig. 5.6(a) to Fig. 5.6(b) compared widt Fig. 5.6(b) to Fig. 5.6(c).

MacPherson Srolovitz Comparison

To directly compare our experiment with the MacPherson-Srolovitz relations, grains were tracked across five out of six of the measured states. Very strict selection criteria led to only 16 of the total initial 2142 grains being selected. The criteria for this selection are as follows:

- Each grain must be internal through the annealing process.
- The volume change between successive anneals must be less than 100%
- Given grains g_n and g_{n+1} from states n and $n+1$, the misorientations between these two grains must be below some threshold value, which is set to 5°.
- It must be possible to track forward and backwards through the five anneals.

These criteria were used to ensure that no grains are misidentified across the different states, which turns out to be a relatively common error. Because most grains do not grow isotropically, the center of mass tends to shift as the microstructure evolves. These effect coupled with the occurrence of annealing twins, turns out to be make grain tracking surprisingly difficult.

Mean width for a triangular mesh approximation of a closed surface S is defined by

$$L(\mathbf{D}) = \frac{1}{2\pi} \sum_i e_i \alpha_i \tag{5.9}$$

where e_i is the length of the edge shared by the two facets in the mesh [70]. The turning angle, α_i is positive when the surface is locally convex and negative otherwise. To obtain the turning angle from a triangular surface mesh, one uses

$$\alpha_i = \cos^{-1}(\hat{n_a} \cdot \hat{n_b}) \tag{5.10}$$

where $\hat{n_a}, \hat{n_b}$ are the normals of the two facets sharing the edge e_i. Note that no mention of topological properties of the region enclosed by the S is made. Specifically, the region is not guaranteed to be simply connected, which tends to occur when the surface represents a grain with an in-growing twin (Fig. 5.3).

From Fig. 5.4.2, we can see that little or no correlation can be found between volume changes and the linear measure Eq. (5.8) for the 16 grains analyzed. This is not particularly surprising, as it is well known that nickel has anisotropic grain boundary mobilities and energies that range across four orders of magnitude [80].

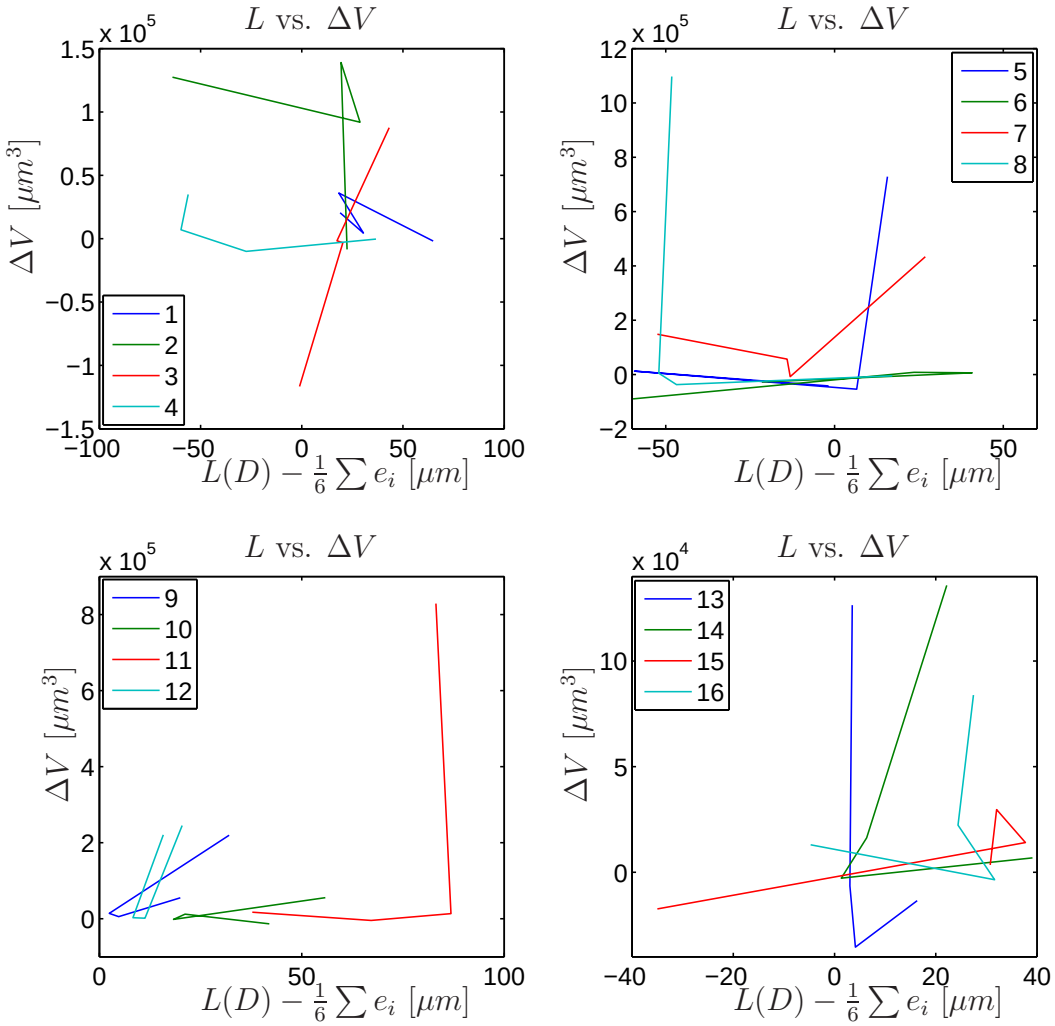

Figure 5.10: A test of the MacPherson-Srolovitz relationship $dV = -2\pi M\gamma(L(D) - \frac{1}{6}\sum e)$ *for the 16 grains tracked across four volumes. Aside from globally not following MacPherson-Srolovitz's relationship, deviation for each of the grain is markedly different from what is expected for isotropic grain growth.*

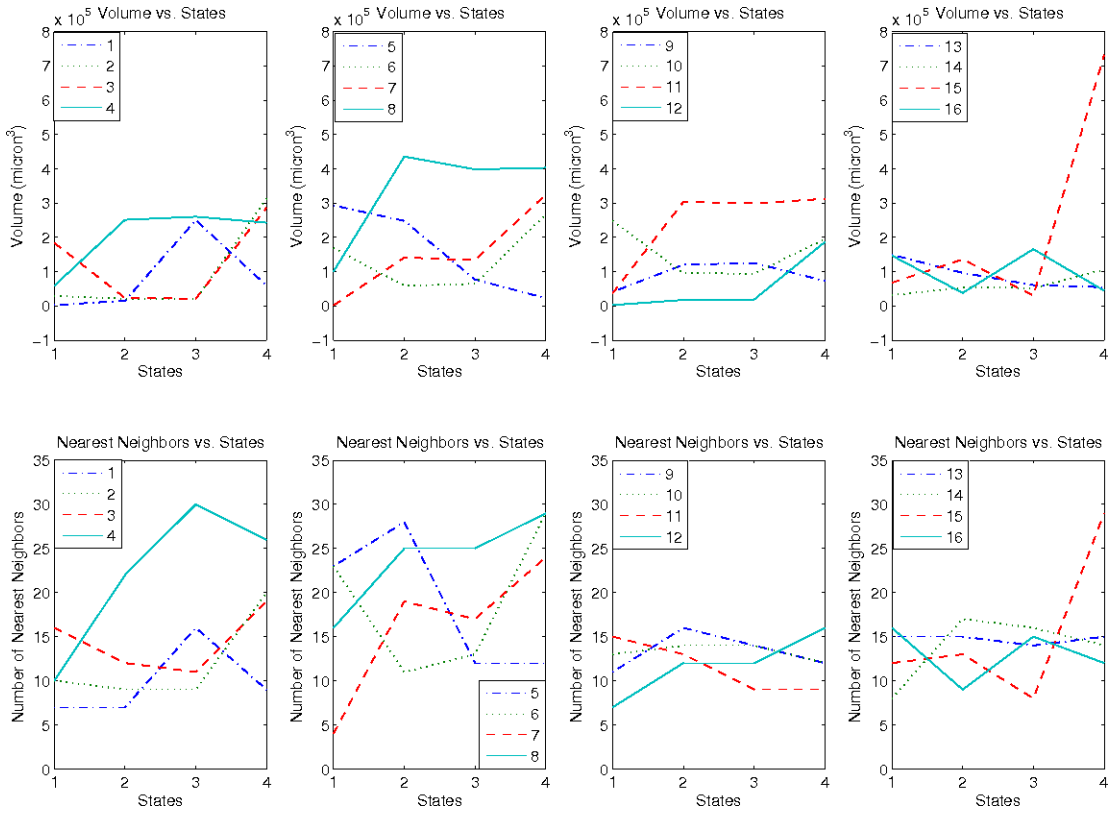

Figure 5.11: Evolution of topological class and volume for 16 grains tracked across four of the six anneal states. It is shown that the change of grain volume is correlated with the change in topological classes.

5.4.3 Direct Observations of Grain Topology Evolution

Significant interest has been expressed in the topological evolution of 3D microstructures during grain coarsening [34]. Specifically, while topological evolution of microstructures in 2D is completely determined by the Von Neumann relation Eq. (5.7), grain coarsening in 3D is significantly more complicated Eq. (5.8). As expected, this is yet another quantity that is difficult to measure using 2D surface techniques. By using the extracted geometry from the volumetric orientation maps produced by HEDM, we are able to track the topological evolution of the same 16 grains examined above. As shown in Fig. 5.11, the topological evolution is correlated with the volume changes for each of the grains. While this result itself is not entirely surprising, it serves to improve one's confidence in the MacPherson-Srolovitz comparison, which appears to be completely random (Fig. 5.4.2). It should be noted that while volume changes between successive states is incremental, the topological evolution seems to vary significantly, indicating multiple critical events, or disappearance of grains in the microstructure. This is further attributed to the fact that a small number of boundaries and grains are responsible for a large portion of the dynamics.

5.5 Discussion

We have seen in this chapter the application of HEDM to non-destructive grain growth experiments, and a set of initial results are shown to both validate and demonstrate Forward Modeling reconstruction's capabilities. Grain boundary motions are analyzed, and a majority of boundaries were found to have moved minimally. While this spells inconclusive results that in qualitative comparisons with simulation and theoretical predictions are not possible, the results highlight the consistency and precision of the HEDM method. The grain boundary motion distribution peaking at $\approx 2.5\mu m$ indicates that the majority of the near idle boundaries were repeatedly measured to a great precision. In fact, this measurement is currently limited by sample discretization resolution, i.e., the boundary noise is dominated by the voxel size. This problem will be addressed in on-going analysis.

As seen in this chapter, the usual statistics, such as grain-to-grain misorientation distribution can easily be measured by HEDM, with the advantage of the capability to track the same populations of grains through the experiment. This is particularly useful in the case of GBCD observations. Other work has found that population of grain boundaries are inversely related with grain boundary energies [94, 7]. In principle, energy measurements could be done with the current HEDM volumes. In addition, higher resolution volumetric and surface meshes will produce much more reliable measurements of mean width and local boundary curvatures. Combined with calculations of grain boundary energy from triple lines, and mobility measurements from boundary shifts, we can directly compare our results with some of the recent advances in simulation and theory [70, 79, 80].

5.6 Future Work

Up to this point, the majority of the alignment and grain tracking work in the literature has been mostly manually. This was not a particular concern in past measurements [55, 88] where only a few grains are tracked, but it becomes nearly impossible for our sample with well over 1000 grains throughout the six volumes. Current obstacles in automated grain tracking are mostly due to the anisotropic nature of grain growth in Ni. Oftentimes one side of a grain would be growing while the other side shrinks. Consequently, the resulting orientation map would seem as if the grain has shifted. On-going improvement in grain tracking will certainly help alleviate most of these problems.

Significant improvement in triple line reconstruction will also be needed to obtain grain boundary energy estimates to fully test the anisotropic nature of grain growth. Coupled with improvement in sample alignment, grain boundary mobilities could be estimated. This will be combined with local curvature measurement on the grain boundary network mesh. A lot of this work is partially completed at the time of this writing, pending cross checks and simulation validation.

To fully take advantage of the six volumes of data we have, direct comparison with simulated models would be needed. For example, comparison with Potts and phase field models would help elucidate the nature of anisotropy in the boundary movement. Work by Hefferan and company [39] is in the process of producing a comparison of grain boundary mobility with results from atomistic simulations [79, 80]. Direct validation of this type is currently unavailable, as non-destructive volumetric orientation maps of bulk materials have been elusive until the recent advances of X-ray techniques. Finally, some small improvement of the current reconstruction software is necessary to achieve the optimal resolution of our orientation maps, which will reduce some of the aliasing effects of extracted grain boundaries.

Chapter 6

In Situ Observation of Spatially Resolved Orientation Evolution in the Deformation of High Purity Copper Wire

6.1 Preliminaries

The experiment described in this chapter was preceded by two prototype development runs at Argonne National Laboratory, which led to improvements in various aspects of the apparatus, calibration methods, data acquisition methods, and sample preparation. Useful feedback were obtained from the data sets measured in these prototype experiments, which served to improve validation the application of Forward Modeling reconstruction method to deformed microstructures. To limit the scope of this chapter, those results have been omitted.

6.2 Introduction

It is well known that anisotropies in material properties play a prominent role in the evolution of microstructures during deformation [53]. In particular relevance to our experiment, elastic moduli for most materials are directionally dependent; hence for a single crystal, the mode of deformation differs as stress is applied from different directions. In the case of polycrystalline materials, this anisotropy manifests itself as an intimate connection between the crystallographic orientation and strain state of each grain. Specifically, grains with different orientations respond to external mechanical stimuli differently; consequently, the stress states inside a material could vary significantly depending on local orientations. On the other hand, crystallographic orientation for each grain changes as the bulk sample undergoes plastic deformation.

This is commonly observed as lattice rotation, low angle boundary formation, and increase of orientational mosaicity across a grain. In general, the ability to produce spatially resolved orientation maps proves to be an invaluable tool in studying deformed materials.

Until recently, spatially resolved orientation measurements have been considered all but impossible. With the advent of electron backscattering diffraction microscopy (EBSD), orientation maps become much more readily available. However, EBSD is limited to surface measurements, and therefore it is particularly difficult to apply EBSD to the study of deformation. Deformation is an inherently three-dimensional problem, as quantities such as dislocation densities are measured through $3D$ spatial derivatives of the orientation field representing the microstructure. Many attempts were made to infer and extract three-dimensional information from $2D$ orientation maps [114]. However, strain measurements from EBSD tend not to be reliable, partly due to relaxation of the free surface [92, 108](CITE: Field). Recent advances in synchrotron X-ray based techniques, such as DAXM [55], 3DXRD [88, 90], and near- and far-field HEDM [116, 83, 71, 62] have led to the possibility of measuring orientation and strain states inside a bulk polycrystalline sample. Of these techniques, near-field HEDM is best suited to measure spatially resolved three-dimensional orientation maps for deformed bulk materials. In contrast to the far-field HEMD [62, 71, 83], near-field HEDM has a much higher spatial resolution at the cost of lower angular resolution (factor of 10-100). Analysis technique of 3DXRD and Diffraction Contrast Tomography were not designed to handle deformed materials, and DAXM has limited penetration depth and imaging volume size. Consequently, neither of these techniques are suitable for measurement of deformed bulk samples.

In this chapter, application of near-field HEDM to measure *in situ* damage accumulation of high purity copper wire under uniaxial strain will be discussed. The resulting spatially resolved lattice rotation map is shown. We start by describing the experimental method, imaging setup, and sample preparation. A total of five states (one initial and four deformed) of the copper gauge section were measured. The effect of deformation to the diffraction signal was studied; furthermore, spatially resolved volumetric orientation maps were reconstructed and compared across three of the five states using the Forward Modeling Method [116]. Lattice rotation and low angle boundary formation were observed along with formations of sub-grain structures. Because of the novel nature of this experiment, in that a macroscopic sample is deformed and imaged *in situ* until ductile failure, several concerns are raised regarding the reconstruction reliabilities of the forward modeling method. To address these concerns, resolution, convergence, and systematic error studies are performed to validate the correctness and stability of the reconstructed orientation maps. Transmission X-ray tomography on the sample as is reported as cross check of the bulk sample geometry evolution.

6.3 Methods

6.3.1 Adaptation of Near-field HEDM for *in situ* Study of Deformed States

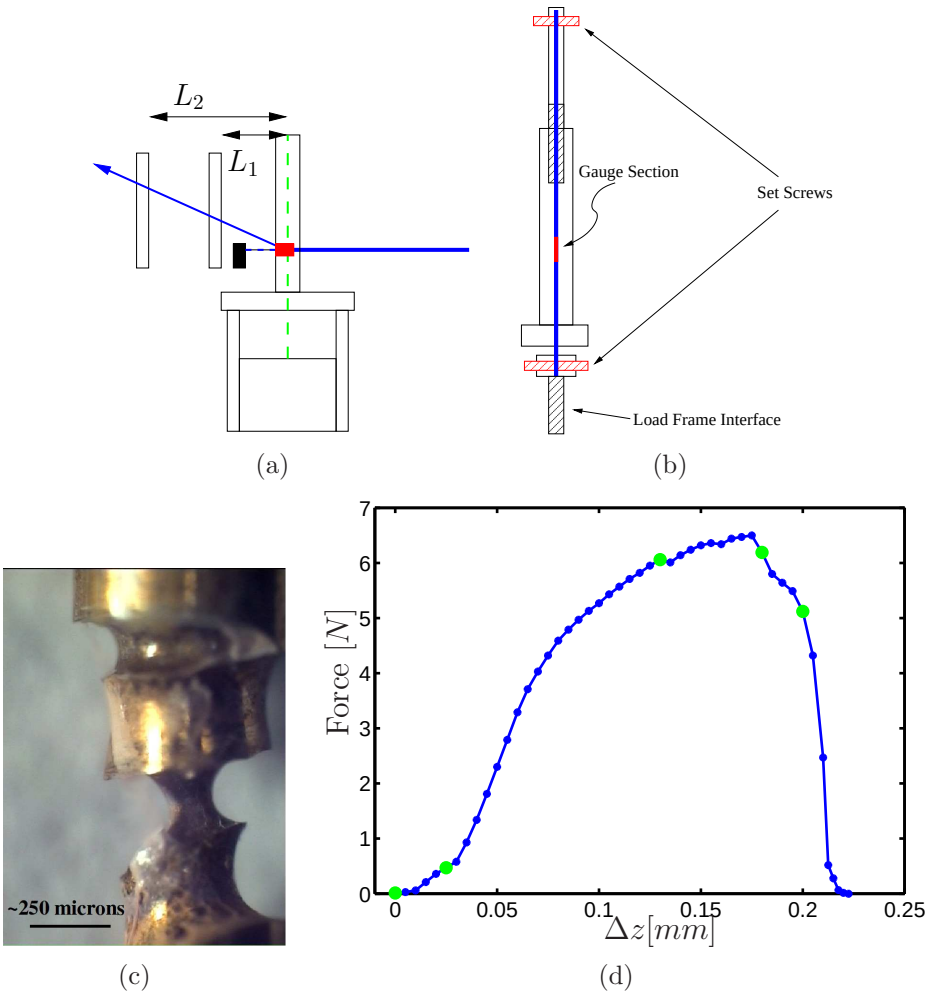

Figure 6.1: (a) Side view schematic of the experiment, with the blue arrow indicating the diffracted X-ray beam. The diffracted peaks are measured at distances L_1 and L_2. The dotted green line indicates the location of the copper wire in tension, and the red region indicates the gauge section being imaged. (b) An expanded side view of the sample holder in (a). The $1mm$ wire can be seen here to be fixed by set screws (red section at the top and bottom). The sample housing around the wire is made out of Macor, an X-ray transparent ceramic. (c) A photograph of the actual sample after electropolishing (the image was cleaned up to remove some of the residual lacquer). The narrowest section of the necked wire is roughly $250\mu m$ in diameter. (d) The load cell reading plotted as a function of displacement. Green dots indicate states where HEDM imaging was performed.

Three-dimensional, spatially resolved orientation maps of *in situ* deformed materials have never been obtained from a bulk material, and there are good reasons why this is the case. Leaving aside the immediate and potentially intractable problem of orientation reconstruction with weak, overlapping diffraction signals from a deformed sample, there is still the concern of sample geometry. In both HEDM and 3DXRD, the sample is required to rotate about a fixed axis. Simultaneously, the "load frame" must be compliant with experimental geometry, i.e., it must be small (radius $r \leq 5mm$), and cylindrically symmetric. Furthermore, the material for the load frame used must be both stiff (high elastic modulus) and X-ray transparent. Many of these problems were solved using a specially designed load frame and Macor sample housing, Fig. 6.1(b), which will be explained in more detail in the next two sections.

Since diffraction peaks from a deformed structure tend to broaden due to effects such as subgrain formation, lattice rotation, and dislocation accumulation [126, 47, 89], significant care must be taken in the experimental design. Specifically, peak broadening in the η direction leads to intensity being spread out across a much larger area on the detector, increasing from the typical width of $\delta\eta \leq 1^\circ$ in the undeformed case to $\delta\eta \approx 10^\circ$ in strained materials; this broadening also reduces the signal to noise ratio. To further complicate matters, higher order diffraction peaks tend to be the most noise sensitive, as they tend to have lower intensity. This could normally be compensated by increasing integration time, but constant rate backgrounds (florescences and stray scattering) are always present and are relatively strong in our case due to the strain apparatus (see below). Specifically to our *in situ* experiment, texture development due to the applied load resulted in orientations that diffract more heavily along the low η direction. Since the integrated intensity for a diffraction peak scales with

$$I_{sim} \propto \frac{|F|^2}{|\sin\eta| \sin 2\theta}, \tag{6.1}$$

a region of disproportionately high intensity is developed in the low 2θ high η area, which saturates the dynamic range of the CCD detector. The best we can do is a judicious choice of integration time.

While validation and characterization of HEDM and the Forward Modeling reconstruction method is sufficiently addressed in the case of well-ordered polycrystalline samples (chapter 3, 4), the same cannot be said about imaging of deformed materials. Specifically, little study has been done on the effect of peak broadening in both the η and ω directions on orientation reconstructions in the HEDM and 3DXRD geometry. A validation and sensitivity study performed to fully characterize the effects is discussed in Sec. 6.4.

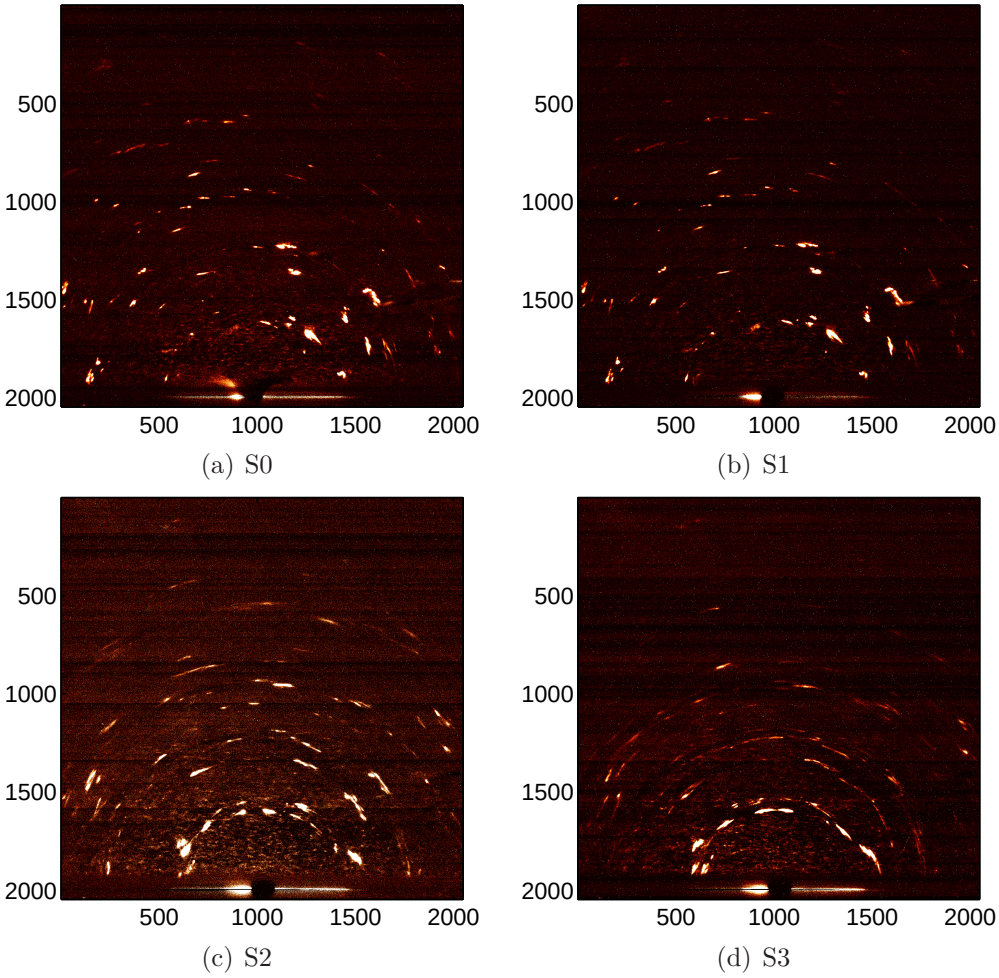

(a) S0 (b) S1

(c) S2 (d) S3

Figure 6.2: Images corresponding to the same 1° integration interval in states S0, S1, S2, and S3. These are background subtracted images for a layer at a sample location equivalent to $z16$, the 16th layer of state S1. Since the sample is moved and deformed noticeably during strain steps, layers measured do not have a direct correspondence between different states. Best match layers are shown here instead. Significant deformation of the sample can be observed as peak broadening in the η direction. Note that we do not expect any observation of elastic strain since it is on the order of 10^{-4} for copper, which is below our resolution limit.

6.3.2 Apparatus and Sample

The tensile sample was fashioned from a piece of copper wire and measured using near-field HEDM while in uniaxial tension. The specimen was prepared from commercially available, $1mm$ diameter 99.9999% purity Cu wire from Alfa Aesar. To focus stress in a small region where the measurement would be done, a narrowed region was created by electropolishing a $1mm$ long section at the center down to a $500\mu m$ diameter (Fig. 6.1(c)). An acetone soluble lacquer (Midas 335-009) was used to protect the rest of the wire. Then a $300\mu m$ long section within the gauge was necked further to an $\approx 250\mu m$ diameter. The polishing was done at $20V$ in a 30% nitric acid/methanol solution kept at -50 to $-30°C$. The use of a two-step polishing process is necessary to reduce stress concentration around sharp edges and corners outside of the imaging region.

The sample holder (Fig. 6.1(b)) forms part of the load frame (Fig. 6.1(a)) and was constructed using the ceramic Macor, which is high energy X-ray transparent but produces a diffuse background. A load cell (Transducer Techniques, GSO-1k, 0.1% sensitivity) was used to provide direct readouts of the force on the wire. The load frame is driven by an elevation stage (Micos ES-50), with a maximum load of $5N$, minimum step size of $1\mu m$, and minimum traveling velocity of $1\mu m/s$.

The sample was mounted on using set screws, penetrating into the surface of the $1mm$ diameter regions. After mounting in the Macor cylinder, the sample was annealed at $400°C$ for 30 minutes to allow for recrystallization and recovery from any damage introduced during processing.

6.3.3 Volume Measurement Procedures

Five different strain states were measured with HEDM with macroscopic true strain of 0%, 0%, 6.2%, 15.3%, and 26.9% (henceforth referenced as S0, S1, S2, S3, and S4). These strains values were determined by the length of the gauge section deduced by the location of fiducial marks on transmission X-ray projection images. The two fiducial marks are the sharp corners at the transition between the $500\mu m$ and $250\mu m$ necks (Fig. 6.1(c)). The error associated with location of the fiducial marks is determined by the sharpness of the X-ray images, which is estimated to be $\pm 15\mu m$. Note that the macroscopic strain between S0 and S1 is undetectable by this estimation scheme. Diffraction images and the load curve also imply that this first "load step" simply brought the wire to a taught state.

The load curve, the force reading from the load cell plotted against macroscopic displacement, is shown in Fig. 6.1(d). The stress state of the sample is not uniform, and therefore not shown in the plot. The use of simulation would be needed to estimate the stress state of the sample with consideration of the non-uniform geometry. Orientation map of the gauge section indicate that the sample consists of roughly ten grains per cross section. As suggested from the literature [69, 28, 35, 120], the deformation behavior in this sample is expected deviate significantly from a continuum

model.

To facilitate alignment and experimental parameter determination, orientation maps were measured at the position of the two fiducial marks using three L-distances. Diffraction signals from the fiducial mark layers remain sharp throughout the experiment, as both layers are well outside of the narrowest and most highly deformed part of the sample. Detector to rotation axis distances (L_1, L_2, L_3) were set based on the physical limitations of the Macor sample housing and the location of the direct beam stop (Fig. 6.1(a)) To ensure the ability to image a significant number (≥ 100) of the diffraction peaks, L_1 was set to $6.40mm$, $L_2 = L_1 + 2mm.$ and $L_2 = L_1 + 3mm.$

The measurement volumes for states S0, S1, and S2 are $200\mu m$ in height, centered on the necked region. A larger volume of $252\mu m$ height was imaged for state S3, to account for the elongated sample. Due to the large deformation seen in most of the sample, only a small region near the fiducial mark was imaged in the state S4. To save time, these measurements were made with two L-distances, with L_1 and L_2 given above. The length of measurement time (approximately 18 hours per volume) requires that the deformation be performed in "stop-action." Load was applied *in situ* and the sample was allowed to relax (approximately 30-60 minutes) before imaging began. The sample was held at constant displacement for up to 24 hours, and the load reading was found to have minimal drift. This indicates that effects of motor movement associated with the HEDM setup is minimal. Load was applied to the sample by discrete displacement steps with minimum step size and velocity of the Micos ES-50 elevator stage. During loading, steps were taken once every few seconds, thus allowing the load frame to stabilize from the motor motions.

6.3.4 Diffraction Signals

The deformation of the copper specimen can be seen from both the load cell reading (Fig. 6.1(d)) and the tomographic reconstructions, Fig. 6.3. By inspection of the tomographic reconstruction, the region with the maximum deformation is located in the center of the electropolished neck. This is further substantiated by the diffraction patterns shown in Fig. 6.2. Reconstruction quality suffers as we approach the narrowest parts of the sample.

We have specifically chosen layer 16 from state S1 (L16S1) as our reference point and as the subject for development of detailed analysis methods. Layers corresponding to L16S1 in states S0 and S2 are used as a basis for comparison. Layer 16 was specifically chosen because it resides in a region that is noticeably deformed, yet orientation reconstruction is still possible. Moreover, since sample alignment between strain states is not perfect, having multiple neighboring layers lets us optimize the state-to-state alignment.

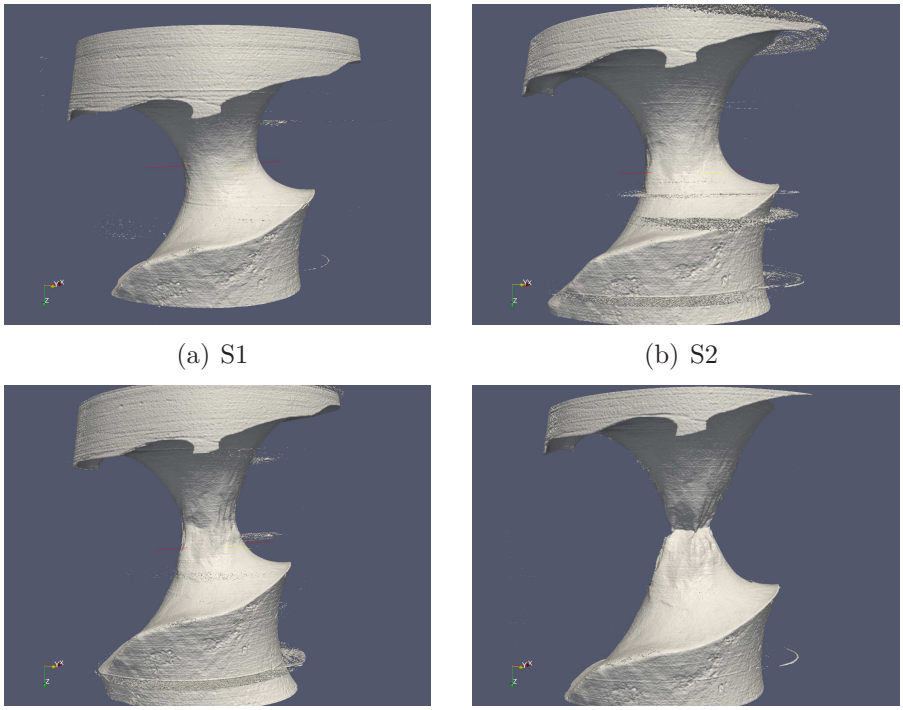

(a) S1 (b) S2

(c) S3 (d) S4

Figure 6.3: Tomographic reconstruction of the four deformed states.

6.4 Analysis

Orientation reconstruction requires fitting of diffraction peaks, but it is not cleared *a priori* that peak-broadening and splitting produced by a deformed sample is tracked by the Forward Modeling algorithm. Specifically, we would need to assert that broadened peaks do not lead to accidental overlaps, which are seen as orientation candidates by the reconstruction. This can be accomplished by tracking and comparing experimental and simulated diffraction peaks across multiple integration intervals. This is in contrast to well-ordered materials, where peak fitting seen in one integration interval is sufficient to substantiate that the diffracted peaks are correctly fitted. To further ensure the reliability of the reconstructed orientations with respect to experimental uncertainties, a sensitivity study was performed on the reference layer (z16). By varying the detector origin and reconstruction resolution, we have found the reconstructed orientations to be stable under significant systematic parameter variation (i.e, $\frac{\Delta L}{L_1} \approx 3\%$, constrasted with $\approx 0.3\%$ in the well-ordered case). The details of these studies are presented in the next two sections.

6.4.1 Forward Modeling Validation

Because splitting and broadening of diffraction peaks are not explicitly input into the diffraction model, it is not entirely clear that the measured diffraction spots would be tracked by the simulation. We examine this peak tracking problem by focusing on a subregion of the detector where an experimental diffraction peak is split and broadened across 20 integration intervals (only nine are shown in Fig. 6.4). Specifically, diffraction spots simulated from the reconstructed microstructure tend to stay closely to, if not directly overlap the experimental peak. It should be noted here that the detector geometry specifying the entire HEDM experiment is bootstrapped at the fiducial layer using the procedures outlined in Chapter 2 and 3. These experimental geometry parameters may therefore contain a certain amount of systematic error, as the detector or sample could potentially drift throughout the experiment.

Simulated intensities plotted in gray scale can be found in Fig. 6.5, which contains some qualitative similarity with the experimentally measured spots. As the diffraction peaks are extended along the $\hat{\eta}$ direction, integrated intensity along the vertical or horizontal direction could provide additional insight in how well the experimental diffraction spots are tracked by the reconstruction. Normalized integrated intensities along vertical and horizontal directions are compared between the experimental and simulated diffraction spots in the region shown in Fig. 6.4 in Fig. 6.6(c) and Fig. 6.6(d). The simulated pixel intensity is the sum of intensities produced by each voxel as described by Eq. (6.1). The stacks of plots show a progression of integrated intensity across the vertical and horizontal direction in successive ω integration intervals. It should be noted here that due to the projection geometry of HEDM (REF Chapter 2 and 3), sample spatial resolution along the direction of the X-ray beam is signifi-

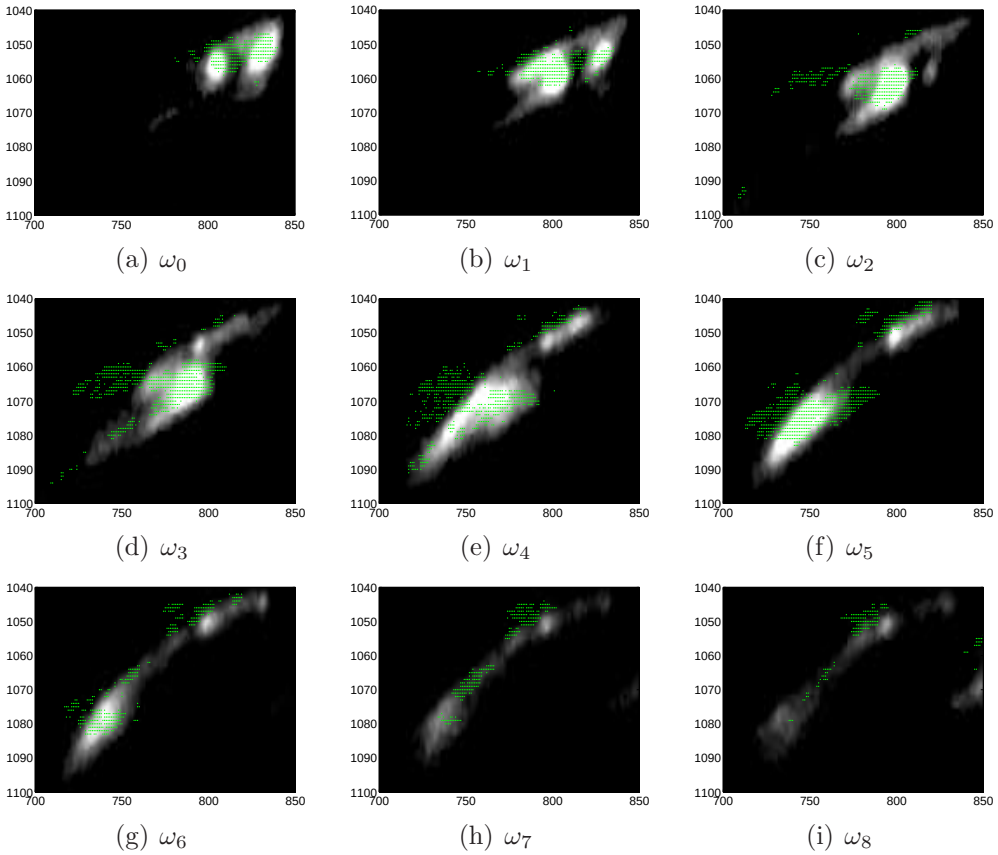

(a) ω_0 (b) ω_1 (c) ω_2

(d) ω_3 (e) ω_4 (f) ω_5

(g) ω_6 (h) ω_7 (i) ω_8

Figure 6.4: (a) - (i) Observed evolution of a diffraction peak as the sample rotates about the $\hat{z}$-axis. Experimental diffracted intensity is shown in grayscale, while simulated pixels are plotted as green dots. The simulation overlap is typically concentrated in the higher intensity area of the experimental peak, in spite of the fact that no explicit intensity fitting is used in this reconstruction. (See Chapter 3).

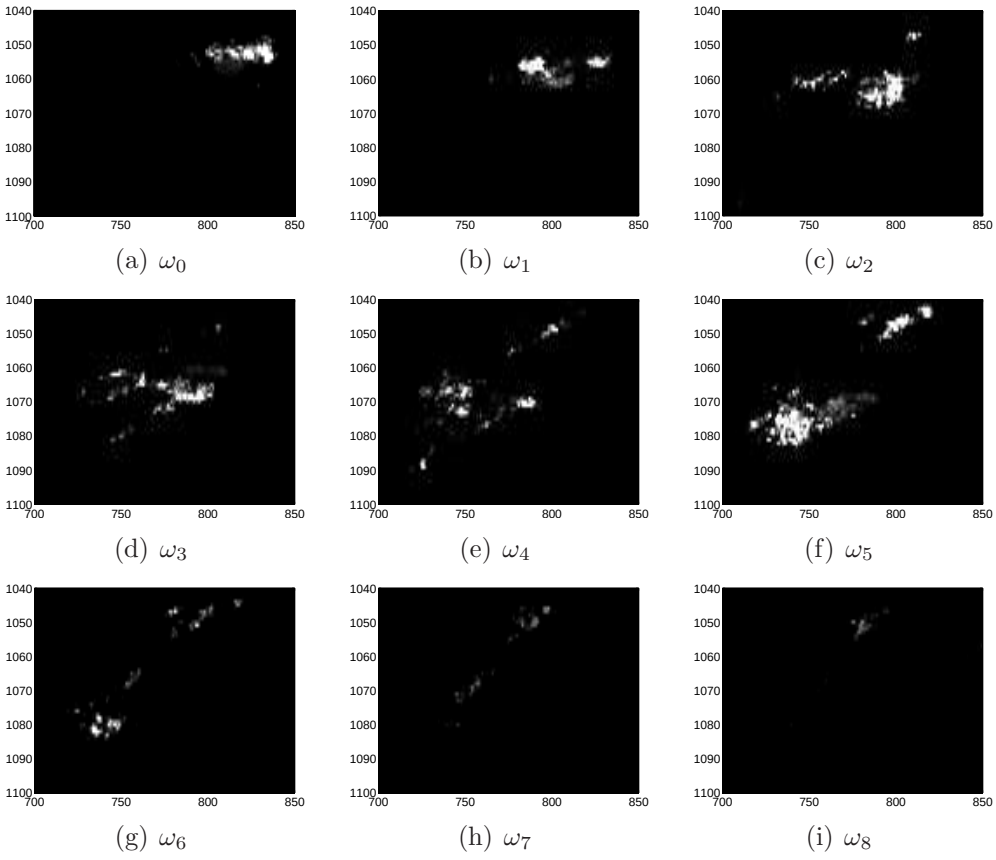

(a) ω_0 (b) ω_1 (c) ω_2

(d) ω_3 (e) ω_4 (f) ω_5

(g) ω_6 (h) ω_7 (i) ω_8

Figure 6.5: Diffraction spots generated from forward modeling reconstruction, with intensity approximated by Eq. (6.1). Each image (a) - (i) shows a diffraction peak in one out of nine consecutive integration intervals. It can be seen that the peak splitting in the simulated result is similar to that in the measured images.

cantly compromised. Consequently, the peak resolution along the vertical direction is typically worse than the horizontal direction. This provides a basis for the generally smoother integrated peak intensities along the vertical direction.

As expected from inspection of the $2D$ detector regions in Fig. 6.4, splitting, broadening, and movement of diffracted peaks are tracked in the integrated intensities. It should be emphasized here that the "intensity model" used in the orientation reconstruction is in fact binary. In other words, the intensities used in the reconstruction are thresholded, and therefore they resemble more closely the figures 6.6(a) and 6.6(b). Overlap between simulated versus experimental lit pixels then completely determines the "goodness-of-fit" for a certain peak (REF Chapter 3). The fact that simulated intensity tracks the experimental intensity so well indicates that intensity variations in each diffraction peak are mostly due to geometrical configurations. In other words, Bragg scattering is sufficient to describe the measured diffraction. This is compatible with the fact that elastic deformation in copper is below the detection resolution of the current HEDM setup. Orientation mosaic resulting from plastic deformation seems to be resolved accurately by the Forward Modeling method, thanks in part to its insensitivity to diffraction signal overlap.

6.4.2 Stability of Forward Modeling Reconstruction

The reliability of the reconstructed orientations is determined by their stability, i.e, small perturbations of reconstruction parameters lead to small changes in the reconstructed orientations. Specifically, the reconstruction is expected to converge reasonably smoothly with increasing spatial and orientation resolution (i.e., changes in resolution should not lead to wildly different reconstructed orientations). While errors in sample geometry are expected to induce changes in grain boundary locations, there should be minimal effect on the global reconstructed orientations. This assumption is justified by the fact that orientation distributions can be measured without spatial sensitivity, as in the case of traditional X-ray measurements. Therefore, Forward Modeling simply resolves the orientation spatially. Sample geometry errors translate directly to sample location uncertainties, which should not affect the set of possible reconstructed orientations. Unfortunately, a theoretical framework to study the stability of the Forward Modeling algorithm is not available, and a sensitivity study must be performed on each data set. We have selected four areas of focus for our sensitivity study:

1. **Detector-to-rotation axis distances (L-distance)**
2. **Diffraction Origin**
3. **Orientation Resolution**
4. **Sample Space Resolution**

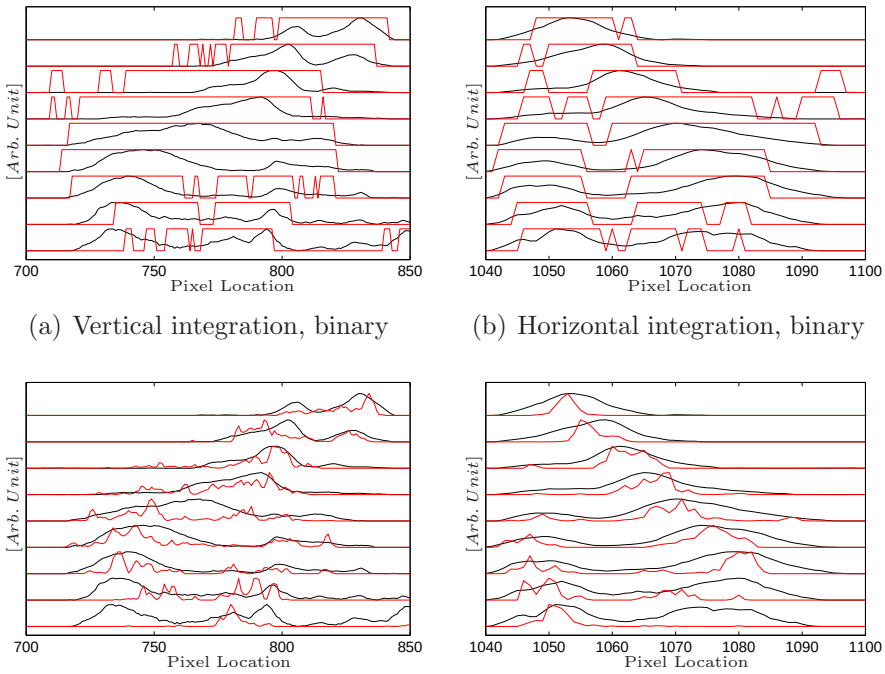

(a) Vertical integration, binary

(b) Horizontal integration, binary

(c) Vertical integration, estimated intensity

(d) Horizontal integration, estimated intensity

Figure 6.6: Vertical and horizontal intensity profiles from Fig. 6.4 and Fig 6.5. The stacking of profiles vertically indicates successive integration intervals. In all four figures, red indicates simulated intensity profile, and black indicates experimental results. (a), (b) Binarized integrated intensity profiles. (c), (d) Integrated intensity using Eq. (6.1) to estimate intensity contributions from each diffracted peak. It is shown in all four cases that diffraction spots and peak splitting are tracked across multiple integration intervals by the Forward Modeling reconstruction method.

It should be noted here that the experimental parameters are typically coupled in a non-trivial way as pointed out in Chapter 2. To account for parameter coupling, constrained optimizations of experimental parameters are performed. In the case of L-distance variations, all experimental parameters were allowed to optimize freely while the L-distance is constrained to below motor movement precision. This procedure is performed for the parameter studies. To be consistent with the rest of the chapter, all sensitivity studies are performed using the reference layer, $z16$ of state S1. To better quantify local orientation variations, a measure, the kernel averaged misorientation, is introduced.

Kernel Averaged Misorientation

Because local orientation variation tends to be small and difficult to see from the orientation maps, characterization of noise is done using a spatial orientation variation known as kernal averaged misorientation (KAM). Two-dimensional KAM maps show both geometrical features (structure and location) and a relative magnitude of deviation. Lines (in 2D) formed by orientation variations are indicative of low angle boundaries. The location and magnitude of KAM features are important for studying plastic deformation in that it serves to quantify deformation accumulation [72, 114]. Geometrical features extracted from KAM maps, such as low angle grain boundaries (LAGBs), delineate regions of subgrain formation, which serves as a path to direct comparison with deformation models [119, 41, 58]. Here, the KAM maps are used to characterize reconstruction sensitivity to experimental geometry.

In our case, kernel averaged misorientation, $K(\vec{x})$ is defined to be

$$K(\vec{x}) = \frac{\sum_i w_i(\vec{x_i}, \vec{x}) d(q(\vec{x_i}), q(\vec{x}))}{\sum_i w_i(\vec{x_i}, \vec{x})}, \tag{6.2}$$

where $q(\vec{x})$ is the orientation at location $\vec{x}$, $d(q, q')$ is misorientation defined in the usual way, and the summation is performed over the N-nearest neighbor points of $\vec{x}$. The weighting factor, $w(\vec{x}'\vec{x})$, is defined as

$$w(\vec{x}'\vec{x}) = \begin{cases} \frac{1}{|\vec{x}'-\vec{x}|} & \text{if } d(q(\vec{x}), q(\vec{x}')) \leq \theta_t \\ 0 & \text{otherwise.} \end{cases} \tag{6.3}$$

The resolution of the kernel averaged misorientation is controlled by selecting the number of nearest neighbors to be consistent with the resolving power of the setup. In our case, this is limited by $1.47\mu m$ pixel size of the detector system. It should be noted that the traditional definition of KAM in the EBSD literature does the $\frac{1}{|\vec{x}-\vec{x}'|}$ weighting factor. The point of using a weighting factor is to produce a metric that can be used across voxels of different resolutions.

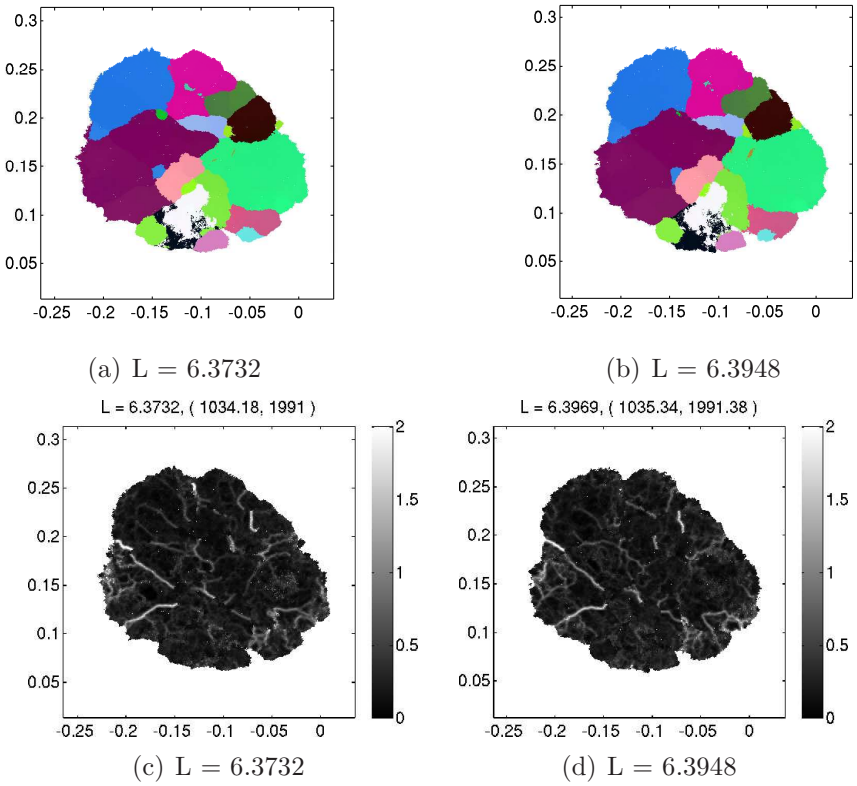

(a) L = 6.3732 (b) L = 6.3948

(c) L = 6.3732 (d) L = 6.3948

Figure 6.7: (a), (b) Orientation reconstruction for the same layer at two different optimized positions ($L_1 = 6.3732$ and $L_1 = 6.3948$). Orientations are represented by a mapping of the Rodriguez vector to RGB (red, green blue) colors. We notice that while small features (i.e., grain in green at the intersection of four other grains) and boundary locations differ across the two maps, the two reconstructions are largely similar. (c), (d): Comparison of local misorientation properties for the corresponding orientation maps. Notice again that qualitative features are similar.

Variations in L-distance

Reduction in measurement spatial sensitivity is expected due to the broader peaks in deformed samples. Two reconstructed orientation maps are produced from L-distances that are approximately $20\mu m$ apart. Note that the constrained local optimization at $L = 6.3948mm$ shifted the beam origin by approximately a pixel, or $1.47\mu m$ in the horizontal direction. This is well within the expected error in the optimization. Deviation of $20\mu m$ corresponds to a factor of 10 larger than the typical errors seen in measurements of well ordered materials; consequently, noticeable but minute changes in the grain boundary are expected and observed in Fig. 6.7 (a) and Fig. 6.7 (b). Meanwhile, orientation reconstruction errors are not typical for $\Delta L = 20\mu m$ in well-ordered samples. Overall, very little difference is seen in Fig. 6.7 (a) and Fig. 6.7 (b).

Kernel averaged misorientation maps are shown in Fig. 6.7 using $\theta_t = 5°$. The use of relatively low threshold is to focus the feature extraction on low angle boundaries. Because the KAM map gray scale is deliberately saturated at 2°, we can see the consistency in the locations of well-ordered regions (low KAM). Observe that some of the low angle boundaries extend through multiple grains; such structures are referred to as shear bands [53, 38].

Large scale features shown in both the orientation and kernel averaged misorientation map were found to remain observable as the L-distance is varied (figures 6.7). However, the spatial location of individual features tend to shift even for high angle grain boundaries. Thus, orientations in the sample are recovered, as evidenced by the orientation maps (Fig. 6.7), but the assignment of these orientations in the sample space vary noticeably when the $L-$distances changes. In other words, variations in L-distances directly alters sharp feature resolution of the reconstructed orientation map. This is not entirely surprising, as deviation of L-distances directly translates into spatial errors in the sample.

Variations in Diffraction Origin

In the HEDM setup, the planar cross section of the sample illuminated by the microfocused beam is responsible for the diffraction signal observed in the detector. Consequently, the diffraction origin is parameterized by the location (z) of the illuminated cross section. With a beam height of $6\mu m$ (FWHM of a Gaussian profile), the diffraction origin is not infinitely sharp; the measured diffraction signals comes from a region $z \in [z_0 - \delta z, z_0 + \delta z]$. This signal is "deconvolved" by the infinitely sharp origin at $z = 0$ used in the reconstruction. Consequently, variations in the scattering origin should lead to small changes in the reconstructed microstructure. This change is expected to be small due to two reasons. First, in the case of materials with large grain size, microstructures do change much over the length scale of a few microns. Secondly, small, sharply contrasting features of sub-micron size tend not to generate a large amount of diffraction signal, as diffracted intensity is proportional to

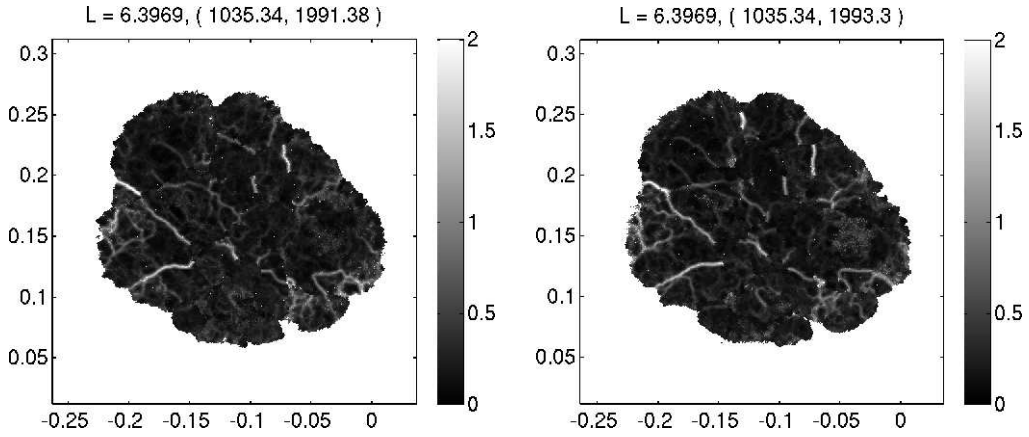

(a) Pixel $k = 1991.38$ (b) Pixel $k = 1993.3$

Figure 6.8: Kernel averaged misorientation computed for reconstructions with the beam origin at different detector pixel k locations ($\approx 3\mu m$ difference in the z direction). This is equivalent to vertical sample position. Note that both reconstructions are done at $Q_{max} = 12\mathring{A}^{-1}$

the volume. A test result can be seen by comparing the Fig. 6.8(a) and Fig. 6.8(b), where only very subtle differences can be seen between the two KAM maps.

Variations in Q_{max}

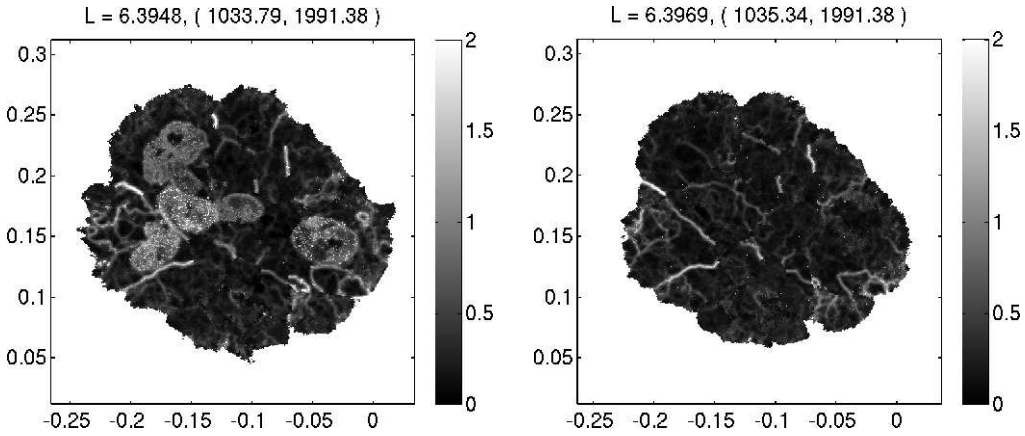

(a) $Q_{max} = 10\mathring{A}^{-1}$ (b) $Q_{max} = 12\mathring{A}^{-1}$

Figure 6.9: Kernel averaged misorientation computed for reconstructions at different Q_{max} and diffraction origin. (a) $Q_{max} = 10\mathring{A}^{-1}$. (b) $Q_{max} = 12\mathring{A}^{-1}$.

Major differences can be seen in the KAM maps between the reconstruction using $Q_{max} = 10\mathring{A}^{-1}$ and $12\mathring{A}^{-1}$ (Fig. 6.9), but their corresponding orientation maps remain very similar (not shown). For copper, with a lattice constant of $a = 3.61\mathring{A}$, $q_{100} \equiv \frac{2\pi}{a} = 1.74\mathring{A}^{-1}$. Thus $Q_{max} = 10\mathring{A}^{-1}$ corresponds to $\sqrt{h^2+k^2+l^2} = 5.74$, whereas at $Q_{max} = 12\mathring{A}^{-1}$, $\sqrt{h^2+k^2+l^2} = 6.89$. The key feature seen here is the appearance of regions with large local orientation variations. This suggests that the orientations in the higher Q_{max} reconstruction may have converged. Because the number of peaks fitted increased between $Q_{max} = 10\mathring{A}^{-1}$ and $12\mathring{A}^{-1}$, significant reduction in orientation noise is expected. Analysis similar to that seen in Sec. 6.4.1 suggests that simulated higher order peaks are indeed consistent with the experiment. It should be noted that the maximum number of peaks observed is highly dependent on the material, as scattered intensity tends to drop off sharply as a function of Q. The difference in scattering intensity between the [100] and [800] peak could easily be more than the dynamic range of the detector. Since reconstruction time is proportional to the number of peaks fitted per voxel, judicious choice of Q_{max} is necessary to optimize computation time and reconstruction accuracy. In present case, we have found $Q_{max} = 12\mathring{A}^{-1}$ to be optimal.

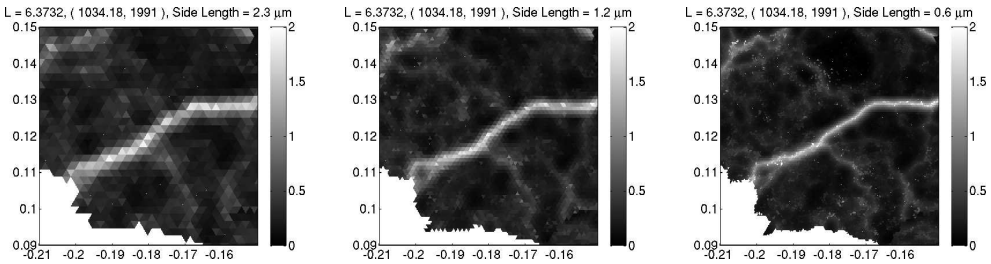

(a) $s = 2.4\mu m$ (b) $s = 1.2\mu m$ (c) $s = 0.6\mu m$

Figure 6.10: Aliasing effects are reduced as sampling rate is increased. As spatial resolution is increased from (a) to (c), sharpening of boundaries is observed. More importantly, the KAM features seem to be converging with the increase of spatial resolution, with no large ($\geq 2.4\mu m$) feature in (b) that is missing in (a). These reconstructions all use $Q_{max} = 12\mathring{A}^{-1}$.

Variations in spatial resolution.

A systematic study was performed on the reconstruction as a function of sample space element, or voxel, size. In general, the minimum resolution of reconstructed features is limited by voxel size. The practical lower bound on this size is typically considered to be the effective pixel size on the detector. However, as pointed out in the last section, sample space resolution is also limited by Q_{max}, so optimization of these two parameters is coupled. With $Q_{max} = 12\mathring{A}^{-1}$, we see in Fig. 6.10 (a) and (b) that reducing the voxel size from $2.4\mu m$ to $1.2\mu m$ (with detector pixels of $1.47\mu m$) does indeed improve definition of features.

Because in any kind of imaging system, pixelation distorts reconstructed features, a so-called "super-resolution" study at half the detector pixel size was performed, as seen in Fig. 6.10(c). Note that each diffraction signal is a projection of a region of the microstructure onto the detector. Since each region generates 100 to 150 such peaks, the measurement samples each region this many times. This is analogous to super-sampling of a spatially continuous intensity signal. Because of the high sampling rate, one can expect features to be resolved to better than the detector resolution. This effect is rather clearly seen in comparing Fig. 6.10(a) to Fig. 6.10(c). The fact that geometrical features converge with increasing resolution is important, as it indicates the reconstruction algorithm is stable (i.e. orientations do not vary wildly around the neighborhood of the solution).

6.5 Results

By comparing the reconstructed orientation maps of the reference layers (layer 16 of state S1, Fig. 6.11) across the first three strain states, we have measured the microstructure evolution of the copper sample under uni-axial tension. Texture evolution of the three states is quantified by inverse pole figures (Fig. 6.12), and lattice rotations are detected between strain states S1 and S2. This is confirmed by a point-to-point misorientation calculation between layer z16 of S1 and its equivalent in S2 (Fig. 6.13). Finally, taking advantage of the high fidelity orientation maps, a spatially resolved lattice rotation map is produced. This is the first ever spatially resolved measurement of texture evolution of an *in situ* deformed sample.

6.5.1 Lattice Rotations

Evolution of [001] Inverse Pole Figure

Lattice rotation is expected during plastic deformation. Traditionally, measurement of lattice rotations is limited to statistical measurements, represented by inverse pole figures of the [001] axis obtained from analyzing measured X-ray diffraction data from a statistical distribution of grains. Since we have measured orientations of grains in the z16 layer, we can generate pole distributions for each state. The crystal axis,

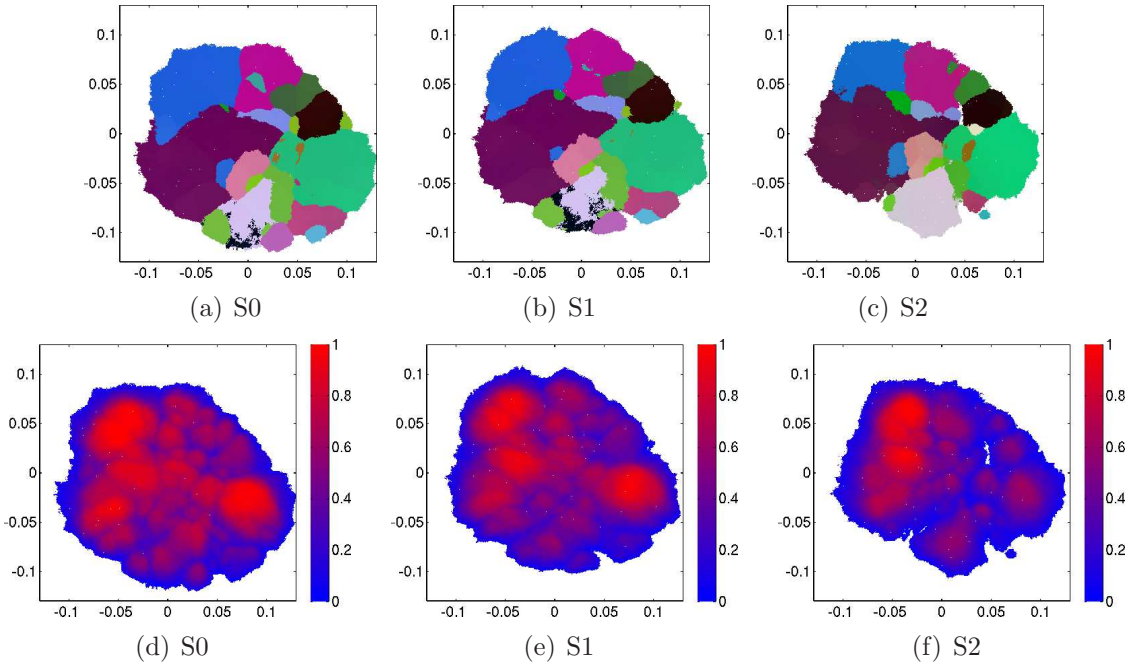

Figure 6.11: (a) - (c) Reconstructed orientation maps for the reference layer of states S0, S1, and S2. Changes in the grain boundaries can be attributed to deformation induced microstructure evolution, but quantitative comparison of geometrical features is difficult due to alignment issues. Texture evolution is observed by comparing the point-to-point misorientation of these three reconstructed maps. (d) - (f) Confidence maps showing the goodness-of-fit for the reconstructed orientations. Degradation of fit quality along the grain boundaries is expected, but marked changes are seen between (e) and (f), resulting in a "hole" in the orientation map. This hole indicates that the diffractions originating from this region have unusually low signal-to-noise ratios.

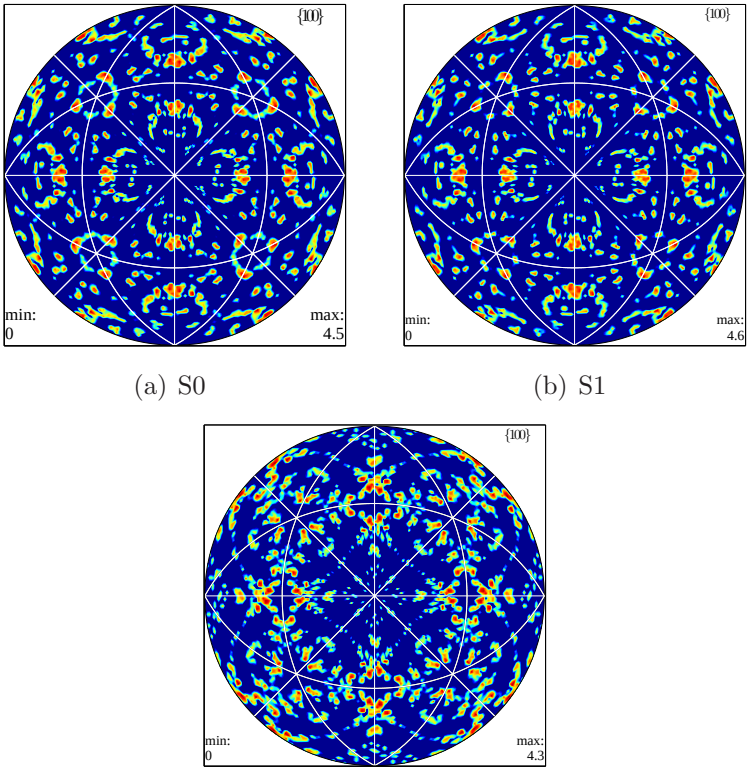

(a) S0 (b) S1

(c) S2

Figure 6.12: Distribution of [001] *crystal axis in the sample frame for the layers corresponding to z16 S1 across all three states. Color represents multiples of random, plotted in* log_{10} *scale.*

[001] in the sample frame, is projected onto a 2D plane, and its distribution is plotted as densities for states S0, S1, and S2, as shown in Fig. 6.12. Lattice rotations are deduced from changes between the different inverse pole figures. Note that the relatively few sharp peaks are due to the small number of grains in the cross section of the sample. As expected from our load curve (Fig. 6.1(d)), little change occurred between the initial and first strain states. In contrast, the second strain state (S2) shows marked differences from S1. A subtle increase of density towards the [110] direction is noticeable, which is consistent with the Bishop and Hill model[41]. The drawback of this pole figure analysis is that without directly tracking individual grains as in the case of ref [89], it is difficult to see what specifically the lattice rotations are, which is crucial for model comparisons.

Spatially Resolved Lattice Rotation

With the use of near-field HEDM, spatially resolved lattice rotations can be measured across different strain states. This is achieved by first aligning orientation maps from different strain states with each other, then performing a point-to-point misorientation calculation. As before, all analysis is referenced against layer 16 of state S1 (z16S1).

Because noticeable sample movement occurred between different strain steps, orientation maps measured at different states do not align exactly. In some cases, measurement planes may not even be parallel to within our measurement precision. Therefore an alignment procedure is necessary before carrying out a point-to-point misorientation calculation. Assuming that not all grains within the sample would rotate the same way, the basis of the alignment is simply to minimize the total misorientation between two different maps. To improve the reliability of the alignment, only voxels with confidence above a threshold, in this case $\mathcal{C}_t = 0.4$ are used for the alignment. A zero temperature Monte Carlo method was used for the alignment optimization. To ensure an optimal match, the alignment procedure was performed on neighboring layers as well, but only the best matched layers are shown in this analysis.

The point-to-point misorientation maps are seen in Fig. 6.13. Only voxels with $\mathcal{C} \geq 0.4$ are included, and misorientations above 15° are excluded in this plot, as they indicate shifts in the grain boundaries. As expected, little or no change can be observed between states S0 and S1, but significant change is seen between S1 and S2. We observe that the amount of rotation is non uniform across the cross section and within each grain. The variations are typically slowly varying within a gain, but discontinuous across grain boundaries. This is, presently, the first *in situ* observation of such spatially resolved rotations.

The misorientations seen between S1 and S2 are much larger than systematic errors of the reconstruction. Moreover, the variations in the angle of lattice rotation seem to have spatial structures. One way to compare the difference in the amount of lattice rotations between steps of S0 to S1 and S1 to S2 is to look at the distri-

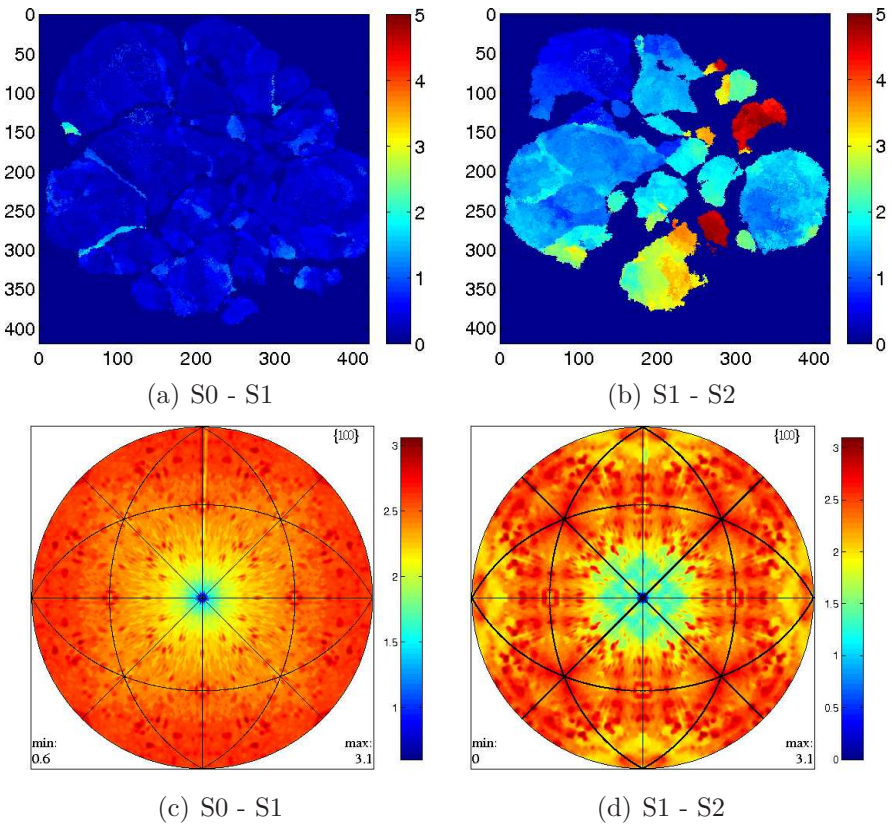

(a) S0 - S1 (b) S1 - S2

(c) S0 - S1 (d) S1 - S2

Figure 6.13: (a), (b) Spatially resolved grain rotation across successive states (S0 to S1, and S1 to S2). The false color represents the magnitude of rotation from one state to the other on a 5° scale. Both images are created first by registering two layers across the two states through minimization of total misorientation. Because the sample both stretched and moved across different states, exact registration is impossible. Only lattice rotation below 5° is shown here to remove misorientation due to boundary shifts between different states. (c), (d) A distribution symmetrizing the projection of the rotation axis from (a) and (b) to the $x-y$ plane of the sample frame, measured in multiples of random. The number of rotation axes along the [001] sample direction (the tensile axis, out of the page) is markedly less than along any other directions.

bution of rotation angles. Here, the misorientation is represented by the axis-angle parameterization $(\hat{n}, \theta)$, and the distribution of the angle θ is shown in Fig. 6.14. The point-to-point misorientation for maps from S1 to S2 with only spatial alignment is also shown (unoptimized). Since no minimization of total misorientation was done in the "unoptimized" case, the distribution of rotation angle is shifted to the right from the optimized version as expected, and thus can be considered as an upper bound. Even in the optimized case, the lattice rotation is significant; its distribution of rotation angle shifted drastically from that of strain step S0 to S1. Note that the majority of the lattice rotations between states S0 and S1 are close to the limit of our detection resolution.

A small population of voxels were rotated by 60° between each pair of strain states. This could correspond to twin formation during plastic deformation, which is known to occur in copper [123, 53, 17]. The population is relatively small, and since a significant amount of twin related grain boundaries already exist in the original microstructure, a good portion of this signal may be due to boundary movement contamination.

To better quantify the character of the lattice rotations, an inverse pole figure of the rotation axis that each voxel is rotated about is plotted in Fig. 6.13(c) and 6.13(d). This is done by representing the misorientation measured in axis-angle pairs, $(\theta, \hat{n})$, and rotating the axis into the initial sample frame. The distributions are plotted in $\log_{10}$ scale of multiples of random to better visualize the structure. Because little has happened between state S0 and S1, most of what is seen in the pole figure is likely to be noise dominated artifacts. From states S1 to S2, the distribution of the rotation axis is clearly shifted away from the [001], or the tensile axis direction (center of pole figure). This is consistent with the fact that torque around the tensile direction should be close to zero. Geometrical alignment between orientation maps of different states also supports this observation.

The movement of the tensile axis $(\hat{z})$ in the crystal frame seen in Fig. 6.12 can be quantified as the difference vector $\delta\hat{z} = \mathbf{O}_1(\vec{x})\hat{z} - \mathbf{O}_0(\vec{x})\hat{z}$, where $\mathbf{O}_1(\vec{x})$ and $\mathbf{O}_2(\vec{x})$ are the orientations of the states located at $\vec{x}$ in the crystal frame. Projection of this vector into the $x - y$ plane is shown in Fig. 6.15(a). The Taylor-Bishop-Hill model suggests the migration of the tensile axis away from the [110] and towards the [001] and [111] directions [41], as is seen in the figure. Some small number of grains deviating from this trend are also observed. This is not entirely surprising, as the tensile load direction is not uniform due to our sample shape (6.1(c)), and the applied stress is far from uni-axial across the thin wire sample.

It should be noted here that in contrast to the studies done in [89], each point in Fig. 6.15(a) is a separate voxel rather than averaged motion of a grain. In general, grain neighborhood and location information are crucial to the understanding of deformation evolution; hence measurements of statistical texture evolution will not suffice. However, because of HEDM's unique ability to spatially resolve orientation points, lattice rotations can be spatially resolved on an intra-granular scale, as shown

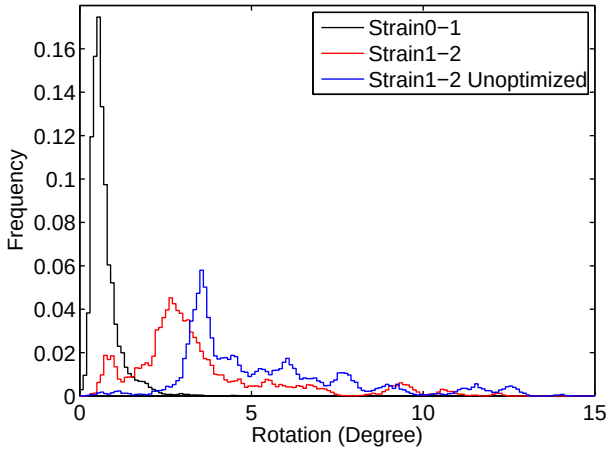

(a) S1 - S2

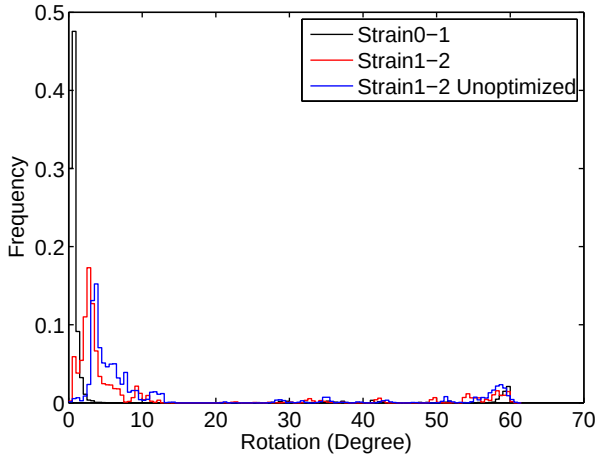

(b) S1 - S2

Figure 6.14: Distribution of the magnitude of lattice rotation between the different strain states at different bin sizes. Marked difference can be observed in the angle distribution between states. (a) and (b) show the same data sets on different horizontal scales. To demonstrate the effects of registration by minimization of misorientation, the unoptimized lattice rotation distribution is also plotted.

in Fig. 6.15(b). While generally speaking, lattice rotations in the same grain (indicated by connected regions of similar colors in Fig. 6.11) tend to follow the same direction, exceptions are observed in at least one of the grains (green in Fig. 6.11). Here, it can be seen that lattice rotation directions are almost perpendicular to each other. While there could still be systematic errors in the sample alignment unaccounted for by the current optimization algorithm, it would be difficult to produce a lattice rotation variation as seen in this grain.

6.6 Conclusions

We have demonstrated the capability of near-field HEDM to measure damage accumulation in a high purity copper wire. We have shown that the forward modeling reconstruction method is capable of tracking diffraction peaks even from grains with significant moasicity. Even without the explicit use of intensity in the reconstruction, reasonably good agreement between simulated and experimental diffraction patterns is still obtained. From our systematic study, we have shown empirically that the forward modeling method is stable, in that small variations in reconstruction parameters do not lead to catastrophic failure in the resulting output. Moreover, fitted orientation maps are shown to converge with increasing reconstruction spatial and orientation resolutions. This convergence behavior is evidenced by reduced orientation noise and aliasing artifacts.

With the help of a sample alignment optimization procedure, we have been able to measure microstructure evolution across three strain states. The microstructure evolution is observed to be similar within most of the grains, as evidenced by the similar lattice rotations. However, an exceptional grain has contrasting orientation evolution. This is not entirely surprising considering the non-uniform load condition resulting from the non-trivial sample shape. To the best of the author's knowledge, this is the first nondestructive, spatially resolved orientation evolution measurement done in a bulk sample.

6.7 On-going and future work

Analysis covered in this chapter currently does not take advantage of the three-dimensional nature of the volumetric orientation maps. To address this problem, on-going effort is placed on both analysis and alignment software development. While it is relatively easy to produce volumetric orientation maps for the earlier strain states, the quality of reconstructed maps deteriorates drastically as the sample approaches ductile failure, and as layers close to the center of the neck are considered. This is due both to the rapidly decreasing grain size, which leads to extremely low signal to noise ratio, as well as increasingly long computation time for reconstructions. Current developments of intensity and strain fitting capabilities will certainly help address

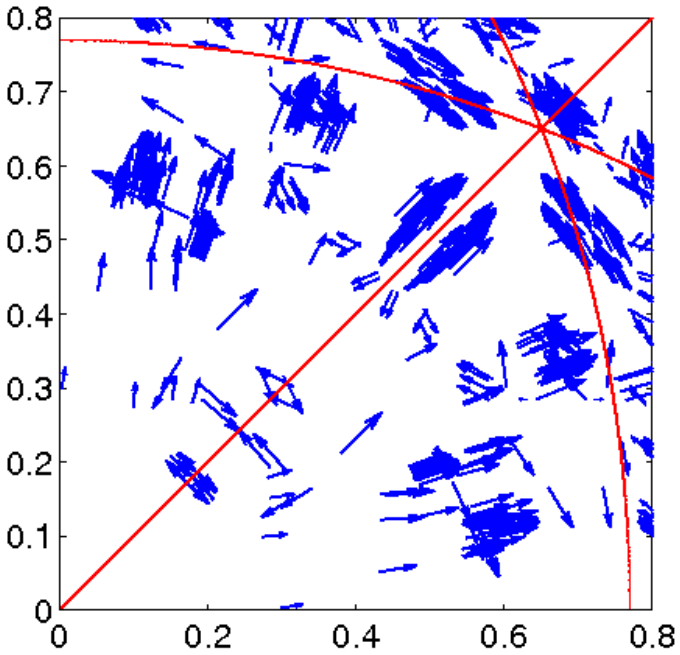

(a) Lattice Rotation

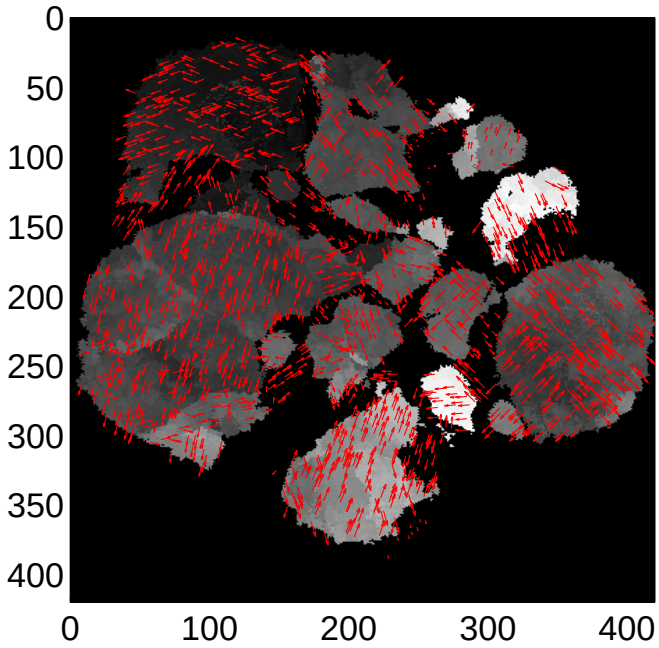

(b) Spatially Resolved Lattice Rotation

Figure 6.15: (a) Lattice rotation of random points selected from the point-to-point misorientation. Here, the lattice rotation is represented by the movement of the tensile axis in the crystal frame, plotted in the usual stereological triangle. (b) Spatially resolved lattice rotation showing the tensile axis movement at each point in the sample space.

some of the worries regarding the uncertainties in the reconstructed orientations. Improvements in signal extraction from raw diffraction images will help remove the ω varying diffuse background from the Macor sample housing. At this point, sensitivity studies are tedious, and it will remain so until more robust theoretical understanding of the reconstruction is achieved.

Coupled with tomographic reconstructions, it is in principle possible to track the origin of void nucleation observed in the experiment (not shown). This would require better alignment optimization to help pinpoint the subvolume of orientation image map surrounding the void position from the earlier strain states. This turns out to be surprisingly difficult, as the deformation rate for the specimen is not uniform. Computational simulations, such as finite element models, may be necessary even for this alignment exercise.

Because we have essentially the same volume of data across multiple strain states, it would be extremely interesting to use this data for calibration and validation of computational models. As the simplest case, the initial state (S0) may be applied as the input to different computational models, which then could be evolved and compared against the experimental results. Such comparisons have been historically difficult due to the very limited access to spatially resolved orientation maps. On-going effort has been focused on the application of a viscoplasticity model [58] on the current data set, and interesting qualitative initial results are already being generated.

Appendix A

Examples of Reconstructed Orientation Maps

Some of examples of reconstructed orientation maps are presented here to demonstrate a recent experiment in applying HEDM to the *in situ* measurement of the structural phase transition in a magneto-caloric material (NiMnGa).

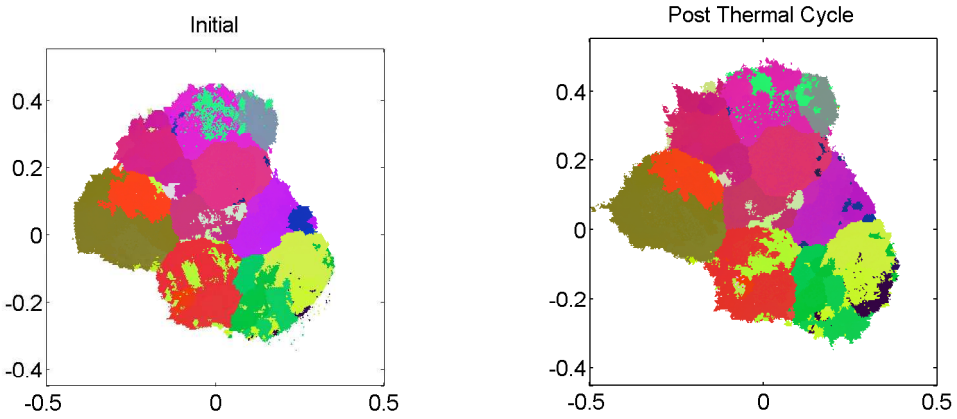

(a) (b)

Figure A.1: Reconstructed orientation maps for the same layer of NiMnGa before (a) and after (b) thermal cycling. Distance is measured in unit of millimeters. False color indicates orientations in the tetragonal fundamental zone. Very minute changes are detected between the two maps. This is attributed to the disconnectedness of each grain as shown in Fig. A.4.

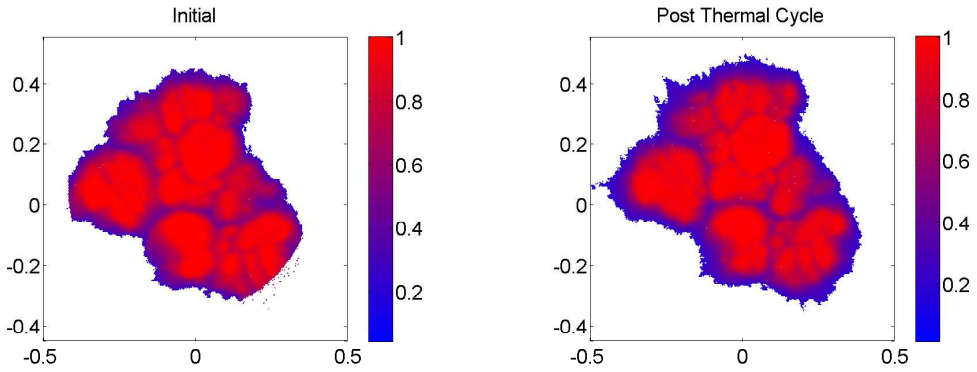

(a) (b)

Figure A.2: Confidence map for the two layers shown in Fig. A.1. The region of low confidence is confirmed to be void by the tomographic reconstruction seen in Fig. A.4. Hints of crack formation after thermal-cycling is seen by comparing the bottom right of (a) and (b), but confirmation requires a full three-dimensional map (not currently available).

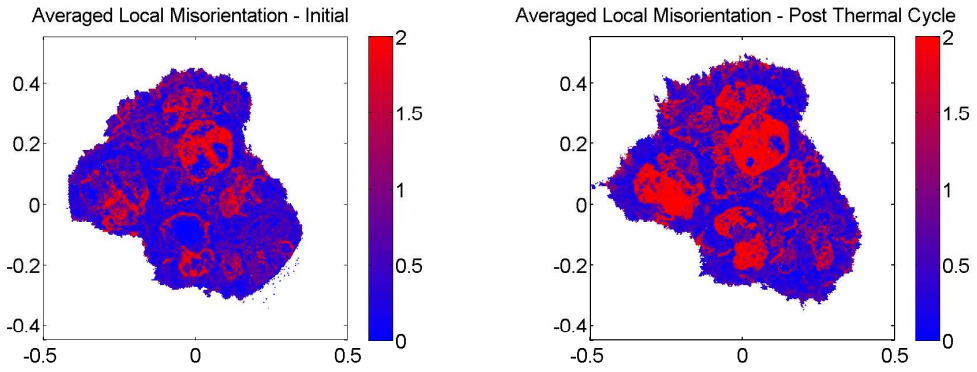

(a) (b)

Figure A.3: Kernel averaged misorientation (KAM) for each of the maps in Fig. A.1. Deformation is expected to scale with local misorientation, thus resulting in higher KAM. The relatively higher KAM and more concentrated KAM values seen here suggest that local deformations is manifested as mosaicity in the orientation of each grain.

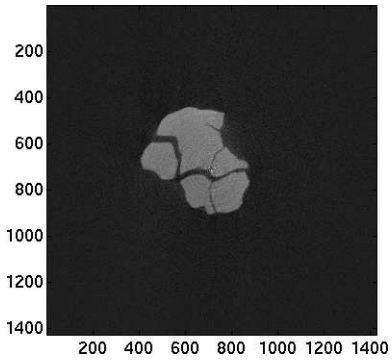

Figure A.4: Reconstruction from X-ray transmission tomography. Scale is shown here as pixels (1.48μm side length). Lighter color is used to indicate regions of high density. The black curves indicate that the sample contains grains that are not in contact at the layers we have imaged.

Appendix B

Reconstructed Surface Meshes

Some reconstructed grain boundary meshes are shown here, and they serve to demonstrate the capabilities of the methods developed in Chapter 4. The orientation maps used for these boundary reconstructions are the same as the ones in the analysis of Chapter 5. Boundary motion analysis from these surface meshes is used for boundary motion estimates.

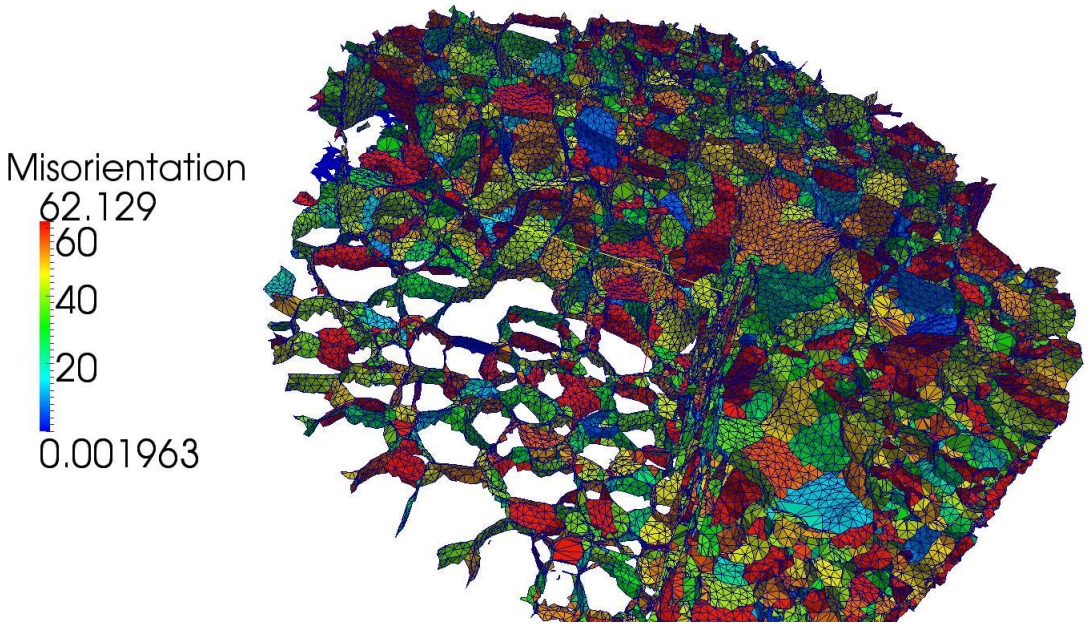

Figure B.1: Grain boundary surface mesh for the initial state of the nickel sample described in Chapter 5. Boundary colors correspond to misorientation in degrees. A corner of the surface mesh is cut away to better show the smoothness of the boundaries.

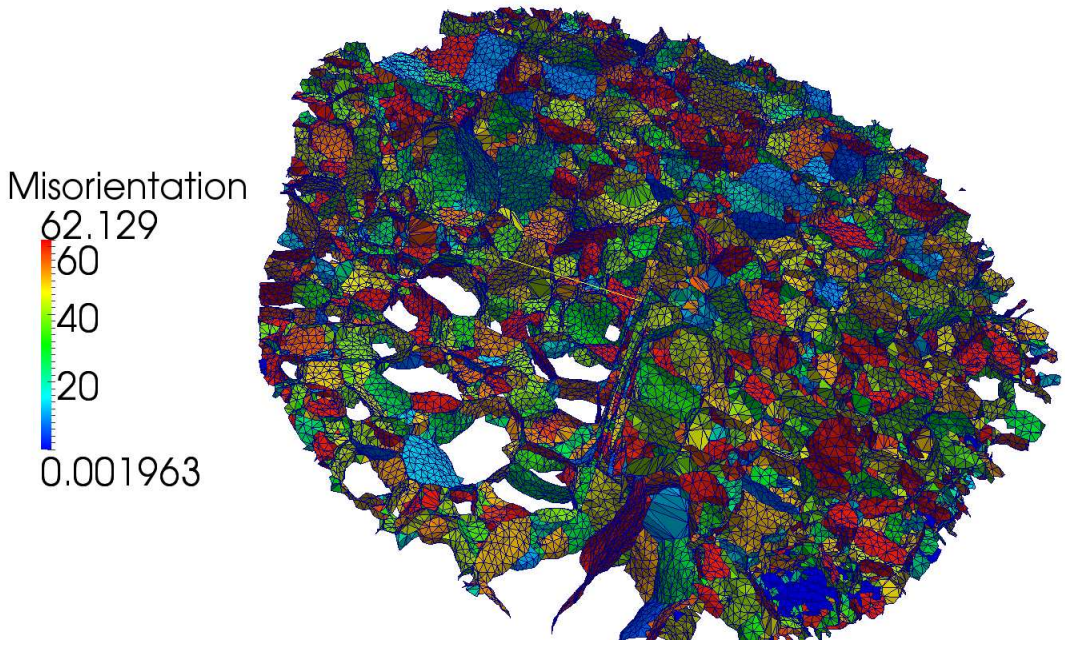

Figure B.2: Grain boundary surface mesh for the first anneal state. Little or no changes is noticeable between the meshes shown here and Fig. B.1, as evidenced by the analysis in Chapter 5.

Appendix C

Volumetric Map Examples

The methods described in Chapter 4 and [3] simultaneously produce a surface and a volumetric mesh, and some of the results are shown here. Recall that the volumes shown are the measurements of the same region of the nickel sample at different anneal states. Grain volume estimates are done by counting the number of tetrahedra in each of the grain. The mean-width calculation also takes advantage of the volume mesh to decide the sign of the surface patch normals. While the volumes shown (Fig. C.1, Fig. C.2, Fig. C.3, Fig. C.4) are not aligned, it is seen that the grain sizes are generally increasing with the later anneals. Sharp "edges" can be found along some of the grains, and these features extend vertically in the direction perpendicular to measurement slices (z). This is a good indication of the consistency in the HEDM technique.

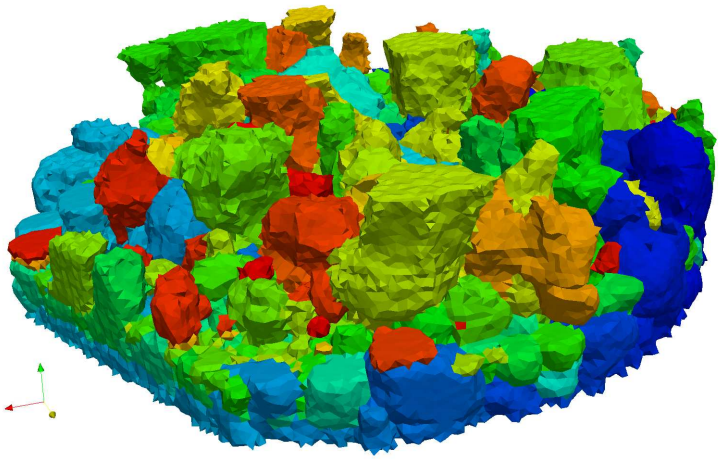

Figure C.1: Initial state of the high purity nickel volume. Each grain ID is associated with a false color (RGB) value.

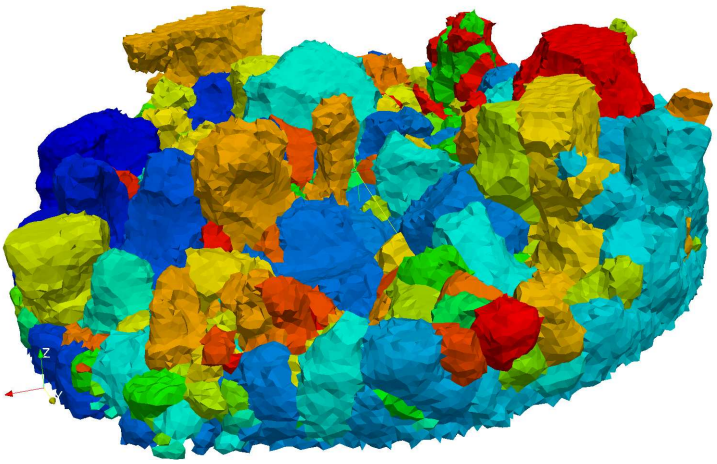

Figure C.2: First anneal state. No noticeable changes can be seen. (Recall that the volumes presented are not yet aligned.)

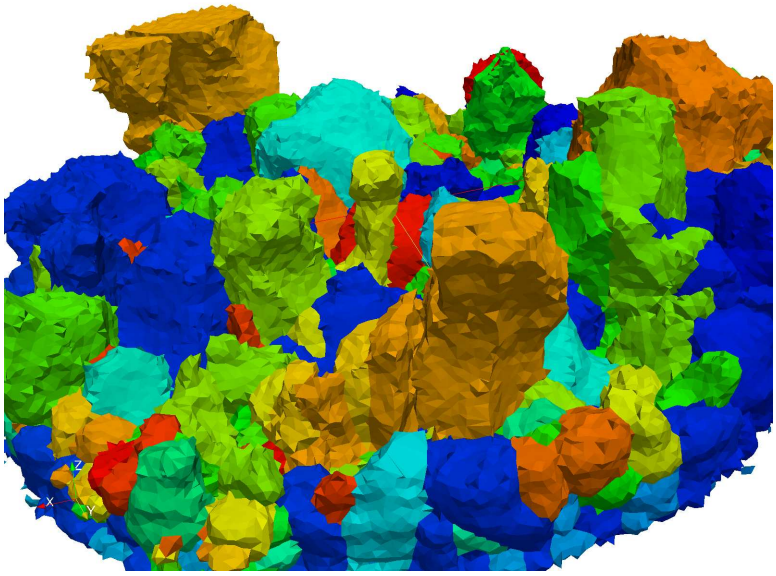

Figure C.3: Second anneal. Grains can be seen to be markedly smoother.

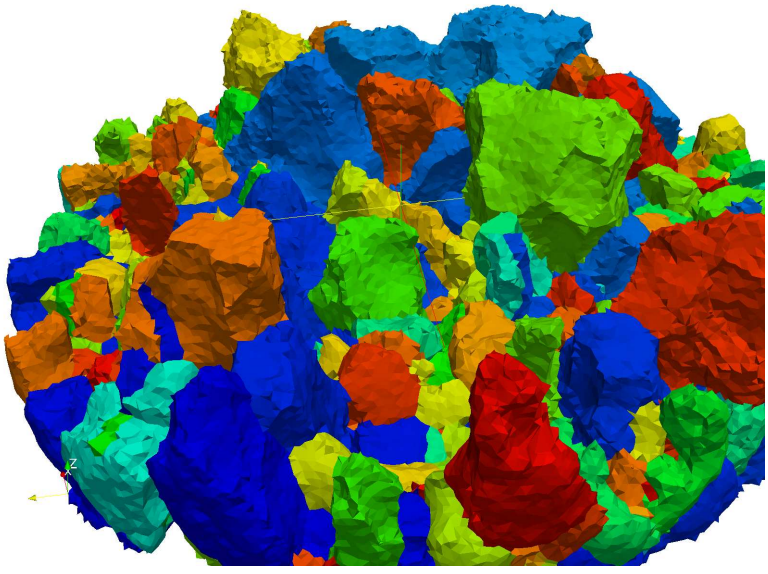

Figure C.4: Third anneal state. Some number of annealing twins can be seen as thin, plate-like grains in the volume (red on the left, blue near the middle inside a grain).

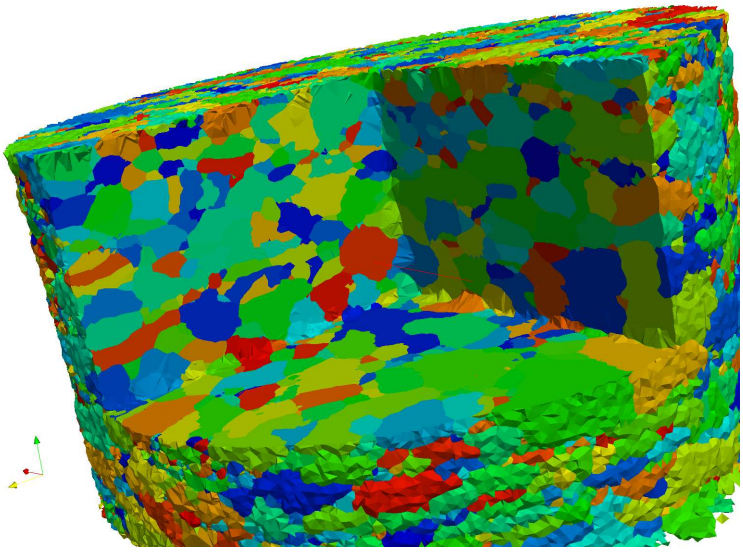

Figure C.5: Three-dimensional grain map of a piece of copper, used as an initial state for an upcoming deformation experiment in collaboration with Los Alamos National Lab. The imaged section of the specimen is). $1.1mm$ *in diameter and* $0.760mm$ *in height. A total of* 11999 *grains were identified.*

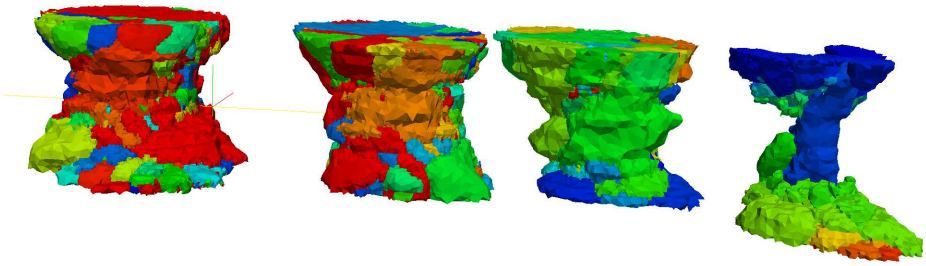

Figure C.6: Progression of a piece of copper wire under uni-axial tension (data from Chapter 6). Starting from left to right, the true strain reads 0%, 0% *(to within sensitivity),* 6.2%, *and* 26.9%. *False color again indicates identified grains (IDs are not related between different states). We caution that this is result from the preliminary analysis, and it is presented here to show some of the cutting-edge applications of HEDM.*

Bibliography

[1] CGAL, Computational Geometry Algorithms Library. http://www.cgal.org. 1.2, 5.3.3

[2] P. Alliez, D. Cohen-Steiner, M. Yvinec, and M. Desbrun. Variational tetrahedral meshing. In *ACM SIGGRAPH 2005 Courses*, SIGGRAPH '05, New York, NY, USA, 2005. ACM. 4.3.1

[3] P. Alliez, L. Rineau, S. Tayeb, J. Tournois, and M. Yvinec. 3D mesh generation. In *CGAL User and Reference Manual*. CGAL Editorial Board, 3.8 edition, 2011. http //www.cgal.org/Manual/3.8/doc_html/cgal_manual/packages.html#Pkg Mesh_3. 1.3, 4.3.1, 4.3.3, 3, 4.3.3, C

[4] J. Als-Nielsen and D. McMorrow. *Elements of Modern X-Ray Physics*. Wiley, 2001. 2.2.1, 2.2.1

[5] N. Amenta and M. Bern. Surface reconstruction by voronoi filtering. In *Proceedings of the fourteenth annual symposium on Computational geometry*, SCG '98, pages 39–48, New York, NY, USA, 1998. ACM. 4.3.3, 4.3.3, 3

[6] N. Amenta, M. Bern, and M. Kamvysselis. A new voronoi-based surface reconstruction algorithm. In *Proceedings of the 25th annual conference on Computer graphics and interactive techniques*, SIGGRAPH '98, pages 415–421, New York, NY, USA, 1998. ACM. 4.3.2, 4.3.2, 4.3.2, 4

[7] K. Barmak, E. Eggeling, M. Emelianenko, Y. Epshteyn, D. Kinderlehrer, R. Sharp, and S. Ta'asan. Critical events, entropy, and the grain boundary character distribution. *Phys. Rev. B*, 83(13):134117, Apr 2011. 5.4.1, 5.5

[8] J.-D. Boissonnat and S. Oudot. Provably good sampling and meshing of surfaces. *Graphical Models*, 67(5):405 – 451, 2005. Solid Modeling and Applications. (document), 4.3.2, 4.3.2, 4.3.2, 4, 4.7, 4.3.3, 4.3.3

[9] D. Boltcheva, M. Yvinec, and J.-D. Boissonnat. Mesh generation from 3d multi-material images. In G.-Z. Yang, D. Hawkes, D. Rueckert, A. Noble, and C. Taylor, editors, *Medical Image Computing and Computer-Assisted Intervention MICCAI 2009*, volume 5762 of *Lecture Notes in Computer Science*, pages 283–290. Springer Berlin / Heidelberg, 2009. 1.3, 4.2.2, 4.3.1, 4.3.3, 4.3.3, 4.3.3, 5.3.3

[10] J. D. Budai, W. Yang, N. Tamura, J.-S. Chung, J. Z. Tischler, B. C. Larson, G. E. Ice, C. Park, and D. P. Norton. X-ray microdiffraction study of growth modes and crystallographic tilts in oxide films on metal substrates. *Nature Materials*, 2(7):487–492, July 2003. 1.1

[11] R. A. Camps, J. E. Evetts, B. A. Glowacki, S. B. Newcomb, R. E. Somekh, and W. M. Stobbs. Microstructure and critical current of superconducting $YBa_2Cu_3O_{7-x}$. *Nature*, 329(6136):229–232, Sep 1987. 1.1

[12] P. Chaudhari, F. K. LeGoues, and A. Segmüller. The microstructure of high-critical current superconducting films. *Science*, 238(4825):342–344, 1987. 1.1

[13] S.-W. Cheng, T. K. Dey, H. Edelsbrunner, M. A. Facello, and S.-H. Teng. Silver exudation. *J. ACM*, 47:883–904, September 2000. 4.4.3

[14] S.-W. Cheng, T. K. Dey, and J. A. Levine. A practical delaunay meshing algorithm for a large class of domains*. In M. L. Brewer and D. Marcum, editors, *Proceedings of the 16th International Meshing Roundtable*, pages 477–494. Springer Berlin Heidelberg, 2008. 10.1007/978-3-540-75103-8_27. 3

[15] S.-W. Cheng, T. K. Dey, and E. A. Ramos. Delaunay refinement for piecewise smooth complexes. In *Proceedings of the eighteenth annual ACM-SIAM symposium on Discrete algorithms*, SODA '07, pages 1096–1105, Philadelphia, PA, USA, 2007. Society for Industrial and Applied Mathematics. 4.3.2, 4, 3

[16] L. P. Chew. Guaranteed-quality mesh generation for curved surfaces. In *Proceedings of the ninth annual symposium on Computational geometry*, SCG '93, pages 274–280, New York, NY, USA, 1993. ACM. 4.3.2, 4.3.2

[17] J. W. Christian and S. Mahajan. Deformation twinning. *Progress in Materials Science*, 39(1-2):1 – 157, 1995. 6.5.1

[18] P. Dawson and D. Boyce. Private communications, 2008. (document), 3.5.5, 3.6

[19] M. de Berg, O. Cheong, M. van Kreveld, and M. Overmars. *Computational Geometry: Algorithms and Application*. Springer, 2008. 2

[20] P. de Bruin, F. Vos, F. Post, S. Frisken-Gibson, and A. Vossepoel. Improving triangle mesh quality with surfacenets. In S. Delp, A. DiGoia, and B. Jaramaz, editors, *Medical Image Computing and Computer-Assisted Intervention MICCAI 2000*, volume 1935 of *Lecture Notes in Computer Science*, pages 69–102. Springer Berlin / Heidelberg, 2000. 4.3.2, 4.3.3, 4.4.3

[21] S. R. Deans. *The Radon Transform and Some of Its Applications*. Dover Publications, 2007. 3.3

[22] M. C. Demirel, A. P. Kuprat, D. C. George, and A. D. Rollett. Bridging simulations and experiments in microstructure evolution. *Phys. Rev. Lett.*, 90(1):016106, Jan 2003. 5.1

[23] M. Desbrun, M. Meyer, P. Schröder, and A. H. Barr. Implicit fairing of irregular meshes using diffusion and curvature flow. In *Proceedings of the 26th annual conference on Computer graphics and interactive techniques*, SIGGRAPH '99, pages 317–324, New York, NY, USA, 1999. ACM Press/Addison-Wesley Publishing Co. 4.3.1

[24] T. Dey and J. Sun. Normal and feature approximations from noisy point clouds. In S. Arun-Kumar and N. Garg, editors, *FSTTCS 2006: Foundations of Software Technology and Theoretical Computer Science*, volume 4337 of *Lecture Notes in Computer Science*, pages 21–32. Springer Berlin / Heidelberg, 2006. 4.3.1, 4.3.2, 3

[25] T. K. Dey. *Curve and Surface Reconstruction*. Cambridge University Press, 2006. 4.3.1, 4.3.2, 4, 3

[26] S. J. Dillon and G. S. Rohrer. *Three-Dimensional FIB-OIM of Ceramic Materials*, pages 117–124. John Wiley & Sons, Inc., 2008. 1.1, 4.1, 5.1

[27] S. J. Dillon and G. S. Rohrer. Characterization of the grain-boundary character and energy distributions of yttria using automated serial sectioning and ebsd in the fib. *Journal of the American Ceramic Society*, 92(7):1580–1585, 2009. 1.1, 4.1, 5.1, 5.4.1

[28] D. Dimiduk, M. Uchic, and T. Parthasarathy. Size-affected single-slip behavior of pure nickel microcrystals. *Acta Materialia*, 53(15):4065 – 4077, 2005. 6.3.3

[29] D. J. Durian, D. A. Weitz, and D. J. Pine. Scaling behavior in shaving cream. *Phys. Rev. A*, 44(12):R7902–R7905, Dec 1991. 5.1

[30] P. Feltham. Grain growth in metals. *Acta Metallurgica*, 5(2):97 – 105, 1957. 5.4.1

[31] M. Frary and C. A. Schuh. Percolation and statistical properties of low- and high-angle interface networks in polycrystalline ensembles. *Phys. Rev. B*, 69(13):134115, Apr 2004. 4.2.1

[32] M. E. Frary and C. A. Schuh. Correlation-space description of the percolation transition in composite microstructures. *Phys. Rev. E*, 76(4):041108, Oct 2007. 4.2.1

[33] H. J. Frost. Stochastic models of grain growth. *Materials Science Forum*, 94-96:903–908, 1992. 5.4.1

[34] M. E. Glicksman. Capillarity-mediated grain growth in 3-d. *Materials Science Forum*, 476-470:1025–1032, 2004. 5.4.3

[35] J. R. Greer, W. C. Oliver, and W. D. Nix. Size dependence of mechanical properties of gold at the micron scale in the absence of strain gradients. *Acta Materialia*, 53(6):1821 – 1830, 2005. 6.3.3

[36] G. S. Grest, M. P. Anderson, and D. J. Srolovitz. Domain-growth kinetics for the q-state potts model in two and three dimensions. *Phys. Rev. B*, 38(7):4752–4760, Sep 1988. 5.1

[37] J. Gruber, H. Miller, T. Hoffmann, G. Rohrer, and A. Rollett. Misorientation texture development during grain growth. part i: Simulation and experiment. *Acta Materialia*, 57(20):6102 – 6112, 2009. 5.1

[38] N. Hansen and D. J. Jensen. Development of microstructure in fcc metals during cold work. *Philosophical Transactions of the Royal Society of London. Series A:Mathematical, Physical and Engineering Sciences*, 357(1756):1447–1469, 1999. 6.4.2

[39] C. Hefferan, S. F. Li, J. Lind, U. Lienert, A. D. Rollett, and R. Suter. Observation of grain growth in high purity nickel. 2012. 5.2.1, 5.6

[40] C. M. Hefferan, S. F. Li, J. F. Lind, U. Lienert, A. D. Rollett, P. Winblatt, and R. M. Suter. Statistics of high purity nickel microstructure from high energy x-ray diffraction microscopy. *Computers, Materials, & Continua*, 14:209–219, 2009. 3.5.5, 5.2.2

[41] R. Hill. *The Meathematical Theory of Plasticity*. Oxford, 1950. 6.4.2, 6.5.1, 6.5.1

[42] M. Hillert. On the theory of normal and abnormal grain growth. *Acta Metallurgica*, 13(3):227 – 238, 1965. 5.4.1

[43] H. Hoppe, T. DeRose, T. Duchamp, M. Halstead, H. Jin, J. McDonald, J. Schweitzer, and W. Stuetzle. Piecewise smooth surface reconstruction. In *Proceedings of the 21st annual conference on Computer graphics and interactive techniques*, SIGGRAPH '94, pages 295–302, New York, NY, USA, 1994. ACM. 4.3.1

[44] F. J. Humphreys and M. Hatherly. *Recrystallization and Related Annealing Phenomena*. A Pergamon Title, 2004. 3.1, 5.1

[45] O. Hunderi and N. Ryum. The kinetics of normal grain growth. *Journal of Materials Science*, 15:1104–1108, 1980. 10.1007/BF00551798. 5.4.1

[46] C. E. K. III and L. Q. Chen. Computer simulation of 3-d grain growth using a phase-field model. *Acta Materialia*, 50(12):3059 – 3075, 2002. 5.1

[47] B. Jakobsen, H. F. Poulsen, U. Lienert, J. Almer, S. D. Shastri, H. O. Sørensen, C. Gundlach, and W. Pantleon. Formation and subdivision of deformation structures during plastic deformation. *Science*, 312(5775):889–892, 2006. 1.1, 1.3, 6.3.1

[48] T. Ju, F. Losasso, S. Schaefer, and J. Warren. Dual contouring of hermite data. *ACM Trans. Graph.*, 21:339–346, July 2002. 4.3.2

[49] M. Kazhdan, M. Bolitho, and H. Hoppe. Poisson surface reconstruction. In *Proceedings of the fourth Eurographics symposium on Geometry processing*, SGP '06, pages 61–70, Aire-la-Ville, Switzerland, Switzerland, 2006. Eurographics Association. 4.3.1

[50] C.-S. Kim, A. D. Rollett, and G. S. Rohrer. Grain boundary planes: New dimensions in the grain boundary character distribution. *Scripta Materialia*, 54(6):1005 – 1009, 2006. Viewpoint set no. 40: Grain boundary engineering. 5.1

[51] D. A. Klain. A short proof of hadwiger's characterization theorem. *Mathematika*, 42(02):329–339, 1995. 4

[52] L. P. Kobbelt, M. Botsch, U. Schwanecke, and H.-P. Seidel. Feature sensitive surface extraction from volume data. In *Proceedings of the 28th annual conference on Computer graphics and interactive techniques*, SIGGRAPH '01, pages 57–66, New York, NY, USA, 2001. ACM. 4.3.2

[53] U. F. Kocks, C. N. Tomé, H. R. Wenk, and H. Mecking. *Texture and Anisotropy: Preferred Orientations in Polycrystals and their Effect on Materials Properties*. Cambridge University Press, 2000. 6.2, 6.4.2, 6.5.1

[54] R. Larsen and B. Adams. New stereology for the recovery of grain-boundary plane distributions in the crystal frame. *Metallurgical and Materials Transactions A*, 35:1991–1998, 2004. 10.1007/s11661-004-0148-y. 3.1, 4.1, 5.1

[55] B. C. Larson, W. Yang, G. E. Ice, J. D. Budai, and J. Z. Tischler. Three-dimensional x-ray structural microscopy with submicrometre resolution. *Nature*, 415(6874):887–890, Feb. 2002. 1.1, 3.1, 5.1, 5.6, 6.2

[56] E. M. Lauridsen, S. Schmidt, R. M. Suter, and H. F. Poulsen. Tracking: a method for structural characterization of grains in powders or polycrystals. *Journal of Applied Crystallography*, 34(6):744–750, Dec 2001. Graindex. 2.4, 3.1, 3.3

[57] S. M. LaValle. *Planning Algorithms*. Cambridge University Press, Cambridge, U.K., 2006. Available at http://planning.cs.uiuc.edu/. 3.5.3

[58] R. A. Lebensohn. N-site modeling of a 3d viscoplastic polycrystal using fast fourier transform. *Acta Materialia*, 49(14):2723 – 2737, 2001. 6.4.2, 6.7

[59] S.-B. Lee, A. D. Rollett, and G. S. Rohrer. Three-dimensional microstructure reconstruction using fib-oim. *Materials Science Forum*, 558-559:6, 2007. Anglais. 1.1, 4.1, 5.1

[60] L. E. Levine, B. C. Larson, W. Yang, M. E. Kassner, J. Z. Tischler, M. A. Delos-Reyes, R. J. Fields, and W. Liu. X-ray microbeam measurements of individual dislocation cell elastic strains in deformed single-crystal copper. *Nat Mater*, 5(8):619–622, Aug. 2006. 3.6.2

[61] J. P. Lewis, F. Pighin, and K. Anjyo. Scattered data interpolation and approximation for computer graphics. In *ACM SIGGRAPH ASIA 2010 Courses*, SA '10, pages 2:1–2:73, New York, NY, USA, 2010. ACM. 4.2.3

[62] U. Lienert, M. Brandes, J. Bernier, J. Weiss, S. Shastri, M. Mills, and M. Miller. In situ single-grain peak profile measurements on ti-7al during tensile deformation. *Materials Science and Engineering: A*, 524(1-2):46 – 54, 2009. Special Topic Section: Probing strains and Dislocation Gradients with diffraction. 1.1, 3.6.2, 6.2

[63] U. Lienert, M. Brandes, J. V. Bernier, M. Mills, H. Miller, C. Hefferan, S. F. Li, J. Lind, and R. Suter. 3dxrd at the advanced photon source: Orientation mapping and deformation studies. In *Proceedings 31st International Risoe Symposium*, 2010. 2.3.3, 3.5.5

[64] W. E. Lorensen and H. E. Cline. Marching cubes: A high resolution 3d surface construction algorithm. *SIGGRAPH Comput. Graph.*, 21:163–169, August 1987. 4.3.2

[65] N. Louat. On the theory of normal grain growth. *Acta Metallurgica*, 22(6):721 – 724, 1974. 5.4.1

[66] P. Lounesto. *Clifford Algebras and Spinors*. Cambridge University Press, 2001. 4.2.2

[67] W. Ludwig, P. Cloetens, J. Härtwig, J. Baruchel, B. Hamelin, and P. Bastie. Three-dimensional imaging of crystal defects by 'topo-tomography'. *Journal of Applied Crystallography*, 34(5):602–607, Oct 2001. Topo-tomography. 3.3

[68] W. Ludwig, S. Schmidt, E. M. Lauridsen, and H. F. Poulsen. X-ray diffraction contrast tomography: a novel technique for three-dimensional grain mapping of polycrystals. I. Direct beam case. *Journal of Applied Crystallography*, 41(2):302–309, Apr 2008. 3.3, 5.3

[69] Q. Ma and D. R. Clarke. Size dependent hardness of silver single crystals. *Journal of Materials Research*, 10:853–863, 1995. 6.3.3

[70] R. D. MacPherson and D. J. Srolovitz. The von neumann relation generalized to coarsening of three-dimensional microstructures. *Nature*, 446(7139):1053–1055, Apr. 2007. 4.3.1, 4, 4.4.1, 4.4.2, 4.4.3, 5.1, 5.4.2, 5.5

[71] M. P. Miller, J. V. Bernier, J.-S. Park, and A. Kazimirov. Experimental measurement of lattice strain pole figures using synchrotron x rays. *Review of Scientific Instruments*, 76(11):113903, 2005. 6.2

[72] S. Mishra, P. Pant, K. Narasimhan, A. Rollett, and I. Samajdar. On the widths of orientation gradient zones adjacent to grain boundaries. *Scripta Materialia*, 61(3):273 – 276, 2009. Kernel averaged misorientation. 4.2.2, 6.4.2

[73] N. J. Mitra and A. Nguyen. Estimating surface normals in noisy point cloud data. In *Proceedings of the nineteenth annual symposium on Computational geometry*, SCG '03, pages 322–328, New York, NY, USA, 2003. ACM. 4.3.1

[74] W. W. Mullins. Two-dimensional motion of idealized grain boundaries. *Journal of Applied Physics*, 27(8):900–904, 1956. 4.4.2, 5.1

[75] W. W. Mullins. The statistical self similarity hypothesis in grain growth and particle coarsening. *Journal of Applied Physics*, 59(4):1341 –1349, feb 1986. 5.4.1

[76] G. M. Nielson. Mc*: Star functions for marching cubes. In *Proceedings of the 14th IEEE Visualization 2003 (VIS'03)*, VIS '03, pages 9–, Washington, DC, USA, 2003. IEEE Computer Society. 4.3.2

[77] G. M. Nielson and B. Hamann. The asymptotic decider: resolving the ambiguity in marching cubes. In *Proceedings of the 2nd conference on Visualization '91*, VIS '91, pages 83–91, Los Alamitos, CA, USA, 1991. IEEE Computer Society Press. 4.3.2

[78] J. Nye. Some geometrical relations in dislocated crystals. *Acta Metallurgica*, 1(2):153 – 162, 1953. 4.2.2

[79] D. L. Olmsted, S. M. Foiles, and E. A. Holm. Survey of computed grain boundary properties in face-centered cubic metals: I. grain boundary energy. *Acta Materialia*, 57(13):3694 – 3703, 2009. 5.1, 5.4.1, 5.5, 5.6

[80] D. L. Olmsted, E. A. Holm, and S. M. Foiles. Survey of computed grain boundary properties in face-centered cubic metals–ii: Grain boundary mobility. *Acta Materialia*, 57(13):3704 – 3713, 2009. 5.4.1, 5.4.2, 5.5, 5.6

[81] S. Osher and N. Paragios. *Geometric Level Set Methods in Imaging,Vision,and Graphics*. Springer-Verlag New York, Inc., Secaucus, NJ, USA, 2003. 3.3, 3.3.1, 4.2.1

[82] J. p. Pons, F. Ségonne, J. d. Boissonnat, L. Rineau, M. Yvinec, and R. Keriven. High-quality consistent meshing of multi-label datasets. In *Information Processing in Medical Imaging*, pages 198–210, 2007. 4.2.2, 4.3.2

[83] J.-S. Park, P. Revesz, A. Kazimirov, and M. P. Miller. A methodology for measuring in situ lattice strain of bulk polycrystalline material under cyclic load. *Review of Scientific Instruments*, 78(2):023910, 2007. 1.1, 3.6.2, 6.2

[84] J. R. Parker. *Algorithms for Image Processing and Computer Vision*. Wiley, 2010. 3.3, 3.3.1, 4.2.1

[85] S. Plantinga and G. Vegter. Isotopic approximation of implicit curves and surfaces. In *Proceedings of the 2004 Eurographics/ACM SIGGRAPH symposium on Geometry processing*, SGP '04, pages 245–254, New York, NY, USA, 2004. ACM. 4.3.2, 4.3.2

[86] D. A. Porter and K. E. Easterling. *Phase Transformations in Metals and Alloys*. CRC Press, 1992. 5.4.1

[87] H. F. Poulsen. A six-dimensional approach to microtexture analysis. *Philosophical Magazine*, 83:2761–2778, Aug. 2003. 3.1, 3.3, 3.3, 3.5.5, 3.6.2

[88] H. F. Poulsen. *Three-Dimensional X-Ray Diffraction Microscopy*. Springer Verlag, 2004. 1.1, 1, 3.3, 3.3, 3.5.5, 5.1, 5.3, 5.6, 6.2

[89] H. F. Poulsen, L. Margulies, S. Schmidt, and G. Winther. Lattice rotations of individual bulk grains: Part i: 3d x-ray characterization. *Acta Materialia*, 51(13):3821 – 3830, 2003. 1.3, 6.3.1, 6.5.1, 6.5.1

[90] H. F. Poulsen, S. F. Nielsen, E. M. Lauridsen, S. Schmidt, R. M. Suter, U. Lienert, L. Margulies, T. Lorentzen, and D. Juul Jensen. Three-dimensional maps of grain boundaries and the stress state of individual grains in polycrystals and powders. *Journal of Applied Crystallography*, 34(6):751–756, Dec 2001. 2.4, 3.6.2, 6.2

[91] H. F. Poulsen and S. Schmidt. Reconstruction of grain boundaries in polycrystals by filtered back-projection of diffraction spots. *Journal of Applied Crystallography*, 36(2):319–325, Apr 2003. Filtered Back Projection method. 3.1, 3.3, 3.5.5

[92] S. Ren, E. Kenik, K. Alexander, and A. Goyal. Exploring spatial resolution in electron back-scattered diffraction experiments via monte carlo simulation. *Microscopy and Microanalysis*, 4(01):15–22, 1998. 6.2

[93] F. Rhines, K. Craig, and R. DeHoff. Mechanism of steady-state grain growth in aluminum. *Metallurgical and Materials Transactions B*, 5:413–425, 1974. 10.1007/BF02644109. 5.1

[94] G. S. Rohrer. Influence of interface anisotropy on grain growth and coarsening. *Annual Review of Materials Research*, 35(1):99–126, 2005. 5.5

[95] G. S. Rohrer, E. A. Holm, A. D. Rollett, S. M. Foiles, J. Li, and D. L. Olmsted. Comparing calculated and measured grain boundary energies in nickel. *Acta Materialia*, 58(15):5063 – 5069, 2010. 5.4.1

[96] G. S. Rohrer, D. M. Saylor, B. E. Dasher, B. L. Adams, A. D. Rollett, and P. Wynblatt. The distribution of internal interfaces in polycrystals. *International Journal of Materials Research and Advanced Techniques*, (4):84, 2004. Allemand. 5.1

[97] A. D. Rollett. Private communications. 4.2.1

[98] A. D. Rollett, S.-B. Lee, R. Campman, and G. Rohrer. Three-dimensional characterization of microstructure by electron back-scatter diffraction. *Annual Review of Materials Research*, 37(1):627–658, 2007. 5.1

[99] D. L. Sahagian and A. A. Proussevitch. 3d particle size distributions from 2d observations: stereology for natural applications. *Journal of Volcanology and Geothermal Research*, 84(3-4):173 – 196, 1998. 3.1, 4.1, 5.1

[100] D. Saylor, J. Fridy, B. El-Dasher, K.-Y. Jung, and A. Rollett. Statistically representative three-dimensional microstructures based on orthogonal observation sections. *Metallurgical and Materials Transactions A*, 35:1969–1979, 2004. 10.1007/s11661-004-0146-0. 4.1

[101] S. Schaefer, T. Ju, and J. Warren. Manifold dual contouring. *IEEE Transactions on Visualization and Computer Graphics*, 13:610–619, 2007. 4.3.2

[102] S. Schaefer and J. Warren. Dual contouring: "the secret sauce". 4.3.2

[103] N. Scheerbaum, Y. Lai, T. Leisegang, M. Thomas, J. Liu, K. Khlopkov, J. McCord, S. Fhler, R. Trger, D. Meyer, L. Schultz, and O. Gutfleisch. Constraint-dependent twin variant distribution in ni2mnga single crystal, polycrystals and thin film: An ebsd study. *Acta Materialia*, 58(14):4629 – 4638, 2010. 3.5.5

[104] S. Schmidt, S. F. Nielsen, C. Gundlach, L. Margulies, X. Huang, and D. J. Jensen. Watching the growth of bulk grains during recrystallization of deformed metals. *Science*, 305(5681):229–232, 2004. 1.1, 5.1

[105] S. Schmidt, H. F. Poulsen, and R. M. Suter. Grainsweeper: an algorithm for generation of three-dimensional orientation maps by x-ray diffraction. 2.4, 3.1

[106] S. Schmidt, H. F. Poulsen, and G. B. M. Vaughan. Structural refinements of the individual grains within polycrystals and powders. *Journal of Applied Crystallography*, 36(2):326–332, Apr 2003. 3.4.5

[107] P. Schröder. What can we measure? In A. I. Bobenko, J. M. Sullivan, P. Schrder, and G. M. Ziegler, editors, *Discrete Differential Geometry*, volume 38 of *Oberwolfach Seminars*, pages 263–273. Birkhäuser Basel, 2008. 10.1007/978-3-7643-8621-4_14 . 4

[108] A. J. Schwartz, M. Kumar, B. L. Adams, and D. P. Field, editors. *Electron Backscatter Diffraction in Materials Science*. Springer, 2009. 3.1, 4.2.1, 5.1, 6.2

[109] J. R. Shewchuk. Tetrahedral mesh generation by delaunay refinement. In *Proc. 14th Annu. ACM Sympos. Comput. Geom*, pages 86–95, 1998. 4.3.2

[110] J. R. Shewchuk. What is a good linear element? - interpolation, conditioning, and quality measures. In *In 11th International Meshing Roundtable*, pages 115–126, 2002. 2

[111] K. Shoemake. Animating rotation with quaternion curves. *SIGGRAPH Comput. Graph.*, 19:245–254, July 1985. 4.2.2

[112] S. Sintay. *Statistical Microstructure Generation and 3D Microstructure Geometry Extraction*. PhD thesis, Carnegie Mellon University, 2010. 4.3.1, 4.3.3, 4.4.3

[113] C. S. Smith. Grain shapes and other metallurgical applications of toplogy. *Metal Interfaces edited by C. Herring (ASM, Metal Park, Ohio, 1952)*, page 65, 1952. 5.1

[114] S. Sun, B. L. Adams, and W. E. King. Observations of lattice curvature near the interface of a deformed aluminium bicrystal. *Philosophical Magazine A*, 80(1):9–25, 2000. 6.2, 6.4.2

[115] R. M. Suter. Simulation code development and checking. 2008. 2.2.2

[116] R. M. Suter, D. Hennessy, C. Xiao, and U. Lienert. Forward modeling method for microstructure reconstruction using x-ray diffraction microscopy: Single-crystal verification. *Review of Scientific Instruments*, 77(12):123905, 2006. 1.1, 1.2, 1.3, 2.2.2, 2.2.2, 3.1, 3.4.3, 3.5, 5.3.1, 6.2

[117] R. E. Tarjan and J. van Leeuwen. Worst-case analysis of set union algorithms. *J. ACM*, 31:245–281, March 1984. 4.2.1

[118] G. Taubin. Distance approximations for rasterizing implicit curves. *ACM Trans. Graph.*, 13:3–42, January 1994. 4.3.2

[119] G. I. Taylor. The mechanism of plastic deformation of crystals. part i. theoretical. *Proceedings of the Royal Society of London. Series A*, 145(855):362–387, 1934. 6.4.2

[120] M. D. Uchic, D. M. Dimiduk, J. N. Florando, and W. D. Nix. Sample dimensions influence strength and crystal plasticity. *Science*, 305(5686):986–989, 2004. 6.3.3

[121] M. D. Uchic, M. A. Groeber, D. M. Dimiduk, and J. Simmons. 3d microstructural characterization of nickel superalloys via serial-sectioning using a dual beam fib-sem. *Scripta Materialia*, 55(1):23 – 28, 2006. 5.1

[122] F. Uyar, S. Wilson, J. Gruber, S.-B. Lee, S. Sintay, R. A. D., and S. D. J. Testing a curvature driven moving finite element grain growth model with the generalized three dimensional von neumann relation. *International Journal of Materials Research*, 100(4):7, 2009. Anglais. 5.1

[123] J. Venables. The electron microscopy of deformation twinning. *Journal of Physics and Chemistry of Solids*, 25(7):685 – 690, IN1–IN6, 691–692, 1964. 6.5.1

[124] D. T. Verebelyi, D. K. Christen, R. Feenstra, C. Cantoni, A. Goyal, D. F. Lee, M. Paranthaman, P. N. Arendt, R. F. DePaula, J. R. Groves, and C. Prouteau. Low angle grain boundary transport in yba[sub 2]cu[sub 3]o[sub 7 - delta] coated conductors. *Applied Physics Letters*, 76(13):1755–1757, 2000. 1.1

[125] J. von Neumann. *Metal Interfaces edited by C. Herring (ASM, Metal Park, Ohio, 1952)*, page 108, 1952. 4.4.2, 5.1

[126] B. E. Warren. *X-Ray Diffraction*. Dover, 1990. 2.2.1, 3.3.1, 3.5.5, 6.3.1

[127] M. Winning, G. Gottstein, and L. S. Shvindlerman. Stress induced grain boundary motion. *Acta Materialia*, 49(2):211 – 219, 2001. 5.1

[128] S. Wright and B. Adams. Automatic analysis of electron backscatter diffraction patterns. *Metallurgical and Materials Transactions A*, 23:759–767, 1992. 10.1007/BF02675553. 5.1

[129] Z. Wu and J. M. Sullivan. Multiple material marching cubes algorithm. *International Journal for Numerical Methods in Engineering*, 58(2):189–207, 2003. 4.2.2

[130] A. Yershova, S. Jain, S. M. LaValle, and J. C. Mitchell. Generating uniform incremental grids on so(3) using the hopf fibration. *The International Journal of Robotics Research*, 29(7):801–812, 2010. 3.5.1

[131] A. Yershova and S. LaValle. Deterministic sampling methods for spheres and so(3). In *Robotics and Automation, 2004. Proceedings. ICRA '04. 2004 IEEE International Conference on*, volume 4, pages 3974 – 3980 Vol.4, 26-may 1, 2004. 3.5.1, 3.5.1, 3.5.1

[132] Y. Zhang, C. Bajaj, and B.-S. Sohn. Adaptive and quality 3d meshing from imaging data. In *Proceedings of the eighth ACM symposium on Solid modeling and applications*, SM '03, pages 286–291, New York, NY, USA, 2003. ACM. 4.3.2

[133] Y. Zhang, C. Bajaj, and B.-S. Sohn. 3d finite element meshing from imaging data. *Computer Methods in Applied Mechanics and Engineering*, 194(48-49):5083 – 5106, 2005. Unstructured Mesh Generation. 4.3.2

[134] Y. Zhang, C. Bajaj, and G. Xu. Surface smoothing and quality improvement of quadrilateral/hexahedral meshes with geometric flow. In B. W. Hanks, editor, *Proceedings of the 14th International Meshing Roundtable*, pages 449–468. Springer Berlin Heidelberg, 2005. 4.3.1

[135] Y. Zhang, T. J. Hughes, and C. L. Bajaj. An automatic 3d mesh generation method for domains with multiple materials. *Computer Methods in Applied Mechanics and Engineering*, 199(5-8):405 – 415, 2010. Computational Geometry and Analysis. 4.2.2, 4.3.2

[136] D. Zollner and P. Streitenberger. Three-dimensional normal grain growth: Monte carlo potts model simulation and analytical mean field theory. *Scripta Materialia*, 54(9):1697 – 1702, 2006. 5.1